DEVELOPMENT OF RAMAN SPECTROSCOPY FOR THE CLINICAL CHARACTERIZATION OF INFLAMMATORY BOWEL DISEASE

By

Isaac James Pence

Dissertation

Submitted to the Faculty of the

Graduate School of Vanderbilt University

in partial fulfillment of the requirements

for the degree of

DOCTOR OF PHILOSOPHY

in

Biomedical Engineering

December, 2016

Nashville, Tennessee

Approved:

Anita Mahadevan-Jansen, Ph.D.

Alan J. Herline, M.D.

E. Duco Jansen, Ph.D.

Yu Shyr, Ph.D.

Keith T. Wilson, M.D

For my family & friends

and

in honor of

Dean Paras

ACKNOWLEDGEMENTS

This work was made possible due to the support from the following funding sources: NIH R01 HD081121, NIH F31 CA168238, NIH grant R01AT004821, an American Society for Laser Medicine and Surgery student research grant, NIH National Institutes of General Medical Sciences R25-sponsored fellowship and travel grant to attend the 2013 national short course in computational Biophotonics, a Department of Veterans Affairs Merit Review grant I01BX001453, the Vanderbilt Digestive Disease Research Center funded by NIH grant P30DK058404, the Vanderbilt Center for Mucosal Inflammation and Cancer, the Vanderbilt CTSA grant UL1 TR000445 from NCATS/NIH, NCI/NIH Cancer Center Support Grant 2P30 CA068485-14, the Vanderbilt Mouse Metabolic Phenotyping Center Grant 5U24DK059637-13, and whole slide imaging was performed in the Digital Histology Shared Resource at Vanderbilt University Medical Center (www.mc.vanderbilt.edu/dhsr).

I would like to thank my advisor Dr. Anita Mahadevan-Jansen for her tireless help guidance. Over the past eight years she has made tremendous efforts to promote my development as a researcher and given me academic freedom and responsibility, along with a significant amount of trust, for which I am truly grateful. My dissertation committee members – Dr. Alan Herline, Dr. Duco Jansen, Dr. Yu Shyr, and Dr. Keith Wilson – were all instrumental to the completion of this multifaceted project. I have also had the benefit of

guidance from several committee-like collaborators including Dr. Jeff Reese, Dr. Kshipra Singh, Dr. Xiaohong Bi, Dr. David Schwartz, Dr. Dawn Beaulieu, Dr. Sarah Horst, Dr. Molly Cone, Dr. Kay Washington, and Dr. William Gibson, all of whom allowed me time to discuss my project, facilitated study execution, allowed me to interfere with their clinical duties, and directed me down the needed research paths despite their busy schedules. Finally, I'd like to thank all of the staff members of the Vanderbilt GI Endoscopy lab, surgical pathology lab, translation pathology shared resource, and digital histology shared resource for their assistance and friendship, without which this project would not have attained the same success.

Over my many years, there have been several students, postdoctoral researchers, faculty, and staff that have helped me to accomplish my PhD. Christine O'Brien has been a constant confidant and collaborator for innumerable questions and Raman spectroscopy projects. Oscar Ayala is another graduate student that has gone above and beyond to assist me with data collection and experimental setup. I have been lucky to work with such driven and capable students. I also would like to thank Dr. Elizabeth Vargis who took me under her wing when I first joined the lab and continues to provide a beacon for me as I search for guidance. Dr. Quyen Nguyen also deserves thanks for hours of discussion, data collection, and understanding that he has provided to me as we developed and explored several avenues for Raman spectroscopy. Furthermore, Dr. Chetan Patil deserves thanks for his willingness for in depth

discussions and explanations of the theories and practices that we undertake on a daily basis, to help me expand my understanding of techniques and instrumentation, and guidance throughout my project and development. It has been through these and many other beneficial interactions that I have developed as a researcher and person.

Finally, I would like to thank my family, friends, and pets for their constant companionship, comradery, and support during my graduate studies. Thank you to my parents and siblings for their unconditional love and support despite the time I have spent away. Also to my partner Amanda who is able to simultaneously practice medicine and conduct research; your constant motivation ad work ethic are traits that I will continue to strive to emulate. Lastly, my cat Carly who was a frequent co-author on my manuscripts and thesis and a constant source of entertainment, distraction, and affection through the late nights and long hours completing my PhD. I hope to have a fraction of her energy, charisma, and focus as I continue down the path to academia.

After so many years being a member of the lab and department, I will continue to pursue new biomedical advancements and technologies with the constant inspiration of a fellow graduate student, close friend, and guide, Dean Paras, who we lost to cancer. His courage, humor, and friendship will continue to inspire my efforts for years to come.

TABLE OF CONTENTS

LIST OF FIGURES

LIST OF TABLES

CHAPTER 1

INTRODUCTION

1.1 Motivation and objectives

The goal of this PhD is to correlate the changes that occur in the colon as part of inflammatory bowel disease to differences seen in Rama spectra. This work demonstrates that the sensitivity of Raman spectroscopy (RS) to colon changes can be used to detect and characterize inflammatory bowel disease in humans and experimental colitis in mice.

In 2015, inflammatory bowel disease (IBD), including ulcerative colitis (UC) and Crohn's colitis (CC), was estimated to affect nearly 1.5 million Americans and 2.2 million Europeans, and the incidence is increasing worldwide.[1-3] Despite advances in therapy, hospitalization rates for IBD, particularly CC, have shown significant increase, incurring a substantial rise in inflation-adjusted economic burden.[4] Ulcerative and Crohn's colitis are two distinct forms of IBD and require different medical and surgical management despite significant overlap in clinical presentation, symptoms, and disease progression. Currently, the distinction between UC and CC is made based on inexact clinical, radiologic, endoscopic, and pathologic features,[5-8] such that in up to 15% IBD cases, indeterminate colitis (IC, or IBD unspecified) is

diagnosed because of the difficulty in distinguishing between UC and CC.[3,9] In these patients, diagnosis ultimately relies on long term follow up based on success or failure of existing treatment and recurrence of disease. Therefore, accurate diagnosis of IBD is of paramount importance for appropriate medical and surgical care, intervention, and prognosis.

Development of new technologies that can improve understanding of IBD and aide objective diagnosis is urgently needed. One of the objectives of this research is to apply RS, an optical technique, as a novel tool to characterize IBD *in vivo* during colonoscopy. In order to develop robust techniques that can effectively evaluate tissue changes several steps must be undertaken including optimization of instrumentation for this application, characterization of the effects of colon variability and disease severity, and evaluate a clinical population to demonstrate feasibility of this technique for further application.

Therefore, the overall objective of this doctoral research is to characterize the effects that IBD related changes in the colon have on Raman spectra in order to develop a viable optical tool for studying IBD and provide and accurate, objective aide for diagnosis and monitoring.

1.2 Specific aims

Aim 1: Develop a multimodal probabilistic Monte Carlo model incorporating absorption, elastic scattering, Raman scattering and

fluorescence to evaluate fiber optic probe designs used for Raman spectroscopy. Fiber optic probes are the primary interface between most Raman instruments and the target samples. Numerous designs have been implemented for *in vivo* applications for soft tissues however most have been optimized based on theoretical performance in low or non-scattering scenarios that are not representative of biomedical applications. In this aim, a probabilistic model incorporating all of the competing optical phenomena detected by fiber optic Raman spectroscopy probes was implemented and experimentally validated in both biological and synthetic phantoms to compare four distinct volume integrating probe designs. Modelling results were evaluated between probe designs relative to experimental results and theoretical design parameters for each probe, such as excitation and collection cone overlap, surface area for detection, and fiber optic collection angle.

Aim 2: Characterize IBD and normal signals *in vivo* during colonoscopy and assess influential patient variables that impact disease discrimination. Previous studies have demonstrated promising disease discrimination for *ex vivo* IBD tissue biopsies based on Raman spectra. To evaluate the performance of Raman spectroscopy *in vivo*, patients undergoing colonoscopy in the VUMC were recruited and measured under this aim. Raman spectra were collected from multiple locations in each segment of the colon and compared with endoscopic findings and tissue biopsies obtained from each measurement site as determined by the clinician. Spectral classification was

implemented using statistical multivariate analysis relative to established diagnosis which served as the gold standard. Subsequent discrimination based on stratification of colon segment and disease severity was implemented to demonstrate potential for improved performance when accounting for relevant patient and disease variables.

Aim 3: Characterize the effects of IBD disease presentation on Raman spectra acquired from the colon in (A) human colectomy specimens and (B) a murine model of experimental colitis. In this aim, Raman spectra were acquired from excised colon tissues to more fully characterize the complex disease presentation as a function of inter-anatomical variability and disease severity. To thoroughly assess the impact of colon segment and histological markers of chronic and acute disease severity, total or partial colon resection samples were collected from patients undergoing colectomy procedures at VUMC. Gross mapping of the tissue with a Raman fiber optic probe was correlated with histologically scored tissue biopsies to establish factors that significantly impact the Raman spectral measurements of inflammatory disease in the colon. To assess the impact of active inflammation on acquired spectra with relative control over disease severity, a murine model of experimental colitis was be evaluated with *ex vivo* Raman microspectroscopic mapping and correlated with clinical disease indicators and histologic scoring of epithelial injury and inflammation. Hypothesis: The degree of active inflammation will impact acquired spectra and controlled

murine models of IBD will yield information to improve classification accuracy *in vivo*.

In Appendix 1, an evaluation of several user, instrument, and physiological factors that influence Raman spectra collected from *in vivo* tissues are discussed. Multiple identical clinical fiber optic probe based Raman spectroscopy systems were used to measure the skin from multiple anatomical sites across a pilot cohort of subjects. This work supports prior reports of intra-anatomical and inter-patient variability sources as influential factors for *in vivo* Raman spectra, as well as provides guidelines for mitigating the impact of non-physiological sources of spectral variability.

The combination of these three Aims and Appendix 1 serves to establish the potential for *in vivo* Raman spectroscopy as a clinical adjunct for disease discrimination and evaluation of inflammatory bowel disease. Further, this work establishes new methods for evaluating instrumentation and provides a characterization of several influential variables from patients and models of inflammatory disease that impact Raman spectral measurements. The completion of this project demonstrates the sensitivity of Raman scattering to subtle biochemical changes in colon tissues associated with anatomic variation and disease presentation. Understanding these influential factors resulted in improved classification of disease type based on decoupling the complex interplay of disease and natural variations in the colon.

1.3 Summary of chapters

Following this introductory chapter, Chapter 2 contains relevant background information on the biology and anatomy of the colon, inflammatory bowel disease, as well as a review of developments for clinical instrumentation and applications of Raman spectroscopy.

In Chapter 3, an assessment of the instrumentation designs utilized for fiber optic probe based Raman spectroscopy *in vivo* is undertaken based on a comparison of results generated from a new multimodal optical model and experimental results from both biological and synthetic phantoms.

Chapter 4 provides the first report on the sensitivity of *in vivo* RS from this research, or any other peer-reviewed work, specifically addressing differences between disease classes, colon segments, and disease severity in measurements obtained during colonoscopy from healthy control, Crohn's disease, or ulcerative colitis patients.

Chapter 5 details the effects of colon tissue variability on Raman spectra obtained from unique locations and disease presentations in colectomy tissues to decouple the interactions of disease and tissue variability effects based on histopathological scoring.

Chapter 6 presents the results of Raman microspectroscopic evaluation of a controlled experimental colitis model to interrogate the effects of disease severity and active inflammation in the colon wall compared with both clinical and histopathological indicators of disease.

Chapter 7 comprises a summary of the major results presented in this dissertation and potential avenues for future directions for this project. It also provides information about the impact of this research on the larger scientific field and society.

Appendix I entails a characterization of sources of variability associated with *in vivo* Raman spectroscopy. This chapter identifies and isolates the contributions from user, instrumentation, and physiology induced sources of variation, and presents guidelines for minimizing these effects for clinical applications of Raman spectroscopy.

1.4 References

1. Ananthakrishnan AN. Epidemiology and risk factors for IBD. Nature reviews Gastroenterology & hepatology. 2015;12(4):205-217.
2. Bernstein CN, Wajda A, Svenson LW, et al. The epidemiology of inflammatory bowel disease in Canada: A population based study. The American journal of gastroenterology. 2006;101(8):1945-1945.
3. Carvalho RS, Abadom V, Dilworth HP, Thompson R, Oliva-Hemker M, Cuffari C. Indeterminate colitis: a significant subgroup of pediatric IBD. Inflamm Bowel Dis. 2006;12(4):258-262.
4. Farrokhyar F, Swarbrick ET, Irvine EJ. A critical review of epidemiological studies in inflammatory bowel disease. Scandinavian journal of gastroenterology. 2001;36(1):2-15.
5. American Society for Gastrointestinal Endoscopy Standards of Practice C, Shergill AK, Lightdale JR, et al. The role of endoscopy in inflammatory bowel disease. Gastrointestinal endoscopy. 2015;81(5):1101-1121 e1101-1113.

6. Baumgart DC. The diagnosis and treatment of Crohn's disease and ulcerative colitis. Dtsch Arztebl Int. 2009;106(8):123-133.

7. Kornbluth A, Sachar DB, Gastroenterology AC. Ulcerative Colitis Practice Guidelines in Adults: American College of Gastroenterology, Practice Parameters Committee. The American journal of gastroenterology. 2010;105(3):500-500.

8. Lichtenstein GR, Hanauer SB, Sandborn WJ. Management of Crohn's disease in adults. The American journal of gastroenterology. 2009;104(2):465-483; quiz 464, 484.

9. Martland GT, Shepherd NA. Indeterminate colitis: definition, diagnosis, implications and a plea for nosological sanity. Histopathology. 2007;50(1):83-96.

CHAPTER 2

BACKGROUND

2.1 Physiology of the normal colon and rectum

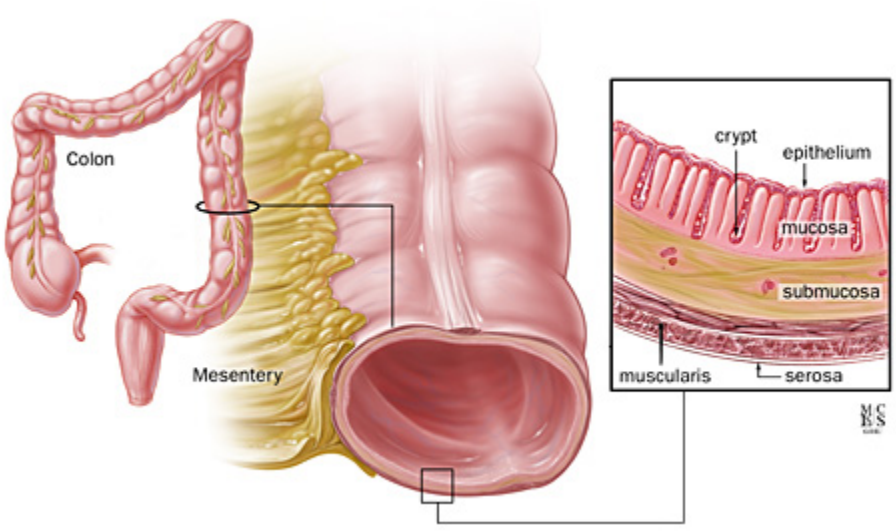

Figure 2.1. Anatomy of healthy human colon (courtesy of Johns Hopkins Gastroenterology and Hepatology).

The colon is the organ in the gastrointestinal (GI) tract responsible for concentrating waste through water and electrolyte absorption, storing and controlled evacuation of waste, and digestion and absorption of undigested food.[1,2] Extracting water, salt, and some fat soluble vitamins from the chyme deposited from the small intestine, the colon stores and transports feces prior to

elimination from the body. The colon is generally divided in to three segments, the right (cecum and ascending colon), transverse, and left (descending and sigmoid colon) colon which connects to the rectum. The outside of the colon is connected to the abdominal wall by folds of peritoneum (mesentery), in ascending, transverse, descending, and sigmoid colon segments.[3,4] As depicted in Figure 2.1, the colon is a muscular organ composed four layers found in other hollow GI organs: the mucosa, submucosa, circular muscle and longitudinal muscle layers. Unlike the small intestine which has a villous projections, the colon mucosa is relatively smooth with crypt invaginations. This mucosal layer, lining the inner lumen is composed of simple (non-ciliated) columnar epithelial cells and mucous secreting goblet cells to promote waste transport.[3,4] Haustral folds are a constantly changing anatomic factor caused by circular muscle contractions that last for hours. The outer longitudinal muscles, called tenia coli, are three equidistantly spaced bands that extend from the cecum to the rectum where they fuse to form a continuous muscular layer. The muscular contractions in the right colon cause mixing to facilitate water absorption, while feces is slowly moved in the left colon prior to reflexes that activate contractions to evacuate stool.[2] Due to the slow movement of waste through this organ, the colon also has a large population of commensal bacteria which are typically harmless and compete with potentially pathogenic microbes, promote motility, help maintain mucosal integrity, and make nutritional contributions.

2.2 Inflammatory bowel disease

Inflammatory bowel disease (IBD) describes a group of disorders in which the inner lining of the GI tract become inflamed. IBD affects nearly 1.5 million people in the United States and 2.2 million in Europe, with increasing incidence worldwide.[5-8] It has recently been cited that IBD is one of the five most prevalent gastrointestinal disease burdens in the US, with an annual overall health care cost of more than $1.7 billion.[9,10] The two major types of IBD are ulcerative colitis (UC) and Crohn's disease (CD), with different causes and discrete mechanisms of tissue damage.[11] Ulcerative colitis is limited to the colon whereas CD can rise in any part of the GI tract, although it often manifests itself in the colon. IBD contributes to significant morbidity and reduced quality of life; the estimated incidence and prevalence of 7-9 and 210-240 per 100,000 and 6-8 and 130-200 per 100,000, for UC and CD respectively.[12,13] Patients with IBD are at increased risk of developing colon cancer.[14,15] They also have an higher risk of endothelial dysfunction and coronary artery disease.[16] Despite advances in therapy, hospitalization and surgery rates for IBD in the United States have increased since 1990.[17,18] With the high drug costs, and up to 75% of CC and 25-33% of UC patients that require surgery in the long-term, IBD is one of the most costly conditions on a per year basis in the US, with expenses for CC surpassing diabetes, coronary artery disease, and chronic obstructive pulmonary disorder.[19,20] This reinforces the need to improve the current diagnostic and therapeutic strategies for IBD.

2.3 Crohn's disease

Crohn's disease is a chronic inflammatory disorder that can affect the entire GI tract. The key pathological feature is an inflammatory process that extends through all layers of the bowel wall. Microscopic examination of tissues from CD reveals lymphoid hyperplasia, diffuse granuloma infiltration, discrete noncaseating granulomas in the submucosa and lamina propria, diffuse edema, and monocytic infiltration in lymph nodules.[2] Aphthous ulcers, small superficial ulcerations, are the earliest mucosal lesion in CD. As disease progresses, these tiny lesions enlarge and coalesce to form longitudinal and transverse ulcers and have a characteristic cobblestone appearance from the deep mucosal ulceration and submucosal thickening.[2] Skip lesions, or discrete locations of inflammation surrounded by tissue without gross or histological abnormalities are also characteristic of Crohn's disease. CD is often signified by thickened fatty mesentery in the vicinity of the disease. As the mesentery are inflamed fibrosis of the bowel tissue can often cause adhesion of and may extend into all layers of the bowel wall, forming fistulae and abscesses (Figure 2.2).

Crohn's disease onset can occur at any age but most commonly begins between 15 and 30 years of age. There is a familial association of CD such that 20-30% of CD patients having a family history of the disorder, further indicating genetic influences.[2,5] In CD, the T-cell response is T-helper 1 (Th1) dominant. The activation of central immune-cell populations is eventually

accompanied by the production of a wide variety of nonspecific mediators of inflammation, such as cytokines, chemokines, and growth factors.[22-24] These mediators enhance the inflammatory process itself and tissue destruction, which eventuate in the clinical manifestations of disease.[25]

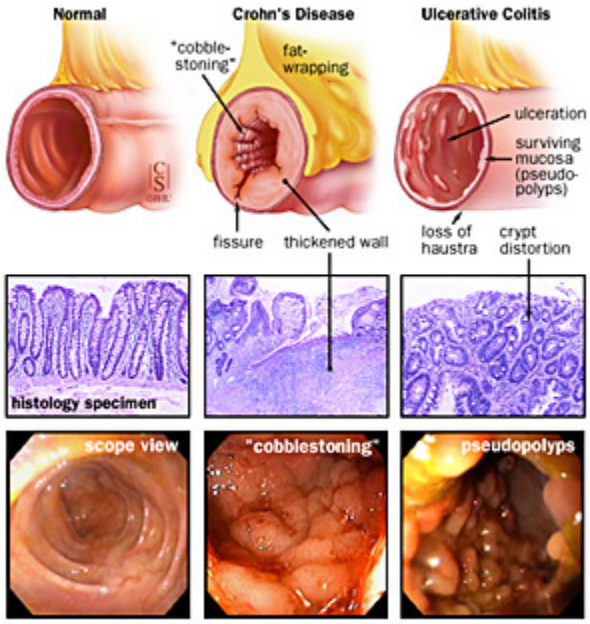

Figure 2.2. Histology slide of an UC and CC case (Courtesy Johns Hopkins Gastroenterology and Hepatology Resource Center, www.hopkins-gi.org).

2.4 Ulcerative colitis

Ulcerative colitis is a chronic inflammatory disease affecting the colonic mucosa from the rectum to the cecum. Characterized by rectal bleeding and diarrhea, remission and relapse, UC is limited to mucosal inflammation that does not become transmural (Figure 2.2).[2,5] Sharp localized abdominal pain and fistula formation are uncommon. Extensive superficial mucosal ulceration develops in conjunction with severe inflammation and the coincident

production of a complex mixture of inflammatory mediators. Histopathological features of UC include the presence of a significant number of neutrophils within the lamina propria and the crypts, where they form micro-abscesses.[21] Crypt abscesses may extend laterally and undermine the integrity of the mucosa on three sides, resulting in the formation of a hanging fragment of mucosa that appears in endoscopy and radiography as a pseudopolyp.[2,5] After mucosal destruction, epithelial healing processes cause the formation of highly vascular granulation tissue is formed.[2,26,27]

Ulcerative colitis typically occurs in patients between 20 and 50 years of age either as an acute attack or a chronic course with little pain. Roughly 70% of patients will have complete remission of symptoms between intermittent attacks, however another 15% will suffer from continuous symptoms without remission.[2,11] As UC is not a distinct clinical entity and has histological features that overlap with several other inflammatory states in the colon, the diagnosis relies on the discovery of several clinical and pathological criteria and exclusion of other causes for colitis such as infection.[2,11] In UC, the response is either Th2 [interleukin (IL) -4, IL-13] or is mediated by specialized cells such as natural killer T cells (NKT).[28,29]

2.5 IBD differentiation

It is extremely important to accurately differentiate between CD and UC as they have different prognoses and differing response to medical and surgical treatment. One method of medical care implements a "bottom-up" approach to treatment, as depicted in Figure 2.3, where the level of severity dictates the avenue for treatment.[2] certain medications have shown efficacy in the treatment of CD (methotrexate, natalizumab, and certolizumab), while others work well for UC (mesalamine). Long-term treatment with antibiotics (nitroimidazoles or clofazimine) is effective in patients with CD[30] while its efficacy in UC is not observed.[31] Current research and clinical trials indicate the development of new drugs that are specific for either UC[32-34] or CD[35-37] with more than 50 personalized medications under investigation.[38,39]

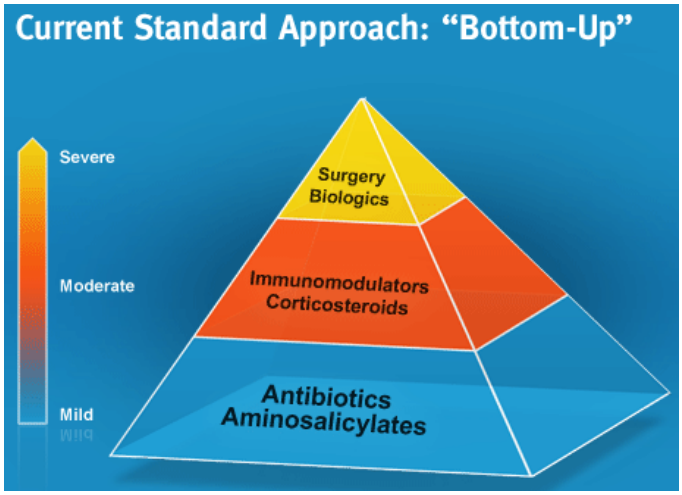

Figure 2.3. Standard approach for medical management of IBD. Courtesy of Crohn's and Colitis Foundation of America.

For surgical intervention and prognosis, it is vital to accurately delineate IBD because an errant diagnosis may result in serious consequences. The vast majority of patients with UC will benefit from surgery, such as restorative proctocolectomy (RPC) with ileal pouch-anal anastomosis (IPAA). In contrast, surgery for CD patients is generally not curative and can lead to severe complications as malnutrition and multiple surgical procedures. In fact, up to 50% of CD patients who undergo RPC with IPAA require removal of the pouch or diversion due to Crohn's recurrence or disease flare-ups in other parts of the GI tract.[40] For therapy and patient outcomes, the proper management of IBD calls for an accurate diagnostic tool that can distinguish between CD and UC, and potentially predict which patients will respond to specific medications and give clinicians an indicator for the most effective treatment option.

Current techniques for differentiating CD and UC have deficiencies in terms of diagnostic accuracy. The American College of Gastroenterology Practice Parameters Committee recommends a combination of clinical, endoscopic, histologic, radiographic and surgical findings to differentiate between CD and UC.[11,41,42] While certain features can be used to differentiate the diseases during routine colonoscopy and other procedures, many cases do not present definitive indicators of disease type. Ulcerative colitis is generally confirmed when a patient that presents with systemic features has colonoscopy and biopsy confirmed colitis and no presence of infectious or non-infectious causes, while the methods for CD diagnosis are more complex and dependent

upon patient presentation.[41] This distinction cannot always be made due to overlapping symptoms, as well as similarities in radiographic and histologic features.[43] Serological markers have limited sensitivity (65% for CD and 76% for UC) in differentiating UC from CD.[44] While 40 susceptibility genes for CD and UC have been identified,[45] testing is not readily available to the clinician nor do these genes account for the majority of IBD cases. The lack of a reliable method for differentiating CD and UC imposes a burden on the medical community. Up to 300,000 patients in the US cannot be diagnosed as UC or CD and they are labeled as indeterminate colitis (IC).[7] Additionally, failure to recognize characteristic signs of CD such as granulomas and transmural inflammation often leads to errors in pathological interpretation in at least 15% of the cases.[46] Thus, there is at least a 15% misdiagnosis rate of CD as UC in addition to the 15% of IC cases.[46] This results in approximately 600,000 patients in the US that cannot be correctly diagnosed as CD or UC and thus do not receive appropriate treatments. Limitations in current diagnostic methods, therefore, highlight the need for a rapid, accurate, automated method that can be used to differentiate patient disease as well as the degree of the inflammation. This could significantly improve the management of the disease with respect to both time and cost.

2.6 Clinical instrumentation and applications of Raman spectroscopy

Clinical diagnostic devices provide new sources of information that give insight about the state of health which can then be used to manage patient care. These tools can be as simple as an otoscope to better visualize the ear canal or as complex as a wireless capsule endoscope to monitor the gastrointestinal tract. It is with tools such as these that medical practitioners can determine when a patient is healthy and to make an appropriate diagnosis when he/she is not. The goal of diagnostic medicine then is to efficiently determine the presence and cause of disease in order to provide the most appropriate intervention. The earliest form of medical diagnostics relied on the eye - direct visual observation of the interaction of light with the sample. This technique was espoused by Hippocrates in his 5th century BCE work *Epidemics*, in which the pallor of a patient's skin and the coloring of the bodily fluids could be indicative of health. In the last hundred years, medical diagnosis has moved from relying on visual inspection to relying on numerous technological tools that are based on various types of interaction of the sample with different types of energy – light, ultrasound, radio waves, x-rays etc. Modern advances in science and technology have depended on enhancing technologies for the detection of these interactions for improved visualization of human health. Optical methods have been focused on providing this information in the micron to millimeter scale while ultrasound, x-ray, and radio waves have been key in aiding in the millimeter to centimeter scale. While a few optical technologies

have achieved the status of medical instruments, many remain in the research and development phase despite persistent effort by many researchers in the translation of these methods for clinical care. Of these, Raman spectroscopy has been described as a sensitive method that can provide biochemical information about tissue state while maintaining the capability of delivering this information in real-time, non-invasively, and in an automated manner. This review presents the various instrumentation considerations relevant to the clinical implementation of Raman spectroscopy and reviews a subset of interesting applications that have successfully demonstrated the efficacy of this technique for clinical diagnostics and monitoring in large ($n \geq 50$) *in vivo* human studies.

2.6.1 Why Raman spectroscopy?

As described by Dr. C.V. Raman in 1928, the Raman signal is usually weak (one in one hundred million incident photons) and "requires very powerful illumination for its observation."[47] Today, advances in laser sources and sensitive detectors enable the application of this scattering event for samples that are more complex than the original "dust-free liquids or gases." Raman peaks are typically spectrally narrow (a few wavenumbers) and in many cases can be associated with the vibration of a particular chemical bond (or normal mode dominated by the vibration of a single functional group) within a molecule.[48] Figure 2.4 displays an example Raman spectrum, that of

phosphatidylcholine, a phospholipid molecule, where each band can be correlated to specific stretching and bending modes of vibration in the molecule, thus providing a molecular fingerprint. Consequently, in tissue, which is composed of a complex mixture of molecules, the presence of the unique bands of phosphatidylcholine can be tracked resulting in the quantitative evaluation of the sample's chemical composition. Such quantitative or qualitative assessment in turn can be used to infer specific biochemical changes associated with tissue pathology or physiology for diagnosis or monitoring.

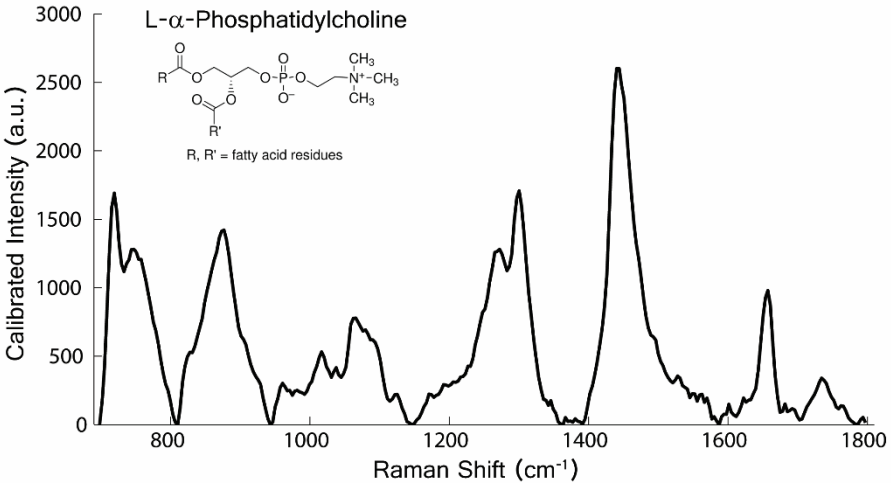

Figure 2.4. Raman spectrum of phosphatidylcholine, a phospholipid known to be present in cells and tissues, measured using a fiber optic probe based Raman system at 785 nm excitation. Characteristic spectral peaks correspond to molecular vibrations of the molecule of interest.

Thus Raman spectroscopy is a molecular specific technique that can be used to develop a fundamental biochemical understanding of tissue physiology and pathology and extend this knowledge for tissue diagnosis and monitoring.

The optical nature of the technique makes it possible to extract this information non-invasively, or at the very least non-intrusively, facilitating the utility of this technique in a clinical setting. Because Raman scattering is both a sensitive and weak phenomenon, instrument considerations for adapting this technique for clinical applications can be challenging. Since the initial reports of *in vivo* human tissue spectra in 1993[49], technological development and technique refinement have enabled Raman measurements in humans with integration times of 0.5-5 seconds allowing real-time assessment of tissue state[50-52]. Spectra can now be collected, corrected for undesirable signal components, processed and analyzed rapidly to provide automated feedback at the time of measurement[53-55]. With these advancements, Raman techniques satisfy many of the criteria required for the adoption of a novel biomedical diagnostic technique in clinical practice: sensitivity to changes in tissue, *in vivo* application, and unique information obtained noninvasively, in real time[56]. This review will focus on the considerations vital to efficiently implementing Raman spectroscopy for *in vivo* clinical applications in diagnosis and sensing and some of the major clinical research under continued investigation.

2.6.2 Clinical instrumentation

A dispersive Raman system is similar to most optical spectroscopic systems and consists of three primary components – light source, sample light delivery and collection, and dispersive element with detector (Figure 2.5). The

specifics of these components are challenged by the needs of the clinical setting and application. Like standard medical instruments, a clinical Raman system should be small and easily transportable, optical alignment and calibration should be robust, sample light delivery and collection should be sterilizable and rugged, and the detection system should be sensitive to the weak biological signals.

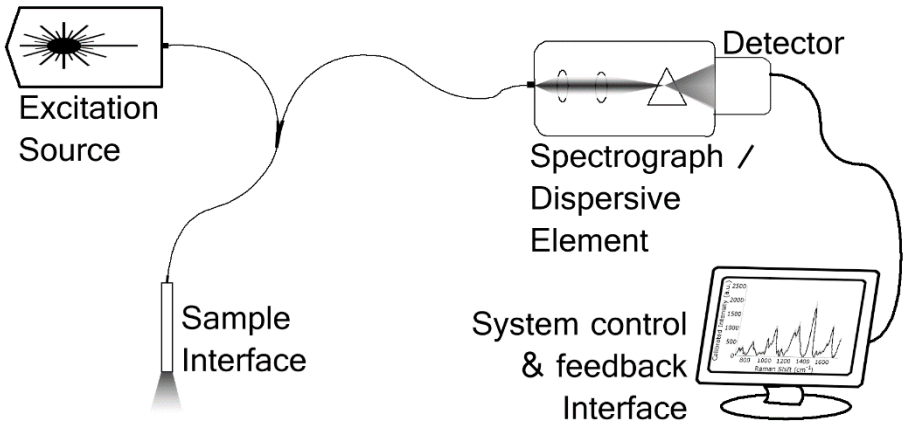

Figure 2.5. Basic schematic of an optical (including Raman) spectroscopic system.

The components that comprise a clinical Raman system can be broadly categorized into excitation and detection branches. Excitation is achieved by delivering the light from a given laser source to the tissue site of interest, in general by means of a fiber-optic probe or an articulated light delivery arm. The Raman scattered light is then collected, often through the same delivery system, and directed to a spectrograph and detector. As the technology utilized *in vivo* for clinical measurements has developed, so too has the breadth of individual

components that have been investigated and accepted within these systems. The following sections will discuss many of the requirements for the individual components in order to perform clinical Raman spectroscopy.

2.6.2.a Lasers

Due to the weak nature of Raman scattering, it is imperative to deliver sufficient power to the sample in order to generate Raman scattered photons for detection in a reasonable integration time relevant to the clinical setting under consideration. However, Raman scattering is mediated by the other competing optical phenomena within the sample. Furthermore, it is important to consider issues such as maximum permissible exposure (determined by ANSI or similar organizations)[57] and temperature increase (relevant to patient comfort and minimizing tissue damage).[58] Laser power then becomes a function of identifying a compromise between signal to noise, patient safety and comfort, and instrumentation considerations. Choice of laser is also governed by other factors such as laser stability especially when using a multimode laser. Raman lines are narrow and highly specific for a given vibrational mode. This then implies that the precise position and width of the Raman line requires the excitation source to be stable in wavelength position, bandwidth, and spatial mode for consistent results. Having accounted for these factors, the properties of the target tissue or sample are one of the major criteria for the choice of laser excitation source for a clinical Raman instrument. Since Raman shifts are relative to the Rayleigh (excitation) line, similar results can theoretically be

obtained from many different instrument configurations. However, the optical properties of the samples, including scattering and total attenuation coefficients as well as excitation, emission, and yield properties for any endogenous fluorophores present in the sample, are critical factors for consideration. The impact of each of these parameters is a function of wavelength.[59] Samples with high attenuation coefficients will limit the ability to deliver and collect the light beyond very superficial layers. Furthermore, strong absorbing molecules in a sample can also lead to the generation of excess heat deposition in the tissue, which can cause damage with high irradiance. Likewise, the presence of strong fluorophores can generate signals that overwhelm the modest Raman peaks that are concurrently detected. Due to the associated decrease in total attenuation coefficient for the major absorbing molecules in many biological tissues (water, melanin, oxy- and deoxy- hemoglobin), NIR excitation sources are commonly chosen for clinical instruments.[60] Further, since few known biological fluorophores have their peak emission in this region of the spectrum, with a noted exception of melanin, moving to the NIR wavelengths for excitation results in lower fluorescence background in the tissue at these wavelengths and simplifies the signal processing needed for extracting the Raman bands compared with visible or UV excitation.[61] As depicted in Figure 2.6, tissues such as the breast (A) that do not have strong autofluorescence signals relative to the Raman features can be collected with several different wavelengths; however, highly autofluorescent tissues like the kidney (B) require the use of

longer excitation wavelengths to obtain useful Raman spectra. Thus tissue properties are vital considerations when choosing the laser source for the clinical application of Raman spectroscopy.

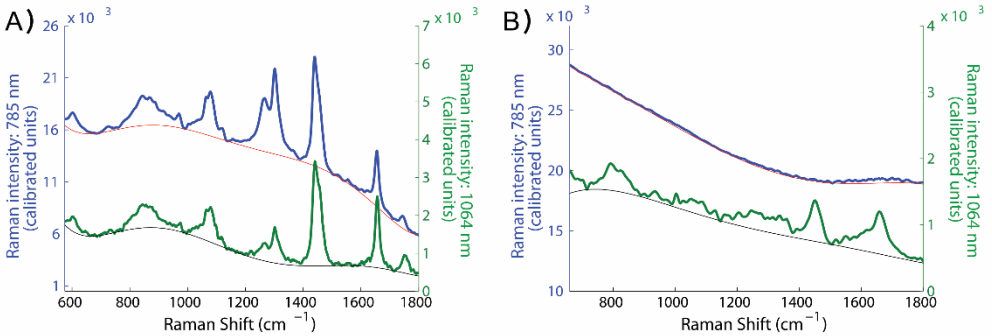

Figure 2.6. Raman scattering and autofluorescence polynomial fit signals for (A) breast and (B) kidney tissues measured *ex vivo* at 785 nm (blue) and 1064 nm (green) excitation wavelengths. Strong Raman features of breast tissue are apparent despite tissue background while low Raman intensities of the kidney are completely overwhelmed by the strong intrinsic signal at 785 nm but more readily visible at 1064 nm.

Early Raman systems were based on the Argon ion laser for visible excitation[62,63], Nd:YAG (Neodymium doped Yttrium Aluminum Garnet) laser for FT-Raman applications[64], and Titanium:Sapphire (Ti:Sapph) laser for NIR excitation. High output powers, single spatial and longitudinal modes of operation, and Gaussian beam profiles enable near-diffraction-limited optical performance for all of these sources.[65] However, the size of these lasers and their electronic and cooling requirements limit their practicality in a portable clinical Raman system. Some current Raman instruments, especially those with confocal capabilities, still use the Ti:Sapph laser. The development and continued advancement of diode laser technology has completely changed the

footprint of a typical Raman system. Diode lasers utilize electro-optical components (diodes), which emit light as a function of both applied current and operating temperature.[66] Diodes themselves are small (<1 mm^3) and require highly accurate controlling electronics to obtain the stable output necessary for Raman excitation. Without highly stabilized thermal and current control, laser diodes are prone to thermo-elastic effects on the laser cavity length (and thus output frequency) and output power fluctuations, respectively. Laser diodes are also characterized by their elliptical beam output (rectangular shape of the output facet) and astigmatism (unequal beam divergence from each dimension of the rectangular facet). These factors complicate free beam coupling of diode lasers, typically requiring beam shaping optics for successful implementation. Most commercial diode lasers are available with a pigtail option to directly couple a fiber to the laser diode to minimize the losses due to astigmatism and elliptical nature of the beam.

More recently, external cavity diode lasers (ECDLs) have emerged as robust and cost-effective light sources for Raman applications. The extended length of the resonant cavity of the laser diode minimizes the effect of small thermo-elastic changes on the output frequency by extending the distance between the diode's longitudinal modes. Compared with a standard laser diode, the ECDL diminishes mode hops, minimizes the spectral bandwidth of output light, permits wavelength tunability, and decreases temperature-dependent frequency response.[67] The laser linewidths of <0.001 nm (at 785 nm) with mode

locking provided by an ECDL is vital for medical applications where measurement repeatability and spectral resolution are important performance parameters. ECDLs are commercially available in tunable Littman–Metcalf or Littrow configurations, and can be made at specific wavelengths using distributed Bragg reflector configurations[68,69]. Mode stabilized diode lasers with powers on the order of 300 mW, either in single mode or multimode configurations, designed specifically for Raman spectroscopy are commercially available, lightening the burden for those developing clinical Raman systems.

2.6.2.b Fiber Optic Probes

Clinical application of Raman spectroscopy requires the delivery and collection of light to and from the sample (tissue). This is typically mediated through the use of optical fibers configured to maximize signal collection while minimizing interfering signals generated in the fibers and related optics themselves[70]. Since fiber optic probes will be discussed in a related manuscript in this special issue, here we only present considerations relevant to clinical translation. Depending upon the constraints of the clinical target, probe designs can be tailored to best interface with a sample and access the region of interest. Design considerations are dependent on the Raman configuration under study (discussed later), location of organ under study, microanatomy of the tissue, and pathophysiology of the disease.

A critical aspect for consideration in translating Raman spectroscopy from the laboratory to the clinic is the inherent nature of Raman scattering.

Raman scattering is a weak phenomenon but most materials are Raman active, and therefore the materials used in the Raman system generate Raman signals that interfere with the detection of sample signal.[71] Most fiber optic probes use optical fibers made of low-OH silica which has been extensively used in many applications of light in a clinical setting.[72] Silica is inherently inert, amenable to sterilization, and relatively low-cost, making it the material of first choice when designing fiber probes. Unfortunately, silica has a strong Raman signal, with several bands that can overwhelm sample signal.[71] This fiber signal can have magnitudes equal to and sometimes greater than that of the sample under study and thus any probe design needs to account for this behavior.[73] Fiber signal can be generated in the delivery fiber core and cladding by the excitation light. In addition, background signal can also be generated in the collection fibers by any excitation wavelength light returning into the collection fiber(s).[73,74] Mathematical techniques typically fail to de-convolve this unwanted fiber signal from sample signal as silica signal strength depends on the reflective and scattering nature of the sample and photon loss due to fiber bending. A feasible probe design that uses silica fibers must therefore prevent silica signal generated in the delivery fiber from illuminating the sample as well as prevent elastically scattered excitation light from entering the collection fibers and generating this signal.

Several different designs have been proposed for potential clinical acquisition of Raman spectra using silica based fiber-optic probes.[71,75] Since

the earliest design reports, most fiber designs have been based on similar concepts with modifications. In general, Raman probe designs utilize a band-pass filter placed after the excitation fiber lens, thus allowing only transmission of the excitation light. To achieve this, dielectric bandpass filters have been used to blue shift the wavelength cutoff with increasing angle of incidence and have therefore been shown to act as a one-way mirror for elastically scattered light[76]. This phenomenon increases the overall efficiency of the probe by preventing multiple scattered incident photons from exiting the tissue and returning into the source fiber. Longpass or notch filters are placed in front of the collection fibers to block the transmission of Fresnel reflected excitation light as well as to prevent the elastically scattered light from entering the collection fibers. These filters can be placed either at the tip of the probe, at fiber connections within the probe, or deposited directly on the end of the fibers themselves to maximize effectiveness, generally requiring sizes in the order of a few millimeters or smaller for distal tip filtering. There is thus a demand for high-quality optical coatings and micro-optical components that will simplify the design of much needed compact fiber-optic probes for Raman spectroscopy in biomedicine. Alternatively, non-silica based materials such as crystalline fibers and hollow waveguides have been evaluated for Raman applications[77,78]; however, these have not been tested for clinical use and as such are not included here.

The different silica fiber based probe designs available commercially yield different sample geometries and probe diameters, which in turn affect the application under consideration. It is therefore critical to consider the anatomy of the sample to be studied along with the pathophysiology of the disease to be measured so that appropriate sampling may be achieved.[79] For example, when studying the inner lining of the colon, where the epithelial lining has a variable layer thickness based on disease status, it is important that the probe be designed to sample only the superficial layers of the tissue and not into the deeper tissue.[80] A number of different sampling probes have been developed in order to meet specific design criteria, such as rapid acquisition time, depth selectivity, or the collection of data sets from complementary modalities.[81-85] Some of the most common probe designs and associated vendors are listed in Table 2.1.

Table 2.1. Summary of typical components used to build a clinically useable portable dispersive Raman system.

Laser	Fiber probe	Spectrograph	CCD
B&W Tek	Visionex*	Kaiser f/1.8i, f/2,2i	Princeton Instruments BRDD[#]
Sacher Lasertechnik	InPhotonics	Andor Technology Shamrock SR-303i	Andor Technology BRDD
Process Instruments	Emvision	Princeton Instrument LS 785	Horiba Synapse
SDL	In-house	Horiba Labram, HE-785	Kodak KAF 1001E
Innovative Photonics Solutions		Ocean Optics QE65000	Ocean Optics QE65000

* These companies do not exist anymore. [#] Back-reflected Deep Depletion (BRDD) CCD chip technology

2.6.2.c Spectrographs and Detectors

A typical dispersive Raman detection system used for potential clinical applications consists of a short focal length imaging spectrograph attached to a cooled charge-coupled device (CCD) camera. Clinical implementation of Raman spectroscopy requires spectral acquisition of no more than a few seconds. This fast acquisition in turn needs a fast spectrograph and a highly sensitive detector, particularly given the weak nature of the Raman signal. A typical CCD camera used in spectroscopy consists of a rectangular chip wherein the horizontal axis corresponds to the wavelength/wavenumber axis and the vertical axis is used to stack multiple fibers for increased throughput, which can subsequently be binned for improved signal to noise ratio (SNR). Technological advances have led to CCD chips with quantum efficiencies on the order of 90% in the NIR (this information can be found on any of the CCD vendors' (Table 2.1) websites). While different types of chips are commercially available for different applications, a back-illuminated, deep-depletion CCD is highly recommended for NIR Raman spectroscopy. These chips are however known to be susceptible to the so-called etaloning effect[86-88], wherein the thin silicon chip acts as an etalon resulting in the introduction of sharp peaks in the sample signal that are hard to resolve from the narrowband Raman signal. However, CCD cameras are now available commercially that effectively eliminate this effect.[86-88] Most CCDs in Raman use a thermoelectric (TE) multistage Peltier system to actively cool the camera down to at least −70°C in

order to realize excellent dark noise performance. In fact, current Raman systems for most biomedical applications are only limited by shot noise.

Tissue background signal is the bane of dispersive Raman spectroscopy, swamping the detector and hindering evaluation of sample Raman spectra. This background, especially in complex tissue samples, can arise from both the broadband emission of autofluorescence and elastic scattering of both stray excitation light and the Raman bands themselves. Non-collimated light and angular dependent filter performance can add substantial background to a spectrum, as can the scattering and spectral broadening of Raman peaks themselves; these phenomena are continuously variable with wavelength.[89] The presence of fluorophores in samples also contribute broad background signal to the collected Raman spectrum and are mediated by the wavelength dependent excitation for the comprising chromophores. However, most tissue fluorophores, with the exception of porphyrins and melanin,[90] have their excitation and emission maxima at UV and visible (UV/VIS) wavelengths.[91] Therefore, longer visible and NIR sources at wavelengths such as 633, 785, and 830 nm are preferred over those in the UV/VIS to reduce the amount of both fluorescence interfering with the detectable Raman signal. Selection of appropriate NIR wavelengths for excitation is often governed by competing factors. The longer the wavelength, the lower is the fluorescence and scattering background to be rejected; however, the Raman scattering also decreases. Again as demonstrated in Figure 2.6, where 785 nm excitation was plagued by

autofluorescence and scattering in kidney tissue (B) that was mitigated by 1064 nm excitation. Further, while silicon CCD detectors are capable of excellent performance over most of the NIR, the quantum efficiency decreases rapidly with wavelength, falling to below 15% at 1000 nm. Therefore, competing parameters of Raman scattering intensity, tissue background, and detector efficiency need to be assessed relative to the tissue under study to determine the wavelength range to be used. Overall, researchers in this field tend to prefer 785 nm excitation as a reasonable compromise for most tissues (as surveyed from the publications reviewed in Table 2.2). It should be noted that when acquiring Raman spectra in the high-wavenumber region (2400–3800 cm^{-1} in tissues) which is about 967–1118 nm for 785 nm excitation, obtaining high SNR Raman signals can be difficult using silicon-based detectors due to the decreasing quantum efficiencies. For detection of wavelengths above 950 nm, other types of detectors such as indium gallium arsenide (InGaAs), germanium, and indium phosphide (InP) detectors need to be used. However, these detectors suffer from lower quantum efficiency and increased noise in comparison to silicon detectors.[92] Nevertheless, instrument configurations utilizing Nd:YAG sources and multichannel InP/InGaAsP detectors have recently reported the feasibility of Raman spectroscopy in tissues such as the lung and gastric tissue at 1064 nm excitation with acquisition times on the order of hundreds of seconds.[93,94] *Ex vivo* reports by the authors have also recently demonstrated the potential for clinically relevant applications of dispersive 1064 nm Raman

instruments, particularly for in tissue type with a high fluorescence background at 785 nm (Figure 2.6).[58,95]

Table 2.2. Overview of large clinical studies (n>50) performed with Raman spectroscopy *in vivo* in humans.

Disease type	Raman method	Group	Publication year	Patient number	Sensitivity	Specificity
Barrett's esophagus	Probe Raman	Wilson *et al.*	2005	65	86% (Dysplastic), 88% (High grade)	88% (non-dysplastic), 89% (non-high grade)
Barrett's esophagus	Confocal Raman	Huang *et al.*	2014	373	87% (High grade)	84.7%
Cervical cancer	Probe Raman	Murali Krishna *et al.*	2014	63	100%	96.7%
Cervical cancer	Probe Raman	Murali Krishna *et al.*	2014	93	100%	93%
Cervical precancer	Probe Raman	Mahadevan-Jansen *et al.*	2009	145	86% (all – multiclass), 96% (premenopausal only)	97% (all), 90% (premenopausal only)
Cervical precancer	Probe Raman	Mahadevan-Jansen *et al.*	2011	172	96.5% (Dysplasia)	97.8%
Cervical precancer	Confocal Raman	Huang *et al.*	2013	84	81% (Dysplasia)	87.1%
Cervical precancer	Probe Raman	Mahadevan-Jansen *et al.*	2007	79	89% (High grade)	81% (benign)
Colon cancer	Probe Raman (HF)	Huang *et al.*	2015	50	90.9%	83.3%
GI cancer	Probe Raman	Huang *et al.*	2011	107	92.6% (gastric) and 90.9% (esophagus)	88.6% (gastric) and 93.9% (esophagus)
GI cancer	Probe Raman	Huang *et al.*	2011	81	97.9% (gastric)	91.5%
GI cancer	Probe Raman (HF)	Huang *et al.*	2015	164	92.5% (beveled probe) 85.8% (volumetric probe)	93.1% (beveled probe) 88.6% (volumetric probe)
GI cancer	Probe Raman	Huang *et al.*	2012	83	83.33% (Dysplasia) 84.91 (adenocarcinoma)	95.8% 95.6%
GI cancer	Probe Raman	Huang *et al.*	2010	67	94% (gastric)	93.4% (gastric)
GI cancer	Probe Raman	Huang *et al.*	2011	67	94.6% (gastric) 89.3% (independent validation)	94.6% 97.8%
GI cancer	Probe Raman	Huang *et al.*	2010	62	80% (overall)	85.7% (overall)
GI cancer	Probe Raman	Huang *et al.*	2014	450	81.3% (prospective)	88.3
GI ulcers	Probe Raman	Huang *et al.*	2010	71	82.1% (malignant ulcers) 84.7% (benign ulcers)	90.8%
Oral cancer	Probe Raman	Murali Krishna *et al.*	2012	104	86% (tumors) 72% (pre-malignant)	74%
Oral cancer	Probe Raman	Gupta *et al.*	2013	199	96% (malignant) 88% (premalignant), 84% (malignant) (multiclass)	99% (normal) 77% (multiclass)
Oral cancer	Probe Raman	Murali Krishna *et al.*	2013	84	92.7% (tumor)	98.7% (healthy control)

						84% (contralateral normal)
Skin cancer	Probe Raman + Fluorescence	Tunnell *et al.*	2014	76	100% (malignant melanoma) 90% (non-melanoma cancer)	100% (pigmented lesion) 85% (normal)
Skin cancer	Probe Raman + Fluorescence	Moryatov *et al.*	2014	50	89% (malignant melanoma)	87%
Skin cancer	Probe Raman	Meinke *et al.*	2015	104	74% (basal +squamous cell)	82%
Skin cancer	Probe Raman	Zeng *et al.*	2012	453	90% (cancer vs benign)	64%
Skin cancer	Probe Raman	Zeng *et al.*	2008	289	91% (cancer vs benign) 97% (malignant melanoma)	75% 78% (pigmented lesion)
Dermatitis	Raman microscopy	Irvine *et al.*	2010	132	98.7%	86.9%
Skin carotenoids	Resonance Raman	Mayne *et al.*	2012	381		
Macular pigment	Resonance Raman	Stevenson *et al.*	2006	97		
Macular Degeneration	Resonance Raman	Stevenson *et al.*	2013	433		
Macular Degeneration	Resonance Raman	Gellerman *et al.*	2002	201		

A Raman-sensitive detection system capable of clinical measurements requires an appropriate imaging spectrograph that couples to the sample interface (such as a fiber probe) on one end and the CCD of choice at the other end. Compact, rugged, spectrographs optimized for Raman use are now commercially available with f-number matching to the numerical aperture (NA) of optical fibers and high throughput for rapid acquisition (See Table 2.1). In order to resolve details of the biological Raman bands, the Raman detection system should have a spectral resolution of at most 8 cm^{-1}. Since spectral resolution depends on coupling optics, slit size (or fiber size if no slit is used), and CCD pixel size, each of these plays a crucial role in the design and selection of the detection system.[96] It is common to use 200-400 micron core diameter fibers in the fiber optic probe for maximum signal collection at the sample. However, this stack of fibers placed at the entrance port of the spectrograph will significantly reduce the spectral resolution of the system. If one assumes 1:1 matching of fiber-spectrograph optics, 200 μm core collection fibers stacked at the entrance port of the spectrograph, no slit (or a 200 μm slit) and 25x25 μm CCD pixel size, the resulting spectral resolution is 15.14 cm^{-1} for a 6.13 nm/mm dispersion of the grating (typical for holographic gratings).[97] One can reduce the entrance slit to 100 μm and/or reduce the collection fibers used to 100 μm core diameter and achieve a spectral resolution of 7.6 cm^{-1} which is close to what is needed to resolve tissue Raman peaks. Since the beams out of the fibers are Gaussian, one can speculate that when using a smaller slit size with larger

fibers, the loss of Raman photons is not as significant since one is only cutting out the tail of the beam. Further, larger fibers are easier to work with when building a filtered probe than smaller diameter fibers. Thus making these spectral calculations when designing the Raman system, particularly with respect to dispersion and therefore spectral resolution needs to be tracked during the selection of each of the components needed for the Raman detection system.

Additional components of the detection system include rejection filters that remove any laser light as well as the elastically scattered light from the detected signal. Holographic notch filters can block the laser wavelength with an optical density of six with steep edges and provide 90% transmission elsewhere with a relatively flat curve.[98] For dispersion, holographic transmissive gratings generally have the highest throughput performance[99], however, most of these are implemented in fixed positions, enabling measurement of only part of the Raman spectrum at a time. Furthermore, the performance of these components can drift over long periods of time (years), potentially due to environmental degradation (humidity, temperature). There has recently been renewed interest in reflective and prism-based approaches to dispersion.[100,101] Reflective gratings can usually cover a larger range of the spectrum at high spectral resolution, but often result in a longer integration time due to lower efficiency and movement of the grating position. Some devices circumvent this issue by including versatile options for either static or full-range spectral measurements, or include gratings with different dispersion elements

to achieve high resolution. In general, instruments with multiple gratings also have a larger footprint than those with fixed gratings. Size is an important consideration when designing a clinical device as the space available in most clinical procedure rooms is at a premium. The needed small footprint is also directly at odds with spectrograph designs that reduce performance-limiting aberrations based on long focal lengths. Some groups have attempted to account for field curvature distortions in transmissive systems by carefully designing the detector end of the fiber probe to have a parabolic shape that will appropriately map to a vertical line on the detector, limiting signal overlap and improving spectral resolution.[102] Newer instrument designs have been implemented using corrective optics or beam shaping techniques to reduce the impact of aberrations, however, these instruments have yet to be reported for clinical investigation. Another technique available for use in the benchtop setting is hyperspectral Raman imaging, collecting high resolution global mapping via monochromatic images.[103] This snapshot technique provides spatial information for samples rapidly however has not been implemented in clinical investigation to this point. Increased research studying the high-wavenumber band has also resulted in the commercial availability of spectrometers with extended spectral coverage at the expense of either resolution, integration time or overall size. However it should be noted that several spectrographs that meet the needs of a portable Raman system are

available; these spectrograph are compact in design and rugged for portable use (see Table 2.1).

Most Raman measurements in medical applications today rely on state-of-the-art, high-cost, high-performance Raman systems that are compact and highly sensitive to the weak biological Raman signals.[104,105] While each researcher has his or her preferences on the specifics of the different components in the system, the design is ultimately driven by the tissue/organ under study and the pathophysiology of the process to be monitored. Table 2.1 presents the most common lasers, fiber probes, spectrographs and CCD cameras used to build clinical Raman systems as described in the papers listed in Table 2.2.

In describing and guiding the selection of each of the components described above, it is presumed that Raman spectroscopy is the only modality under consideration, and the Raman configuration to be used is dispersive Raman spectroscopy, to assess biochemical signatures associated with the biomedical problem under study in the fingerprint or high wavenumber region. These components can be obtained from any number of vendors or developed within a laboratory to assemble a system suitable for the specific study under consideration. It is vital for any clinical application that the individual components integrate into the most efficient instrument configuration possible and all spurious sources of confounding signals be minimized through design

2.6.2.d Data processing and Analysis

2.6.2.d.i Instrument Calibration

Based on the previous section, it becomes readily apparent that to compare Raman spectra acquired from different tissues requires some standardized methods of calibration and processing that enable transferability of these spectra. Figure 2.7 presents a flowchart of the major procedural steps and their order for converting raw measurement data from the detector to signals ready for comparison and analysis. Source compensation is a standard process that can be applied to control for variability in the source from measurement to measurement. This step is critical only when absolute intensities are necessary for analysis. Instrument response variations require two types of calibration: spectral calibration and intensity calibration. Spectral calibration is used to convert the horizontal axis from CCD pixel number to relative wavenumber. The emission spectrum of a known calibrated light source, such as a neon lamp with numerous and narrow bands in the NIR, is typically used to calibrate the horizontal axis into absolute wavenumbers (cm^{-1}). Relative wavenumber calibration is performed using the spectral position of the laser line and then validated using standards with well characterized Raman features and strong Raman scatter, such as naphthalene and acetaminophen. Spectral standards such as the fluorophore rhodamine 6G and a weak Raman scatterer such as methylene blue or vitamin E can be used as additional intensity standards to account for day-to-day variations in the

spectral intensity.[106] Calibration of the intensity axis (spectral response correction) is necessary to account for the wavelength-dependent response of the various components in the detection leg of the system including the grating, the filters, optics as well as the quantum efficiency of the CCD chip. This is typically performed using a calibrated source such as a tungsten lamp certified by the National Institute of Standards and Testing (NIST) to generate intensity correction factors for variations in instrument throughput.[107] This calibration process is essential for comparison of spectra measured across different Raman instruments for the same or similar sample. This calibration is typically performed early in a study and then on a regular basis to validate the accuracy of the correction factors over time. However, perturbation of any of the optical components including those induced by moving the system from the laboratory to the clinic can affect the calibration and therefore an additional method that accounts for day-to-day calibration of the system performance must also be developed. Collection of a NIST lamp intensity spectrum is often impractical in a clinical situation due to the experimental controls necessary to ensure that the bright, diffuse emission of the lamp traverses only its intended path through the Raman instrument to the detector, along with the safety concerns that correspond to the spectral intensity in the UV portion of the spectrum. More recently, spectral intensity standards consisting of green-colored Schott glass have been explored by NIST[108] and other groups[109] as more practical

alternatives for daily calibration, but no consensus has yet to be reached on their applicability as a Raman standard.

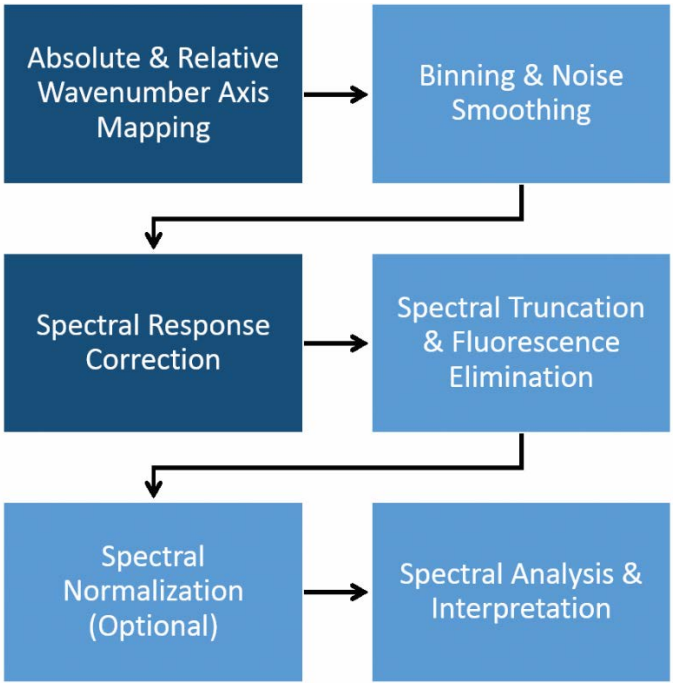

Figure 2.7. Flowchart for typical system calibration and signal processing procedures for clinical Raman spectroscopy systems. The darker shaded boxes indicate steps that require collection of reference spectra prior to data acquisition while the other steps can be implemented in-line per spectrum for system automation.

As indicated in Table 2.1, it is possible to configure a Raman system using different combinations of a laser, spectrograph, probe and detector. In a parametric study of laser, probe, and CCD detector combinations for a single spectrograph, the influence of each component in an instrument configuration on reliability and reproducibility of Raman spectra was investigated (unpublished). The various combinations of these components can be seen in Figure 2.8. By isolating the impact of each instrument, this work identified that

the most significant impact on the obtained signal was driven by the fiber optic probe. When a single probe was maintained across different lasers, spectrographs, and CCDs, the total variance of the detected signals decreased significantly relative to signals obtained when spectra were combined across probes. This data highlights the importance of using a single probe design for data collection for a given clinical application.

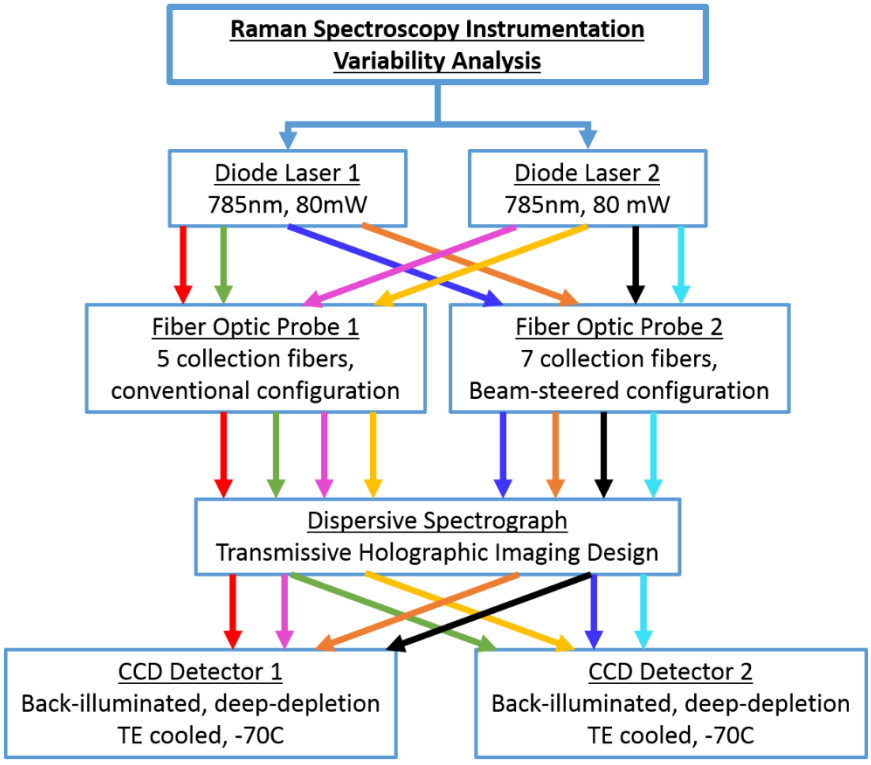

Figure 2.8. Diagram for a comparison study of clinical Raman spectroscopy system components. By varying combinations of instruments, variability studies have investigated the impact of unique components on the acquired spectral signatures. Results show that the collection leg of the system and the design of the fiber probe have the most significant contribution to the instrument variance observed in the spectra.

Even when a single probe design is selected for a given clinical Raman instrument, it is important to precisely account for instrument-induced variability. The aforementioned variability study indicates the importance of using a single probe design for clinical data collection (Figure 2.9A). However, it is not feasible to conduct a large clinical study or manufacture a potential medical device that relies on a single probe for the lifetime of the instrument. As multiple probes built from a single design are used, it should be noted that each optical component can have a similar but ultimately unique wavelength-dependent response. As depicted in Figure 2.9 for different *in vivo* tissue measurements with unique probes of the same design, differences in filtering and throughput can impact not only raw signals (Figure 2.9B) but also impact the resulting, processed spectra (Figure 2.9B, inset). However, current calibration methods do not provide adequate calibration to minimize probe response which in turn affects data analysis when spectra across multiple probes are combined.[106] Practically, this data indicates the necessity of adequately calibrating probe-specific signals thoroughly for successful implementation of Raman techniques and the community needs to work together to develop such methods. In the meantime, it is recommended that investigators acquire multiple probes based from a single design and built at the same time, to minimize this variability.

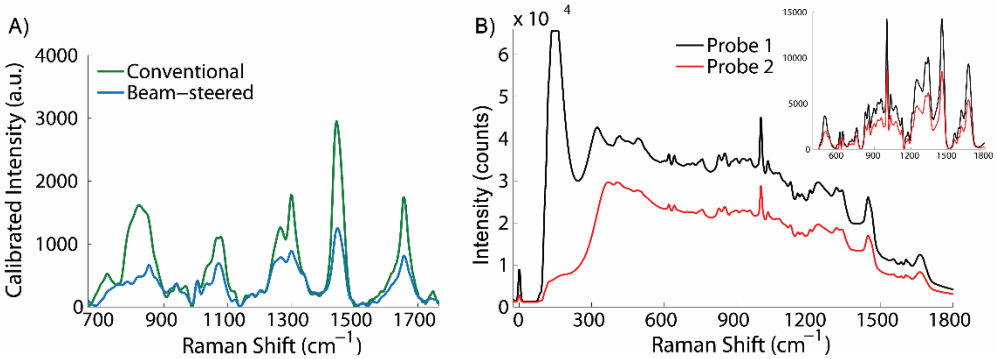

Figure 2.9. Representative Raman spectral differences that can be obtained from a single sample acquired using two different probes. (A) A conventional filtered Raman probe (green) and a beam-steered Raman probe (blue) on skin *in vivo* demonstrate unique line shapes. (B) Two iterations of the same probe design used to measure an albumin sample demonstrate the effect of slightly different inline filters on the raw and resulting processed (inset) Raman spectrum.

2.6.2.d.ii Data processing

2.6.2.d.ii.1 Fluorescence elimination

The increased investigation of Raman spectroscopy for biological and clinical purposes is largely due to its high sensitivity to subtle biochemical changes and its capability for nonintrusive application. One challenge faced in these investigations is that biological applications involve turbid, chemically complex, and widely varying targets. Therefore, significant challenges exist for both acquiring viable Raman signatures and suppressing the noise sources inherent to the target medium. The greatest challenge for obtaining Raman spectra from biological materials is the intrinsic fluorescence and elastic scattering of many organic molecules. Often several orders of magnitude more intense than the modest Raman signals, this background, if left untreated, will

likely dominate the Raman spectrum and hinder analysis and interpretation of tissue biochemistry. To extract Raman signal from the raw spectra acquired, elimination of fluorescence signal is necessary. While most biological fluorescence occurs in the UV/VIS and intensity decreases as a function of wavelength, the fluorescence and scattering background observed for NIR still interferes with the measured Raman spectrum (Figure 2.6B). The intensity of this background is generally dependent upon tissue but is ubiquitously present in almost all tissues studied, meriting attention prior to spectral analysis.

Both hardware and software techniques have been proposed for background subtraction from raw Raman signals. Wavelength shifting and time gating are hardware-based techniques that have been shown to effectively minimize fluorescence interference in Raman spectra but require specific design considerations for the spectroscopic system to achieve their results.[110,111] Several software-based mathematical methods can be implemented without system modification and are generally preferred for fluorescence removal. Such techniques have included first- and second-order differentiation[112,113], frequency domain filtering[110], wavelet transformation[114,115], multistage smoothing[116], and polynomial fitting[53,117,118]. Each of these methods has been shown to be useful in certain situations, however all have their advantages and limitations that must be evaluated before selecting a method for application with a given system.

First and second order differentiation relies on invariant wavelength-dependent fluorescence emission compared with the relative shifts measured in Raman spectra. One way to accomplish this differentiation is by measuring the spectra at two (or more) slightly shifted excitation wavelengths (within a few nanometers) and taking their difference.[119] Integrating the difference spectrum results in the original Raman signal. Similar results can be achieved with a single excitation wavelength by taking the first derivative of the spectrum and integrating the noise-smoothed derivative spectrum following baseline correction.[110,113] The derivative method for fluorescence subtraction is efficient and unbiased, but distorts Raman line shapes and relies on complex mathematical fitting algorithms to reproduce a traditional spectral form.[110] While many of these methods were developed and tested in the early 1990s, shifted excitation methods for removing this undesirable fluorescent signal, coined as modulated wavelength Raman spectroscopy, are coming back into vogue, utilizing multiple closely spaced excitation sources and signal processing algorithms to remove fluorescence signal.[120] Newer sources allow the use of multiple excitation wavelengths to improve the accuracy of the method; however, removal of the DC offset remains an issue.

Frequency filtering and polynomial fitting are other common methods for fluorescence elimination. Frequency filtering can be achieved with fast Fourier transform (FFT), transforming the spectrum to the frequency domain by taking the FFT which is then be multiplied with a linear digital filter to

eliminate the fluorescence. The inverse FFT yields the Raman spectrum free of fluorescence.[110] If the frequency elements of the Raman and noise features are not well separated, this method can generate artifacts in the processed spectra. A more direct method to subtract fluorescence that is both simple and accurate is to fit the measured spectrum containing both Raman and fluorescence information to a polynomial of sufficient order to describe the fluorescence line shape without capitulating the higher-frequency Raman lineshape.[53] Polynomial curve fitting has an advantage over other fluorescence reduction techniques due to its inherent ability to retain the spectral contours and intensities of the input Raman spectra and can be easily implemented in MATLAB® or other computing platforms for automated performance.

Individual techniques have advantages and disadvantages; the method used should be selected based on the specific application and best matched to measurement technique. Mosier-Boss *et al.* tested the use of the shifted excitation, first derivative, and FFT techniques for fluorescence subtraction and indicated a preference for using the FFT based on its ability to filter random noise from the spectrum.[110] In an analysis of the different techniques by the author for *in vivo* tissue applications, the use of a polynomial fit was found to be the optimal technique for both experimental and computational considerations. More recently, a modified polynomial fitting algorithm that accounts for noise levels has been proposed[118,121] which has been shown to minimize the presence of artificial peaks in low SNR spectra that are common

in measurements of tissues with high autofluorescence. It should be noted that order of the polynomial used is specific to the sample fluorescence line shape and as such should be determined before utilizing this technique (Figure 2.10).

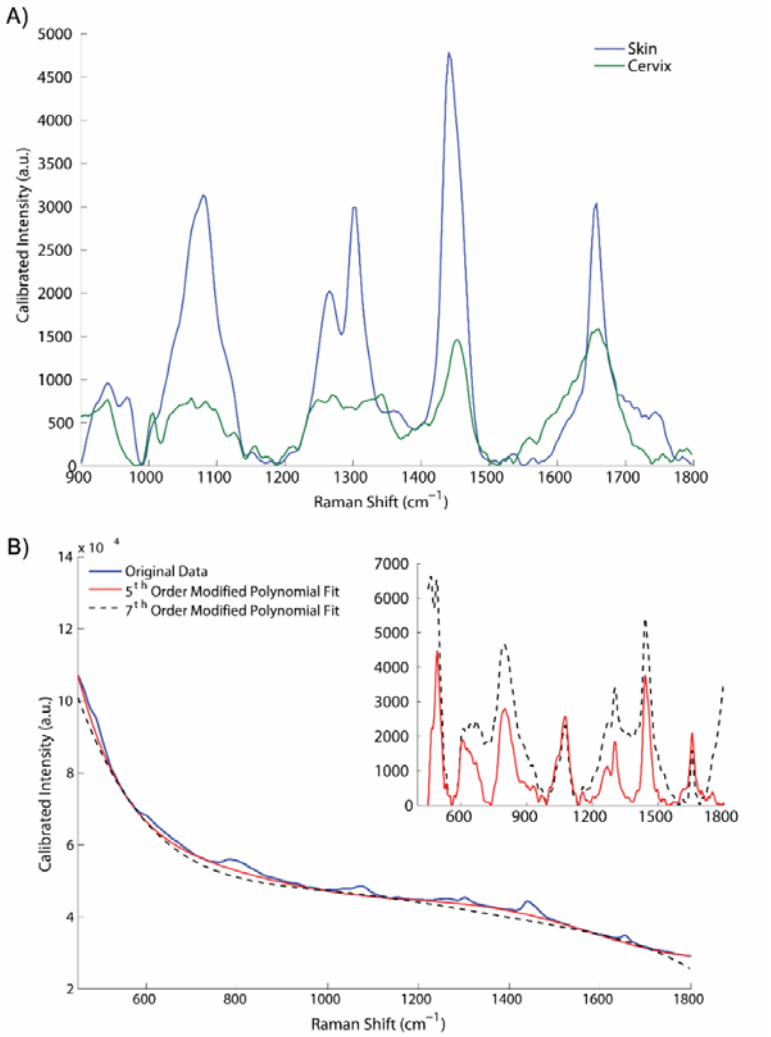

Figure 2.10. Impact of background elimination varies based on the sample or tissue measured. Fluorescence subtraction using (A) 5th order polynomial in skin and cervix yield unique shapes due to compositional differences. (B) Using a 5th versus 7th order polynomial in colon (processed spectra inset) demonstrates that a single polynomial fitting order may not be appropriate for all samples; higher order polynomials are used to simulate background fluorescence and subtracted to enhance the underlying Raman signal from the sample.

Other methods have utilized advanced signal processing techniques to separate underlying autofluorescence from the desired Raman signals. Wavelet decomposition, penalized least-squares fitting techniques[122] and principal component analysis (PCA) have been described for suppression of the confounding signal components.[123] Wavelet transformation is dependent on the decomposition method used and the shape of the fluorescence background, whereas PCA assumes that the highest signal variance is due to the fluorescence background, which may be invalid for some applications. Thus, there are tradeoffs for each method and the choice may be governed both by the application at hand and the preference of the investigator.

2.6.2.d.ii.2 Noise Smoothing and Binning

Since Raman scattering is such a weak phenomenon, the SNR of most measured Raman spectra require significant noise smoothing in order to extract the underlying Raman bands. Various types of noise smoothing filters have been effectively used. These include the median filter, the moving average window filter, the Gaussian filter whose full width at half maximum is typically set equal to half the spectral resolution of the system, and the Savitzky–Golay filter of various orders.[105,124-127] Other methods include using PCA, genetic algorithms, and other multivariate statistical approaches to remove the higher order components and effectively removing noise[128,129]. In using any of these or other methods of noise smoothing, care should be taken to retain the integrity of the spectral line shape especially when dealing with samples with multiple peaks that are close to each other. Validating the method using spectra from

weak Raman samples (with low SNR) should be an essential step in the development process.

Other preprocessing methods typically applied include binning of the spectral data set due to the large number of variables (which is dependent of CCD chip size) for computational ease. Depending on the variability in the acquired data and the needs of the analysis methods used, various normalization methods may also be applied to allow comparison of the spectra. Normalization methods include normalization to intensity standards, normalization to a spectrum's own maximum intensity or area under the curve, and mean scaling to the average spectrum acquired from a given patient. Some researchers prefer to use difference spectra to achieve the same normalization effect to account for intra- and interpatient variability observed.

2.6.2.d.ii.3 Data Analysis

One of the advantages of spectroscopic diagnosis is automation, which allows objective and real-time diagnosis of pathologies. Spectral differences observed as a function of tissue physiology or pathology can be incorporated into diagnostic algorithms that can in turn be implemented in real-time to yield classification using univariate and multivariate statistical methods; several statistical approaches have been identified and applied for feature extraction and classification of tissues towards automated, clinical diagnosis. Since Raman spectroscopy is a biochemically specific technique, chromophore and scattering molecule contributions can be extracted from the measured spectra.

These can then be used in diagnostic algorithms as well as in understanding of the spectral signature as it pertains to the disease process. For example, the extracted contributions can be used to quantify blood analytes for applications such as glucose sensing.[130]

Original analyses for Raman signals were based on differences in intensity, shape, and location of the various Raman bands between normal and abnormal cells and tissues. Observed differences between the different tissue types under study were selected for classification algorithms based on empirical methods using changes in intensity or ratios of intensities or number and location of peaks. For example, the intensity ratio of the CH_2 bending vibrational mode at 1440 cm^{-1} to the Amide I vibrational mode at 1655 cm^{-1} has been observed to vary with disease in several applications including breast cancers and gynecologic cancers and precancers.[131,132] The limitation to this approach however, is that diagnostically useful information may be contained in more than just the peaks or valleys observed in tissue; a method of analysis and classification that includes all the available spectral information may be important for the accuracy of detection. Further, empirical methods tend to be biased in favor of the spectral differences specific to the data set used for the analysis and these methods do not hold under validation. To obtain an unbiased estimate of the performance of algorithms for Raman data, multivariate statistical techniques have become the accepted practice for the development of discrimination and classification algorithms for diagnostic applications.

In the past few years, great strides have been made in the application of multivariate techniques for spectroscopic data analysis in disease detection.[107] Discrimination techniques such as linear and non-linear regression as well as classification techniques such as neural networks have been employed.[107,133] Data compression tools such as PCA are still commonly used to reduce the dimensionality of the data matrix and have been used to account for the variability in the data.[134] Linear and nonlinear methods have also been used for feature extraction. Subsequently, methods such as hierarchical cluster analysis (HCA)[135] and linear discriminant analysis (LDA)[133] have been used to yield classification algorithms for disease differentiation. Partial least squares, a regression-based technique, as well as hybrid linear analysis, have been used to model tissue based on component spectra, finding component contributions for disease detection and extracting accurate concentrations of analytes such as glucose using NIR Raman spectra for transcutaneous blood analysis.[136,137] More complex multivariate and machine learning methods have also been utilized, including support vector machines[138], logistic regression models[95,139], genetic algorithms[128], neural networks[140], decision trees[141], optimization techniques[137], and generalized linear models. These methods allow the integration of non-Gaussian constraints and variable weights to optimize classification performance. However it should be noted that these complex methods may not necessarily provide a significant improvement in the diagnostic performance of

Raman spectroscopy and as such most studies tend to rely on simpler (and often linear) albeit multivariate methods of discrimination.

In small sample sets, one often relies on the leave-one-out or K-fold methods of cross validation, as well as nested methods for multiple optimization steps. Rigorous, unbiased estimates may be obtained by developing robust discrimination algorithms using a test set and its performance quantified in a validation set. Ideally, these two sets are formed by random distribution of the subject population into two equal data sets. The true measure of success of Raman spectroscopy for tissue diagnosis requires validation of the tested algorithm in an extensive unbiased (and independent) validation set.[142]

Analyzing Raman signals for spectral differences and developing diagnostic algorithms for the purpose of disease classification are one facet of the clinical application of Raman spectroscopy for tissue diagnostics. However, the wealth of information provided in Raman spectra especially with respect to molecular composition enables identification of the nature and biochemical processes responsible for these changes. This information can be used to enhance fundamental understanding of various biological processes as well as inform the improvement of diagnostic performance.

Several researchers have harnessed the benefit of extracting physiologically relevant markers from Raman spectra of tissues. Puppels *et al*. obtained quantitative information about skin hydration based on Raman spectra.[143] Feld *et al*. developed comprehensive models for biochemical

component extraction that were used for disease classification.[144] More recently, Huang *et al*. performed semi-quantitative biomolecular least-squares modeling based on representative basis spectra in order to distinguish spectral sources for neoplastic lesions in multiple patients.[145] Each of these methods is based on the acquisition of Raman spectra from individually identified chromophores either as morphological tissue components, as extracted biochemical constituents, or commercially available pure chemicals. Pixelated Raman microspectroscopy has been used (with or without confocality) to measure Raman spectra from individual morphologic tissue components using tissue sections. A Raman spectrometer is coupled to a microscope and is scanned across the tissue section to obtain Raman images that can then be correlated with serial hematoxylin- and eosin (H&E) stained sections to identify relevant morphologic components and their Raman signature. Alternatively, tissue scatterers can be extracted from biochemical assays and Raman spectra can be acquired from each of these extracted chromophores using the same instrument as used to measure the biological specimen. Using mathematical models such as those developed by the Feld group, contributions of each of the extracted or morphologic components can be calculated for the intact tissue.

Thus, a portable, clinically viable instrument with a fiber-optic probe can be used to acquire Raman spectra *in vivo*. The ability of Raman spectroscopy in a particular tissue can be tested in animals *in vivo* or *in vitro* and subsequently applied for *in vivo* human detection. The acquired spectra can

then be processed and analyzed and information extracted about the performance of the technique as well as about the biochemical components that contribute to the signals obtained by the method.

2.6.2.d.ii.4 Technology interface, control, and automation

A major feature that is paramount for translation of Raman spectroscopy or any other laboratory technology to a medical clinic is the constraint of an intuitive, automated interface. Given the inherent weakness of Raman scattering and the complexity of the generated signals, great care and effort must be spent in developing the instrument interface prior to deployment for a medical application. Thankfully, the instrument components discussed above can be combined in a manner appropriate for a detection target so that signals can be detected quickly. Once detected, the speed of modern computing technology can be utilized for real-time processing for background removal, component extraction, and class prediction. Optimizing algorithms for each step is vital for an intuitive interface along with practical considerations including how to best display feedback to the end-user. The first step towards successful integration is to implement a clinically-relevant user control. Hands-free enabled data collection with foot pedals or buttons at the probe interface are features that will enable clinical use, along with instruments that operate in real-time and provide continuous feedback. Zeng *et al.* and Huang *et al.* have reported systems that integrate data collection, processing, and analysis in times as low as 100ms.[52,102,146,147] Even with the integration of rapid processing, the

information provided by a complicated tool based on Raman spectra could be overwhelming. Combining this information into an easily interpreted display or audible feedback are vital steps for the clinical integration so that with minimal training, these devices can be deployed to benefit clinical medicine.

2.6.3 Raman configurations

Several different modalities of Raman scattering have been used to analyze the structure of various biological molecules.[148,149] Some of these techniques include ultraviolet (UV), visible or NIR dispersive Raman, Fourier transform Raman (FT-Raman), surface-enhanced Raman (SERS), and ultraviolet resonance Raman (UVRR) spectroscopy[48,150]. More recently developed techniques include stimulation Raman (SRS), tip-enhanced Raman (TERS), and coherent anti-Stokes Raman scattering (CARS).[151-153] Early adoption of Raman spectroscopy for biological applications with minimal interference from fluorescence relied on FT-Raman spectroscopy, where the Fourier transform of the scattered signal is detected, and subsequently inverse-transformed to give the actual Raman signature. This technique yields improved signal-to-noise ratio of hard to detect events but requires long collection times[143] that are not practical for clinical and *in vivo* implementation. With the recent developments in laser and detector technology, FT-Raman methods have become more or less obsolete at least as it pertains to clinical diagnosis and as such are not discussed here. Pursued extensively as a viable technique for *in*

vivo human application, NIR dispersive Raman scattering is typically excited in the range of 780–1100 nm where minimal fluorescence is produced making detection of the weak Raman signal easier, particularly in biological materials. However, several other configurations of Raman spectroscopy have been implemented *in vivo* and a summary of some of these as they pertain to potential clinical application are described below.

2.6.3.a UV/VIS

While most implementations for clinical Raman spectroscopy rely on NIR excitation (785 or 830nm), some researchers continue to use visible wavelengths for biomedical applications. The tradeoff between high Raman scattering cross-sections at lower excitation wavelengths and decreased penetration depth, higher absorption, autofluorescence, and heat generation usually limit the potential of *in vivo* clinical application with visible techniques. However, some studies continue to apply these more readily available excitation sources for various studies, particularly where direct interaction with the patient is not required.[154-156] Especially in applications of Raman spectroscopy for pathology analysis for which clinical protocols for *ex vivo* cytology and histology commonly employ conventional glass slides as the substrate, visible sources, such as 532nm, demonstrate significant improvements in background signal relative to NIR excitation.[157] Other *ex vivo* work continues for several malignancies, including skin and oral neoplasia, with visible wavelengths that show promising results.[158-161]

Resonance Raman activation may be achieved when the excitation wavelength approaches electronic absorption of a molecule.[162] Resonance Raman excitation increases scattering signal intensity by several orders of magnitude. However, typical absorption frequencies of biological molecules such as proteins and nucleic acids occur at ultraviolet wavelengths where these wavelengths may cause photolysis of the sample and destroy it over time.[163] Further, the mutagenicity of UV radiation makes this technique inviable for clinical *in vivo* use.[164,165] As such, few researchers have pursued this approach for potential clinical applications in recent years.

2.6.3.b Raman Imaging

The weak nature of Raman scattering hinders the imaging of Raman features in biological materials such as cells and tissues with dispersive Raman spectroscopy in clinically feasible integration times. Intrinsic Raman imaging has been performed using the intensity of a specific Raman band or ratio of bands to build an image from cells and tissues.[166] As mentioned above, one method acquires a hyperspectral stack of monochromatic images over relatively large spatial areas. Another approach involves compiling a three dimensional data cube by measuring Raman spectra through point or line scanning of the excitation and collection beams.[167] The voxel size may be governed by the spatial resolution needed for the study and can be as small as the confocal pinhole up to ~100s of micrometers. Both methods of imaging are performed on a Raman microscope and may require several minutes to hours to acquire an

image depending on the spatial resolution thus making it infeasible for real-time clinical applications. Most studies with point or line scanned Raman imaging have been used to improve our understanding of biological processes in cells and tissues *in vitro* as well as in animal models.[65,168,169] Other methods of Raman imaging include nonlinear Raman techniques such as coherent anti-Stokes Raman spectroscopy (CARS) and stimulated Raman scattering that take advantage of nonlinear processes for increased and selective signals. Both of nonlinear methods have been applied to study biochemical interactions in cells and tissues *in vitro* and *in vivo* applications have been confined to mouse models.[153,170-173] However, all these imaging techniques are restricted by the limited number of available Raman photons and therefore the long integration times necessary to acquire a Raman image successfully. As such none of these approaches have successfully been applied *in vivo* in humans and are not directly practical for clinical use.

2.6.3.c Fingerprint versus High wavenumber

While the majority of researchers applying Raman spectroscopy for clinical applications have primarily been focused on spectral differences in the fingerprint range (up to about 1800 cm^{-1}), some studies have investigated the diagnostic utility of spectral features in the high-wavenumber, generally 2200 – 4500 cm^{-1} where distinct and strong features of lipids, proteins and water may be observed (Figure 2.11). The fewer but broader features that occur in the high wavenumber region can be much higher in intensity relative to competing

optical signals. Several studies have demonstrated the potential of high wavenumber Raman spectroscopy alone or in combination with fingerprint Raman methods to discriminate and classify disease *in vivo*.[174] Detecting high wavenumber Raman features pose different requirements on the Raman system design. Because the high wavenumber signal is inherently at a higher wavelength than the fingerprint, different gratings, filters and more importantly detectors may be necessary in order to efficiently collect signals especially when using common NIR Raman excitation sources (described in the detector section above). Alternatively, because the separation between the Rayleigh line and the detected Raman bands is so large, inline filtering can be mitigated, which has the potential to simplify probe designs and reduce cost, thus increasing the potential for clinical translation.

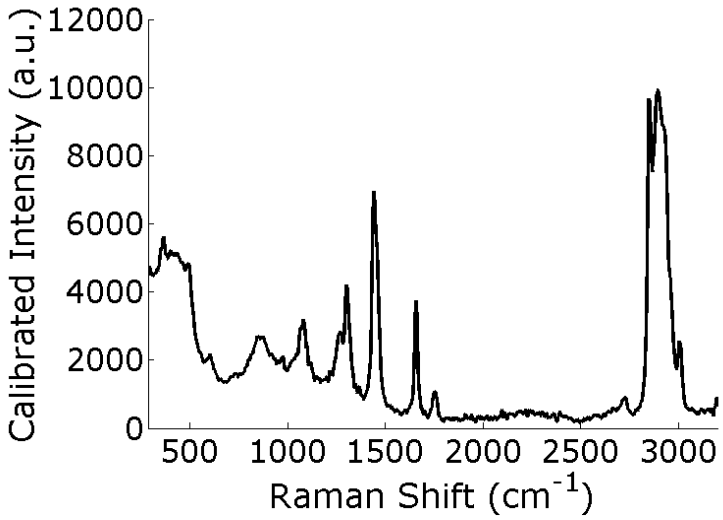

Figure 2.11. Fingerprint and high-wavenumber Raman spectrum of *ex vivo* breast tissue depicts the broad, strong features characteristic of lipid components in the tissue. Both segments of the Raman spectrum can provide valuable information for evaluation of complex sample composition.

2.6.3.d SORS

Perhaps the most impactful configuration of Raman spectroscopy in recent years has been the discovery of spatially offset Raman spectroscopy (SORS). Photon migration theory dictates that photons incident on the tissue surface that reemerge after only a few scattering events are likely to undergo minimal transverse shift and travel through the most superficial depths. Photons that undergo many scattering events are more likely to undergo a larger transverse shift and also travel deeper within the tissue, due to the fact that the scattering phase function of tissue is primarily in the forward direction. The combination of spatial offset with the Raman effect introduces depth selectivity in the spectral measurements expanding the ability of Raman spectroscopy to

sub-surface phenomenon in biomedical applications.[175] The intensity of the Raman-scattered light at zero spatial offset includes contributions from both the superficial and underlying layers. However, as the spatial offset increases, the signal intensity from the superficial layers falls off more rapidly than the intensity of the signal from the underlying layers, which increases the relative proportion of signal from the deeper layers. The SORS signal can be collected through a range of spatial offsets, and computational techniques such as least-squares regression can be applied to separate the spectral signatures from individual layers.[176,177] It is important to note that while SORS can yield Raman spectra from deep within the tissue, it does so in a probabilistic fashion that relies on the layered architecture of tissues in which the spectral signatures of the layers are distinct. This is in contrast to confocal Raman spectroscopy, which explicitly rejects out-of-focus light and collects spectra from a well-defined depth. This makes SORS better suited for *low-resolution* depth-dependent measurement of features and at greater depths (~centimeters) than confocal Raman spectroscopy (~100s μm). Several researchers have applied SORS towards clinical applications in the bone and breast.[176,178,179] This approach has been extended to other configurations such as inverse SORS where the source and detection fibers are switched[180] and Raman tomography[169], where SORS is combined with computed tomography and modeling of optical properties to obtain three dimensional Raman maps.

2.6.3.e SERS

Surface enhanced Raman spectroscopy (SERS) is used to investigate the vibrational properties of single adsorbed molecules.[48,150,181] It was discovered that the rather weak Raman effect can be greatly strengthened (by a factor of up to 14 orders of magnitude) if single molecules are attached to metal nanoparticles of a suitable material and roughness to capitalize on both electromagnetic (surface plasmon resonance) and chemical enhancement.[182-184] Many groups have used SERS to detect single molecules attached to colloidal silver particles that are either adhered to a glass slide or in an aqueous solution. Single-molecule detection is of great practical interest in chemistry, biology, medicine, and pollution monitoring; examples include DNA sequencing and the tracing of interesting molecules such as those used in bioterrorism. In medicine, the feasibility of SERS to track targeted molecules *in vivo* in a mouse model was successfully demonstrated by Gambhir *et al*.[185] Since that report, numerous groups have applied targeted SERS-activated nanoparticles to track various cancer biomarkers *in vivo* in animal models.[186-190] However, the biggest limitation of SERS is the need to introduce a tag with related toxicity issues which makes this approach infeasible for human clinical applications at this time. Vo-Dinh *et al*. developed a single fiber SERS sensor that has the potential to extend SERS for *in vivo* human use without the need for a targeted particle.[191] However, no reports of *in vivo* testing of this sensor were found. Another configuration is a combination of the surface enhancement with deep Raman

spectroscopy, known as SESORS. First reported by Stone *et al.*, this technique has demonstrated the potential for detecting molecule-specific SERS particles buried deeply within layers of tissues.[192,193] While this technology has not yet been implemented clinically, research for nanoparticle confinement in substrates may reduce the potential for toxicity issues.

Despite the various configurations described above, the most common configuration used in the application of Raman spectroscopy in a clinical setting is based on dispersive Raman spectroscopy in the fingerprint and/or high wavenumber region of spectrum. Spatial offset and confocal are modifications to this approach that have also been implemented and tested in a clinical setting. All the other approaches have been mostly applied to develop an improved understanding of a biological and biochemical processes rather than clinical diagnosis. Combining dispersive Raman spectroscopy with other optical (and non-optical) methods has been researched in an effort to improve performance of Raman spectroscopy alone in solving a clinical problem. Raman spectroscopy has been combined with optical coherence tomography[194-196], optical tomography[197], confocal reflectance microscopy[198,199], fluorescence and diffuse reflectance spectroscopy[200,201] to provide complementary information that can be used to further enhance the diagnostic capability of any one of these methods alone. The instrumentation considerations for making such multi-modal approaches feasible are usually challenged by the need to combine a narrow bandwidth laser and sensitive detector, essential for the very weak

Raman signals with the source and detector considerations of a much brighter signal acquired using these other modalities. The resulting combinations yield a much more complicated instrument design accompanied with a higher cost device. Nevertheless, various researchers have successfully demonstrated the diagnostic advantage of these multi-modal approaches.

2.6.4 Clinical applications of Raman spectroscopy

Numerous research groups have investigated the potential of Raman spectroscopy for clinical use over the past decades and continue to find interesting medical problems for which the noted sensitivity of Raman scattering holds great promise. Various implementations of the instruments described above have been utilized in clinical studies that demonstrate the potential of Raman spectroscopy to impact medical care. In this section, we present a review of large ($n > 50$), clinical *in vivo* studies that are focused on the application of Raman spectroscopy for disease detection and sensing. These studies provide a snapshot of the current state of the field in the clinical implementation of this technique (Table 2.2). By far, the most common clinical target under investigation with Raman spectroscopy is cancer. Large clinical studies have seen ongoing work in several organ systems, all of which have traits in common: a need for improved early detection with high sensitivity and specificity, well-characterized disease processes, and relative ease of access to the organ under study. The specific instruments utilized in these studies differ

slightly but all of the designs are driven by the anatomical target of interest. It is also of interest to note that all published studies of large clinical studies have been performed by the same few research groups pointing to the need for more research to translate the scope of Raman spectroscopy to *in vivo* human studies (Table 2.2).

2.6.4.a Cervix

Cervical cancer is a highly preventable disease, as progression from precancer (or dysplasia) to cancer takes many years, providing a wide detection and treatment window. Developed countries have implemented vigorous screening programs that have dramatically reduced cervical cancer rates. Unfortunately, in developing nations where limited resources prevent large-scale screening, cervical cancer is one of the most common causes of cancer-related death among women comprising approximately 90% of 265,000 cervical cancer deaths worldwide.[202] Raman spectroscopy has been evaluated as an early diagnostic tool for cervical cancers and precancers over the past two decades. Our group demonstrated that Raman scattering was sensitive to normal, benign, low grade, and high grade dysplastic tissues *in vivo*.[203] By integrating analytical algorithms with data collection, diagnostic accuracies as high as 88% were achieved. Further investigation found that by incorporating hormonal/menopausal status, the predictive performance improved to 94%.[204] Continuing work has identified cervical inflammation, parity status, and body mass index as additional variables to be considered but identified limited

influence of other patient variables including race/ethnicity and socio-economic status on Raman scattering based disease discrimination.[139,205]

The well-defined nature of the disease and easy accessibility of the cervix have allowed many researchers to pursue diagnostic research in this organ *in vivo*. Several different groups have used fiber based Raman systems for diagnosis and correlated their findings with colposcopy. These have used a variety of fiber probe designs and different multivariate statistical methods to achieve a range of performance estimates as shown in Table 2.2.[139,203,206-209] In other cervical cancer studies, Huang *et al*. developed a simultaneous fingerprint and high-wavenumber confocal Raman system for cervical precancer detection and demonstrated the performance of this combined approach in 84 patients with sensitivity of 81% and specificity of 87%.[209] Zeng *et al* tested the feasibility of a label free blood test based on blood plasma SERS on samples from 60 cervical cancer patients and obtained a sensitivity and specificity of 96% and 92% respectively when using multivariate diagnostic algorithms.[210] Other results have demonstrated the potential of Raman spectroscopy to differentiate between responders and non-responders to radiotherapy on biopsies from patients with cervical cancer[211] and to detect high risk strains of the human papilloma virus in cervical cells.[212] However these results need to be independently validated in a large study cohort. A recent review article on the application of Raman spectroscopy for cervical cancer presents an excellent summary of all relevant studies in a table.[213] Beyond the realm of cancer

detection, our group has demonstrated the potential of Raman spectroscopy to track biochemical changes in the cervix during pregnancy and develop an understanding of cervical remodeling that occurs throughout pregnancy and parturition.[214,215]

2.6.4.b Skin

As the major organ in the integumentary system, the skin is both the outer barrier of the body to the external world as well as the tissue that is easiest to interrogate with light. Melanocytic and non-melanocytic cancers have different cellular origins, but collectively comprise the most common cancers in the world.[216] As a surface organ malignancy, skin cancers are among the easiest to study with optical techniques; however, the complex, turbid nature of the skin makes it one of the most challenging clinical targets for optical diagnostics and monitoring. Early studies used Raman spectroscopy to extract water concentration profiles in human skin while demonstrating the feasibility of *in vivo* Raman spectroscopy for clinical monitoring.[217] Since then, much of skin Raman research has focused on the investigation of Raman based diagnostics. These studies also resulted in developing portable systems that were directly applicable to the clinical workflow, with instruments that can make measurements with integration times under 1 second.[52,54,102] A number of groups have invested significant effort in studying skin cancers in order to improve patient care and as a result, skin cancer studies have some of the highest recruitment of any Raman studies published, as related in Table

2.2.[52,200,218-220] Zeng *et al*. utilized a Raman instrument to study melanocytic and non-melanocytic as well as malignant and premalignant melanocytic lesions from 453 patients: discrimination of cancer and precancer versus benign lesions demonstrated a 90-99% sensitivity, with a related specificity of 15-54%.[52] This work suggests that Raman techniques can be used to reduce the need for unnecessary biopsies to a significant degree, potentially by 50-100%. Other groups have utilized multimodal approaches, leveraging the strengths of Raman spectroscopy with a combination of fluorescence and diffuse reflectance techniques in order to improve diagnostic outcomes. In one such report of 76 patients, Raman spectroscopy alone was demonstrated to achieve 100% sensitivity and specificity for discriminating melanoma from benign pigmented lesions, but only 72 % sensitivity and 64% specificity in separating non-melanoma skin cancers from precancers and 68% sensitivity and 55% specificity for distinguishing non-melanoma cancers and precancers from normal tissues. However, when combined with fluorescence and diffuse reflectance features, those same comparisons achieved 100/100%, 95/71%, and 90/85% sensitivities/specificities, respectively.[200] In other Raman skin research not related to cancer, Irvine *et al.* studied atopic dermatitis in 132 children, correlating natural moisturizing factor signals obtained via Raman scattering with genetic screening for filaggrin mutations common in atopic dermatitis.[221] The results of this study found that Raman signals achieved 98.7% sensitivity and 86.8% specificity in identifying atopic dermatitis associated with these

mutations. Raman spectral signatures of skin carotenoids have also been investigated using a 488 nm based resonance approach to profile the intake of fruits and vegetables in preschool aged children.[161] This study demonstrated a correlation of Raman signatures with parent-reported family participation in a nutritional-education and -quality program, further demonstrating the exquisite sensitivity of Raman scattering to biochemical components.

2.6.4.c Gastrointestinal tract

The gastrointestinal tract encompasses the digestive system from the mouth, through the esophagus, stomach, intestines, colon to the rectum. The entire organ system, with the exception of parts of the small intestine, is accessible directly (to the mouth) or via an endoscope. In developing Raman spectroscopy as a diagnostic tool for the GI tract, the challenge is in the development of a fiber probe that can be inserted through the endoscope and placed in contact with the tissue of interest in a stable manner for the duration of data acquisition. Numerous groups have focused their attention on various parts of this organ for Raman based detection.

2.6.4.c.i Mouth

Oral tissue is particularly easy to access since endoscopy is not required, mitigating the size constraints of the probe for *in vivo* Raman measurements. Oral cancer incidence has been increasing over the last 40 years in the US and is a larger problem globally, For example, it accounts for 10% of all cancers in

India.[202] This cancer can rapidly spread, which emphasizes the need for early detection and monitoring. Murali Krishna et al. report the discrimination of normal control, premalignant, and cancerous sites from 104 patients with prediction accuracies ranging from 72-96%.[222] In a more recent study, the same group investigated the potential for Raman spectroscopy to detect malignancy associated changes/cancer field effects in a cohort of 84 oral cancer and age-matched control patients.[223] Comparison of non-cancer locations in a smoking and non-smoking population demonstrated prediction accuracies from 75-98% with most of the misclassifications occurring between control locations in cancer patients and locations in smoking healthy controls. This work further demonstrates the sensitivity of Raman scattering to subtle biochemical changes which may precede macroscopic disease.[224,225] Another group reported the discrimination of normal oral tissue from three separate lesion categories with per-class accuracies ranging from 82-89% in 199 patients and 96% sensitivity and 99% specificities for normal versus malignant and 99% and 98% respectively, for normal versus potentially malignant.[226] One variability study of age and tobacco-related pathological change for oral cancer and precancer demonstrated sensitivity to age-related changes in Raman spectra, however the inclusion of this diverse control population had no impact on classification of normal and abnormal conditions.[227] Given the critical need for oral cancer detection particularly in low resource settings and the excellent performance that can be achieved in its detection with Raman spectroscopy, this area of

research is ripe for clinical translation but needs a low cost instrument for its success. The optical device market has seen a recent increase in the number of handheld Raman devices available commercially; these are sold mostly for the identification of pure chemicals and trace elements. However, these devices indicate that the technology exists for the miniaturization of current clinical Raman systems which could in turn make the prospect of commercial translation of Raman systems in low resource settings a reality.

2.6.4.c.ii Esophagus

Barrett's esophagus is a consequence of gastroesophageal reflux that has been associated with an increased risk of esophageal adenocarcinoma. By adapting Raman fiber optic probe designs for endoscopic compatibility, *in situ* measurements of this disease target have been enabled by many groups. Wilson *et al* demonstrated the potential for *in vivo* spectral acquisition in a cohort of 65 Barrett's esophagus patients, with sensitivities and specificities of 86-88% and 88-89%, respectively for discriminating dysplastic and high-risk lesions from non-dysplastic and low-risk cases.[128] This demonstration of a clinically-useful Raman instrument with endoscopic compatibility and 5 second integration times was an early indication of the ability of *in vivo* Raman spectroscopy to access an internal organ. More recent work by another group has demonstrated real-time performance of Raman spectroscopy during endoscopy in 373 patients with integration times of 0.2 seconds per acquisition and could discriminate high-grade dysplastic Barrett's esophagus from normal and non-

dysplastic tissue with 87% sensitivity and 84.7% sensitivity.[147] Other work has demonstrated the importance of considering the anatomical location of a Raman measurement; in a study of 107 patients, inter-organ variability (between the esophagus and stomach) was significant compared to intra-organ variability and neoplastic change.[145] These results support the need for comprehensive libraries of disease spectra and a thorough understanding of healthy and diseased tissues.

2.6.4.c.iii Stomach

As a leading cause of cancer-related death worldwide[202], stomach cancer has been another popular detection target for Raman spectroscopy.[228-230] As with the esophagus, integrating Raman fiber probes with standard endoscopes has enabled *in vivo* evaluation of gastric malignancies. Utilizing an endoscope compatible probe, linear component tissue model, and classification and regression trees, Huang *et al*. reported 94% sensitivity and 93.4% specificity for discriminating normal gastric tissue from cancer in 67 patients undergoing endoscopy with biopsy.[231] Huang *et al.* have also reported a statistically robust study where 450 patients undergoing upper endoscopy were measured with Raman spectroscopy to train a discrimination algorithm.[232] This work was one of the first reports to prospectively discriminate gastric precancer in real-time using Raman spectroscopy, achieving a sensitivity of 81% and a specificity of 88%. In another study by the same group, researchers investigated stomach ulcers in 71 patients and found that Raman endoscopic measurements could differentiate normal mucosa, benign and malignant ulcers with 82-90%

sensitivity and 93-95% specificity.[233] A related report by this group investigated the ability of Raman techniques to perform multi-class discrimination of normal, precancer, and early stage gastric cancer in a cohort of 83 patients, and demonstrated sensitivity to early stages of the carcinogenic process.[234] Finally, a report combining Raman techniques with near-infrared autofluorescence signatures (n=81, 97.9% sensitivity & 91.5% specificity)[235] demonstrated similar results for *in vivo* detection for cohorts gastric cancer patients.

2.6.4.c.iv Colon/Intestine

Colorectal cancer is a major disease entity, ranking among the top three cancers worldwide for estimated new cases and cancer-related deaths.[202] Colonoscopy is the most sensitive technique available for screening and early detection of cancer or precancerous polyps and routine colonoscopy screening for adults over 50 has become the standard in countries like the United States. However, benign polyps often develop, which can limit its sensitivity and potentially complicate intervention. Preliminary Raman studies based on *ex vivo* samples and small *in vivo* cohorts have been reported, discriminating benign and malignant polyps. One *in vivo* study has investigated the impact of the colon segment on the acquired Raman signal from 50 colonoscopy patients, but found that the between-segment variability was less influential than malignant status.[236] The same group has since reported an *in vivo* study combining both fingerprint and high-wavenumber Raman spectroscopy during endoscopy in order to achieve 90% sensitivity and 83% specificity for

separating adenomatous and hyperplastic polyps in real-time.[174] In other studies, our group has demonstrated the potential for endoscopic Raman spectroscopy to discriminate inflammatory bowel diseases in a 53 patient cohort, demonstrating the potential of Raman spectroscopy to detect subtle changes in tissues related to inflammatory diseases,[80] another significant clinical problem that has seen a rise in incidence in recent years.

2.6.4.d Other diagnostic targets

While the majority of reports published on large clinical *in vivo* Raman studies have been focused on the above tissues, other diseases have also been studied with Raman spectroscopy. Lung cancer is one of the most common causes of cancer related death impacting millions of people annually.[202] Similar to other endoscopic studies with Raman scattering, investigation of this disease has been conducted in *ex vivo* samples with near 100% accuracy. A bronchoscope compatible Raman fiber probe has been used to study the potential of Raman spectroscopy for the detection of pre-neoplastic lesions in the bronchial tree in 26 patients.[237] However, no reports on the performance of this technique for a large cohort of lung cancers *in vivo* were found.

Surgical guidance is another areas of active research for clinical Raman spectroscopy, where researchers have developed biopsy-needle compatible fiber probes to detect micro-calcifications for breast cancer diagnosis as well as SORS techniques to determine breast cancer margin status during surgical resection with excellent results. Raman spectra of core needle biopsies could

successfully be used to identify the presence of micro-calcification in these specimens with 82% accuracy.[238] Depth-resolved SORS was used to assess the ability of this technique to detect the presence of cancer cells in excised breast specimens for margin assessment with 95% sensitivity and 100% specificity.[178] A large clinical study is currently in progress to validate these findings intra-operatively. Another study has focused on the ability of Raman spectroscopy to assess axillary lymph nodes during breast surgery.[239] Preliminary reports for this study utilized frozen tissue section of lymph nodes from 58 patients immediately after excision from the body and reported 81% sensitivity and 97% specificity. However, the authors indicate that freshly excised samples could be analyzed for intra-operative evaluation. Another application for Raman spectroscopy in surgical guidance is for brain surgery. While restricted to small cohort studies at this point, researchers have characterized a surgery compatible Raman probe based system[240] and demonstrated discrimination of normal brain from dense cancer and normal brain invaded by cancer cells with up to 93% sensitivity and 91% specificity for grade 2 to grade 4 gliomas in 17 patients.[241] This work shows continued promise for surgical guidance based on Raman scattering techniques however, it also requires expanded recruitment for validation.

A majority of the research for Raman spectroscopy techniques has focused on disease diagnosis of tissues *in situ.* However, clinically relevant diagnostics have also been investigated for samples removed from the body,

especially pertaining to blood analytes. Puppels *et al.* published work utilizing a spectral library to prospectively and rapidly evaluate blood cultures for bacterial and fungal pathogens, achieving 92% classification accuracy from 121 patient samples.[242] More commonly, researchers introduce SERS particles into *ex vivo* specimens in order to improve sensitivities. These have been applied for numerous detection endpoints including a recent publication for nasopharyngeal cancer detection[243] where blood plasma samples from 156 patients were analyzed with SERS. The study demonstrated 95% sensitivity and 91% specificity for discriminating healthy volunteers from cancer patients. Liu *et al.* used SERS particles with serum from healthy and bladder cancer patients in order to improve early stage detection. By combining the sensitivity of SERS with advanced machine learning genetic algorithms, the researchers were able to achieve 94% diagnostic accuracy in a cohort of 91 patients.[244] Zeng *et al.* have likewise investigate SERS techniques for blood plasma analysis aimed at improved gastric cancer detection.[245] Samples from 65 patients were analyzed with polarized illumination of SERS particles and multivariate techniques. The study indicated great promise for specific circularly-polarization regimes with 100% sensitivity and 97% specificity for non-invasive gastric cancer detection. Another long-standing non-invasive target includes blood glucose monitoring. Feld *et al.* developed compound hyper- and parabolic concentrators for transdermal blood glucose measurements, however, there have been no large cohort studies reported with this device.[84,130] Other reports have utilized Raman

scattering to look at cerebral spinal fluid samples from 61 patients *ex vivo* to diagnoses tuberculous meningitis and achieved 91% sensitivity and 82% specificity.[246] This is just a glimpse of the numerous *ex vivo* applications of Raman spectroscopic techniques that are relevant for clinical detection and diagnostics.

Raman spectroscopy has been used in the eye to study such conditions as macular degeneration. Gellerman *et al*. developed a resonance Raman approach at 488 nm to study the impact of carotenoids in the skin and eye.[159] In one application of this approach, Chakaravarthy *et al.,* measured macular pigment from 107 patients and correlated with heterochromatic flicker photometry to evaluate antioxidant pigment of the retina, however, the correlations were low and further investigation was merited.[160] Using the same approach, Stevenson *et al*. demonstrated the improved effect of antioxidant supplementation in age related macular degeneration patients in a study of 433 patients *in vivo*.[158]

2.6.5 Summary

Despite the impressive work presented here in a selection of clinical fields, there remain a number of challenges that stand in the way of clinical translation for Raman based technologies for widespread human use. Demonstrating the safety of these devices to regulatory agencies is a vital step that must be undertaken for translation. Practically speaking, there is a need for

robust system design with consistent internal calibration, such that with little training, a user can setup a system and collect repeatable data. For this to be realized, low-cost or long-lasting, durable, high-performance fiber optic probes (or an equivalent light delivery device) are required. Having reliable and consistent performance for interfacing the sample and system is pivotal for the transition from research instrument to clinical relevance. To this end, there is also a need for inter-system calibration and large libraries of spectral data that can be transferred and compared between instruments, to expand the utility of the devices for multiple medical targets. Standardized and reliable methods for data analysis are necessary to condense the feature-rich Raman spectra obtained by these instruments into not only the salient features used for a clinical evaluation, but also communicated to the user in a simple, easily interpretable format, including clinically relevant metrics for evaluation (ROC, sensitivity/specificity). Preliminary work on many of these aspects for clinical translation are ongoing, but continued effort is needed to facilitate the transition from benchtop to bedside. Of course, it is of the utmost importance that the technologies developed provide new and meaningful information about a clinical target; therefore, seeking collaboration and input from the medical community is paramount to ensure that research efforts of Raman techniques are directed at relevant needs in medicine and surgery. Finally, the largest obstacle at this point to clinical translation is the need to demonstrate the added value of these optical technologies over or in parallel with existing medical

devices in large cohorts studies based on patient outcomes and relative to meaningful and accepted gold standards.

The various applications described above demonstrate the potential of Raman spectroscopy to affect patient care. And yet few systems based on Raman spectroscopy have been processed through regulatory approval and commercialized successfully. The external barriers towards the adoption of this technology lies in the limited size of the target market revenue which tends to hold back potential industrial partners and investors. Regardless, there have been some successes including the system by River Diagnostics which has successfully sold Raman instruments for the assessment of skin in the cosmetic industry (albeit not for a clinical application) and Verisante Technology which has most recently released Raman based devices for oral and skin cancer diagnosis. These commercial devices indicate that the barriers to the clinical implementation of Raman spectroscopy are not insurmountable and widespread acceptance of this technology can be achieved.

2.7 References

1. Granger DN, Barrowman JA, Kvietys PR. *Clinical Gastrointestinal Physiology.* Saunders; 1985.
2. Shaffer EA, Thomson ABR. *First Principles of Gastroenterology: The Basis of Disease and an Approach to Management.* Canadian Association of Gastroenterology; 1997.
3. Ross MH, Pawlina W. *Histology.* Lippincott Williams & Wilkins; 2006.

4. Young B. *Wheater's functional histology : a text and colour atlas.* Edinburgh: Churchill Livingstone/Elsevier; 2006.

5. Ananthakrishnan AN. Epidemiology and risk factors for IBD. *Nature reviews Gastroenterology & hepatology.* 2015;12(4):205-217.

6. Bernstein CN, Wajda A, Svenson LW, et al. The epidemiology of inflammatory bowel disease in Canada: A population based study. *The American journal of gastroenterology.* 2006;101(8):1945-1945.

7. Carvalho RS, Abadom V, Dilworth HP, Thompson R, Oliva-Hemker M, Cuffari C. Indeterminate colitis: a significant subgroup of pediatric IBD. *Inflamm Bowel Dis.* 2006;12(4):258-262.

8. Farrokhyar F, Swarbrick ET, Irvine EJ. A critical review of epidemiological studies in inflammatory bowel disease. *Scandinavian journal of gastroenterology.* 2001;36(1):2-15.

9. Baldassano RN, Piccoli DA. Inflammatory bowel disease in pediatric and adolescent patients. *Gastroenterology clinics of North America.* 1999;28(2):445-458.

10. Sandler RS, Everhart JE, Donowitz M, et al. The burden of selected digestive diseases in the United States. *Gastroenterology.* 2002;122(5):1500-1511.

11. Kornbluth A, Sachar DB, Gastroenterology AC. Ulcerative Colitis Practice Guidelines in Adults: American College of Gastroenterology, Practice Parameters Committee. *The American journal of gastroenterology.* 2010;105(3):500-500.

12. Kappelman MD, Rifas-Shiman SL, Kleinman K, et al. The prevalence and geographic distribution of Crohn's disease and ulcerative colitis in the United States. *Clin Gastroenterol Hepatol.* 2007;5(12):1424-1429.

13. Loftus EV, Jr. Clinical epidemiology of inflammatory bowel disease: Incidence, prevalence, and environmental influences. *Gastroenterology.* 2004;126(6):1504-1517.

14. Gillen CD, Walmsley RS, Prior P, Andrews HA, Allan RN. Ulcerative colitis and Crohn's disease: a comparison of the colorectal cancer risk in extensive colitis. *Gut.* 1994;35(11):1590-1592.

15. Goldacre MJ, Wotton CJ, Yeates D, Seagroatt V, Jewell D. Cancer in patients with ulcerative colitis, Crohn's disease and coeliac disease:

record linkage study. *European journal of gastroenterology & hepatology.* 2008;20(4):297-304.

16. Roifman I, Sun YC, Fedwick JP, et al. Evidence of endothelial dysfunction in patients with inflammatory bowel disease. *Clin Gastroenterol Hepatol.* 2009;7(2):175-182.

17. Bewtra M, Su C, Lewis JD. Trends in hospitalization rates for inflammatory bowel disease in the United States. *Clin Gastroenterol Hepatol.* 2007;5(5):597-601.

18. Sonnenberg A. Hospitalization for Inflammatory Bowel Disease in the United States Between 1970 and 2004. *Journal of Clinical Gastroenterology.* 2009;43(4):297-300.

19. Gunnarsson C, Chen J, Rizzo JA, Ladapo JA, Lofland JH. Direct Health Care Insurer and Out-of-Pocket Expenditures of Inflammatory Bowel Disease: Evidence from a US National Survey. *Dig Dis Sci.* 2012;57(12):3080-3091.

20. Stone CD. The economic burden of inflammatory bowel disease: clear problem, unclear solution. *Dig Dis Sci.* 2012;57(12):3042-3044.

21. Xavier RJ, Podolsky DK. Unravelling the pathogenesis of inflammatory bowel disease. *Nature.* 2007;448(7152):427-434.

22. Berrebi D, Besnard M, Fromont-Hankard G, et al. Interleukin-12 expression is focally enhanced in the gastric mucosa of pediatric patients with Crohn's disease. *Am J Pathol.* 1998;152(3):667-672.

23. Heller F, Florian P, Bojarski C, et al. Interleukin-13 is the key effector Th2 cytokine in ulcerative colitis that affects epithelial tight junctions, apoptosis, and cell restitution. *Gastroenterology.* 2005;129(2):550-564.

24. Parronchi P, Romagnani P, Annunziato F, et al. Type 1 T-helper cell predominance and interleukin-12 expression in the gut of patients with Crohn's disease. *Am J Pathol.* 1997;150(3):823-832.

25. Podolsky DK. Inflammatory bowel disease. *N Engl J Med.* 2002;347(6):417-429.

26. Mutsaers SE, Bishop JE, McGrouther G, Laurent GJ. Mechanisms of tissue repair: from wound healing to fibrosis. *Int J Biochem Cell Biol.* 1997;29(1):5-17.

27. Rieder F, Brenmoehl J, Leeb S, Scholmerich J, Rogler G. Wound healing and fibrosis in intestinal disease. *Gut.* 2007;56(1):130-139.

28. Cobrin GM, Abreu MT. Defects in mucosal immunity leading to Crohn's disease. *Immunol Rev.* 2005;206:277-295.

29. Targan SR, Karp LC. Defects in mucosal immunity leading to ulcerative colitis. *Immunol Rev.* 2005;206:296-305.

30. Feller M, Huwiler K, Schoepfer A, Shang A, Furrer H, Egger M. Long-term antibiotic treatment for Crohn's disease: systematic review and meta-analysis of placebo-controlled trials. *Clinical infectious diseases : an official publication of the Infectious Diseases Society of America.* 2010;50(4):473-480.

31. Prantera C, Scribano ML. Antibiotics and probiotics in inflammatory bowel disease: why, when, and how. *Current opinion in gastroenterology.* 2009;25(4):329-333.

32. D'Haens GR, Panaccione R, Higgins PD, et al. The London Position Statement of the World Congress of Gastroenterology on Biological Therapy for IBD with the European Crohn's and Colitis Organization: when to start, when to stop, which drug to choose, and how to predict response? *The American journal of gastroenterology.* 2011;106(2):199-212; quiz 213.

33. Sandborn WJ, Ghosh S, Panes J, et al. Tofacitinib, an oral Janus kinase inhibitor, in active ulcerative colitis. *N Engl J Med.* 2012;367(7):616-624.

34. Warner B, Harris AW. Adalimumab induces and maintains clinical remission in patients with moderate-to-severe ulcerative colitis. *Gastroenterology.* 2012;143(1):e42; author reply e42.

35. Sandborn WJ, Gasink C, Gao LL, et al. Ustekinumab induction and maintenance therapy in refractory Crohn's disease. *N Engl J Med.* 2012;367(16):1519-1528.

36. Seminerio JL, Loftus EV, Jr., Colombel JF, Thapa P, Sandborn WJ. Infliximab for Crohn's disease: the first 500 patients followed up through 2009. *Dig Dis Sci.* 2013;58(3):797-806.

37. Kane SV, Horst S, Sandborn WJ, et al. Natalizumab for moderate to severe Crohn's disease in clinical practice: the Mayo Clinic Rochester experience. *Inflamm Bowel Dis.* 2012;18(12):2203-2208.

38. Melmed GY, Targan SR. Future biologic targets for IBD: potentials and pitfalls. *Nature reviews Gastroenterology & hepatology.* 2010;7(2):110-117.

39. Plevy SE, Targan SR. Future therapeutic approaches for inflammatory bowel diseases. *Gastroenterology.* 2011;140(6):1838-1846.

40. Baumgart DC. The diagnosis and treatment of Crohn's disease and ulcerative colitis. *Dtsch Arztebl Int.* 2009;106(8):123-133.

41. American Society for Gastrointestinal Endoscopy Standards of Practice C, Shergill AK, Lightdale JR, et al. The role of endoscopy in inflammatory bowel disease. *Gastrointestinal endoscopy.* 2015;81(5):1101-1121 e1101-1113.

42. Lichtenstein GR, Hanauer SB, Sandborn WJ. Management of Crohn's disease in adults. *The American journal of gastroenterology.* 2009;104(2):465-483; quiz 464, 484.

43. Martland GT, Shepherd NA. Indeterminate colitis: definition, diagnosis, implications and a plea for nosological sanity. *Histopathology.* 2007;50(1):83-96.

44. Zholudev A, Zurakowski D, Young W, Leichtner A, Bousvaros A. Serologic testing with ANCA, ASCA, and anti-OmpC in children and young adults with Crohn's disease and ulcerative colitis: diagnostic value and correlation with disease phenotype. *The American journal of gastroenterology.* 2004;99(11):2235-2241.

45. Cooney R, Jewell D. The genetic basis of inflammatory bowel disease. *Dig Dis.* 2009;27(4):428-442.

46. Corman ML. *Colon and rectal surgery.* Lippincott; 1989.

47. Raman C, Krishnan K. A new type of secondary radiation. *Nature.* 1928;121(3048):501-502.

48. Ferraro JR, Nakamoto K. *Introductory Raman Spectroscopy.* San Diego, CA: Academic Press; 1994.

49. Williams AC, Barry BW, Edwards HG, Farwell DW. A critical comparison of some Raman spectroscopic techniques for studies of human stratum corneum. *Pharm Res.* 1993;10(11):1642-1647.

50. Bergholt MS, Zheng W, Ho KY, et al. Fiberoptic confocal raman spectroscopy for real-time in vivo diagnosis of dysplasia in Barrett's esophagus. *Gastroenterology.* 2014;146(1):27-32.

51. Huang Z, Teh SK, Zheng W, et al. Integrated Raman spectroscopy and trimodal wide-field imaging techniques for real-time in vivo tissue Raman measurements at endoscopy. *Opt Lett.* 2009;34(6):758-760.

52. Lui H, Zhao J, McLean D, Zeng H. Real-time Raman Spectroscopy for In Vivo Skin Cancer Diagnosis. *Cancer Res.* 2012;72(10):2491-2500.

53. Lieber CA, Mahadevan-Jansen A. Automated method for subtraction of fluorescence from biological Raman spectra. *Appl Spectrosc.* 2003;57(11):1363-1367.

54. Zhao J, Lui H, McLean DI, Zeng H. Integrated real-time Raman system for clinical in vivo skin analysis. *Skin Res Technol.* 2008;14(4):484-492.

55. Motz JT, Gandhi SJ, Scepanovic OR, et al. Real-time Raman system for in vivo disease diagnosis. *J Biomed Opt.* 2005;10(3):031113.

56. Hanlon EB, Manoharan R, Koo TW, et al. Prospects for in vivo Raman spectroscopy. *Physics in medicine and biology.* 2000;45(2):R1-R59.

57. Standard A. Z136. 1. American national standard for the safe use of lasers. American National Standards Institute. *Inc, New York.* 1993.

58. Patil CA, Pence IJ, Lieber CA, Mahadevan-Jansen A. 1064 nm dispersive Raman spectroscopy of tissues with strong near-infrared autofluorescence. *Opt Lett.* 2014;39(2):303-306.

59. Welch AJ. The Thermal Response of Laser Irradiated Tissue. *IEEE J Quantum Electron.* 1984;20(12):1471-1481.

60. Manoharan R, Wang Y, Boustany NN, et al. Raman spectroscopy for cancer detection: instrument development and tissue diagnosis. Paper presented at: International Symposium on Biomedical Optics Europe'941994; Lille, France.

61. Frank CJ, McCreery RL, Redd DC. Raman spectroscopy of normal and diseased human breast tissues. *Anal Chem.* 1995;67(5):777-783.

62. Clarke RH, Hanlon EB, Isner JM, Brody H. Laser Raman spectroscopy of calcified atherosclerotic lesions in cardiovascular tissue. *Appl Opt.* 1987;26(16):3175-3177.

63. Yu N-T, East EJ. Laser Raman spectroscopic studies of ocular lens and its isolated protein fractions. *J Biol Chem.* 1975;250(6):2196-2202.

64. Nie S, Bergbauer K, Ho J, Kuck J, Yu N. Applications of near-infrared Fourier transform Raman spectroscopy in biology and medicine. *Spectroscopy.* 1990;5(7):24.

65. Puppels G, De Mul F, Otto C, et al. Studying single living cells and chromosomes by confocal Raman microspectroscopy. 1990.

66. Coldren LA, Corzine SW, Mashanovitch ML. *Diode Lasers and Photonic Integrated Circuits.* Wiley; 2012.

67. Fleming MW, Mooradian A. Spectral Characteristics of External-Cavity Controlled Semiconductor-Lasers. *IEEE J Quantum Electron.* 1981;17(1):44-59.

68. Rudder SL, Connolly JC, Steckman GJ. Hybrid ECL/DBR wavelength and spectrum stabilized lasers demonstrate high power and narrow spectral linewidth. 2006:61010I-61010I.

69. Wang W, Major A, Paliwal J. Grating-Stabilized External Cavity Diode Lasers for Raman Spectroscopy—A Review. *Appl Spectrosc Rev.* 2011;47(2):116-143.

70. Latka I, Dochow S, Krafft C, Dietzek B, Popp J. Fiber optic probes for linear and nonlinear Raman applications - Current trends and future development. *Laser Photonics Rev.* 2013;7(5):698-731.

71. Myrick M, Angel S. Elimination of background in fiber-optic Raman measurements. *Applied Spectroscopy.* 1990;44(4):565-570.

72. Utzinger U, Richards-Kortum RR. Fiber optic probes for biomedical optical spectroscopy. *J Biomed Opt.* 2003;8(1):121-147.

73. Myrick ML, Angel SM, Desiderio R. Comparison of some fiber optic configurations for measurement of luminescence and Raman scattering. *Applied optics.* 1990;29(9):1333-1344.

74. Mahadevan-Jansen A, Richards-Kortum R. Raman Spectrscopy for the Detection of Cancers and Precancers. *Journal of Biomedical Optics.* 1996;1(1):31-70.

75. Shim MG, Wilson BC, Marple E, Wach M. Study of fiber-optic probes for in vivo medical Raman spectroscopy. *Applied Spectroscopy.* 1999;53(6):619-627.

76. Matousek P. Raman signal enhancement in deep spectroscopy of turbid media. *Appl Spectrosc.* 2007;61(8):845-854.

77. Broeng J, Barkou SE, Sondergaard T, Bjarklev A. Analysis of air-guiding photonic bandgap fibers. *Opt Lett.* 2000;25(2):96-98.

78. Broeng J, Mogilevstev D, Barkou SE, Bjarklev A. Photonic crystal fibers: A new class of optical waveguides. *Opt Fiber Technol.* 1999;5(3):305-330.

79. AnitaMahadevan J, ChetanApatil, Isaac JP. Raman Spectroscopy: From Benchtop to Bedside. *Biomedical Photonics Handbook, Second Edition*: CRC Press; 2014:759-802.

80. Pence IJ, Nguyen QT, Bi X, et al. Endoscopy-coupled Raman spectroscopy for in vivo discrimination of inflammatory bowel disease. 2014.

81. Mahadevan-Jansen A, Mitchell MF, Ramanujam N, Utzinger U, Richards-Kortum R. Development of a fiber optic probe to measure NIR Raman spectra of cervical tissue in vivo. *Photochem Photobiol.* 1998;68(3):427-431.

82. Motz JT, Hunter M, Galindo L, Kramer JR, Dasari RR, Feld MS. Development of Optical Fiber Probes for Biological Raman Spectroscopy. Paper presented at: Biomedical Optical Spectroscopy and Diagnostics, OSA Biomedical Topical Meetings Technical Digest2002.

83. Schwab SD, McCreery RL. Versatile, efficient Raman sampling with fiber optics. *Analytical Chemistry.* 1984;56(12):2199-2204.

84. Tanaka K, Pacheco MT, Brennan III JF, et al. Compound parabolic concentrator probe for efficient light collection in spectroscopy of biological tissue. *Applied optics.* 1996;35(4):758-763.

85. Dochow S, Latka I, Becker M, et al. Multicore fiber with integrated fiber Bragg gratings for background-free Raman sensing. *Optics express.* 2012;20(18):20156-20169.

86. Instruments P. Spectroscopic etaloning in back illuminated ccds. *CCD Primer* http://www.princetoninstruments.com/cms/index.php/library/51-ccd-primer/149-spectroscopic-etaloning-in-back-illuminated-ccds.

87. Technologies A. Optical Etaloning in CCDs and EMCCDs.

88. Scientific H. Etalon Fringe Suppression.

89. Bonnier F, Ali S, Knief P, et al. In vitro analysis of immersed human tissues by Raman microspectroscopy (vol 42, pg 888, 2011). *J Raman Spectrosc.* 2011;42(8):1711-1711.

90. Huang ZW, Zeng HS, Hamzavi I, et al. Cutaneous melanin exhibiting fluorescence emission under near-infrared light excitation. *J Biomed Opt.* 2006;11(3).

91. Lakowicz J. Principles of fluorescence spectroscopy. 1983.

92. Instruments P. Introduciton to Scientific InGaAs FPA cameras. 2012.

93. Kawabata T, Mizuno T, Okazaki S, et al. Optical diagnosis of gastric cancer using near-infrared multichannel Raman spectroscopy with a 1064-nm excitation wavelength. *Journal of Gastroenterology.* 2008;43(4):283-290.

94. Min YK, Yamamoto T, Kohda E, Ito T, Hamaguchi H. 1064 nm near-infrared multichannel Raman spectroscopy of fresh human lung tissues. *Journal of Raman Spectroscopy.* 2005;36(1):73-76.

95. Pence IJ, Patil CA, Lieber CA, Mahadevan-Jansen A. Discrimination of liver malignancies with 1064 nm dispersive Raman spectroscopy. *Biomed Opt Express.* 2015;6(8):2724-2737.

96. Lerner JM. Imaging spectrometer fundamentals for researchers in the biosciences - A tutorial. *Cytometry A.* 2006;69A(8):712-734.

97. Battey DE, Slater JB, Wludyka R, Owen H, Pallister DM, Morris MD. Axial Transmissive F/1.8 Imaging Raman Spectrograph with Volume-Phase Holographic Filter and Grating. *Appl Spectrosc.* 1993;47(11):1913-1919.

98. Tedesco JM, Owen H, Pallister DM, Morris MD. Principles and Spectroscopic Applications of Volume Holographic Optics. *Anal Chem.* 1993;65(9):A441-A449.

99. T. J. Kessler, J. Barone, C. Kellogg, Huang H. *Holographic Transmission Gratings for Spectral Dispersion.* Springfield, VA: University of Rochester Laoratory for Laser Energetics;2000.

100. Keltner Z, Kayima K, Lanzarotta A, et al. Prism-based infrared spectrographs using modern-day detectors. *Appl Spectrosc.* 2007;61(9):909-915.

101. Lieber CA, Kanter EM, Mahadevan-Jansen A. Comparison of Raman spectrograph throughput using two commercial systems: transmissive versus reflective. *Appl Spectrosc.* 2008;62(5):575-582.

102. Huang Z, Zeng H, Hamzavi I, McLean DI, Lui H. Rapid near-infrared Raman spectroscopy system for real-time in vivo skin measurements. *Opt Lett.* 2001;26(22):1782-1784.

103. Marcet S, Verhaegen M, Blais-Ouellette S, Martel R. Raman spectroscopy hyperspectral imager based on Bragg tunable filters. 2012.

104. Stone N, Stavroulaki P, Kendall C, Birchall M, Barr H. Raman spectroscopy for early detection of laryngeal malignancy: preliminary results. *The Laryngoscope.* 2000;110(10 Pt 1):1756-1763.

105. Utzinger U, Heintzelman DL, Mahadevan-Jansen A, Malpica A, Follen M, Richards-Kortum R. Near-infrared Raman spectroscopy for in vivo detection of cervical precancers. *Appl Spectrosc.* 2001;55(8):955-959.

106. Pence IJ, Vargis E, Mahadevan-Jansen A. Assessing Variability of In Vivo Tissue Raman Spectra. *Appl Spectrosc.* 2013;67(7):789-800.

107. Mahadevan-Jansen A, Richards-Kortum R. Raman Spectroscopy for the detection of cancers and precancers. *J Biomed Opt.* 1996;1(1):31-70.

108. Choquette SJ, Etz ES, Hurst WS, Blackburn DH, Leigh SD. Relative intensity correction of Raman spectrometers: NIST SRMs 2241 through 2243 for 785 nm, 532 nm, and 488 nm/514.5 nm excitation. *Appl Spectrosc.* 2007;61(2):117-129.

109. Krishnamoorthi H, Mahadevan-Jansen A. Calibration of Raman systems for biomedical and clinical applications. Paper presented at: SPIE Photonics West2010; San Francisco, CA.

110. Mosier-Boss PA, Lieberman S, Newbery R. Fluorescence rejection in Raman spectroscopy by shifted-spectra, edge detection, and FFT filtering techniques. *Appl Spectrosc.* 1995;49(5):630-638.

111. Van Duyne RP, Jeanmaire DL, Shriver D. Mode-locked laser Raman spectroscopy. New technique for the rejection of interfering background luminescence signals. *Anal Chem.* 1974;46(2):213-222.

112. O'Grady A, Dennis AC, Denvir D, McGarvey JJ, Bell SE. Quantitative Raman spectroscopy of highly fluorescent samples using pseudosecond derivatives and multivariate analysis. *Anal Chem.* 2001;73(9):2058-2065.

113. Zhang D, Ben-Amotz D. Enhanced chemical classification of Raman images in the presence of strong fluorescence interference. *Appl Spectrosc.* 2000;54(9):1379-1383.

114. Barclay V, Bonner R, Hamilton I. Application of wavelet transforms to experimental spectra: smoothing, denoising, and data set compression. *Anal Chem.* 1997;69(1):78-90.

115. Cai TT, Zhang D, Ben-Amotz D. Enhanced chemical classification of raman images using multiresolution wavelet transformation. *Appl Spectrosc.* 2001;55(9):1124-1130.

116. Chen K, Zhang HY, Wei HY, Li Y. Improved Savitzky-Golay-method-based fluorescence subtraction algorithm for rapid recovery of Raman spectra. *Appl Opt.* 2014;53(24):5559-5569.

117. Vickers TJ, Wambles RE, Mann CK. Curve fitting and linearity: data processing in Raman spectroscopy. *Appl Spectrosc.* 2001;55(4):389-393.

118. Zhao J, Lui H, McLean DI, Zeng H. Automated autofluorescence background subtraction algorithm for biomedical Raman spectroscopy. *Appl Spectrosc.* 2007;61(11):1225-1232.

119. Baraga JJ, Feld MS, Rava RP. Rapid near-Infrared Raman-Spectroscopy of Human Tissue with a Spectrograph and Ccd Detector. *Appl Spectrosc.* 1992;46(2):187-190.

120. De Luca AC, Mazilu M, Riches A, Herrington CS, Dholakia K. Online fluorescence suppression in modulated Raman spectroscopy. *Anal Chem.* 2009;82(2):738-745.

121. Zhang ZM, Chen S, Liang YZ. Baseline correction using adaptive iteratively reweighted penalized least squares. *Analyst.* 2010;135(5):1138-1146.

122. Cadusch PJ, Hlaing MM, Wade SA, McArthur SL, Stoddart PR. Improved methods for fluorescence background subtraction from Raman spectra. *J Raman Spectrosc.* 2013;44(11):1587-1595.

123. Zhang ZM, Chen S, Liang YZ, et al. An intelligent background-correction algorithm for highly fluorescent samples in Raman spectroscopy. *J Raman Spectrosc.* 2010;41(6):659-669.

124. Savitzky A, Golay MJE. Smoothing and Differentiation of Data by Simplified Least Squares Procedures. *Anal Chem.* 1964;36(8):1627-1639.

125. Edgell WF, Schmidlin E, Balk MW. A Computer-Spectrometer Interactive System for Infrared Spectroscopy. *Appl Spectrosc.* 1980;34(4):420-434.

126. Bussian BM, Hardle W. Robust Smoothing Applied to White Noise and Single Outlier Contaminated Raman-Spectra. *Appl Spectrosc.* 1984;38(3):309-313.

127. Feuerstein D, Parker KH, Boutelle MG. Practical Methods for Noise Removal: Applications to Spikes, Nonstationary Quasi-Periodic Noise, and Baseline Drift. *Anal Chem.* 2009;81(12):4987-4994.

128. Wong Kee Song L-M, Molckovsky A, Wang KK, et al. Diagnostic potential of Raman spectroscopy in Barrett's esophagus. 2005.

129. Ramos PM, Ruisanchez I. Noise and background removal in Raman spectra of ancient pigments using wavelet transform. *J Raman Spectrosc.* 2005;36(9):848-856.

130. Kong CR, Barman I, Dingari NC, et al. A novel non-imaging optics based Raman spectroscopy device for transdermal blood analyte measurement. *AIP advances.* 2011;1(3).

131. Liu C, Glassman WS, Zhu H, et al. Near-IR Fourier transform Raman spectroscopy of normal and atherosclerotic human aorta. *Lasers in the life sciences.* 1992;4(4):257-264.

132. Liu CH, Das BB, Sha Glassman WL, et al. Raman, fluorescence, and time-resolved light scattering as optical diagnostic techniques to separate diseased and normal biomedical media. *Journal of photochemistry and photobiology.* 1992;16(2):187-209.

133. Petrich W. Mid-infrared and Raman spectroscopy for medical diagnostics. *Appl Spectrosc Rev.* 2001;36(2-3):181-237.

134. Mahadevan-Jansen A, Mitchell MF, Ramanujam N, et al. Near-infrared Raman spectroscopy for in vitro detection of cervical precancers. *Photochem Photobiol.* 1998;68(1):123-132.

135. Choo-Smith LP, Edwards HG, Endtz HP, et al. Medical applications of Raman spectroscopy: from proof of principle to clinical implementation. *Biopolymers.* 2002;67(1):1-9.

136. Berger AJ, Koo TW, Itzkan I, Horowitz G, Feld MS. Multicomponent blood analysis by near-infrared Raman spectroscopy. *Appl Opt.* 1999;38(13):2916-2926.

137. Huang Z, Teh SK, Zheng W, et al. In vivo detection of epithelial neoplasia in the stomach using image-guided Raman endoscopy. *Biosens Bioelectron.* 2010;26(2):383-389.

138. Barman I, Dingari NC, Saha A, et al. Application of Raman Spectroscopy to Identify Microcalcifications and Underlying Breast Lesions at Stereotactic Core Needle Biopsy. *Cancer Res.* 2013;73(11):3206-3215.

139. Vargis E, Kanter EM, Majumder SK, et al. Effect of normal variations on disease classification of Raman spectra from cervical tissue. *Analyst.* 2011;136(14):2981-2987.

140. Lednev IK, Ryzhikova E, Kazakov O, et al. Raman Spectroscopy of Blood for Alzheimer's Disease Diagnostics. *Annals of neurology.* 2014;76:S94-S94.

141. Teh SK, Zheng W, Ho KY, Teh M, Yeoh KG, Huang Z. Diagnosis of gastric cancer using near-infrared Raman spectroscopy and classification and regression tree techniques. *J Biomed Opt.* 2008;13(3):034013-034013-034018.

142. Mahadevan-Jansen A, Mantsch HH, Puppels GJ, Society of Photo-optical Instrumentation Engineers. *Biomedical vibrational spectroscopy II : 19-20 January, 2002, San Jose, California USA.* Bellingham, Wash.: SPIE; 2002.

143. Caspers P, Lucassen G, Bruining H, Puppels G. Automated depth-scanning confocal Raman microspectrometer for rapid in vivo determination of water concentration profiles in human skin. *J Raman Spectrosc.* 2000;31(8-9):813-818.

144. Shafer-Peltier KE, Haka AS, Fitzmaurice M, et al. Raman microspectroscopic model of human breast tissue: implications for breast cancer diagnosis in vivo. *J Raman Spectrosc.* 2002;33(7):552-563.

145. Bergholt MS, Zheng W, Lin K, et al. Characterizing variability in in vivo Raman spectra of different anatomical locations in the upper gastrointestinal tract toward cancer detection. *J Biomed Opt.* 2011;16(3).

146. Huang ZW, Teh SK, Zhen W, et al. Integrated Raman spectroscopy and trimodal wide-field imaging techniques for real-time in vivo tissue Raman measurements at endoscopy. *Opt Lett.* 2009;34(6):758-760.

147. Bergholt MS, Zheng W, Ho KY, et al. Fiberoptic Confocal Raman Spectroscopy for Real-Time In Vivo Diagnosis of Dysplasia in Barrett's Esophagus. *Gastroenterology.* 2014;146(1):27-32.

148. Carey P. Biochemical Applications of Raman and Resonance Raman Spectroscopies. *Journal ofMoiecularStructure.* 1984;112:337.

149. Twardowski J, Anzenbacher P. *Raman and IR Spectroscopy in Biology and Biochemistry.* New York: Ellis Horwood; 1994.

150. Colthup NB, Daly LH, Wiberley SE. *Introduction to infrared and Raman spectroscopy.* New York, NY: Academic Rress; 1990.

151. Bailo E, Deckert V. Tip-enhanced Raman scattering. *Chem Soc Rev.* 2008;37(5):921-930.

152. Masihzadeh O, Ammar DA, Kahook MY, Lei TC. Coherent anti-Stokes Raman scattering (CARS) microscopy: a novel technique for imaging the retina. *Investigative ophthalmology & visual science.* 2013;54(5):3094-3101.

153. Saar BG, Freudiger CW, Reichman J, Stanley CM, Holtom GR, Xie XS. Video-rate molecular imaging in vivo with stimulated Raman scattering. *Science.* 2010;330(6009):1368-1370.

154. Larsson K, Hellgren L. Study of Combined Raman and Fluorescence Scattering from Human-Blood Plasma. *Experientia.* 1974;30(5):481-483.

155. Zhou Y, Liu CH, Sun Y, et al. Human brain cancer studied by resonance Raman spectroscopy. *J Biomed Opt.* 2012;17(11):116021.

156. Liu CH, Zhou Y, Sun Y, et al. Resonance Raman and Raman spectroscopy for breast cancer detection. *Technology in cancer research & treatment.* 2013;12(4):371-382.

157. Byrne HJ, Baranska M, Puppels GJ, et al. Spectropathology for the next generation: quo vadis? *Analyst.* 2015;140(7):2066-2073.

158. Beatty S, Chakravarthy U, Nolan JM, et al. Secondary outcomes in a clinical trial of carotenoids with coantioxidants versus placebo in early age-related macular degeneration. *Ophthalmology.* 2013;120(3):600-606.

159. Bernstein PS, Zhao DY, Wintch SW, Ermakov IV, McClane RW, Gellermann W. Resonance Raman measurement of macular carotenoids in normal subjects and in age-related macular degeneration patients. *Ophthalmology.* 2002;109(10):1780-1787.

160. Hogg RE, Anderson RS, Stevenson MR, Zlatkova MB, Chakravarthy U. In vivo macular pigment measurements: a comparison of resonance Raman spectroscopy and heterochromatic flicker photometry. *The British journal of ophthalmology.* 2007;91(4):485-490.

161. Scarmo S, Henebery K, Peracchio H, et al. Skin carotenoid status measured by resonance Raman spectroscopy as a biomarker of fruit and vegetable intake in preschool children. *European journal of clinical nutrition.* 2012;66(5):555-560.

162. Szymanski HA. Raman Spectroscopy: Theory and Practice. Paper presented at: Raman Spectroscopy: Theory and Practice1967; New York.

163. Boustany NN, Manoharan R, Dasari RR, Feld MS. Ultraviolet resonance Raman spectroscopy of bulk and microscopic human colon tissue. *Appl Spectrosc.* 2000;54(1):24-30.

164. Asher SA. UV resonance Raman spectroscopy for analytical, physical, and biophysical chemistry. *Anal Chem.* 1993;65(4):201A-210A.

165. Feld MS, Kramer JR. Mutagenicity and the XeCl excimer laser: a relationship of consequence? *Am Heart J.* 1991;122(6):1803-1805.

166. Klein K, Gigler AM, Aschenbrenne T, et al. Label-Free Live-Cell Imaging with Confocal Raman Microscopy. *Biophys J.* 2012;102(2):360-368.

167. Kline NJ, Treado PJ. Raman chemical imaging of breast tissue. *J Raman Spectrosc.* 1997;28(2-3):119-124.

168. Kirsch M, Schackert G, Salzer R, Krafft C. Raman spectroscopic imaging for in vivo detection of cerebral brain metastases. *Anal Bioanal Chem.* 2010;398(4):1707-1713.

169. Schulmerich MV, Cole JH, Dooley KA, et al. Noninvasive Raman tomographic imaging of canine bone tissue. *J Biomed Opt.* 2008;13(2):020506.

170. Patel II, Steuwe C, Reichelt S, Mahajan S. Coherent anti-Stokes Raman scattering for label-free biomedical imaging. *J Optics-Uk.* 2013;15(9).

171. Imitola J, Cote D, Rasmussen S, et al. Multimodal coherent anti-Stokes Raman scattering microscopy reveals microglia-associated myelin and axonal dysfunction in multiple sclerosis-like lesions in mice. *J Biomed Opt.* 2011;16(2).

172. Evans CL, Xu XY, Kesari S, Xie XS, Wong STC, Young GS. Chemically-selective imaging of brain structures with CARS microscopy. *Optics express.* 2007;15(19):12076-12087.

173. Huff TB, Cheng JX. In vivo coherent anti-Stokes Raman scattering imaging of sciatic nerve tissue. *J Microsc-Oxford.* 2007;225(2):175-182.

174. Bergholt MS, Lin K, Wang J, et al. Simultaneous fingerprint and high-wavenumber fiber-optic Raman spectroscopy enhances real-time in vivo diagnosis of adenomatous polyps during colonoscopy. *Journal of biophotonics.* 2015;9999(9999).

175. Matousek P, Clark IP, Draper ER, et al. Subsurface probing in diffusely scattering media using spatially offset Raman spectroscopy. *Appl Spectrosc.* 2005;59(4):393-400.

176. Schulmerich MV, Finney WF, Fredricks RA, Morris MD. Subsurface Raman spectroscopy and mapping using a globally illuminated non-confocal fiber-optic array probe in the presence of Raman photon migration. *Appl Spectrosc.* 2006;60(2):109-114.

177. Eliasson C, Matousek P. Noninvasive authentication of pharmaceutical products through packaging using spatially offset Raman spectroscopy. *Anal Chem.* 2007;79(4):1696-1701.

178. Keller M, Vargis E, Granja N, et al. Development of a spatially offset Raman spectroscopy probe for breast tumor surgical margin evaluation. *J Biomed Opt.* 2011;16(7).

179. Sowoidnich K, Churchwell JH, Buckley K, et al. Spatially offset Raman spectroscopy for photon migration investigations in long bone. 2015.

180. Matousek P, Draper ER, Goodship AE, Clark IP, Ronayne KL, Parker AW. Noninvasive Raman spectroscopy of human tissue in vivo. *Appl Spectrosc.* 2006;60(7):758-763.

181. Cialla D, März A, Böhme R, et al. Surface-enhanced Raman spectroscopy (SERS): progress and trends. *Anal Bioanal Chem.* 2012;403(1):27-54.

182. Kneipp K, Wang Y, Kneipp H, et al. Single molecule detection using surface-enhanced Raman scattering (SERS). *Phys Rev Lett.* 1997;78(9):1667-1670.

183. Fleischmann M, Hendra PJ, Mcquilla.Aj. Raman-Spectra of Pyridine Adsorbed at a Silver Electrode. *Chem Phys Lett.* 1974;26(2):163-166.

184. Jeanmaire DL, Vanduyne RP. Surface Raman Spectroelectrochemistry .1. Heterocyclic, Aromatic, and Aliphatic-Amines Adsorbed on Anodized Silver Electrode. *J Electroanal Chem.* 1977;84(1):1-20.

185. Zavaleta CL, Smith BR, Walton I, et al. Multiplexed imaging of surface enhanced Raman scattering nanotags in living mice using noninvasive Raman spectroscopy. *Proc Natl Acad Sci U S A.* 2009;106(32):13511-13516.

186. Maiti KK, Dinish US, Fu CY, et al. Development of biocompatible SERS nanotag with increased stability by chemisorption of reporter molecule for in vivo cancer detection. *Biosens Bioelectron.* 2010;26(2):398-403.

187. Maiti KK, Dinish US, Samanta A, et al. Multiplex targeted in vivo cancer detection using sensitive near-infrared SERS nanotags. *Nano Today.* 2012;7(2):85-93.

188. Wang YL, Seebald JL, Szeto DP, Irudayaraj J. Biocompatibility and Biodistribution of Surface-Enhanced Raman Scattering Nanoprobes in Zebrafish Embryos: In vivo and Multiplex Imaging. *ACS Nano.* 2010;4(7):4039-4053.

189. Dinish US, Balasundaram G, Chang YT, Olivo M. Sensitive multiplex detection of serological liver cancer biomarkers using SERS-active photonic crystal fiber probe. *Journal of biophotonics.* 2014;7(11-12):956-965.

190. Dinish US, Balasundaram G, Chang YT, Olivo M. Actively Targeted In Vivo Multiplex Detection of Intrinsic Cancer Biomarkers Using Biocompatible SERS Nanotags. *Scientific reports.* 2014;4.

191. Stokes DL, Vo-Dinh T. Development of an integrated single-fiber SERS sensor. *Sensor Actuat B-Chem.* 2000;69(1-2):28-36.

192. Stone N, Faulds K, Graham D, Matousek P. Prospects of Deep Raman Spectroscopy for Noninvasive Detection of Conjugated Surface Enhanced Resonance Raman Scattering Nanoparticles Buried within 25 mm of Mammalian Tissue. *Anal Chem.* 2010;82(10):3969-3973.

193. Stone N, Kerssens M, Lloyd GR, Faulds K, Graham D, Matousek P. Surface enhanced spatially offset Raman spectroscopic (SESORS) imaging - the next dimension. *Chem Sci.* 2011;2(4):776-780.

194. Khan KM, Krishna H, Majumder SK, Rao KD, Gupta PK. Depth-sensitive Raman spectroscopy combined with optical coherence tomography for layered tissue analysis. *Journal of biophotonics.* 2014;7(1-2):77-85.

195. Patil CA, Kalkman J, Faber DJ, Nyman JS, van Leeuwen TG, Mahadevan-Jansen A. Integrated system for combined Raman spectroscopy-spectral domain optical coherence tomography. *J Biomed Opt.* 2011;16(1):011007.

196. Maher JR, Chuchuen O, Kashuba A, Katz D, Wax A. Combined Raman Spectroscopy and Optical Coherence Tomography for MeasuringAnalytes in Targeted Tissues. Paper presented at: Optics in the Life Sciences; 2015/04/12, 2015; Vancouver.

197. Desroches J, Goyette A, Pichette J, et al. Towards the combined use of Raman Spectroscopy and interstitial Optical Tomography to improve the safety and diagnostic accuracy of brain needle biopsies. Paper presented at: Optics in the Life Sciences; 2015/04/12, 2015; Vancouver.

198. Patil CA, Arrasmith CL, Mackanos MA, Dickensheets DL, Mahadevan-Jansen A. A handheld laser scanning confocal reflectance imaging-confocal Raman microspectroscopy system. *Biomedical optics express.* 2012;3(3):488-502.

199. Wang H, Lee AM, Lui H, McLean DI, Zeng H. A method for accurate in vivo micro-Raman spectroscopic measurements under guidance of advanced microscopy imaging. *Scientific reports.* 2013;3:1890.

200. Lim L, Nichols B, Migden MR, et al. Clinical study of noninvasive in vivo melanoma and nonmelanoma skin cancers using multimodal spectral diagnosis. *J Biomed Opt.* 2014;19(11).

201. Haka AS, Kramer JR, Dasari RR, Fitzmaurice M. Mechanism of ceroid formation in atherosclerotic plaque: in situ studies using a combination of Raman and fluorescence spectroscopy. *J Biomed Opt.* 2011;16(1).

202. Torre LA, Bray F, Siegel RL, Ferlay J, Lortet-Tieulent J, Jemal A. Global Cancer Statistics, 2012. *Ca-Cancer J Clin.* 2015;65(2):87-108.

203. Kanter EM, Vargis E, Majumder S, et al. Application of Raman spectroscopy for cervical dysplasia diagnosis. *Journal of biophotonics.* 2009;2(1-2):81-90.

204. Kanter EM, Majumder S, Kanter GJ, Woeste EM, Mahadevan-Jansen A. Effect of hormonal variation on Raman spectra for cervical disease detection. *Am J Obstet Gynecol.* 2009;200(5):512 e511-515.

205. Vargis E, Byrd T, Logan Q, Khabele D, Mahadevan-Jansen A. Sensitivity of Raman spectroscopy to normal patient variability. *J Biomed Opt.* 2011;16(11):117004.

206. Robichaux-Viehoever A, Kanter EM, Shappell H, Billheimer D, Jones III H, Mahadevan-Jansen A. Characterization of Raman Spectra Measured in Vivo for the Detection of Cervical Dysplasia. *Appl Spectrosc.* 2007;61(9):986-993.

207. Shaikh R, Dora TK, Chopra S, et al. In vivo Raman spectroscopy of human uterine cervix: exploring the utility of vagina as an internal control. *J Biomed Opt.* 2014;19(8).

208. Rubina S, Sathe P, Dora TK, Chopra S, Maheshwari A, Krishna CM. In vivo Raman spectroscopy of cervix cancers. 2014.

209. Duraipandian S, Zheng W, Ng J, Low JJH, Ilancheran A, Huang ZW. Near-infrared-excited confocal Raman spectroscopy advances in vivo diagnosis of cervical precancer. *J Biomed Opt.* 2013;18(6).

210. Feng S, Lin D, Lin J, et al. Blood plasma surface-enhanced Raman spectroscopy for non-invasive optical detection of cervical cancer. *Analyst.* 2013;138(14):3967-3974.

211. Vidyasagar MS, Maheedhar K, Vadhiraja BM, Fernendes DJ, Kartha VB, Krishna CM. Prediction of radiotherapy response in cervix cancer by Raman spectroscopy: A pilot study. *Biopolymers.* 2008;89(6):530-537.

212. Vargis E, Tang YW, Khabele D, Mahadevan-Jansen A. Near-infrared Raman Microspectroscopy Detects High-risk Human Papillomaviruses. *Transl Oncol.* 2012;5(3):172-179.

213. Ramos I, #xea, Martins sR, Malkin A, Lyng FM. Current Advances in the Application of Raman Spectroscopy for Molecular Diagnosis of Cervical Cancer. *BioMed research international.* 2015;2015:9.

214. Vargis E, Brown N, Williams K, et al. Detecting Biochemical Changes in the Rodent Cervix During Pregnancy Using Raman Spectroscopy. *Ann Biomed Eng.* 2012.

215. O'Brien CM, Vargis E, Paria BC, Bennett KA, Mahadevan-Jansen A, Reese J. Raman spectroscopy provides a noninvasive approach for determining biochemical composition of the pregnant cervix in vivo. *Acta Paediatr.* 2014;103(7):715-721.

216. *Cancer Facts and Figures.* Atlanta: American Cancer Soceity;2012.

217. Caspers PJ, Lucassen GW, Carter EA, Bruining HA, Puppels GJ. In vivo confocal Raman microspectroscopy of the skin: noninvasive determination of molecular concentration profiles. *J Invest Dermatol.* 2001;116(3):434-442.

218. Schleusener J, Gluszczynska P, Reble C, et al. In vivo study for the discrimination of cancerous and normal skin using fibre probe-based Raman spectroscopy. *Experimental dermatology.* 2015.

219. Zakharov VP, Bratchenko IA, Myakinin OO, et al. Combined Raman spectroscopy and autofluoresence imaging method for in vivo skin tumor diagnosis. 2014.

220. Zhao J, Lui H, McLean DI, Zeng H. Real-time Raman spectroscopy for non-invasive skin cancer detection - preliminary results. *Conf Proc IEEE Eng Med Biol Soc.* 2008;2008:3107-3109.

221. O'Regan GM, Kemperman PMJH, Sandilands A, et al. Raman profiles of the stratum corneum define 3 filaggrin genotype-determined atopic dermatitis endophenotypes. *J Allergy Clin Immun.* 2010;126(3):574-U270.

222. Singh SP, Deshmukh A, Chaturvedi P, Krishna CM. In vivo Raman spectroscopic identification of premalignant lesions in oral buccal mucosa. *J Biomed Opt.* 2012;17(10).

223. Singh SP, Sahu A, Deshmukh A, Chaturvedi P, Krishna CM. In vivo Raman spectroscopy of oral buccal mucosa: a study on malignancy associated changes (MAC)/cancer field effects (CFE). *Analyst.* 2013;138(14):4175-4182.

224. Keller MD, Kanter EM, Mahadevan-Jansen A. Raman spectroscopy for cancer diagnosis. *Spectroscopy.* 2006;21(11):33-41.

225. Keller MD, Kanter EM, Lieber CA, et al. Detecting temporal and spatial effects of epithelial cancers with Raman spectroscopy. *Disease markers.* 2008;25(6):323-337.

226. Krishna H, Majumder SK, Chaturvedi P, Sidramesh M, Gupta PK. In vivo Raman spectroscopy for detection of oral neoplasia: a pilot clinical study. *Journal of biophotonics.* 2014;7(9):690-702.

227. Sahu A, Deshmukh A, Ghanate AD, Singh SP, Chaturvedi P, Krishna CM. Raman spectroscopy of oral buccal mucosa: a study on age-related physiological changes and tobacco-related pathological

changes. *Technology in cancer research & treatment.* 2012;11(6):529-541.

228. Bergholt MS, Zheng W, Lin K, et al. In vivo diagnosis of gastric cancer using Raman endoscopy and ant colony optimization techniques. *Int J Cancer.* 2011;128(11):2673-2680.

229. Teh SK, Zheng W, Ho KY, Teh M, Yeoh KG, Huang Z. Near-infrared Raman spectroscopy for early diagnosis and typing of adenocarcinoma in the stomach. *Brit J Surg.* 2010;97(4):550-557.

230. Wang J, Lin K, Zheng W, et al. Comparative study of the endoscope-based bevelled and volume fiber-optic Raman probes for optical diagnosis of gastric dysplasia in vivo at endoscopy. *Anal Bioanal Chem.* 2015.

231. Huang ZW, Teh SK, Zheng W, et al. In vivo detection of epithelial neoplasia in the stomach using image-guided Raman endoscopy. *Biosens Bioelectron.* 2010;26(2):383-389.

232. Bergholt MS, Zheng W, Ho KY, et al. Real-time depth-resolved fiber optic Raman endoscopy for in vivo diagnosis of gastric precancer. 2014.

233. Bergholt MS, Zheng W, Lin K, et al. Raman endoscopy for in vivo differentiation between benign and malignant ulcers in the stomach. *Analyst.* 2010;135(12):3162-3168.

234. Bergholt MS, Zheng W, Ho KY, et al. Fiber-optic Raman spectroscopy probes gastric carcinogenesis in vivo at endoscopy. *Journal of biophotonics.* 2013;6(1):49-59.

235. Bergholt MS, Zheng W, Lin K, et al. Combining near-infrared-excited autofluorescence and Raman spectroscopy improves in vivo diagnosis of gastric cancer. *Biosens Bioelectron.* 2011;26(10):4104-4110.

236. Bergholt MS, Zheng W, Lin K, et al. Characterizing variability of in vivo Raman spectroscopic properties of different anatomical sites of normal colorectal tissue towards cancer diagnosis at colonoscopy. *Anal Chem.* 2015;87(2):960-966.

237. Short MA, Lam S, McWilliams AM, Ionescu DN, Zeng HS. Using Laser Raman Spectroscopy to Reduce False Positives of Autofluorescence Bronchoscopies A Pilot Study. *Journal of Thoracic Oncology.* 2011;6(7):1206-1214.

238. Saha A, Barman I, Dingari NC, et al. Raman spectroscopy: a real-time tool for identifying microcalcifications during stereotactic breast core needle biopsies. *Biomedical optics express.* 2011;2(10):2792-2803.

239. Horsnell J, Stonelake P, Shetty G, Kendall C, Hutchings J, Stone N. Assessment of axillary lymph nodes using raman spectroscopy-intraoperative use is possible. *Brit J Surg.* 2011;98:26-26.

240. Desroches J, Jermyn M, Mok K, et al. Characterization of a Raman spectroscopy probe system for intraoperative brain tissue classification. *Biomedical optics express.* 2015;6(7):2380-2397.

241. Jermyn M, Mok K, Mercier J, et al. Intraoperative brain cancer detection with Raman spectroscopy in humans. *Sci Transl Med.* 2015;7(274):274ra219.

242. Maquelin K, Kirschner C, Choo-Smith LP, et al. Prospective study of the performance of vibrational spectroscopies for rapid identification of bacterial and fungal pathogens recovered from blood cultures. *J Clin Microbiol.* 2003;41(1):324-329.

243. Lin D, Chen GN, Feng SY, et al. Development of a rapid macro-Raman spectroscopy system for nasopharyngeal cancer detection based on surface-enhanced Raman spectroscopy. *Appl Phys Lett.* 2015;106(1).

244. Li S, Li L, Zeng Q, et al. Characterization and noninvasive diagnosis of bladder cancer with serum surface enhanced Raman spectroscopy and genetic algorithms. *Scientific reports.* 2015;5:9582.

245. Feng S, Chen R, Lin J, et al. Gastric cancer detection based on blood plasma surface-enhanced Raman spectroscopy excited by polarized laser light. *Biosens Bioelectron.* 2011;26(7):3167-3174.

246. Sathyavathi R, Dingari NC, Barman I, et al. Raman spectroscopy provides a powerful, rapid diagnostic tool for the detection of tuberculous meningitis in ex vivo cerebrospinal fluid samples. *Journal of biophotonics.* 2013;6(8):567-572.

CHAPTER 3

APPLICATION DRIVEN ASSESSMENT OF PROBE DESIGNS FOR RAMAN SPECTROSCOPY

3.1 Abstract

In vivo Raman spectroscopy has been utilized for non-invasive, non-destructive assessment of tissue pathology or physiological state in a variety of applications largely through the continued development of fiber optic probes to interface with samples of interest. Fiber optic probes can be designed to optimize collection of Raman-scattered photons from application-dependent depths, and this critical consideration should be addressed when planning a study. Herein we investigate four unique probe geometries for sensitivity to superficial and deep signals through a Monte Carlo model that incorporates Raman scattering and fluorescence for the first time. Experimental validation was conducted using biological tissues and TiO_2 and polytetrafluoroethylene (PTFE) phantoms, with the intention of more accurately recapitulating *in vivo* performance scenarios. The behavior of each probe design evaluated (unmodified collection, Gaser, superficially focused micro lens, and deep focused micro lens) was modeled and demonstrated strong correlation with experimental results obtained through biological tissue and phantom testing.

Testing in biological tissues revealed that superficially focused micro lens and Gaser designs had superior performance at shallow depths (< 1 mm), whereas the deep focused design yielded the highest signals deep within tissue. The probes demonstrated similar performance for TiO_2 and PTFE experiments at all depths investigated. The contrast in results between the TiO_2/PTFE and biological tissues underscores the importance of incorporating the optical properties of a given application when designing a fiber optic probe, as the high reduced scattering coefficients of the synthetic phantoms negated the benefits of beveling and lenses that were originally optimized for use in air. The model presented here can be easily extended for optimization of entirely novel probe designs prior to fabrication, reducing time and cost while improving data quality.

3.2 Introduction

In vivo Raman spectroscopy has been utilized for non-invasive, non-destructive assessment of tissue pathology or physiological state in a variety of applications.[1] The majority of such applications are enabled by use of fiber optic probes to interface with samples of interest. Almost all fiber optic probe designs collect and integrate the signal obtained from a small volume of the sample beneath the probe tip. Due to the weak nature of the Raman Effect, it is important to maximize the signal to noise ratio obtained from the tissue of

interest at the particular depth of interest. Fiber optic probes can be designed to optimize collection of Raman-scattered photons from application-dependent depths, and this critical consideration should be addressed when planning a study. The desired depth alone does not provide sufficient information to optimize the design for a specific application. There is a need for a platform that allows investigators to 1) predict Raman scattered photon distribution in the sample of interest and 2) optimize fiber optic probe excitation and collection geometries to ensure maximum signal to noise at the desired depth. Such a tool must take into consideration Raman scattering, fluorescence, elastic scattering, and absorption in order to accurately predict how a probe design will perform for a given application.

The clinical applications driving innovative probe designs are vast, and have been recently reviewed by Pence *et al.*[1] Broadly, these applications can be grouped into three depth ranges: superficial (10-200 μm),[2-13] subsurface (200-2000 μm),[14-18] and deep (greater than 2000 μm);[19-22] examples of such applications are provided in Table 3.1. Raman probe designs have been developed within each of these depth categories to optimize data collection for specific applications as reviewed by Stevens *et al.*[23] Two distinct probe designs have been demonstrated for superficial as well as multiple millimeter depths. For increased performance at shallow depths, a confocal detection design was implemented by Wang *et al.*[24] This probe design combined beveled fibers and a spherical ball lens to achieve increased signal performance in the first 300 μm

of tissue relative to unmodified fiber probe designs. At the other extreme, the standard for detecting signals buried deep in scattering tissues is based on principles of random walk and multiple scattering. Spatially offset Raman spectroscopy (SORS) probes have been designed and constructed for specific applications such as bone in order to take advantage of the probabilistic paths for photons to travel deeper into the sample when the source and detector elements of the probe have a greater separation.[17, 25] Between these two extremes lies a spectrum of probe designs that incorporate various strategies to steer both the excitation and collection fibers to measure relatively shallow or deep layers.[23] Each of these probe designs collects a volume-averaged signal from the sample beneath the probe tip; however, properly considering the application can enable dramatically improved signal detection from the targeted sample depth.

Table 3.1. Depth-sensitive pathologies from Raman spectroscopy literature.

Superficial (10-200 μm)	-Epithelial precancers and cancers (cervix,[26] esophagus,[27] stomach,[28] colon,[29] skin,[30,31] lung,[32] oral cavity,[33] and bladder[34]) -Dermatitis[35] -Inflammatory bowel disease[36] -Barrett's esophagus[37]
Subsurface (200-2000 μm)	-Cervical remodeling during pregnancy (stroma)[38,39] -Vulnerable plaque assessment in arteries[40] -Tumor margin assessment (breast,[41] brain[42])
Deep (greater than 2 mm)	-Transcutaneous assessment of bone[43,44] -Detection of malignant breast calcifications[45] -Detection of urologic stones[46]

Probe designers generally use ray tracing to determine optimal light delivery and collection geometries for probe performance in air. Ray tracing

software allows for determination of the excitation and collection cone angles and their overlap. However, optimizing designs for use in non-scattering media does not fully predict performance in biological tissue where optical scattering can be substantial. Accounting for the interactions between light and tissue is vital to accurately determine probe behavior. Prediction of light transport in tissue can be modeled using Monte Carlo (MC) simulations, in which the radiative transport equation can be solved for complex scenarios with an accuracy that depends upon the computational burden. MC models were originally developed to track photon distribution and absorption in turbid media and have been extended for numerous and varied optical applications including fluorescence and Raman scattering.[10, 25-30] Application-driven probe design must bridge these two approaches, ray tracing and laser-tissue interaction models, to truly optimize fiber optic probes for biological targets.

Specifically for Raman scattering, a few groups have implemented these MC models. Matousek *et al.* developed an MC model for layered media for investigation of chemical powders.[25] Enejder *et al.* investigated system geometry effects on blood spectra[31] and Shih *et al.* used an MC model to correct Raman spectra for tissue scattering and absorption artifacts.[29] Two separate MC models have been developed for evaluating superficial fiber optic probe collection geometries for epithelial detection applications.[10, 30] Furthermore, Keller *et al.* developed an MC model for investigating SORS approaches in turbid media.[28] Reble *et al.* implemented a Raman MC model to systematically

investigate the impact of tissue absorption and scattering properties on the performance of probes with different collection geometries.[32] Each of these models has proven valuable for investigating detection of Raman signals in complex turbid media; however all have investigated Raman scattering effects in isolation. As a Raman fiber optic probe detects competing signals from tissue, especially fluorescent and diffusely scattered photons, it is vital for a model to consider each of these competing phenomena while identifying the optimal probe design for a target application.

Herein, we investigate the impact of incorporating application-specific parameters when choosing or developing a Raman probe to measure depth dependent signals using a MC model that tracks Raman and fluorescent photons paired with experimental validation in both common optical phantoms and biological tissues. This approach allows researchers to more accurately recapitulate and/or predict *in vivo* performance scenarios.

3.3 Methods

3.3.1 Fiber optic probes

Four unique fiber optic probes were experimentally tested and their performance was modeled using the MC simulation explained below. All of the fiber optic probes investigated in this study were designed for excitation at 785 nm and have seven collection fibers (300 μm diameter) surrounding one

excitation fiber which total 2.1 mm in outer diameter. All of the probes have filters on the excitation fiber such that only 785 nm light passes to the sample and all of the collection fibers have filters that block the 785 nm laser light. Each probe that was evaluated has a unique configuration, which are all drawn to scale based upon results from ray tracing software (Radiant Zemax, Bellevue, WA) shown in Figure 3.1. The four probes include 1) a conventional design that has no lenses or beveling with standard 0.22 NA fibers (±12.7° acceptance angles, 400 μm diameter excitation fiber, EmVision LLC) (Figure 3.1A**)**; 2) a beveled collection fiber design that has superficial overlap of the excitation and collection cone angles (35-55.3° acceptance angles, 400 μm diameter excitation fiber, Gaser probe by Visionex Inc.) (Figure 3.1B); 3) a micro lens design with a polished 3 mm diameter sapphire plano convex lens coupled to a 1 mm thick MgF_2 window that yields excitation and collection cone overlap deep within a sample (5-33.8° acceptance angles, 200 μm diameter excitation fiber, EmVision LLC) (Figure 3.1C); and 4) a micro lens design with a polished 2 mm diameter sapphire plano convex lens coupled to a 1 mm thick MgF_2 window that results in excitation and collection cone overlap at the surface of the sample (21.2-35.8° acceptance angles, 200 μm diameter excitation fiber, EmVision LLC) (Figure 3.1D). Probe-specific acceptance angles and collection fiber surface cross-sectional areas are listed in Table 3.2.

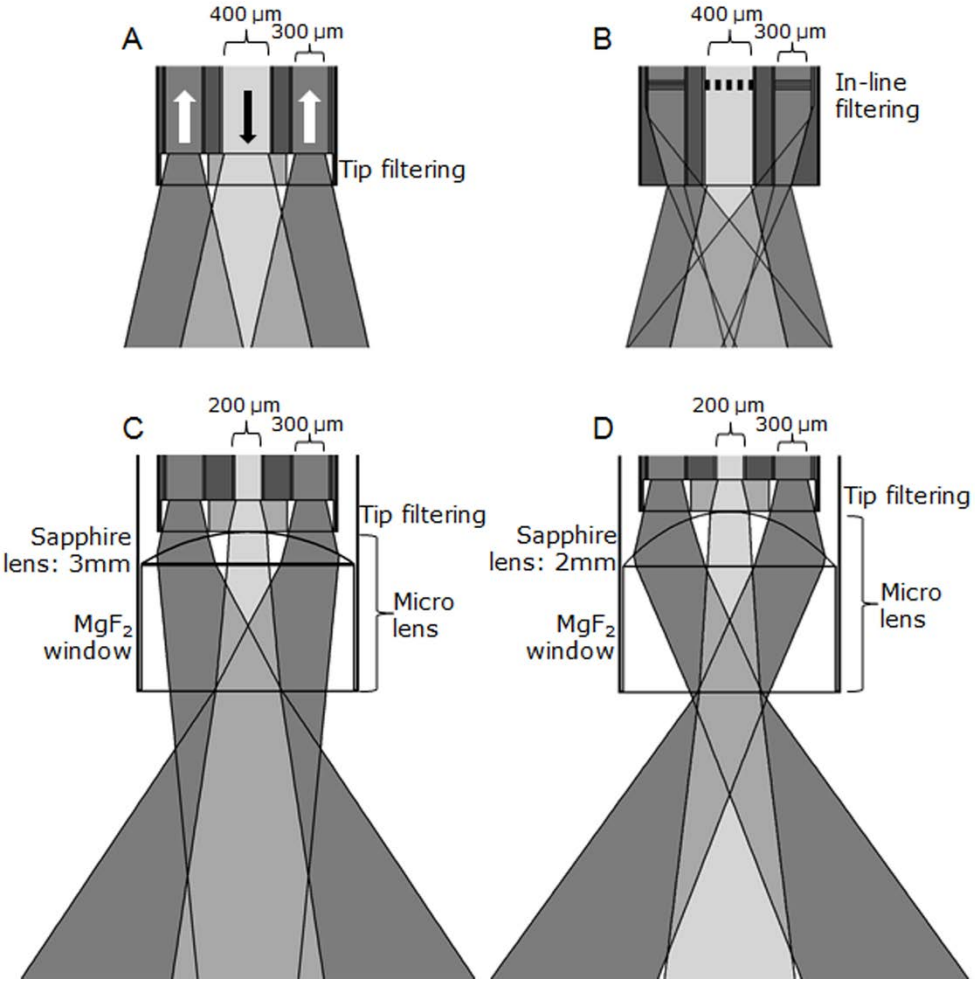

Figure 3.1. Probe collection geometries. Probe geometry cross section based on ray tracing: (A) unmodified, (B) beveled, (C) deep micro lens, and (D) superficial micro lens. Overlap between excitation and collection cones denote theoretic probe performance in air.

Table 3.2. Probe specifications.

	Unmodified	Beveled	Micro lens deep	Micro lens shallow
Collection surface cross-sectional area	0.753 mm^2	0.487 mm^2	1.359 mm^2	0.372 mm^2
Acceptance angle	± 12.7°	-12.7° to 38.0°	4.9° to 33.8°	21.2° to 35.8°

3.3.2 Monte Carlo model

A multimodal MC model, incorporating diffuse reflectance, fluorescence, and Raman scattering was developed in MATLAB (The Mathworks, Inc., Natick, MA) by incorporating a previously existing multilayer model for diffuse reflectance.[26] Fluorescence generation and photon propagation were incorporated as previously described.[27,28] Raman scattering and photon propagation were also incorporated based on prior work.[29] Finally, angular dependent photon injection and collection was included to investigate the influence of probe geometry at the sample interface. The general algorithm for the multimodal MC model can be seen in Figure 3.2**.** Briefly, 100,000 seed photons are injected from the excitation fiber (Gaussian profile) into the top layer of the sample and propagate in the presence of absorption and elastic scattering. After a photon migrates and deposits a discrete photon weight (based on Beer's law), Raman scattering can occur (probability check: $\xi < k_{RS}\frac{\mu_{s,Ex}}{\mu_{s,Ex}+\mu_{a,Ex}}$), where ξ is a random number [0,1].[29] If no Raman event occurs, then fluorescence absorption and emission is possible (probability check: $\xi < 1 - e^{-\mu_{a,Fl}\delta}$), where δ is the calculated photon step size.[30] For any of these events (elastic scattering, Raman scattering, or fluorescence), a new photon trajectory is calculated and the photon propagates (based on appropriate layer optical parameters) until either the photon weight is decremented and ended as per standard MC roulette routines or the photon escapes the model layers. If a

photon is scattered through the surface of the topmost layer and within the detection diameter and acceptance angle for the collection fiber, the remaining photon weight is considered detected. For this model, Raman scattering and fluorescence generation are considered competing processes with respect to excitation photons. A few assumptions have been made for the implementation of this code: 1) photon weight is deposited in the voxel at the end of the photon step, 2) Raman scattering determination happens prior to fluorescence absorption (Raman scattering is an instantaneous process whereas fluorescence occurs between 10^{-7} to 10^{-9} seconds), 3) secondary Raman scattering and fluorescence generation are neglected, 4) all Raman and fluorescence photons are modeled at a single wavelength for simplicity, 5) Raman scattering and fluorescence events are isotropic, and 6) the model is implemented as a plane bisecting the center of the excitation fiber and a single collection fiber, and could be extended via rotational symmetry. Due to the relatively low concentrations and cross-sections of Raman scatterers in biological tissue, the likelihood of a Raman event was scaled by 10^4 to reduce computational burden. This scaling factor of 10^4 was chosen such that the model had roughly equal probability for Raman scattering and fluorescence without the computational burden of modeling 10^6 fluorescence photons per single Raman scattering event. All modeling sets were run at least 3 times to ensure consistent performance.

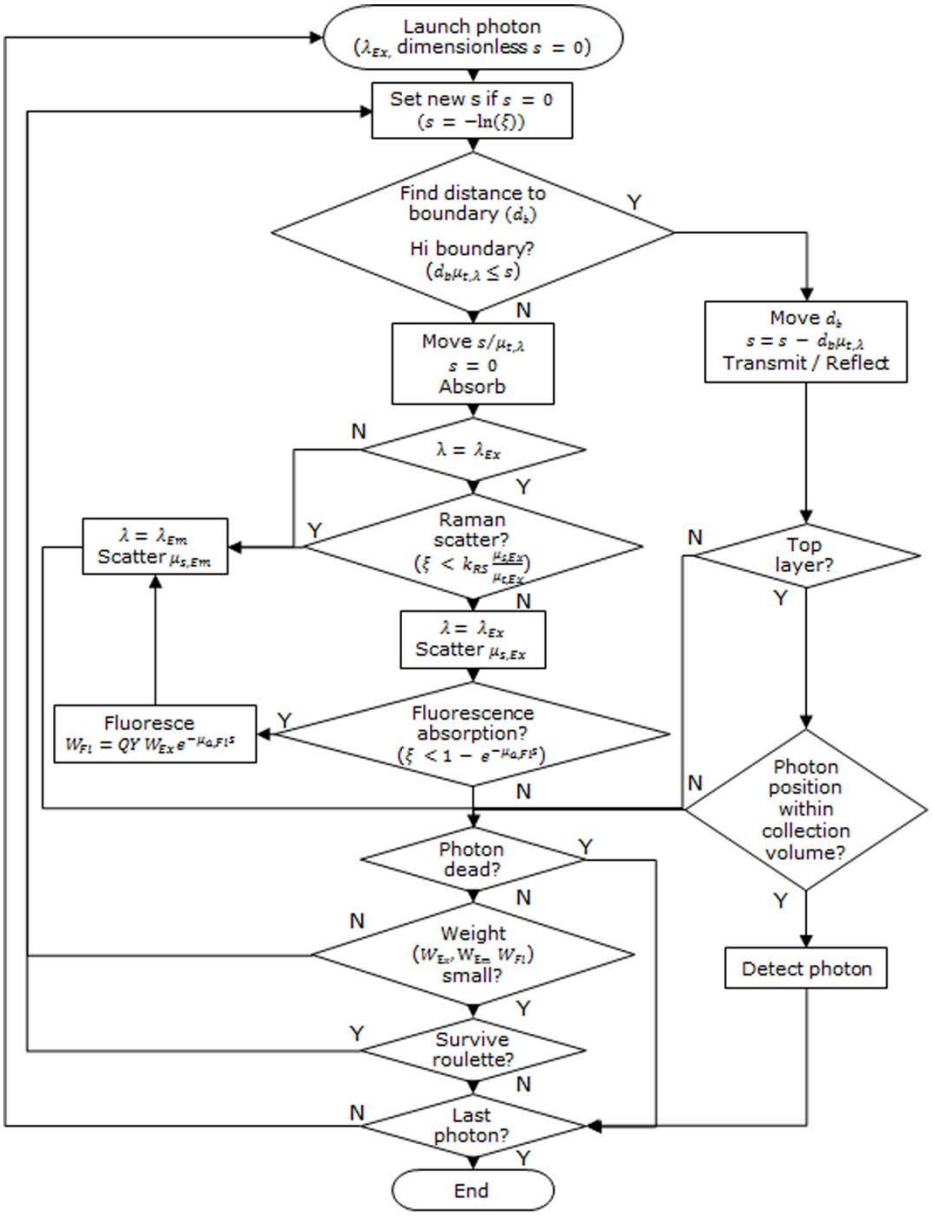

Figure 3.2. Flowchart for tracing photons in multi-layered media with multimodal Monte Carlo simulation. Model parameters: λ_{Ex}= wavelength, excitation photon; s = photon step size; d_b = distance to layer boundary; $\mu_{t,\lambda}$ = total attenuation coefficient at λ; λ_{Em} = wavelength, emission photon; ξ = random number [0,1]; k_{RS} = Raman scattering cross section; $\mu_{s,Ex}$ = scattering coefficient at λ_{Ex}; $\mu_{s,Em}$ = scattering coefficient at λ_{Em}; $\mu_{a,Fl}$ = fluorescence absorption coefficient; W_{Ex} = photon weight at λ_{Ex}; W_{Em} = photon weight at λ_{Em}; W_{Fl} = photon weight of fluorescence at λ_{Em}; QY = fluorescence quantum yield.

The optical properties used as inputs in this model (Table 3.3) were based on both published values[26] (absorption and scattering coefficients, index of refraction, and anisotropy factors) as well as experimentally derived values (Raman cross section and fluorescence quantum yield). To mitigate the impact of experimental setup on model parameters, experimental results were averaged across all four probe designs prior to simulation.

Table 3.3. Input parameters of the Monte Carlo simulation.

Optical Properties	Muscle	Adipose
$\mu_{a,Ex}$ at 800 nm (1/cm)	0.54*	1.08*
$\mu_{s,Ex}$ at 800 nm (1/cm)	66.70*	202.00*
$\mu_{a,Em}$ at 900 nm (1/cm)	0.32*	1.25*
$\mu_{s,Em}$ at 900 nm (1/cm)	88.70*	108.00*
Scattering anisotropy (g)	0.93*	0.90*
Raman cross-section (k_{RS})	0.92	7.43
$\mu_{a,Fl}$ fluorescence (1/cm)	7.20	3.60
Fluorescence quantum yield	1.34	0.34
Index of refraction (n)	1.37*	1.45*
*Denotes values reported in [26]		

3.3.3 Raman spectroscopy system

All Raman measurements were acquired using a cart-based clinical Raman spectroscopy system which used a 785 nm diode laser (Innovative Photonics Solutions, Monmouth Junction, NJ) coupled to an imaging spectrograph (Holospec f/1.8i, Kaiser Optical Systems, Ann Arbor, MI) and a thermoelectrically cooled charge-coupled device camera (Pixis 256BR, Princeton Instruments, Princeton, NJ), all operated by a laptop computer. The system was wavelength calibrated using a neon-argon lamp, and the Raman

shifts were calculated using acetaminophen and naphthalene standards. Spectral response correction was determined using a National Institutes of Standards and Technology (NIST)-calibrated tungsten lamp. All measurements were background subtracted, noise smoothed, and fluorescence subtracted as described previously.[27]

3.3.4 Adipose and muscle tissue experiments

Raman signals were acquired from semi-infinite porcine muscle and adipose tissues to simulate biological samples. The porcine tissues were commercially acquired and refrigerated until use, and were kept on ice throughout the experiment. Three hundred μm thick slices of muscle tissue were obtained via cryosection and were layered over the semi-infinite slab of adipose tissue in 300 μm steps until a total muscle tissue thickness of 1800 μm was achieved (Figure 3.3A-B). Raman spectra were acquired at all thicknesses with each probe, and their ability to detect the superficial (muscle) and deep (adipose) tissues was assessed using two methods: the first method calculated the ratio of a peak intensity specific to muscle (1003 cm^{-1} peak corresponding to symmetric aromatic ring breathing in phenylalanine[27]) and a peak intensity specific to adipose tissue (1066 cm^{-1} peak corresponding to C-C stretch[28]) (Figure 3.3 C). These peaks were chosen due to the similar intensities exhibited in pure measurements so that stable peak ratios could be calculated. The second method used non-negatively constrained partial least squares (PLS) to

determine the contributions made by the muscle and the adipose tissue as a function of muscle thickness using the full spectrum.[27]

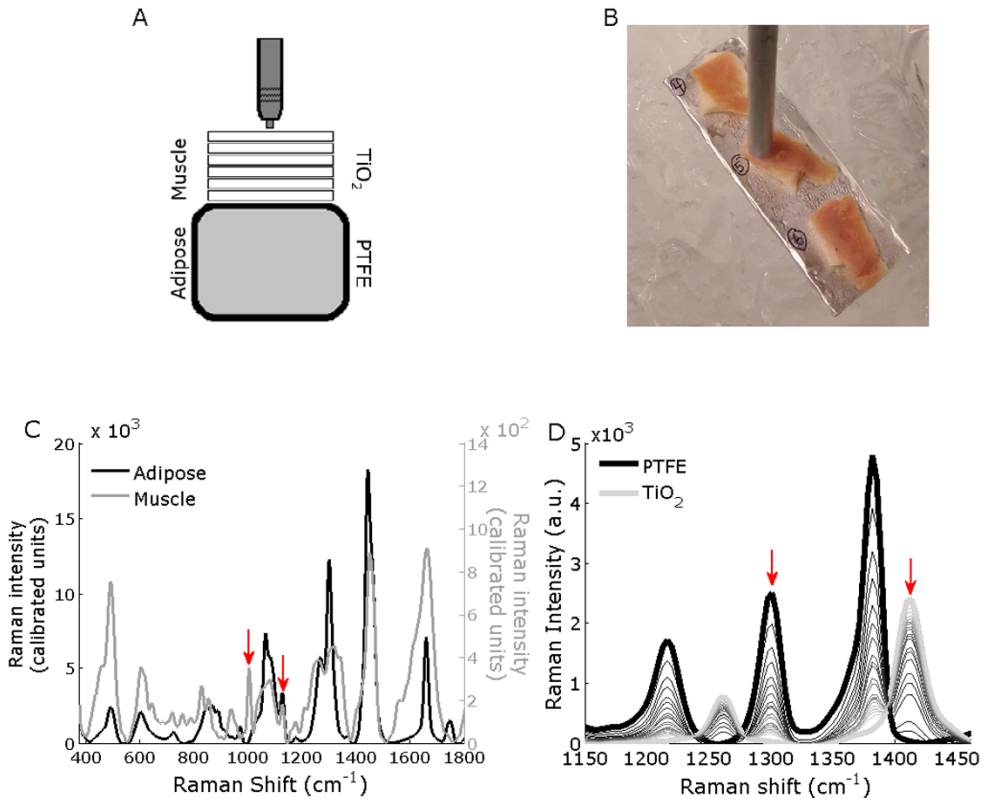

Figure 3.3. Experiment setup: (A) Schematic of experimental setup and (B) image for depth response characterization with probe contacting the surface of the superficial layers (porcine muscle or TiO_2) above a semi-infinite base (porcine adipose or PTFE, figure not to scale). (C) Pure spectral components measured from porcine adipose and muscle tissue samples of semi-infinite thickness (beveled probe design). (D) Representative signal tradeoff between pure components with increasing thickness of superficial TiO_2 layer (100 μm steps, beveled probe design). Arrows in (C) and (D) indicate peak positions used in ratiometric analyses.

3.3.5 Synthetic phantom experiments

Raman spectra were acquired separately from a polytetrafluoroethylene (PTFE) puck and sheets of titanium dioxide (TiO_2) particles[27] in a silicone-elastomer base to determine their "pure" Raman signals. Next, 100 μm thick sheets of the TiO_2 phantom were serially placed over a semi-infinite PTFE puck (1 cm thick) until a TiO_2 thickness of 1800 μm was achieved (Figure 3.3A). The spectral tradeoff as a function of TiO_2 layer thickness is displayed in Figure 3.3D. Pure PTFE is shown in black, which transitions down to an 1800 μm thick TiO_2 layer shown in light gray, with steps in 100 μm increments. As the TiO_2 layer thickness increased, the signal changed from a dominant PTFE signature to a primarily TiO_2 spectral shape. Raman spectra were collected at each thickness using all four probes to assess the efficacy of each probe in measuring superficial (TiO_2) and deep (PTFE) Raman signals obtained as a function of superficial thickness. Again, the ratio of the TiO_2 to PTFE signal was assessed using two methods: the first method calculated the ratio of the TiO_2 layer peak (1412 cm^{-1} corresponding to CH_3 bending[28]) to the PTFE layer peak (1300 cm^{-1} corresponding to CF_2 asymmetric stretching[29]) (Figure 3.3D). The second method used non-negatively constrained PLS to determine the respective contributions made by the TiO_2 phantom and the PTFE puck.[30]

3.4 Results and discussion

3.4.1 MC simulations

The mean results ± standard deviation of triplicate runs from the MC model simulation for porcine adipose and muscle tissue are depicted in Figure 3.4. A ratio of muscle tissue signal to adipose tissue signal was calculated by integrating the Raman photons detected from the muscle and adipose tissue layers respectively, as shown in Figure 3.4A. An increase in muscle to adipose tissue signal ratio as the muscle thickness increases is observed in all probe designs, and the modified probe designs have higher muscle to adipose ratios at muscle thicknesses ≥ 600 μm. The total Raman photons detected in the MC model from each probe at each muscle tissue thickness are shown in Figure 3.4B. The deep focused micro lens probe detected the most photons at all muscle tissue thicknesses, which has the highest cross-sectional area (Table 3.2), has the largest excitation and collection cone overlap (Figure 3.1), as well as wide acceptance angles (Table 3.2). The shallow focused micro lens and the beveled design detected about half the number of photons compared to the deep focused micro lens. The unmodified design detected by far the fewest photons of all of the designs at all depths simulated, which has the lowest volumetric overlap of excitation and collection cones (Figure 3.1) and narrow acceptance angles (Table 3.2).

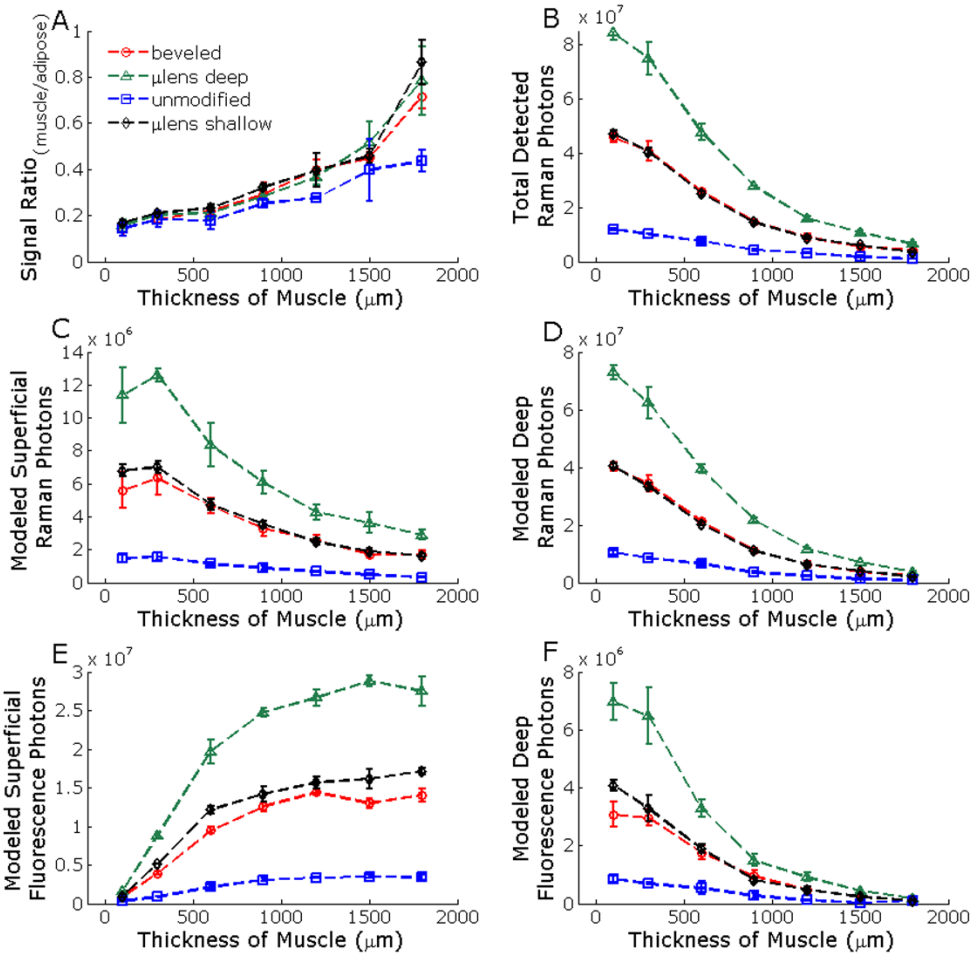

Figure 3.4. MC simulation results for probe designs as a function of superficial muscle layer thickness. (A) Modeled ratio of Raman muscle to adipose tissue. (B) Total Raman photons detected. (C) Raman photons detected from superficial layer. (D) Raman photons detected from deep layer. (E) Fluorescence photons detected from superficial layer. (F) Fluorescence photons detected from deep layer.

Detected photons originating in the superficial muscle tissue and the underlying adipose tissue were separately analyzed to evaluate depth sensitivity for each probe. For the detected superficial layer Raman photons, the signal intensity between 100 µm to 300 µm thick muscle tissue remained

approximately equal for all probe designs (Figure 3.4C). Beyond 300 μm thick muscle tissue, detected Raman signal from the superficial layer decreased with muscle thickness. Similarly for deep layers, detected Raman photons decreased monotonically from 100 μm to 1800 μm of muscle layer thickness for all probe designs (Figure 3.4D). It is also worth noting that as expected, the total number of Raman photons generated in the superficial layer did increase with the thickness of the muscle layer, despite the decreasing detection of these photons in the model.

In addition to tracking Raman photons, detected fluorescent photons were plotted based on the layer of tissue in which they originated. All probe designs detected higher fluorescence signal from the superficial muscle layer as the layer thickness increased (Figure 3.4E), whereas fluorescence from the deep layer decreased with muscle thickness in all probe designs (Figure 3.4F). The highest signals for both layers were detected by the deep focused micro lens probe design while almost equal values for both superficial and deep layers were collected by beveled and shallow focused micro lens designs. The muscle tissue has higher fluorescence absorption and quantum yield coefficients compared to the adipose tissue (Table 3.3). The higher fluorescence and increasing thickness of the muscle layer account for the increase in fluorescence detection from the superficial muscle layer (Figure 3.4E) and the decrease in fluorescence detection from the deep adipose tissue (Figure 3.4F) as the muscle tissue thickness increases. Probe designs that more efficiently collect Raman

scattered photons are also more efficient at detecting the broad spectrum autofluorescence from the samples.

With the exception of detected superficial Raman photons (Figure 3.4C), these simulation results all agree with theoretical understanding of bulk material properties for photon distribution. Since nearly 90% of the excitation photons are converted into these optical endpoints, it is likely that the decreased detection of Raman photons observed in Figure 3.4C is due to the complex interaction of superficial layer thickness and the probabilities for Raman scattering and fluorescence events in that top layer. While the superficial layer remains thin, appreciable excitation photons are Raman scattered prior to the overwhelming fluorescence generation that is evident at thicker superficial layers. To verify this result, non-competing simulations were conducted for the same layers (either only Raman scattering in modeled layers or only fluorescence). In each of these simulations, the trends for detected Raman scattering and fluorescence phenomena in superficial and deep layers matched the curves in Figure 3.4E-F, which agree with photon distribution theory for turbid media. This result indicates the importance of accounting for not only relative changes in scattering and absorption within a tissue of interest, but also the relative strength of competing optical processes for a target application.

While implementing a numerical simulation may be simpler than precisely controlling tissue phantoms and biological samples, models rely on assumptions with associated limitations. Like all probabilistic or stochastic

models, this simulation requires many photons to develop an accurate result. To exacerbate this requirement, the competing optical phenomena integrated in this simulation would require the use of extremely large numbers of photons if scaling factors were not utilized in order to obtain consistent and reliable results. To circumvent this requirement, the probability of a Raman scattering event was scaled by 10^4 times for layer properties relative to the probability of fluorescence generation. Furthermore, for every scattering step of an excitation photon, a discretely weighted computational fluorescence sub-photon could be generated that propagates based on layer parameters. As this model was implemented in a MATLAB environment and the inclusion of multiple optical phenomena add additional calculations for independent tracking, relatively small simulations (100,000 photons) were implemented for model comparison. Due to the high probabilities of both Raman scattering and fluorescence, each simulation resulted in roughly 10^8 – 10^9 photons that were tracked through extinction or detection. To verify model stability, models with 10^6 seed photons were also run for multiple depths and probe designs (data not shown). These model outputs fell well within the standard deviations indicated for the smaller model runs. Like many MC models for Raman scattering and fluorescence, this model neglects secondary Raman and fluorescence events. Inclusion of these events would likely be incremental, but could more accurately represent optical interactions, especially due to the relatively high frequency of fluorescence that has the potential to cause secondary fluorescence and Raman scattering. These

secondary events could also be included as model noise for a more direct SNR comparison with experimental values.

Despite these limitations, this model provides valuable insight into the complex interaction of multiple optical processes detected by fiber optic probes. These simulation results afford a probabilistic basis for comparison with experimental data as a means to evaluate the performance of these unique probe designs, including collection angle and surface area for photon collection. By evaluating Raman probe designs in scenarios that resemble tissue studies rather than ray-tracings in air, accurate selection of optimized configurations can be enabled for a specific application such as those listed in Table 3.1.

3.4.2 Biological tissue experimental results

Results from muscle tissue to adipose tissue specific peak ratio analysis (1003/1066 cm^{-1}) and partial least squares analysis both reveal an overall increase in the muscle tissue signal as muscle tissue layer thickness increases, as well as a decrease in adipose tissue signal as muscle tissue thickness increased (Figure 3.5A-D). The signal to noise ratio (SNR) obtained from peak ratio analysis of muscle tissue signal and adipose tissue signal are plotted in Figure 3.5A and Figure 3.5B respectively. The shallow focused micro lens design collected the highest SNR from muscle tissue at all of the layer thicknesses measured, which is due to the selectively superficial overlap of the excitation and collection cone angles based on ray tracing results modeled in

air (Figure 3.1D). The highest SNR of adipose tissue was measured by the deep focused probe, which is explained by the deep overlap of excitation and collection cone angles from ray tracing models in air (Figure 3.1C), and by the highest cross-sectional area for photon collection of all of the probes tested (Table 3.2). In the PLS analysis results, the beveled probe design yields the most muscle tissue signal, followed by the superficial micro lens design (Figure 3.5C). The modified probe designs appear to detect more signal from the deep layer than the unmodified design, especially at small muscle tissue thicknesses (Figure 3.5D). However, adipose tissue signal overwhelms the muscle tissue signal generated at small muscle tissue thicknesses and results in large variances and in some cases artificially low coefficients for muscle tissue signal. This is an inherent limitation of using the non-negative PLS analysis, which performs best when pure components have uncorrelated spectra,[27] enabling easy separation of components even when a small amount of a substance is present in the sample. This is the main reason that peak ratio analysis was the preferred method for assessing deep versus superficial signal collection, as tissue-type specific peak ratios were more sensitive to small changes in muscle tissue thickness compared to the PLS analysis.

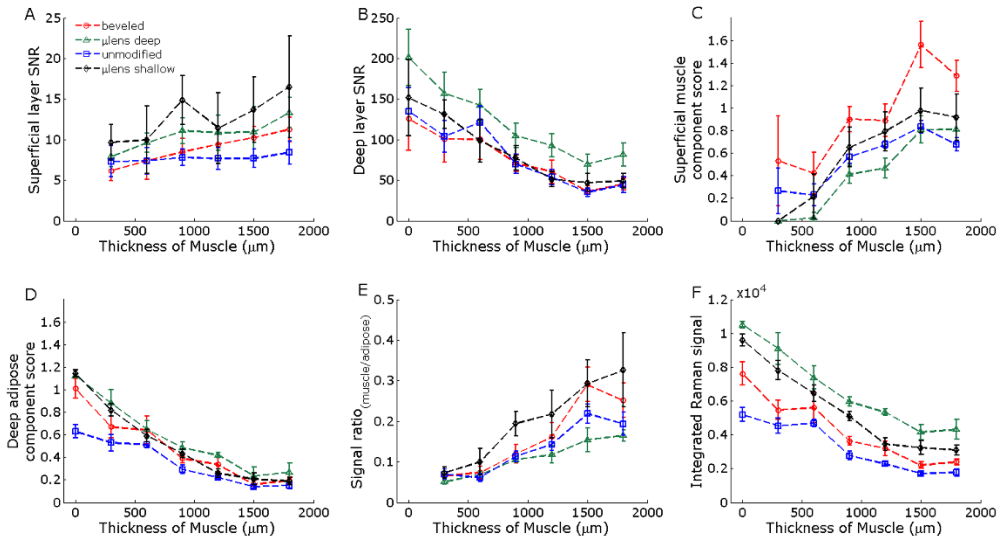

Figure 3.5. Biological optical phantom probe characterization. Adipose and muscle tissue experiments: (A) Mean ± standard deviation signal to noise ratio of superficial muscle layer peak signal (1003 cm^{-1}, arrow in (3C)) as a function of increasing superficial layer thickness. (B) Mean ± standard deviation signal to noise ration of deep adipose layer peak signal (1066 cm^{-1}, arrow in (3C)) as a function of increasing superficial layer thickness. (C) Nonnegative partial least squares for muscle tissue signal contribution versus superficial layer thickness. (D) Nonnegative partial least squares for adipose tissue signal contribution versus superficial layer thickness. (E) Ratio of superficial layer peak signal (1003 cm^{-1} muscle tissue peak) to deep layer peak signal (1066 cm^{-1} adipose tissue peak) as a function of increasing superficial layer thickness. (F) Integrated signal intensity of peaks (arrows, Figure 3.3C) as a function of superficial layer thickness.

A ratio of the experimentally measured peak signals from muscle tissue to adipose tissue was calculated for each probe (Figure 3.5E**)** and reveals a general linear rise with increase in muscle tissue thickness. This is expected due to the increasing thickness of muscle tissue that contributes to the overall signal. The shallow focused micro lens design had the highest values across muscle tissue thicknesses, which is in large part due to having the highest muscle SNR

of all four probes. The deep focused micro lens design has the lowest ratio beyond 1200 μm thicknesses which likely results from the more efficient collection of adipose tissue signal at these depths. This plot shows similar results as the MC simulation, with an increase in the signal ratio of muscle tissue to adipose tissue as the muscle tissue thickness increases observed across all of the probes.

The total integrated Raman signal measured with each probe as a function of depth is plotted in Figure 3.5F. The deep focused design has the highest collection efficiency at all depths, followed by the shallow focused micro lens design. The unmodified design has the lowest integrated signal intensity at all tissue thicknesses. The MC results also show the deep focused micro lens design as collecting the most Raman photons, and the unmodified design collecting the least.

Overall, the experimental results agree with the MC model for determining probe performance as a function of muscle tissue thickness when using optical properties that are realistic for biological tissue. The spread of results between the probes evaluated demonstrates how small changes in probe design can significantly alter their performance. This validation is an important first step in developing a tool for optimizing the choice or design of a fiber optic probe when beginning a study. In addition, the modified Raman probe designs demonstrate significant improvement in collection efficiency through experimental testing and MC models. Regardless of application, such

modifications can increase the excitation-collection cone overlap and collection fiber surface area so that maximum Raman photons can be detected.

3.4.3 Synthetic phantom experiments

The peak SNR obtained from analysis of the superficial material (TiO_2) from each probe (1412 cm^{-1}) design is shown in Figure 3.6A as a function of TiO_2 thickness. TiO_2 SNR increases as the TiO_2 thickness increases up to 1000 μm, after which the SNRs plateau. This plateau likely occurs because the transport mean free path ($1/\mu_s'$) for TiO_2 is small due to low scattering anisotropy (Table 3.3) and thus it takes a shorter absolute depth to be considered semi-infinite, resulting in a plateau in SNR.[27] The shallow focused micro lens probe yields the highest SNR at TiO_2 thicknesses between 100 - 1000 μm, with the highest separation observed in 100 - 400 μm thicknesses. This SNR improvement at small TiO_2 thicknesses is in agreement with results published by Agenant *et al.*,[28] and correspond to superficial overlap of excitation and collection cone angles determined via Zemax ray tracing (Figure 3.1D).

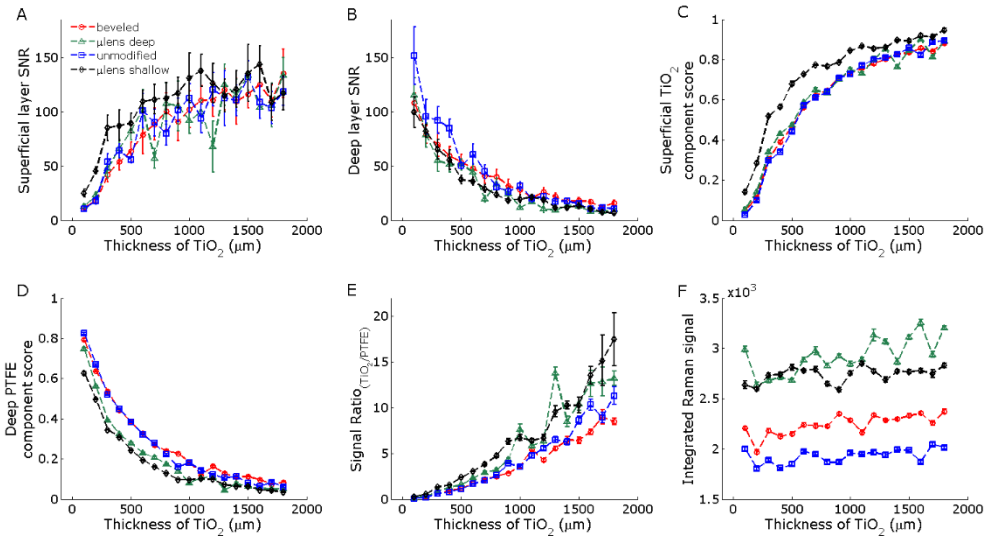

Figure 3.6. Synthetic phantom probe characterization. Controlled optical phantom experiments: (A) Mean ± standard deviation signal to noise ratio of superficial layer peak signal (1412 cm^{-1} TiO_2 peak, arrow in (3D)) as a function of increasing superficial layer thickness. (B) Mean ± standard deviation signal to noise ratio of deep layer peak signal (1300 cm^{-1} PTFE peak, arrow in (3D)) as a function of increasing superficial layer thickness. (C) Mean ± standard deviation nonnegative partial least squares for TiO_2 signal contribution versus superficial layer thickness. (D) Mean ± standard deviation nonnegative partial least squares for PTFE signal contribution versus superficial layer thickness. (E) Mean ± standard deviation ratio of superficial layer peak signal (1412 cm^{-1} peak) to deep layer peak signal (1300 cm^{-1} peak) as a function of increasing superficial layer thickness. (F) Mean ± standard deviation integrated signal intensity of peaks (arrows indicated in Figure 3.3D) as a function of superficial layer thickness.

The SNR of the deep layer (PTFE, peak at 1300 cm^{-1}) is plotted as a function of TiO_2 thickness up to 1800 µm in Figure 3.6B. As the TiO_2 thickness increases, the SNR from the PTFE exponentially decreases in all probe designs. The unmodified probe design demonstrates the highest deep layer SNR in samples with 100 – 500 µm thick TiO_2 layers. This may be explained by the overlap of the excitation and collection cone angles deep in the sample seen in

the unmodified design ray tracing results (Figure 3.1A). This result differs from biological testing in which the deep focused micro lens design has the highest SNR for the deep adipose tissue. In addition, the decay in SNR for deep layers is exponential in the synthetic phantom compared to a linear decrease in the biological tissues, highlighting the influence of optical properties on probe performance.

In addition to SNR results based on TiO_2 and PTFE-specific peaks, results from the non-negative partial least squares analyses are provided in Figure 3.6C-D. Similar to results in Figure 3.6A, the shallow focused micro lens design demonstrates the highest TiO_2 component score up to 1800 μm thick layers of TiO_2 sheets. The unmodified probe design also displays high PTFE component scores; however, the deep focused probe design does not appear to bring any advantage for enhancing detection of PTFE signal as would be expected based on its deep overlap range of the excitation and collection fibers (Figure 3.1C). It is likely that the extremely high reduced scattering coefficients of the synthetic phantoms help to improve the detection of PTFE in the other Raman probes, negating the benefits that would otherwise be seen with the deep focused micro lens design. It logically follows that as the transport mean free path decreases due to higher reduced scattering coefficients, the theoretical collection-excitation cone overlap volume (calculated in air) becomes increasingly irrelevant for highly scattering media. This finding underscores the large influence that application-specific optical properties have on fiber optic

probe performance, and provides an example in which the specialized fiber optic probes provide little to no advantages at probing specific depths. In this work we chose biologically relevant absorption and scattering coefficients for the MC model, but these may not be representative of all biological tissue types. While beyond the scope of this work, a systematic modeling evaluation of probe design performance with respect to scattering and absorption coefficients, similar to the approach reported by Reble *et al.*, may provide more insight into attenuation thresholds for which tailored probe designs are beneficial.[27]

The ratio of superficial (TiO_2) versus deep (PTFE) signal is plotted in Figure 3.6E**,** and reveals a linear increase in TiO_2 to PTFE signal with increasing thickness of TiO_2 scatter sheets. The performance of the probes was similar across the TiO_2 thicknesses, with a slightly higher ratio generally seen in the shallow focused micro lens design. Biological tissue testing similarly reveals a linear increase in superficial (muscle tissue) to deep (adipose tissue) signals, and consistent with the synthetic phantom results, the shallow focused micro lens design generally yields the highest ratio as a function of muscle tissue thickness.

The total signal measured by each probe was determined by integrating the area under the curve of the peaks used for SNR calculation at each thickness, and these results are plotted in Figure 3.6F. Similar to results from MC simulations and biological tissue experiments, the deep focused micro lens design collects the highest overall signal. This design has wide acceptance

angles (4.9°-33.8°) paired with a high cross-sectional area through which photons can be coupled (Table 3.2) and large excitation and collection cone overlap (Figure 3.1C), which together results in the highest integrated Raman signal. The second highest signal was recorded with the shallow focused micro lens design, which has narrower acceptance angles (21.2°-35.8°) and low cross-sectional area (Table 3.2), but has a superficial overlap of excitation and collection cone angles that appears to increase signal collection efficiency (Figure 3.1D). Wide cone angles, large surface areas through which photons can be effectively coupled per collection fiber, and high volumetric overlap between the excitation and collection fibers logically explain the overall increased collection efficiency observed with the micro lens designs. Although the beveled design has the widest acceptance angles, the collection efficiency is limited due to lower cross sectional area through which photons can be coupled and reduced overlap of the excitation and collection cones (Figure 3.1B). The unmodified design has the lowest overall signal at all depths, the smallest acceptance angles (0°-12.7°), and the lowest degree of excitation and collection cone overlap, and therefore has the lowest collection efficiency for all four probe designs. The interplay of these three factors (collection fiber acceptance angles, collection fiber surface area, and excitation-collection cone overlap) ultimately dictates the collection efficiency of this class of fiber optic probes. These factors should be maximized to improve probe throughput for tissue applications.

As evidenced in Table 3.1, important biological investigations span many depth regimes. Work by Wang *et al.* which designed and evaluated a confocal ball lens probe remains the optimal design reported for detecting superficial (<100 um) signals of biological tissues with limited contribution from deeper layers.[28] At the other extreme, spatially offset designs demonstrated by numerous investigators have proven most effective at interrogating deep layers of highly scattering media.[29,30] Within these extremes of the spectrum of optical detection, volume integrating fiber probes can be tailored for preferential detection and increased SNR for an application of interest. This work demonstrates improved signal collection efficiency obtained when integrating micro lens components into a probe tip design that can expand the overlap in excitation and collection cone angles as well as increase the surface area for light detection compared with conventional fiber probe designs. Beyond high collection efficiencies, micro lens designs can be optimized to superficial and deep targets based on the choice of lens as demonstrated in the biological experiments and MC simulations. Beveled and superficially focused micro lens designs have superior performance in shallow samples whereas the deep focused micro lens design had highest collection efficiency and SNR in deep tissue layers. The conventional design has overall the lowest collection efficiencies and SNR at all tissue layer thicknesses. All of these evaluations have utilized muscle and adipose-mimicking phantoms paired with MC simulation results, and thus conclusions across these studies are

straightforward.[28,29] The volume-integrating probes evaluated here demonstrate variable performance with depth as a function of sample optical properties (synthetic versus biological phantoms), most notably the reduced scattering coefficient. At larger scattering values, the improvements of a particular configuration are diminished. These results further support the need for instrument development within the context of tissue properties for a targeted application, which may perform differently from theoretical models commonly employed for optical design.

3.5 Conclusions

A platform for optimizing selection and/or design of a Raman fiber optic probe that incorporates application specific optical properties for prediction of probe performance has been developed and evaluated. The expanded Monte Carlo model includes Raman scattering, fluorescence, elastic scattering, and absorption, and shows strong agreement with experimental results from biological tissue including prediction of collection efficiency and SNR at superficial and deep layers. Fluorescence tracking also agrees with experimental results for biological samples. As a competing optical phenomenon with a likelihood of generation over 1000 times higher than Raman photons in biological tissues, this important feature cannot be

overlooked when optimizing fiber optic probes for Raman spectroscopy applications.

Fiber optic probe based Raman spectroscopy has been applied to many biological targets. Modeling and experimental testing demonstrate variations in performance based on probe design but also target sample properties; the depth of the desired signal source and the optical parameters of the sample are necessary considerations prior to the start of a fiber based probe study. Experimental results in highly scattering TiO_2 and PTFE samples ($\mu_s' > 50\ cm^{-1}$) did not vary based on probe design, whereas results from muscle and adipose issues more closely resembled predictions made for air but with large variability, particularly in extremely shallow or deep samples. This underscores the importance of incorporating application-specific optical properties during probe design optimization.

Although this investigation focused on four particular probe geometries, a robust Monte Carlo model allows extension to other probe designs for any application with known optical properties. The model presented here can be easily extended to both confocal and spatially offset geometries, and can be used to optimize entirely novel probe designs prior to fabrication, reducing time and cost while improving data quality.

3.6 Acknowledgements

This work has been supported by NIH R01 HD081121, NIH F31 CA168238, ASLMS student research grant, and the Vanderbilt CTSA grant UL1 TR000445 from NCATS/NIH. The authors thank Dr. E. Duco Jansen and Dr. Paul Stoddart for valuable feedback and discussion during the preparation of this manuscript, and Dr. Elaine Shelton and Naoko Brown for assistance in biological tissue testing.

3.7 References

1. Pence, I.; Mahadevan-Jansen, A., Clinical instrumentation and applications of Raman spectroscopy. Chemical Society reviews 2016, 45 (7), 1958-79.
2. Mahadevan-Jansen, A.; Mitchell, M. F.; Ramanujam, N.; Utzinger, U.; Richards-Kortum, R., Development of a fiber optic probe to measure NIR Raman spectra of cervical tissue in vivo. Photochemistry and photobiology 1998, 68 (3), 427-31.
3. Almond, L. M.; Hutchings, J.; Kendall, C.; Day, J. C.; Stevens, O. A.; Lloyd, G. R.; Shepherd, N. A.; Barr, H.; Stone, N., Assessment of a custom-built Raman spectroscopic probe for diagnosis of early oesophageal neoplasia. Journal of biomedical optics 2012, 17 (8), 081421-1.
4. Huang, Z.; Teh, S. K.; Zheng, W.; Lin, K.; Ho, K. Y.; Teh, M.; Yeoh, K. G., In vivo detection of epithelial neoplasia in the stomach using image-guided Raman endoscopy. Biosensors & bioelectronics 2010, 26 (2), 383-9.
5. Bergholt, M. S.; Lin, K.; Wang, J.; Zheng, W.; Xu, H.; Huang, Q.; Ren, J. L.; Ho, K. Y.; Teh, M.; Srivastava, S.; Wong, B.; Yeoh, K. G.; Huang, Z., Simultaneous fingerprint and high-wavenumber fiber-optic Raman spectroscopy enhances real-time in vivo diagnosis of

adenomatous polyps during colonoscopy. Journal of biophotonics 2016, 9 (4), 333-42.

6. Lim, L.; Nichols, B.; Migden, M. R.; Rajaram, N.; Reichenberg, J. S.; Markey, M. K.; Ross, M. I.; Tunnell, J. W., Clinical study of noninvasive in vivo melanoma and nonmelanoma skin cancers using multimodal spectral diagnosis. Journal of biomedical optics 2014, 19 (11), 117003.

7. Schleusener, J.; Gluszczynska, P.; Reble, C.; Gersonde, I.; Helfmann, J.; Fluhr, J. W.; Lademann, J.; Rowert-Huber, J.; Patzelt, A.; Meinke, M. C., In vivo study for the discrimination of cancerous and normal skin using fibre probe-based Raman spectroscopy. Experimental dermatology 2015, 24 (10), 767-72.

8. Short, M. A.; Lam, S.; McWilliams, A. M.; Ionescu, D. N.; Zeng, H., Using laser Raman spectroscopy to reduce false positives of autofluorescence bronchoscopies: a pilot study. Journal of thoracic oncology: official publication of the International Association for the Study of Lung Cancer 2011, 6 (7), 1206-14.

9. Krishna, H.; Majumder, S. K.; Chaturvedi, P.; Sidramesh, M.; Gupta, P. K., In vivo Raman spectroscopy for detection of oral neoplasia: a pilot clinical study. Journal of biophotonics 2014, 7 (9), 690-702.

10. Agenant, M.; Grimbergen, M.; Draga, R.; Marple, E.; Bosch, R.; van Swol, C., Clinical superficial Raman probe aimed for epithelial tumor detection: Phantom model results. Biomedical optics express 2014, 5 (4), 1203-16.

11. O'Regan, G. M.; Kemperman, P. M.; Sandilands, A.; Chen, H.; Campbell, L. E.; Kroboth, K.; Watson, R.; Rowland, M.; Puppels, G. J.; McLean, W. H.; Caspers, P. J.; Irvine, A. D., Raman profiles of the stratum corneum define 3 filaggrin genotype-determined atopic dermatitis endophenotypes. The Journal of allergy and clinical immunology 2010, 126 (3), 574-80.e1.

12. Pence, I. J.; Nguyen, Q. T.; Bi, X.; Herline, A. J.; Beaulieu, D. M.; Horst, S. N.; Schwartz, D. A.; Mahadevan-Jansen, A. In Endoscopy-coupled Raman spectroscopy for in vivo discrimination of inflammatory bowel disease, 2014; pp 89390R-89390R-10.

13. Bergholt, M. S.; Zheng, W.; Ho, K. Y.; Teh, M.; Yeoh, K. G.; Yan So, J. B.; Shabbir, A.; Huang, Z., Fiberoptic confocal Raman spectroscopy

for real-time in vivo diagnosis of dysplasia in Barrett's esophagus. Gastroenterology 2014, 146 (1), 27-32.

14. O'Brien, C. M.; Vargis, E.; Slaughter, C.; Rudin, A. P.; Herington, J. L.; Bennett, K. A.; Reese, J.; Mahadevan-Jansen, A. In Characterization of human cervical remodeling throughout pregnancy using in vivo Raman spectroscopy, 2015; pp 93032F-93032F-6.

15. Vargis, E.; Brown, N.; Williams, K.; Al-Hendy, A.; Paria, B. C.; Reese, J.; Mahadevan-Jansen, A., Detecting biochemical changes in the rodent cervix during pregnancy using Raman spectroscopy. Annals of biomedical engineering 2012, 40 (8), 1814-24.

16. Motz, J. T.; Fitzmaurice, M.; Miller, A.; Gandhi, S. J.; Haka, A. S.; Galindo, L. H.; Dasari, R. R.; Kramer, J. R.; Feld, M. S., In vivo Raman spectral pathology of human atherosclerosis and vulnerable plaque. Journal of biomedical optics 2006, 11 (2), 021003.

17. Keller, M. D.; Majumder, S. K.; Mahadevan-Jansen, A., Spatially offset Raman spectroscopy of layered soft tissues. Optics letters 2009, 34 (7), 926-8.

18. Jermyn, M.; Mok, K.; Mercier, J.; Desroches, J.; Pichette, J.; Saint-Arnaud, K.; Bernstein, L.; Guiot, M. C.; Petrecca, K.; Leblond, F., Intraoperative brain cancer detection with Raman spectroscopy in humans. Science translational medicine 2015, 7 (274), 274ra19.

19. Matousek, P.; Draper, E. R.; Goodship, A. E.; Clark, I. P.; Ronayne, K. L.; Parker, A. W., Noninvasive Raman spectroscopy of human tissue in vivo. Applied spectroscopy 2006, 60 (7), 758-63.

20. Schulmerich, M. V.; Dooley, K. A.; Morris, M. D.; Vanasse, T. M.; Goldstein, S. A., Transcutaneous fiber optic Raman spectroscopy of bone using annular illumination and a circular array of collection fibers. Journal of biomedical optics 2006, 11 (6), 060502.

21. Stone, N.; Baker, R.; Rogers, K.; Parker, A. W.; Matousek, P., Subsurface probing of calcifications with spatially offset Raman spectroscopy (SORS): future possibilities for the diagnosis of breast cancer. The Analyst 2007, 132 (9), 899-905.

22. Prieto, M. C.; Matousek, P.; Towrie, M.; Parker, A. W.; Wright, M.; Ritchie, A. W.; Stone, N., Use of picosecond Kerr-gated Raman spectroscopy to suppress signals from both surface and deep layers in

bladder and prostate tissue. Journal of biomedical optics 2005, 10 (4), 44006.

23. Stevens, O.; Iping Petterson, I. E.; Day, J. C.; Stone, N., Developing fibre optic Raman probes for applications in clinical spectroscopy. Chemical Society reviews 2016, 45 (7), 1919-34.

24. Wang, J.; Bergholt, M. S.; Zheng, W.; Huang, Z., Development of a beveled fiber-optic confocal Raman probe for enhancing in vivo epithelial tissue Raman measurements at endoscopy. Optics letters 2013, 38 (13), 2321-3.

25. Matousek, P.; Clark, I. P.; Draper, E. R.; Morris, M. D.; Goodship, A. E.; Everall, N.; Towrie, M.; Finney, W. F.; Parker, A. W., Subsurface probing in diffusely scattering media using spatially offset Raman spectroscopy. Applied spectroscopy 2005, 59 (4), 393-400.

26. Wang, L.; Jacques, S. L.; Zheng, L., MCML--Monte Carlo modeling of light transport in multi-layered tissues. Computer methods and programs in biomedicine 1995, 47 (2), 131-46.

27. Vishwanath, K.; Pogue, B.; Mycek, M. A., Quantitative fluorescence lifetime spectroscopy in turbid media: comparison of theoretical, experimental and computational methods. Physics in medicine and biology 2002, 47 (18), 3387-405.

28. Keller, M. D.; Wilson, R. H.; Mycek, M. A.; Mahadevan-Jansen, A., Monte Carlo model of spatially offset Raman spectroscopy for breast tumor margin analysis. Applied spectroscopy 2010, 64 (6), 607-14.

29. Shih, W.-C.; L. Bechtel, K.; Feld, M. S., Intrinsic Raman spectroscopy for quantitative biological spectroscopy Part I: Theory and simulations. Opt. Express 2008, 16 (17), 12726-12736.

30. Mo, J.; Zheng, W.; Huang, Z., Fiber-optic Raman probe couples ball lens for depth-selected Raman measurements of epithelial tissue. Biomedical optics express 2010, 1 (1), 17-30.

31. Enejder, A. M.; Koo, T. W.; Oh, J.; Hunter, M.; Sasic, S.; Feld, M. S.; Horowitz, G. L., Blood analysis by Raman spectroscopy. Optics letters 2002, 27 (22), 2004-6.

32. Reble, C.; Gersonde, I.; Lieber, C. A.; Helfmann, J., Influence of tissue absorption and scattering on the depth dependent sensitivity of

Raman fiber probes investigated by Monte Carlo simulations. Biomedical optics express 2011, 2 (3), 520-533.

33. Boas, D.; Culver, J.; Stott, J.; Dunn, A., Three dimensional Monte Carlo code for photon migration through complex heterogeneous media including the adult human head. Opt Express 2002, 10 (3), 159-70.

34. Everall, N.; Hahn, T.; Matousek, P.; Parker, A. W.; Towrie, M., Photon migration in Raman spectroscopy. Applied spectroscopy 2004, 58 (5), 591-7.

35. Bashkatov, A. N.; Genina, E. A.; Tuchin, V. V., Optical properties of skin, subcutaneous, and muscle tissues: a review. Journal of Innovative Optical Health Sciences 2011, 4 (01), 9-38.

36. Lieber, C. A.; Mahadevan-Jansen, A., Automated method for subtraction of fluorescence from biological Raman spectra. Applied spectroscopy 2003, 57 (11), 1363-7.

37. Wei, F.; Zhang, D.; Halas, N. J.; Hartgerink, J. D., Aromatic amino acids providing characteristic motifs in the Raman and SERS spectroscopy of peptides. The journal of physical chemistry. B 2008, 112 (30), 9158-64.

38. Czamara, K.; Majzner, K.; Pacia, M. Z.; Kochan, K.; Kaczor, A.; Baranska, M., Raman spectroscopy of lipids: a review. Journal of Raman Spectroscopy 2015, 46 (1), 4-20.

39. Buschman, H. P.; Deinum, G.; Motz, J. T.; Fitzmaurice, M.; Kramer, J. R.; van der Laarse, A.; Bruschke, A. V.; Feld, M. S., Raman microspectroscopy of human coronary atherosclerosis: biochemical assessment of cellular and extracellular morphologic structures in situ. Cardiovascular pathology: the official journal of the Society for Cardiovascular Pathology 2001, 10 (2), 69-82.

40. de Bruin, D. M.; Bremmer, R. H.; Kodach, V. M.; de Kinkelder, R.; van Marle, J.; van Leeuwen, T. G.; Faber, D. J., Optical phantoms of varying geometry based on thin building blocks with controlled optical properties. Journal of biomedical optics 2010, 15 (2), 025001.

41. Hernandez-Santana, A.; Irvine, E.; Faulds, K.; Graham, D., Rapid prototyping of poly (dimethoxysiloxane) dot arrays by dip-pen nanolithography. Chemical Science 2011, 2 (2), 211-215.

42. Mihály, J.; Sterkel, S.; Ortner, H. M.; Kocsis, L.; Hajba, L.; Furdyga, É.; Mink, J., FTIR and FT-Raman spectroscopic study on polymer based high pressure digestion vessels. Croatica chemica acta 2006, 79 (3), 497-501.

43. Ntziachristos, V., Going deeper than microscopy: the optical imaging frontier in biology. Nature methods 2010, 7 (8), 603-14.

CHAPTER 4

CLINICAL CHARACTERIZATION OF *IN VIVO* INFLAMMATORY BOWEL DISEASE WITH RAMAN SPECTROSCOPY

4.1 Abstract

Inflammatory bowel disease (IBD), including ulcerative colitis (UC) and Crohn's disease (CD), affects over 1 million Americans and 2 million Europeans, and the incidence is increasing worldwide. While these diseases require unique medical care, the differentiation between UC and CD lacks a gold standard, and therefore relies on long term follow up, success or failure of existing treatment, and recurrence of the disease. Here, we present colonoscopy-coupled fiber optic probe-based Raman spectroscopy as a minimally-invasive diagnostic tool for IBD of the colon (UC and Crohn's colitis). This pilot in vivo study of subjects with existing IBD diagnoses of UC (n=8), CD (n=15), and normal control (n=8) aimed to characterize spectral signatures of UC and CD. Samples were correlated with tissue pathology markers and endoscopic evaluation. The collected spectra were processed and analyzed using multivariate statistical techniques to identify spectral markers and discriminate IBD and disease classes. Confounding factors including the presence of active inflammation and the particular colon segment measured

were investigated and integrated into the devised prediction algorithm, reaching 90% sensitivity and 75% specificity to CD from this in vivo dataset. These results represent significant progress towards improved real-time classification for accurate and automated in vivo detection and discrimination of IBD during colonoscopy procedures.

4.2 Introduction

Inflammatory bowel disease (IBD), which includes ulcerative colitis (UC) and Crohn's disease (CD), affects nearly one million Americans and two million Europeans, and the incidence is increasing worldwide.[1] This complex illness is characterized by both chronic and acute disease states, with periods of inflammatory flare, quiescence, and relapse. Ulcerative colitis is almost always confined to the colon and Crohn's disease may occur in any part of the gastrointestinal tract from the mouth to the rectum. Numerous overlapping risk factors including ethnic origin, lifestyle, geographic region, and susceptibility regions on at least 12 chromosomes confound physiological understanding of this disease.[2, 3] Patients with IBD have an elevated risk of gastrointestinal cancer and experience dramatic decreases in quality of life. Despite advances in therapy, hospitalization rates for IBD, particularly CD, have shown significant increase, incurring a substantial rise in inflation-adjusted economic burden. With the high drug costs and rates of surgery (up to 75% of CD and 25-33% of

UC patients), IBD is one of the costliest conditions on a per year basis in the US, with expenses for CD surpassing diabetes, coronary artery disease, and chronic obstructive pulmonary disease.[4, 5]

Despite the overlap in presentation, symptoms, and progression of CD and UC, discriminating IBD subtype is vital for selection of the most appropriate therapeutic or surgical intervention and patient prognosis, a determination often made by assessing the severity of active inflammation during evaluation. For instance, UC can be cured in many patients by surgical removal of the colon, however, CD surgeries are rarely curative and often require further procedures. The goal of IBD treatment is to rapidly induce remission and prevent disease complications. Currently, the distinction between UC and CD is made based on inexact clinical, radiologic, endoscopic, and pathologic features[6-9]; in up to 15% of IBD cases indeterminate colitis (IC, or IBD unspecified) is diagnosed because of the difficulty in distinguishing between UC and CD. In these patients, diagnosis ultimately relies on long term follow up based on success or failure of existing treatment and recurrence of disease. A further challenge is that another 5-14% of cases are reclassified within IBD based on long-term follow up.[10, 11] All of these determinations are complicated by the lack of a definitive, recognized gold standard for diagnosis. Therefore, accurate differential diagnosis of IBD is critically needed for appropriate medical and surgical care, intervention, and prognosis. The

development of new technologies that can improve understanding of IBD and aid objective diagnosis may help meet this need.

Clinically, diagnosis is made primarily based upon symptom presentation (abdominal pain, number and consistency of stools, etc.) and biopsy informed video endoscopy (White Light Reflectance, WLR). While the disease may manifest in a typical and easily characterized fashion in some patients, expert endoscopists often face non-differentiating disease appearance and histopathologists can only identify features of chronic or acute colon inflammation that are consistent with both IBD subtypes. The lack of a definitive, biochemically specific characterization tool that can investigate IBD subtypes directly hinders delivery of appropriate care. Numerous investigations have been pursued to develop tools to improve diagnosis, including computed tomography, magnetic resonance imaging, optical coherence tomography, laser endomicroscopy, wireless capsule endoscopy, and elastic scattering spectroscopy.[12-16] All of these techniques are based on structure either at the macroscopic (appearance under widefield imaging) or microscopic scale (cell morphology and optical scattering properties of tissues). However, structural changes in tissue are a downstream effect of underlying disease presentation and have not proven effective for IBD differentiation. Raman scattering, on the other hand, is sensitive to the constituent biomolecular makeup of a sample, and can be utilized to capture a fingerprint of the vibrational modes of chemical bonds present within tissue. It is expected that unique biochemical alterations

associated with inflammatory response pathways will precede macroscopic tissue changes.[17, 18] These disease specific changes in tissues that are associated with disease status, on both the macro- and microscopic scales should provide valuable information to differentiate IBD in the colon.

Raman spectroscopic techniques have been investigated for numerous clinical diagnostic applications to aid in real-time objective disease evaluation.[19] Specifically addressing IBD, Raman techniques have been applied for ex vivo tissues to develop preliminary biomarkers and identify spectral signatures consistent with disease subtype. The goal of this study is to demonstrate the potential for Raman spectroscopy to detect tissue changes consistent with inflammatory bowel disease in the colon as a potential diagnostic adjunct. This report presents results from an endoscopic study using Raman spectroscopy to characterize IBD from human subjects in vivo. This work characterizes the disease presentation from a diverse patient population and demonstrates disease discrimination based on spectral changes measured across subjects in vivo. Furthermore, this work sought to elucidate confounding factors that limit predictive performance and incorporate these factors to improve rates of disease classification. Overall, results demonstrate the potential for endoscopic Raman spectroscopy as a diagnostic adjunct for IBD.

4.3 Methods

4.3.1 Subject recruitment and measurement protocol

Following written informed consent, 23 patients with IBD diagnoses (Table 4.1) that were scheduled for a routine surveillance and evaluation colonoscopy at the Vanderbilt GI Endoscopy lab were recruited according to IRB protocol (IRB #111609). Furthermore, healthy control subjects with no history of inflammatory disease were recruited from the population of colon cancer screening patients at the endoscopy lab. Following standard colonoscopy protocol but prior to biopsy as indicated, spectra were obtained from normal and/or inflamed sites within the colon, making measurements at two distinct sites in each segment: right (cecum or ascending), transverse, and left (descending or sigmoid) colon, as well as two sites in the rectum. The surface of the colon at each measurement site was flushed with saline to clear mucus, blood, or debris prior to spectral acquisition. The probe was introduced through the endoscope accessory channel once the measurement location was reached. With the probe touching the mucosal surface with sufficient pressure to ensure gentle contact while maintaining position during each measurement, spectra were collected and averaged per site while the endoscope's white light was disabled. The probed site was then biopsied and the tissue samples were fixed in formalin for routine histopathology. Spectra were compared with the combined physician evaluation based on endoscopy, histopathology, and

patient history (consistent with standard of care) for the respective gold standard patient diagnosis. Between subjects, the probe was detached from the system for cleaning, soaked in ortho-Phthalaldehyde (Cidex OPA, Johnson & Johnson, Arlington, TX) and rinsed thoroughly with water, in accordance with clinical protocols for high-level disinfection.

Table 4.1. Description of study participants.

Normal control (NC)	**n=8**
Age (years)	56.6 ± 9.3
BMI	31.3 ± 6.9
Gender	6F, 2M
Crohn's disease (CD)	**n=15**
Age	39.7 ± 7.6
BMI	26.1 ± 4.3
Gender	12F, 3M
Ulcerative colitis (UC)	**n=8**
Age	44.8 ± 12.2
BMI	27.0 ± 5.8
Gender	3F, 5M

4.3.2 Raman instrumentation, calibration and processing

In vivo Raman spectra were collected using a portable clinical Raman spectroscopy system coupled to a standard clinical endoscope (Fig. 4.1). A 785 nm diode laser (Innovative Photonics Solutions, Monmouth Junction, NJ) was coupled to a custom-fabricated superficially focused fiber-optic probe (EmVision LLC, Loxahatchee, FL) which delivered 80 mW to the surface of the colon. Briefly, the endoscope compatible fiber optic probe contains a 200 μm core diameter excitation fiber with bandpass filtering surrounded by seven 300 μm collection fibers with long pass filters. A shallow focusing micro lens composed of a plano-convex sapphire lens and MgF2 optical window is placed

in front of the filters to maximize collection efficiency at the probe tip.[20] The probe tip is physically packaged in a 2.1 mm diameter rigid metal tube that is approximately 6 mm in length to couple with standard endoscope technology. Each measurement utilized three integrated spectra of 250 ms acquisitions to achieve a sufficient signal to noise ratio (SNR ≥15).[21] Longer integration times could not be utilized due to the substantial background and autofluorescence signals generated by the tissue. The Raman scattered light was collected in reflectance mode and coupled into an f ⁄1.8 spectrograph (Kaiser Optical Systems, Inc.) with a fixed volume phase holographic grating resulting in spectral coverage from 450 to 1950 cm−1 and a spectral resolution of 7 cm−1. The detector was a back-illuminated deep-depletion CCD which was thermoelectrically cooled to −70°C (Pixis 256BR, Princeton Instruments). Spectral calibration was performed using a neon–argon lamp with naphthalene and acetaminophen standards to correct for day-to-day variations. A National Institute of Standards and Technology-certified quartz-tungsten halogen lamp was used to account for the wavelength-dependent response of the instrument. The spectra were processed for fluorescence subtraction and noise smoothing using the modified polynomial fit and Savitzky–Golay methods, and subsequently normalized to the spectrum mean as described previously.[22] All calibration steps were performed in the procedure room prior to the beginning of each case, and post-processing steps were completed within 1-2 seconds after each measurement. The collection parameters were optimized during the first

two procedures based upon sensitivity of the probe design and system. Statistical differences for integrated spectral intensity and colons segment were performed independently using ANOVA with $\alpha = 0.05$.

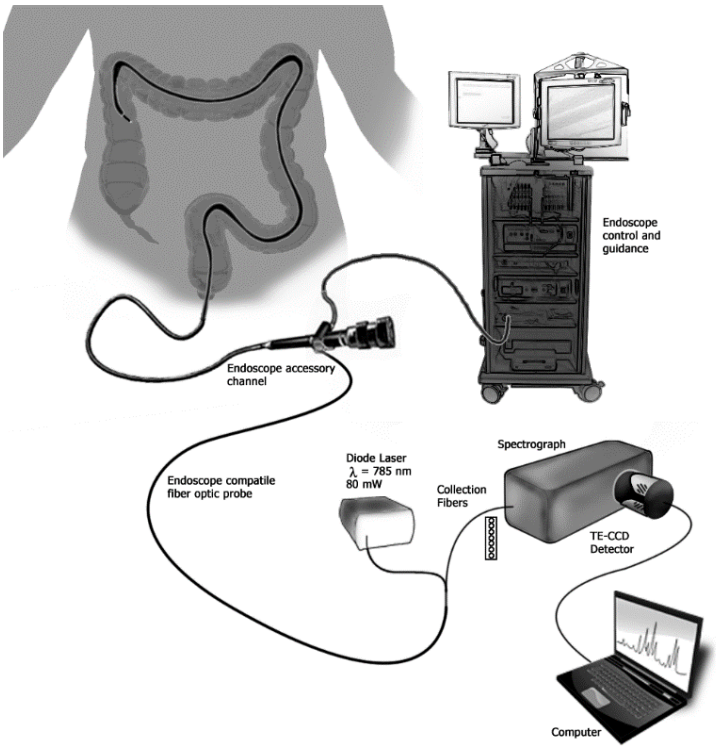

Figure 4.1. Schematic of integrated Raman and endoscope instrumentation for *in vivo* subject measurement. Components are not drawn to scale.

4.3.3 Classification algorithm: sparse multinomial logistic regression

The resulting spectra were classified with a Bayesian machine learning algorithm, sparse multinomial logistic regression (SMLR), to quantitatively determine the potential for Raman spectra to separate healthy and diseased colon tissues. SMLR is a versatile multiclass iterative algorithm that reduces the high dimensionality of Raman data to only those spectral basis features

needed for discrimination.[23, 24] SMLR reduces the dataset by creating a transformation of the original data in which distinguishing spectral basis features were weighted based on their ability to successfully separate classes of training data. The training and classification procedure implemented here used a Laplacian prior, a direct kernel, no bias, z-scored spectral normalization, component–wise updates, and leave-one-subject-out cross validation. A posterior probability of membership in each class was then calculated for each individual spectrum using a classifier trained only with spectra from other subjects. The final sensitivity and specificity for each classification test is reported either in relation to detecting disease (control versus IBD), or for differential discrimination (CD versus UC), to detecting Crohn's disease. Stratified classification based on variable disease presentation is achieved through using the appropriate subset of data prior to model training and cross validation.

4.4 Results

A comparison between mean spectra obtained from subjects within each disease category is depicted in Fig. 4.2. All signatures comprised lipid-rich features, with strong, narrow bands at 1300 cm^{-1}, 1440 cm^{-1}, and 1658 cm^{-1}. These average signals exhibit subtle interclass variations that indicate separation across the Raman fingerprint region (450-1800 cm^{-1}). Multivariate

analysis techniques can be employed for pattern recognition and feature selection to take advantage of the feature rich signals for Raman spectra and IBD.[24-26] Fig. 4.3 depicts the performance of SMLR, where the separation of spectra measured from normal control subjects and from those with IBD is displayed for leave-one-subject-out cross validation along with several of the salient spectral features utilized for discrimination. The SMLR algorithm selects peaks and shoulders that significantly contribute to discrimination and is not limited to only prominent features. Tentative peak assignments for these discriminating features include 425 cm^{-1} (δ (CCC) skeletal backbone), 610 cm^{-1} (ρ(CH) wagging in proteins), 1080 cm^{-1} (ν(C−C) of lipids), 1440 cm^{-1} shoulder (δ(CH2) deformation of proteins and lipids), 1160 cm^{-1} and 1525 cm^{-1} (β-carotene), and 1741 cm^{-1} (ν(C=O) in lipids).[27, 28]

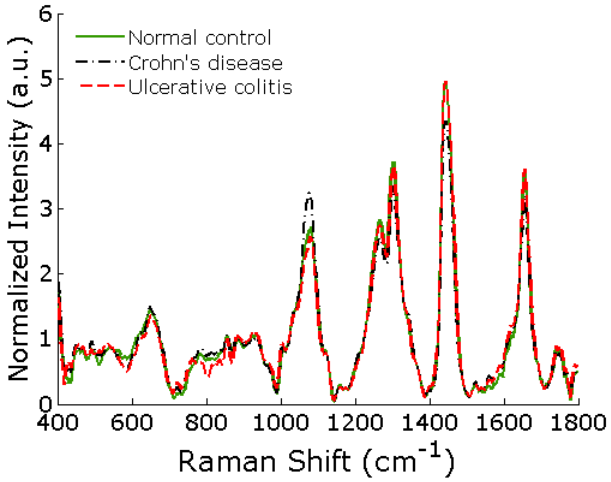

Figure 4.2. Normalized mean in vivo Raman spectra obtained from subjects within each disease class.

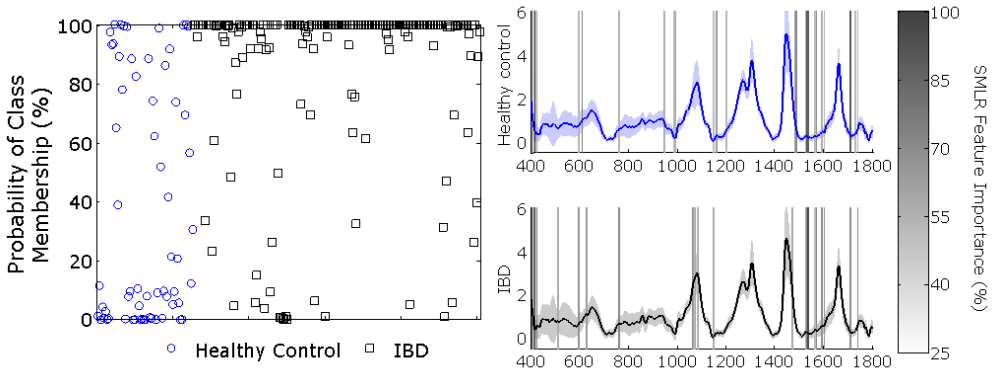

Figure 4.3. (Left) Prediction performance describing the probability of group membership for in vivo spectra obtained from normal control and IBD subjects. (Right) Mean ± standard deviation spectra and 26 features utilized for discrimination are depicted.

This in vivo dataset spans a diverse population of subjects and disease presentations; as such, multiple discrimination comparisons were of interest for this dataset as indicated in the first column of Table 4.2. Independent training and cross validation sets were conducted to gauge unbiased classification performance for each comparison of interest. Table 4.2 comprises the results for several of these analyses including discrimination between disease and control as well as differential discrimination of IBD subtype. In general, test sensitivity was high when discriminating IBD from normal controls, but specificity was poor, achieving 86% and 39%, respectively. When discriminating spectra from control subjects and spectra measured from IBD subjects with active inflammation (determined during WLR endoscopy), specificity increased to 57%. For comparisons of normal control and inactive disease, specificity was lower, indicating that active inflammation is a factor

that requires further attention. In discriminating between IBD subtypes, substantial differences in performance occur when considering subjects with active inflammation (83% sensitivity and 55% specificity) compared with quiescent disease (62% sensitivity and 22% specificity). Subsequent analysis addresses the impact of potential confounding factors through data stratification to evaluate classification performance.

Table 4.2. Classification performance for *in vivo* comparisons.

Comparison	**Sensitivity (%)**	**Specificity (%)**
Control v. IBD	86.2	39.7
Control v. Inactive IBD	81.1	44.4
Control v. Active IBD	78	57.1
Inactive IBD v. Active IBD	67.1	74.5
Inactive CD v. Inactive UC	62	22.9
Active CD v. Active UC	83.3	55.9

As demonstrated by the results comprising Table 4.2, the impact of active inflammation requires investigation and can be readily visualized in Fig. 4.4. In spectra measured from normal and quiescent IBD subjects (all inactive), mean spectral lineshapes exhibit strong and narrow lipid features and vary consistently across the majority of the fingerprint range regardless of disease class. By comparison, the mean spectra from actively inflamed colon segments are broader and less intense, resembling protein-based signatures rather than those of lipids. Furthermore, as visualized in Fig. 4.4 (right), there is a statistically significant decrease in spectral intensity as active inflammation occurs, and a decreasing trend as inflammation progresses in severity. These changes in spectral response due to severity of inflammation indicates a need

to account for this factor in the discrimination algorithm. However, for all of the analyses presented in Table 4.2 disease subtype (CD and UC) and/or levels of inflammation activity (inactive – severe) were combined. Likewise, these comparisons did not address the impact caused by the segment of the colon from which the spectrum was acquired. Fig. 4.5 depicts the mean and standard deviation of spectral variations present when in vivo measurements from normal control subjects are isolated to particular segments of the colon. Several prominent and subtle features differ in intensity between colon segment spectra: potential band assignments include 873 cm^{-1} (ρ(CH2) in proteins), 1160 cm^{-1} (β-carotene), 1265 cm^{-1} (ν(C-N) of Amide III), 1300 cm^{-1} (δ(CH2) deformation of proteins and lipids), 1372 cm^{-1} (lipid), and 1658 cm^{-1} (ν(C=O), Amide I and lipids).[18, 27-29] These differences indicate the potential influence of colon segment on measured spectra and may impact to classification performance.

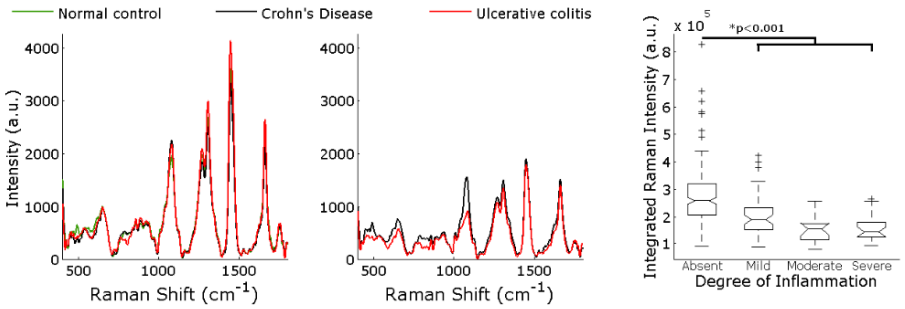

Figure 4.4. Impact of active inflammation: Mean Raman spectra from all disease classes when no activity is present (left) and from IBD subtypes when active disease is present (center). Integrated Raman spectra for all data by level of activity (right) indicates significant differences between disease presentation and the potential for the development of an objective metric to characterize inflammatory disease activity.

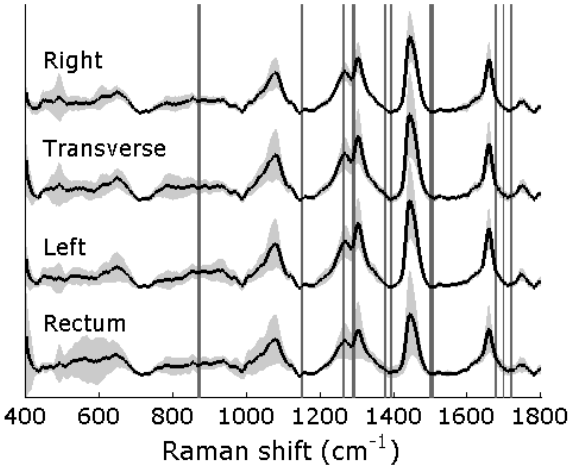

Figure 4.5. Mean spectra from colon segments obtained from normal control subjects. Shaded regions along spectra indicate standard deviations. Variations can be seen across the spectral lineshapes between segment and significant features have been identified as a function of wavenumber (vertical gray bands).

Stratified classifiers were implemented by appropriately selecting spectra from a subset of the recruitment population in order to control for factors of disease location and severity. Based on the spectral changes imparted by both colon segment measured and the presence of active inflammation, these factors were incorporated into stratified classifiers, each resulting in a different number of patients (n, Table 4.3) that were considered for the evaluation. Table 4.3 comprises the results of leave-one-subject-out cross validation for 2-class IBD discrimination. The stratified classifier improves sensitivity and specificity compared with the prior performance for differentiating CD and UC when location and disease presentation are averaged (Table 4.2, Active CD versus Active UC). Once the measurement location and the severity of disease are incorporated, sensitivity to CD increases, for example from 83% to 90% and

specificity from 56% to 75% in the right colon. While the performance varies between colon segments, in general, inclusion of inflammation and location factors caused an increase in a combination of sensitivity and specificity for spectra acquired during colonoscopy. These results support further investigation of influential variables for IBD discrimination, yet demonstrate the potential to improve classification accuracy for these complex, heterogeneous diseases.

Table 4.3. Classification performance for *in vivo* spectra from subjects with active IBD stratified by colon segment.

Colon Segment	**Sensitivity (to CD) %**	**Specificity (to CD) %**
Right (n=9)	90	75
Transverse (n=5)	75	67
Left (n=12)	85	45
Rectum (n=11)	71	56

4.5 Discussion

Here, we report our recently developed endoscopy-coupled Raman spectroscopy technique that enables real-time measurements of tissue biomolecular constituents for in vivo differentiation and characterization of IBD in the colon. Prior work has demonstrated that Raman spectroscopy is sensitive to IBD subtype specific signatures in ex vivo tissue sample evaluations. In this work, we have applied this technique to probe the specific biochemical composition of the colon in real-time to provide an objective characterization of the colon tissue and disease status, discerning more

information which could serve as a valuable adjunct for differential diagnosis of UC and CD and minimize the need for random sample biopsy protocols. While classic clinical parameters associated with a diagnosis of CD (lack of rectal disease, patchy colitis, and the presence of granulomas (found unusually) in histology) may all be indicators of a CD diagnosis, currently there is in general no universal feature that serves as a gold standard for differential diagnosis for IBD. As such, the results of this study were evaluated relative to the established diagnoses for the recruited patients that were made based upon patient history, clinical presentation, therapeutic response, histopathologic findings, and video endoscopy findings. The Vanderbilt Inflammatory Bowel Disease Center is a regional referral center, with extensive expertise following over 1,000 patients annually. For this study, no patients exhibiting IBD unspecified presentation were included in the analysis. These patients with indeterminate colitis are of particular interest as they could most benefit from new tools for disease differentiation.

Our endoscopy compatible Raman spectroscopy system has enabled rapid in vivo biochemically specific measurements from a diverse patient population with representative disease presentations (Table 4.1). The fiber optic probe design utilized herein enabled rapid, high SNR ($\geq$15) contact measurements of the colon constituent biochemistry (Fig. 4.2) and coupled with standard endoscope accessory channel (Fig. 4.1). Prior work has demonstrated that excess pressure can alter spectral signatures, and thus attempts were made

to minimize this factor.[30] Preliminary distinction of the study sample based on disease diagnosis generally indicates high sensitivity and low specificity, with a wide margin of performance depending upon the classification target (Table 4.2). When considering all study subjects together without controlling for disease presentation or subtype, discriminating disease from control has 86% sensitivity but only 39% specificity. This low specificity is further demonstrated in Figure 4.3 (left), where a majority of spectra from IBD patients are correctly classified but few spectra from control subjects were correct. This classification was based on the selection of 26 features from the Raman spectrum, however in a separate classification step using a higher sparsity promoting factor yielded identical performance based on only 13 features. In considering the differential discrimination tests, sensitivity and specificity to Crohn's disease is drastically lower for quiescent (inactive) disease (62% and 22%, respectively; Table 4.2) compared with spectra acquired from patients with active disease (83% sensitivity and 55% specificity). These variations in prediction performance based on different classification targets reinforce the impact of disease variables on the acquired spectra and the need to properly control for disease variables.

The distinction between spectra from control subjects and those with quiescent disease in Table 4.2 (81% sensitivity, 41% specificity) indicates that colitis imparts a detectible change even when no active inflammation is present, a finding supported by changes to the vascular appearance of the tissue noted

during WLR endoscopy.[6] When separating controls from IBD, combining spectra from subjects with and without active disease causes significant blurring of spectral distinct lineshapes (Fig. 4.4) and confounds the classifier. This result prompted further investigation of the influential sources of variance within the dataset that, if accounted for, may allow improved performance. Active disease in the colon presents in a gradient of severity that has been discretized by the endoscopists in this study. However, when considering signals measured from subjects without active disease (including the normal control population), spectra are significantly stronger and exhibit intense lipid features (Fig. 4.4). However, when considering only spectra from active locations from IBD subjects, regardless of disease, the spectra are much weaker, and exhibit peak broadening consistent with increased protein content, potentially from fibrin and collagen and consistent with ulceration and edema.[14, 17] While these features themselves do not provide discrimination between CD and UC, there remains the potential that an objective metric for disease activity could be developed; such a metric could be used to evaluate therapeutic response after initiation of medication, for which a relative measure of active inflammation over time could be critical.

The differences in tissue for both disease presentation and healthy colon, which is functionally and biologically varied, require a thorough evaluation of inter-anatomical sites in order to characterize the impact on performance for disease separation. Based on the low sensitivity displayed for

several tests in Table 4.2, including differential discrimination of active CD and UC, we hypothesized that other factors were confounding disease prediction. This in vivo study represents a pilot evaluation of some of these native factors that cannot be investigated with ex vivo tissue sections and indicates the potential for in vivo characterization and discrimination. Studies by other groups investigating ex vivo discrimination of IBD or the influence of colon segment and disease activity have produced outcomes that support our findings and may lead to an improved understanding of the factors that belie the detected spectral differences.[17, 25, 26] While the report of spectral differences between anatomical sites (Fig. 4.5) is corroborated by other investigations in the stomach and colon[31, 32], the exact cause of the spectral changes is thus far uncertain. Potential differences include bowel thickness and mucosal morphology, vascular density, proximity to mesentery, gland content and microbe distribution, among others.[33-35] The complexity of these in vivo measurements, impacted by both biomolecular and morphological changes in the tissue, require further characterization that is beyond the scope of this study. However, classification performance improved when colon segment was integrated into the algorithm, further supporting the need of improved characterization.

Disease severity and colon segment are only a few of the potential influences on the performance for IBD evaluation and discrimination based on in vivo Raman spectra. Other factors not yet considered based on subject recruitment for this pilot study include gender, age, BMI, diet, and prior

therapeutic treatments, among others. While such factors likely impact classification, incorporation of both colon segment and disease severity factors into the IBD discrimination algorithm achieved increases to 90% sensitivity and 75% specificity to IBD subtype in the right colon (Table 4.3). The variation in prediction performance appears to be linked to the relative distribution of IBD subtypes for patients included in the classification but with expanded recruitment, these values will approach the true prediction rate. These results demonstrate that by properly assessing disease related variables and including them in the analysis, prediction performance can be improved for *in vivo* Raman spectroscopy applications. This also implies the need for a priori knowledge for inclusion in distinct classifiers; however, colon segment and disease activity can be determined during video endoscopy in real-time. Furthermore, the duration of data acquisition, processing, and prediction are short enough that such information could be incorporated into the real-time interface providing immediate feedback to the clinicians during routine evaluations. The results of this work demonstrate the potential for in vivo Raman spectroscopy to impact IBD evaluation and the prospect for staging and discrimination. Continued development of this sensitive technique could also provide new information to better understand and categorize disease for patients with indeterminate colitis diagnoses.

In summary, this study indicates that in vivo Raman spectra for IBD can be acquired non-destructively and in real-time in human subjects from the colon

during routine surveillance endoscopy with high SNR. The resultant spectra have a wealth of information content that can discriminate between IBD and normal colon, as well as indicate the level of disease activity present. Furthermore, preliminary investigation of influential factors for discrimination indicate that disease severity and colon segment measured should be accounted for during evaluation. In combination with standard endoscopic evaluation, Raman spectroscopy has the potential for providing previously unobtainable biochemical information that may be useful as a diagnostic adjunct for IBD.

4.6 Acknowledgements

The authors would like to acknowledge Dr. Quyen Nguyen for invaluable discussion as well as the staff of the Vanderbilt GI Endoscopy lab that helped facilitate patient recruitment and measurement. We would like to acknowledge funding support from American Society for Lasers in Medicine and Surgery student research grant and National Institutes of Health NRSA F31 predoctoral fellowship.

4.7 References

1. A. N. Ananthakrishnan, "Epidemiology and risk factors for IBD," Nature reviews. Gastroenterology & hepatology **12**, 205-217 (2015).
2. R. N. Baldassano and D. A. Piccoli, "Inflammatory bowel disease in pediatric and adolescent patients," Gastroenterology clinics of North America **28**, 445-458 (1999).

3. R. S. Sandler, J. E. Everhart, M. Donowitz, E. Adams, K. Cronin, C. Goodman, E. Gemmen, S. Shah, A. Avdic, and R. Rubin, "The burden of selected digestive diseases in the United States," Gastroenterology **122**, 1500-1511 (2002).

4. C. Gunnarsson, J. Chen, J. A. Rizzo, J. A. Ladapo, and J. H. Lofland, "Direct Health Care Insurer and Out-of-Pocket Expenditures of Inflammatory Bowel Disease: Evidence from a US National Survey," Dig. Dis. Sci. **57**, 3080-3091 (2012).

5. C. D. Stone, "The economic burden of inflammatory bowel disease: clear problem, unclear solution," Dig. Dis. Sci. **57**, 3042-3044 (2012).

6. A. K. Shergill, J. R. Lightdale, D. H. Bruining, R. D. Acosta, V. Chandrasekhara, K. V. Chathadi, G. A. Decker, D. S. Early, J. A. Evans, R. D. Fanelli, D. A. Fisher, L. Fonkalsrud, K. Foley, J. H. Hwang, T. L. Jue, M. A. Khashab, V. R. Muthusamy, S. F. Pasha, J. R. Saltzman, R. Sharaf, B. D. Cash, and J. M. DeWitt; C. American Society for Gastrointestinal Endoscopy Standards of Practice, "The role of endoscopy in inflammatory bowel disease," Gastrointestinal endoscopy **81**, 1101-1121 e1101-1113 (2015).

7. A. Kornbluth, D. B. Sachar, and A. C. Gastroenterology, "Ulcerative Colitis Practice Guidelines in Adults: American College of Gastroenterology, Practice Parameters Committee," The American journal of gastroenterology **105**, 500-500 (2010).

8. G. R. Lichtenstein, S. B. Hanauer, and W. J. Sandborn, "Management of Crohn's disease in adults," The American journal of gastroenterology **104**, 465-483; quiz 464, 484 (2009).

9. D. C. Baumgart, "The diagnosis and treatment of Crohn's disease and ulcerative colitis," Dtsch Arztebl Int **106**, 123-133 (2009).

10. M. L. Corman, *Colon and rectal surgery* (Lippincott, 1989).

11. G. T. Martland and N. A. Shepherd, "Indeterminate colitis: definition, diagnosis, implications and a plea for nosological sanity," Histopathology **50**, 83-96 (2007).

12. D. H. Bruining and E. V. Loftus, Jr., "Technology Insight: new techniques for imaging the gut in patients with IBD," Nature clinical practice. Gastroenterology & hepatology **5**, 154-161 (2008).

13. B. A. Mackalski and C. N. Bernstein, "New diagnostic imaging tools for inflammatory bowel disease," Gut **55**, 733-741 (2006).

14. E. Rodriguez-Diaz, C. Atkinson, L. I. Jepeal, A. Berg, C. S. Huang, S. R. Cerda, M. J. O'Brien, I. J. Bigio, F. A. Farraye, and S. K. Singh, "Elastic scattering spectroscopy as an optical marker of inflammatory bowel disease activity and subtypes," Inflamm Bowel Dis **20**, 1029-1036 (2014).

15. B. Shen, G. Zuccaro, Jr., T. L. Gramlich, N. Gladkova, P. Trolli, M. Kareta, C. P. Delaney, J. T. Connor, B. A. Lashner, C. L. Bevins, F. Feldchtein, F. H. Remzi, M. L. Bambrick, and V. W. Fazio, "In vivo colonoscopic optical coherence tomography for transmural inflammation in inflammatory bowel disease," Clin Gastroenterol Hepatol **2**, 1080-1087 (2004).

16. R. Sinha, "Recent advances in intestinal imaging," Indian Journal of Radiology and Imaging **21**, 170 (2011).

17. J. Addis, N. Mohammed, O. Rotimi, D. Magee, A. Jha, and V. Subramanian, "Raman spectroscopy of endoscopic colonic biopsies from patients with ulcerative colitis to identify mucosal inflammation and healing," Biomedical optics express **7**, 2022-2035 (2016).

18. R. Malini, K. Venkatakrishna, J. Kurien, K. M. Pai, L. Rao, V. B. Kartha, and C. M. Krishna, "Discrimination of normal, inflammatory, premalignant, and malignant oral tissue: a Raman spectroscopy study," Biopolymers 81, 179-193 (2006).

19. I. Pence and A. Mahadevan-Jansen, "Clinical instrumentation and applications of Raman spectroscopy," Chem. Soc. Rev. **45**, 1958-1979 (2016).

20. M. Agenant, M. Grimbergen, R. Draga, E. Marple, R. Bosch, and C. van Swol, "Clinical superficial Raman probe aimed for epithelial tumor detection: Phantom model results," Biomedical optics express 5, 1203-1216 (2014).

21. R. L. McCreery, *Raman spectroscopy for chemical analysis* (New York : John Wiley & Sons, New York, 2000).

22. C. A. Lieber and A. Mahadevan-Jansen, "Automated method for subtraction of fluorescence from biological Raman spectra," Appl. Spectrosc. **57**, 1363-1367 (2003).

23. B. Krishnapuram, L. Carin, M. A. T. Figueiredo, and A. J. Hartemink, "Sparse multinomial logistic regression: Fast algorithms and generalization bounds," Ieee Transactions on Pattern Analysis and Machine Intelligence **27**, 957-968 (2005).

24. I. J. Pence, C. A. Patil, C. A. Lieber, and A. Mahadevan-Jansen, "Discrimination of liver malignancies with 1064 nm dispersive Raman spectroscopy," Biomedical optics express **6**, 2724-2737 (2015).

25. X. Bi, A. Walsh, A. Mahadevan-Jansen, and A. Herline, "Development of spectral markers for the discrimination of ulcerative colitis and Crohn's disease using Raman spectroscopy," Diseases of the colon and rectum **54**, 48-53 (2011).

26. C. Bielecki, T. W. Bocklitz, M. Schmitt, C. Krafft, C. Marquardt, A. Gharbi, T. Knosel, A. Stallmach, and J. Popp, "Classification of inflammatory bowel diseases by means of Raman spectroscopic imaging of epithelium cells," J. Biomed. Opt. **17**, 076030 (2012).

27. B. W. Barry, H. G. M. Edwards, and A. C. Williams, "Fourier-Transform Raman and Infrared Vibrational Study of Human Skin - Assignment of Spectral Bands," J. Raman Spectrosc. **23**, 641-645 (1992).

28. D. C. B. Redd, Z. C. Feng, K. T. Yue, and T. S. Gansler, "Raman-Spectroscopic Characterization of Human Breast Tissues - Implications for Breast-Cancer Diagnosis," Appl. Spectrosc. **47**, 787-791 (1993).

29. R. Manoharan, Y. Wang, and M. S. Feld, "Histochemical analysis of biological tissues using Raman spectroscopy," Spectrochimica Acta Part a-Molecular and Biomolecular Spectroscopy **52**, 215-249 (1996).

30. I. J. Pence, E. Vargis, and A. Mahadevan-Jansen, "Assessing Variability of In Vivo Tissue Raman Spectra," Appl. Spectrosc. **67**, 789-800 (2013).

31. M. S. Bergholt, W. Zheng, K. Lin, K. Y. Ho, M. Teh, K. G. Yeoh, J. B. Y. So, and Z. W. Huang, "Characterizing variability in in vivo Raman spectra of different anatomical locations in the upper gastrointestinal tract toward cancer detection," J. Biomed. Opt. **16**(2011).

32. M. S. Bergholt, W. Zheng, K. Lin, J. F. Wang, H. Z. Xu, J. L. Ren, K. Y. Ho, M. Teh, K. G. Yeoh, and Z. W. Huang, "Characterizing Variability of In Vivo Raman Spectroscopic Properties of Different Anatomical Sites of Normal Colorectal Tissue towards Cancer Diagnosis at Colonoscopy," Anal. Chem. **87**, 960-966 (2015).

33. D. N. Granger, J. A. Barrowman, and P. R. Kvietys, *Clinical Gastrointestinal Physiology* (Saunders, 1985).

34. M. H. Ross and W. Pawlina, *Histology* (Lippincott Williams & Wilkins, 2006).

35. B. Young, *Wheater's functional histology : a text and colour atlas* (Churchill Livingstone/Elsevier, Edinburgh, 2006).

CHAPTER 5

CHARACTERIZING THE INFLUENCE OF DISEASE VARIABLES ON RAMAN SPECTRA ACQUIRED FROM COLECTOMY SAMPLES OF INFLAMMATORY BOWEL DISEASE

5.1 Abstract

Inflammatory bowel disease (IBD), including Crohn's disease and ulcerative colitis, is a complex condition that affects millions of people around the world. These diseases are both caused by autoimmune responses to gut flora but medical management can differ greatly. To aid the provision of optimal treatment, new tools for *in vivo* characterization and discrimination of IBD are under investigation. One such tool is Raman spectroscopy, an optical technique that is sensitive to subtle biochemical constituents in tissues related to disease and physiological processes. Raman techniques have shown great promise for disease detection and differentiation, however several groups have reported that measured spectra are sensitive to variations between patients, anatomy, and disease presentation. To investigate the complex interactions that disease and patient variables impose on Raman spectra in IBD cases, this study utilized resected colon tissues from colon resection (colectomy) patients. Raman

measurements were made in many locations across the excised specimens, and each measurement location was marked, biopsied, and independently processed. Tissue biopsies were assessed by a trained gastrointestinal histopathologist for evaluation of disease metrics related to anatomical changes, chronic disease, and acute inflammation. Multivariate statistical models based on generalized estimating equations and generalized linear models of Raman peak ratios and histolopathological markers were implemented to decouple the influence of individual disease metrics and colon segment. Patient BMI was a significant predictor for Raman peak ratio response while age had no effect. The IBD diagnosis was highly correlated with multiple peak ratios and indicate large interclass differences between ulcerative colitis and Crohn's disease tissues. Raman peak ratios were significantly associated by chronic changes to the colon tissue architecture and acute inflammation severity, along with differences between anatomical segments of the bowel. Finally, Raman peak ratios were modeled by the presence of submucosal fat deposition, a reported physiologic occurrence with potential associations to IBD, in combination with disease severity. The results reported here agree with prior work indicating the influence of both anatomic location and disease severity, and identify patient and disease specific factors that should be included in algorithms for improved IBD discrimination.

5.2 Introduction

Inflammatory bowel disease (IBD) is a complex autoimmune condition that affects more than one million Americans and more than two million Europeans, with incidences increasing around the world. IBD is characterized by disease flares separated by periods of remission and significant patient morbidity.[1] Both ulcerative colitis (UC) and Crohn's disease (CD) are forms of IBD with overlapping symptoms and often have large variations in patient presentation. These complex diseases arise due to dysregulated immune responses to commensal bacteria in a genetically susceptible host.[1] As autoimmune diseases with differing treatments and gaps in understanding pertaining to etiology, new tools are needed to help quantify disease presentation and provide objective diagnosis. One such tool that has seen increased interest in the past two decades is Raman spectroscopy, an optical technique that can be applied *in vivo* and is sensitive to the vibrational bonds in a sample or tissue. While prior work has demonstrated that Raman spectroscopy has the potential to discriminate IBD type and stage disease severity based on differences detected in the biochemical profiles of disease, there is a wide range of sensitivity and specificity values.[2,3] Bi *et al.* was the first to report discrimination of IBD tissues based on *ex vivo* Raman spectra with 100% sensitivity and specificity, however the sample set for this pilot evaluation was relatively small.[2] Subsequently, Bielecki *et al.* performed high resolution Raman microspectroscopic mapping of IBD tissues.3 This work found that after

isolating signals detected from the epithelial cell layers, a statistical algorithm was able to separate measurements from CD, UC, and healthy controls with over 98% classification accuracy. Our research group has used a portable probe-based Raman spectroscopy system with colonoscopy to evaluate the performance of these techniques *in vivo* for the first time.[4,5] The sensitivity and specificity rates of this work have ranged between 62-90% and 22-75% respectively, depending upon which patient and measurement variables were accounted for during analysis. Based on the previous reports of the sensitivity of Raman spectroscopy to both normal patient variations and disease processes, there is a demonstrated need for a thorough assessment of which of these factors significantly impact Raman spectra acquired from colon tissues.

Developers of Raman spectroscopy techniques must overcome variations in classification rates for disease detection for this technology to benefit clinical medicine.[6] Significant sources of variation, attributable only to the inherent variability in healthy physiology, establish a minimum threshold for any detection technique: if the differences between disease classes (or other discrimination targets) are smaller than those found within natural, healthy variation, there is little chance for successful separation of target classes. Such variations have been reported for colon tissue measurements, as noted above. Fortunately, several groups are advancing Raman spectroscopy for colonoscopy applications and have shown that by accounting for patient variations, sensitivity and specificity for Raman discrimination increase.

Similar work on innate patient variability has been demonstrated in the breast[7], upper gastrointestinal (GI) tract[8], cervix[9], and skin[10]. In most cases, accounting for the variations in tissue has resulted in increased sensitivity and specificity rates for classifying disease spectra relative to healthy controls.

In each of the previous reports of using Raman spectroscopy in the colon, significant variability has been noted throughout the organ.[11] Similar to the other organs of the GI system, the anatomy of the colon and rectum vary along the length of the tissue. The distributions of cellular content and composition of the bowel wall, as well as the anatomical connections each differ between the separate right, transverse, and left colon segments and the rectum.[12,13] Several major factors have been implicated as impacting *in vivo* discrimination performance of Raman spectra for IBD including bowel segment and severity of disease presentation. The proximal colon is primarily responsible for absorbing water and electrolytes as well as promoting fermentation of undigested sugars in the chime, while the distal colon is responsible for storing and evacuating stool. These functional differences correlate with distributions of epithelial cells that vary according to anatomical location within the colon and rectum; it is likely that these cellular differences also impart molecular changes along the colon that are detected by Raman spectroscopy.[12,13] The influence of these and other factors on measured Raman spectra remains to be fully understood. The need exists to characterize the both extent of variability in Raman spectra acquired from different locations of

colorectum and the interaction of disease severity and inter-anatomical variation. Bergholt *et al.* has investigated the impact of these different anatomical locations with respect to changes associated with colorectal cancers and noted that inter-anatomical variability was a non-significant factor for discrimination between healthy and cancerous tissues.[11] Similar findings have also been reported for *in vivo* Raman spectra for skin cancer discrimination.[14] However, it is possible that the biochemical differences relied upon to discriminate between normal and dysplasia are more pronounced than those present between two related inflammatory processes. In fact, most Raman spectroscopy studies that have included inflammation classes in the analyses do so as a transition grouping between normal and low grade dysplasia.[15,16] Hence, this study aims to characterize the variability in Raman spectra acquired from different anatomical locations and disease presentations for excised colorectal tissue associated with IBD.

In this work we seek to characterize the influence and interactions of variable anatomy and heterogeneity of disease presentation on Raman spectra acquired from *ex vivo* human colon tissues. By comparing Raman spectra acquired from numerous anatomical locations along the colon and rectum with histopathological evaluation of the measurements, and also with global patient variables that may correlate with underlying patient markers for disease, we will determine which variables need to be accounted for due to their imposed influence on optical measurements. To this end, we have applied clinical Raman

spectroscopy and multivariate statistical analysis to measurements of various healthy and diseased colorectal specimens (i.e., ascending colon, transverse colon, descending colon, sigmoid, and rectum) following colectomy. The goal of this work is to characterize the impact of disease variation on Raman spectra obtained from human colon tissues.

5.3 Materials and methods

5.3.1 Patient recruitment

Colorectal specimens for this study were collected from patients following standard partial or total (procto-) colectomy procedures (surgical removal of the colon). Potential study subjects were identified based on diagnosis (UC, CD, or diverticulosis) and planned procedure at Vanderbilt University Medical Center (VUMC). Patients with expected dysplasia were excluded to mitigate potential confounding factors. Following written informed consent (IRB #150157) specimens were excised and immediately transported to a surgical pathology suite according to standard clinical practice for optical measurements. The specimen was opened lengthwise to expose the entire lumen of the colorectum. Excess blood and debris was rinsed with saline and blotted prior to measurement. All measurements were acquired within two hours of resection and prior to formalin fixation in an interior pathology room with no lights. Patient specific variables including gender, age, body mass index

(BMI, kg/m^2), relevant diagnosis, and the procedure performed where recorded for subsequent analysis (Table 5.1). For this analysis, diverticulosis colon tissues were utilized as non-IBD controls.

Table 5.1. Study subject description.

Case ID	Gender	Age	BMI	Diagnosis	Procedure*
1	F	66	23.3	Ulcerative colitis	Proctocolectomy (R,T,L,M)
2	M	78	19.7	Diverticulosis	Partial colectomy (L)
3	F	46	27.4	Ulcerative colitis	Proctocolectomy (R,T,L,M)
4	F	46	25.0	Ulcerative colitis	Proctocolectomy (R,T,L,M)
5	M	54	24.6	Crohn's disease	Total colectomy (R,T,L)
6	M	36	22.8	Crohn's disease	Partial colectomy (R,T)
7	M	44	21.7	Diverticulosis	Partial colectomy (L)
8	F	29	20.5	Crohn's disease	Partial colectomy (R)
9	M	54	16.2	Crohn's disease	Partial colectomy (R)

* Indicates segments resected/measured: R – right colon, T – transverse colon, L – left colon, M – rectum.

5.3.2 Raman instrumentation and measurement

The spectroscopic system utilized for this study as depicted in Figure 5.1, is identical to that used for the previously reported *in vivo* IBD study.[4,5] Briefly, the excitation leg of the Raman system consisted of a 785 nm diode laser (Innovative Photonics Solutions, Monmouth Junction, NJ), a 7-around-1 superficially focused micro lens fiber optic probe with tip filtering (EmVision LLC, Loxahatchee, FL) to deliver 80 mW of power at the sample. Light collected by the probe was delivered to a holographic imaging spectrograph (Holospec f/1.8i, Kaiser Optical Systems, Inc. Ann Arbor, MI) and detected by a thermoelectrically cooled, deep-depletion charge couple device (Pixis 256BR, Princeton Instruments Acton, MA). With the probe touching the mucosal surface in gentle contact, 5 spectra were acquired from each tissue location with

250 ms acquisition times and 3 summed accumulations. The measured sites were immediately marked with medical marking dye (Davison marking system, Bradley Products, Inc. Bloomington, MN) for histopathology and subsequent comparison with the measured spectra. Each site was initially categorized for disease presence by the surgeon using visual inspection. After pathology sections were collected from the specimen according to standard of care, separate sections were collected from measured locations. All marked sites on the specimen were separately processed and read by a fellowship trained gastrointestinal (GI) histopathologist at VUMC for several markers of acute and chronic disease as well as physiological differences (Table 5.2). The histopathological identities of these sites formed the gold standard for spectral analyses. Other patient specific variables including age, gender, and BMI were recorded for correlation with the spectral data. Between patients, the probe was detached from the system for cleaning, soaked in ortho-Phthalaldehyde (Cidex OPA, Johnson & Johnson, Arlington, TX) and rinsed thoroughly with water, following protocols for high-level disinfection.

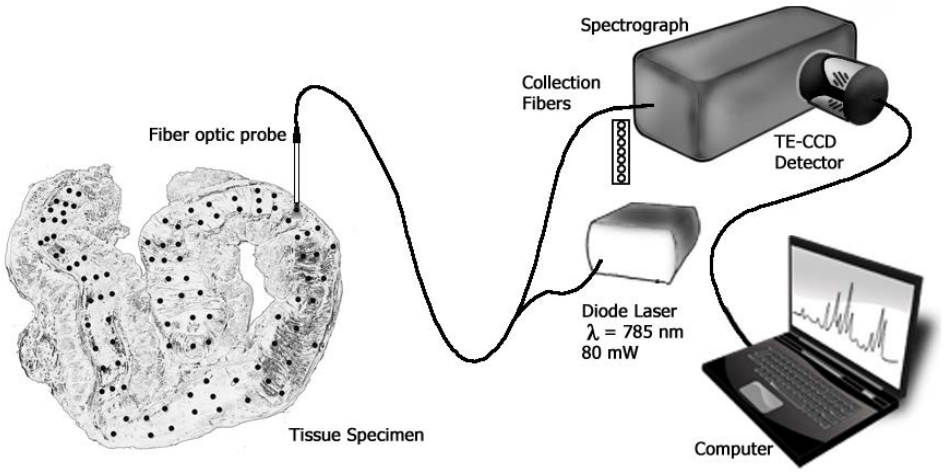

Figure 5.1. Schematic of Raman spectroscopy system and colon specimen for experimental setup. Black dots on colon indicate locations of Raman measurement.

Table 5.2. Histopathology scoring metrics for colectomy specimen sections.

Acute Inflammation	
Severity	Absent (0) – Severe (3)
Extent of coverage	Minimal (0), Patchy (1), or Diffuse (2)
Depth	Absent (0), Mucosal (0), Submucosal (2), Transmural (3)
Basal plasmacytosis	Absent (0) or Present (1)
Surface ulceration	Absent (0), $25\% \leq x < 50\%$ (1), $x \geq 50\%$ (2)
Chronic disease	
Architectural distortion	Absent (0) – Severe (3)
Extent of distortion	Minimal (0), Patchy (1), or Diffuse (2)
Lymphoid hyperplasia	Absent (0) – Severe (3)
Gross changes	
Submucosal fat deposition	Absent (0) – Severe (3)
Submucosal vascular prominence	Absent (0) or Present (1)
Bowel layer thickness	
mucosa	Percentage of section thickness
submucosa	Percentage of section thickness
muscularis mucosa	Percentage of section thickness

5.3.3 Multivariate statistical analysis

Raman spectra were analyzed using ordinary least squares regression based on generalized linear models (GLM) in the statistical software R, using the rms package. The rate of change of various Raman peak ratios was modeled

as the dependent variable and regression coefficients were calculated for independent variables such as patient descriptors and histopathological scoring metrics (listed in Table 5.1 and Table 5.2, respectively). To make comparisons as these independent variables changed with disease presentation, generalized estimating equations (GEE) were employed (as previously described) to enable clustering of measurements obtained from a single specimen.[17,18] The generated regression curves for different segments (right, transverse, left, rectum) and disease variables were compared. Raman peak ratios were used as a way to normalize comparisons across many data sets that have varying levels of signal intensity and signal to noise ratios. Specifically for this analysis, the Raman peak ratio of interest was the dependent variable and the disease severity (continuous), colon segment measured (categorical), or other patient descriptors were included as independent variables. Peak ratios of interest were identified based on Pearson's correlation ($r \geq 0.7$) with histopathological scoring values evaluated for the corresponding tissue section (Table 5.2). Due to the highly variable signal strength that can be detected during Raman spectral measurements of biological tissue, the spectral intensity (measured as the intensity of the 1440 cm^{-1} peak) was utilized as another dependent variable (continuous) in every model to control for these intensity fluctuations. Heteroscedasticity in the dataset was addressed by using the robust covariance function created in the rms package ('robcov') to adjust the standard errors. Finally, to look at interactions between specific disease and anatomic variables,

an ANOVA was performed on the generated GLM regression curves from the developed regression model.

5.4 Results

Mean Raman spectra from each colon segment without acute inflammation are presented in Figure 5.2 and represent averages of colon segments measured across the nine tissue specimens. The spectra depict several regions that differ between segments despite the similarities in overall line shape. Of particular interest are the changes seen in the protein and lipid features (indicated by gray bands at 1006, 1265, 1300, and 1658 cm^{-1}) between segments. The visually apparent differences between these few spectral features indicate the significant changes imparted by the colon segment measured, especially in the tissue that is free of disease. Prior studies have demonstrated that disease presentation and colon segment should be decoupled. A thorough evaluation of several patient and disease variables are investigated herein to address this need.

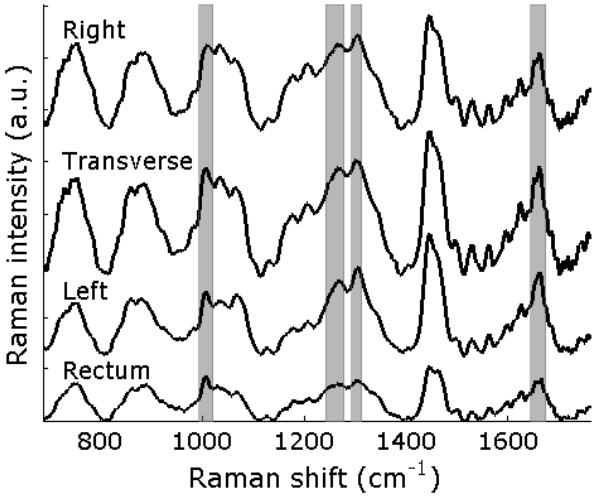

Figure 5.2. Mean spectra from colon segments without histopathological markers of acute inflammation. Spectral line shapes agree with previously reported differences between colon segments. Gray bands indicate protein and lipid spectral features that dramatically vary between segments.

5.4.1 Patient variables

An initial comparison of spectral features in relation to patient specific variables was conducted for patient age and BMI. Overall, the GEE models for patient age had low robustness ($R^2 = 0.15$) and therefore no relationships were considered. Alternatively, patient BMI strongly correlated with several peak ratios that are assigned to collagen and tryptophan (1209 to 1559 cm^{-1}, r = -0.71; 1335 to 1559 cm^{-1}, r = -0.73). Figure 5.3 depicts a representative GEE regression curve where the peak ratio (1335 to 1559 cm^{-1}) is modeled versus BMI as a continuous variable, as an example of the consistent trends demonstrated by both ratios. These ratios were robust models across the dataset (Table 5.3), however because each patient has only one BMI value for all spectral measurements, it is not appropriate to investigate interactions for either

colon segment or disease presentation. A larger data set may enable further clarification regarding the impact of these patient specific variables on the variability of detected Raman spectra.

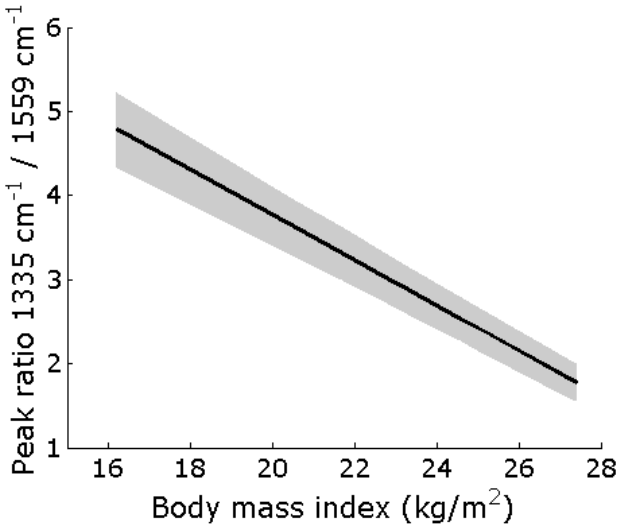

Figure 5.3. GEE for peak ratio of 1335 cm^{-1} to 1559 cm^{-1} versus patient BMI demonstrate high correlations and robust model performance across the entire data set.

Table 5.3. Multivariate statistical model results for associations between Raman spectral data and histological scores of colectomy specimens.

Comparison	Peak Ratio	Coefficient p-values	Model R^2	Tentative band assignments
Patient and tissue variables				
Age	All ratios	Age: $p > 0.05$	NS	
Body Mass Index (BMI)	1209 to 1559 cm^{-1}	BMI: $p < 0.0001$	0.58	Collagen[19] to Tryptophan[19]
	1335 to 1559 cm^{-1}	BMI: $p < 0.0001$	0.55	
Disease Diagnosis	754 to 1209 cm^{-1}	Disease type: $p < 0.0001$	0.85	Lipid[20] to Collagen[19]
	1125 to 1160 cm^{-1}	Disease type: $p < 0.0001$	0.75	Lipid[20] to Carotenoid[21]
Thickness ratio (mucosa/submucosa)	All ratios	Thickness ratio: $p > 0.05$	NS	
Chronic disease				
Chronic disease and colon segment	1006 to 1209 cm^{-1}	Architectural distortion: $p < 0.0001$ Segment: $p < 0.0001$	0.55	Phenylalanine[19] to Collagen[19]
Lymphoid hyperplasia	All ratios	Lymphoid hyperplasia: $p > 0.05$	NS	
Acute disease				
Active disease and colon segment	1265 to 1304 cm^{-1}	Inflammation: $p < 0.0001$ Segment: $p < 0.0001$	0.56	Protein[19] to Lipid[20]
	859 to 1524 cm^{-1}	Inflammation: $p > 0.05$ Segment: $p < 0.0001$	0.53	Collagen[19] to Carotenoid[21]
	1335 to 1332 cm^{-1}	Inflammation: $p < 0.0001$ Segment: $p < 0.0001$	0.49	Collagen content [19]
Submucosal fat and active inflammation	1265 to 1304 cm^{-1}	Inflammation: $p < 0.0001$ Fat deposition: $p > 0.05$	0.55	Protein[19] to Lipid[20]

5.4.2 IBD type differentiation

Analyses comparing peak ratios modeling inflammatory bowel disease type (CD, UC, or non-IBD/normal) are presented in Table 5.3 and Figure 5.4. The first ratio (754 to 1209 cm^{-1}) represents lipid to collagen content while the second represents lipids to carotenoids (1125 to 1160 cm^{-1}). Both ratios are robust predictors across patients/specimens ($R^2 \geq 0.75$) and have significant coefficients for disease diagnosis ($p < 0.0001$). For both of these ratios, the difference between ulcerative colitis and the other diagnoses exhibits a large separation, while Crohn's disease and non-IBD/normal colon are not

significantly different. A histologic feature related to disease type is the relative thickness of mucosa to submucosa. As scored by the GI histopathologist, relative mucosal thickness did not strongly correlate with any other markers of disease, including diagnosis. In agreement with the global correlations for histological metrics, all of the peak ratios modeled by GEEs had non-significant coefficient values for the ratio of thickness for mucosa to submucosa ($p > 0.05$). Based on this dataset, the relative thickness of the bowel wall layers did not significantly alter the Raman spectra obtained from the colon. These trends represent the average signals for disease types while combining all levels of either acute or chronic disease severity. It is likely that these factors could significantly alter the ratios obtained from CD or UC specimens, however, further patient recruitment/specimen collection is warranted prior to drawing conclusions.

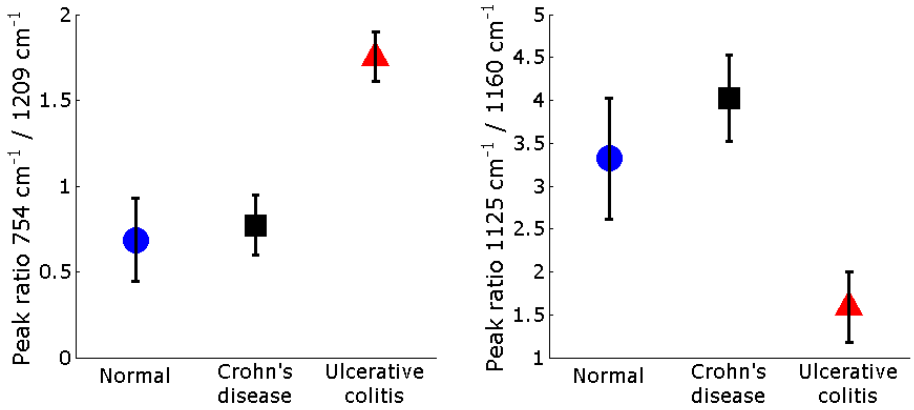

Figure 5.4. Results for GEE models of peak ratio versus patient disease diagnosis (mean & 95% confidence interval).

5.4.3 Chronic disease

Having isolated Raman peak ratios that correlated with patient variables and inflammatory bowel disease type, GEE models were developed for markers of chronic inflammation and colon segment. Some of the markers for the presence of chronic disease (severity of architectural distortion and extent of distortion, Table 5.2) were highly correlated in histopathological evaluation ($r = 0.79$), but lymphoid hyperplasia was not strongly correlated with any other inflammatory metrics. As listed in Table 5.3, a similar result was obtained for correlations between lymphoid hyperplasia and Raman peak ratios. As before with patient age and mucosal thickness ratio, all models of lymphoid hyperplasia demonstrated low scores for robustness and non-significant coefficients. On the other hand, one GEE model of chronic disease severity and colon segment displayed significant differences for both coefficients ($p < 0.0001$). The Raman features that contribute to this ratio are tentatively assigned to phenylalanine and collagen. However, regression curves for individual segments displayed different slopes as severity increased, limiting the utility of this feature. Despite the differences in regression curves between segments, mean values from segments without chronic disease were significantly lower than those with markers of severe chronic disease ($p < 0.05$).

5.4.4 Acute inflammation

The complex presentation of active disease and colon segment have been confounding factors in previous investigations of Raman spectroscopy for IBD. To evaluate the impact of colon segment and acute severity, GEE models were implemented that allow for modeling the peak ratios of interest with each dependent variable. For the GEE models, acute severity score (Table 5.2) was utilized to evaluate acute disease. This was determined after all markers for acute inflammation were verified as highly correlated ($r \geq 0.73$). Results for the three most robust GEE models are reported in Table 5.3. As depicted in Figure 5.5, the 1265 to 1304 cm^{-1} ratio reveals monotonic decreases in protein to fat across all colon segments as acute disease severity increases. The curves for mean peak ratio values and 95% confidence intervals indicate that for this ratio, there are no differences between segments at a fixed level of active disease. However, the mean value for each segment in the absence of active disease is significantly higher than the mean value for each segment in the presence of severe activity, supporting the interplay between disease severity and colon segment in this pilot data set. All colon segments demonstrate a similar monotonic increase in collagen to carotenoid with increasing acute severity (859 to 1524 cm^{-1}, Table 5.3). However, for the latter ratio, there is not a significant difference between the mean values of different colon segments with inflammation.

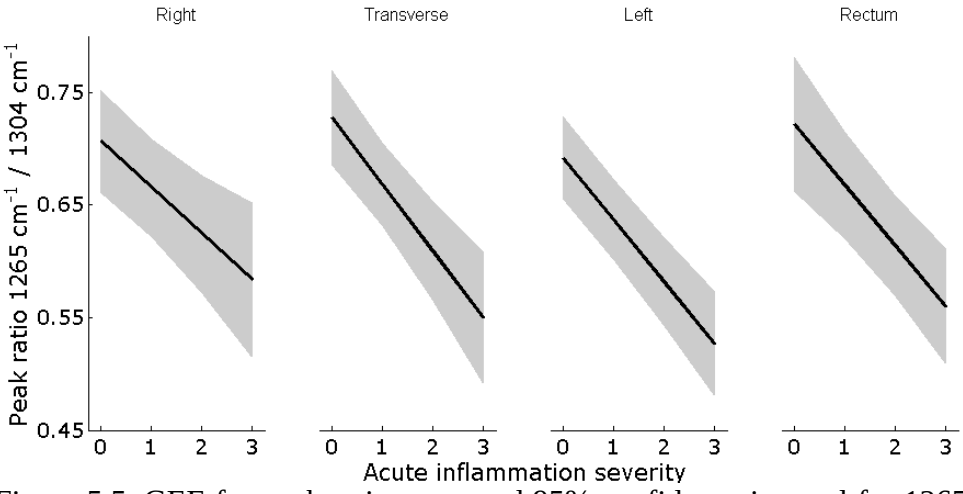

Figure 5.5. GEE for peak ratio mean and 95% confidence interval for 1265 to 1304 cm^{-1} modeled by severity of acute inflammation and colon segment.

The GEE regression curves in Figure 5.6 reveal that in the proximal colon (right and transverse segments), the collagen content (1335 to 1332 cm^{-1}) increases with severity while in the distal colon (left and rectum) this same ratio decreases. In the absences of acute disease (severity 0), these curves show that the mean values for collagen content in the proximal colon segments are not significantly different from one another. However, at moderate and severe acute disease levels (severity 2-3), the mean ratio for the right colon is significantly lower than that of the transverse colon ($p < 0.05$). The GEE regression curves for the distal colon (left colon and rectum) show that if the severity of acute disease is held constant, there are no significant differences between the collagen content. This ratio is significantly different for inactive disease in both of these segments compared with severe disease ($p < 0.05$). Furthermore, the transitions in collagen content are more pronounced in the

rectum than the left colon as acute disease severity increases. Table 5.3 also shows that the GEE model results for the global comparisons of acute inflammation and colon segment for each of these ratios have significant coefficients ($p < 0.0001$) for colon segment (all three models) or acute inflammation severity (protein to lipid ration and collagen content). These significant p-values indicate that there are differences detected in the Raman spectra between colon segments and disease states. As both of these factors are significant, it follows that an algorithm based on Raman spectra must account for the influence of colon segment as you measure IBD severity.

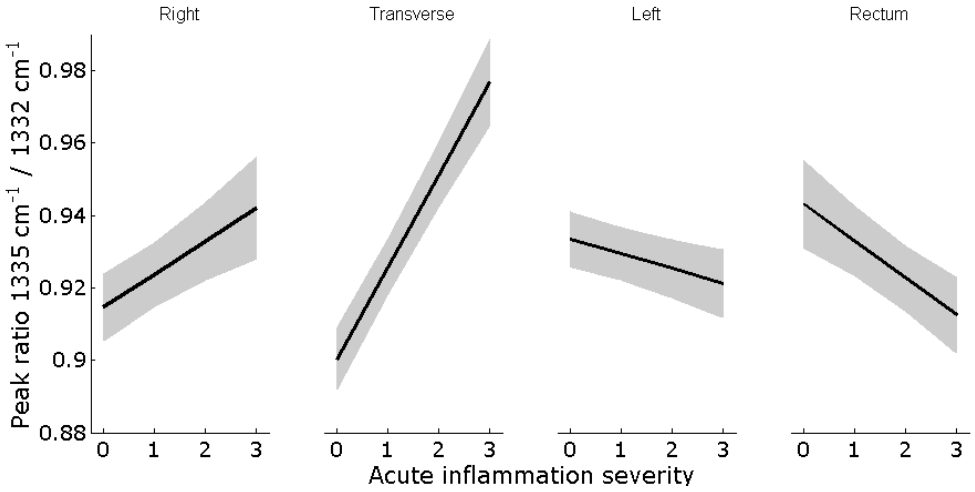

Figure 5.6. GEE for peak ratio mean and 95% confidence interval for 1335 to 1332 cm^{-1} modeled by severity of acute inflammation and colon segment.

5.4.5 Submucosal fat deposition

When modeling peak ratios as a function of acute disease and submucosal fat deposition, the most robust ratio ($R^2 = 0.55$), representing protein to lipid content, slightly decreases with increasing fat deposition (Table

5.3). Interestingly, this ratio indicates a significant coefficient value for acute disease severity ($p < 0.0001$) but a non-significant coefficient for submucosal fat. As these factors may not be truly independent, it is interesting to note that the peak ratio for moderate or severe submucosal fat deposition (2-3) is significantly lower than the ratio for samples absent of this fat deposition, regardless of inflammation severity. The GEE model of this spectral feature supports the relationship between IBD severity and submucosal fat deposition as detected by Raman spectroscopy.

5.5 Discussion

Raman spectroscopy is an optical technique that is sensitive to subtle biochemical changes associated with disease processes and physiological variation. However, as a sensitive technique, Raman spectroscopy can also be influenced by patient variables not associated with disease processes. The healthy human colon is a large organ with diverse and complex functions that differ along the extent of the tissue. As depicted in Figure 5.2, segmental variations exist in the complex Raman spectra measured from healthy colon. The variation in organization of this tissue enables the unique functions performed by different parts of the organ. However, these variations also complicate detection based on light-tissue interactions. The movement of fecal matter through this organ is accomplished by unique formations of musculature

across the length of the colon. In the rectum, motility is enabled by the continuous sheet of muscle that lines the outside of the tissue as compared to the tenia coli which are three equidistantly spaced longitudinal muscles that run the length of the colon.[22] This increased muscularity of the rectum may account for the increase in protein signatures (1247-1265 cm^{-1} Amide III, 1006 cm^{-1} phenylalanine, 1658 cm^{-1} Amide I) and decreased lipid peaks in the rectum compared with the colon (Figure 5.2). Another difference between colon segments is the connection to peritoneum in the abdominal cavity. Both the ascending (right) and descending (left) colon are retroperitoneal, and not directly connected to the sheet of adipose tissue that stabilizes the colon in the abdomen. Conversely, the transverse and sigmoid (left) colon segments are suspended by the fat-rich mesocolons. The low absorption of near infrared light coupled with the high scattering coefficients and the forward dominated scattering of tissues allow for 785 nm light to travel deep within biological tissues (>5 mm) to generate detectable Raman scattering signals. The increased lipid signals in the left colon (Figure 5.2, 1265 cm^{-1} and 1300 cm^{-1}) may be caused in part by the excess mesocolon attached to the outside of this tissue after resection relative to other colon segments. Similar to the added mesocolon, the distal colon has larger and more prevalent appendices epiploicae (fat protrusions on the serosa) that may contribute to the added adipose signatures detected in these colon segments.[22] These natural variations in the anatomy of

the healthy colon support the need for careful consideration of latent effects that confound *ex vivo* and *in vivo* Raman spectral measurements.

While diverticulosis specimens were included in this study as non-inflammatory controls, a more appropriate analysis of healthy colon might be obtained from cadaver tissues with no indications of GI pathology. For this work, these diverticulosis patient specimens were confirmed through histopathologic evaluation to lack all markers of inflammatory processes and were thus utilized as controls.

5.5.1 Patient variables

Numerous patient variables associated with the specimens could impart significant influences on the measured Raman spectra. Due to the limited size of this pilot investigation, and the disease conditions indicating surgical resection of the colon, many of these factors are not addressed in this analysis. Specifically, no effort was made to control of duration of patient disease nor prior therapeutic/surgical interventions. Both of these features, as well as other variables not related to IBD such as patient age, gender, or BMI could have significant impacts on the measured Raman spectra.[9] The interpretation of such variables is therefore limited. Age related effects did not exhibit robust correlations across the recruited patients. However, the peak ratios that significantly correlated with patient BMI indicated that with increased BMI there may be more reserves of tryptophan in the tissue that can act as part of a

small labile reserve of protein. Alternatively, this signal ratio could be related to the remodeling of the colon tissue as a result of disease, and requires both a larger data set and greater investigation to elucidate the relationship.

5.5.2 IBD type differentiation

One of the goals for utilizing Raman spectroscopy *in vivo* for IBD is to help enable discrimination of the disease type. Preliminary work has demonstrated the potential for this discrimination through Raman fiber optic probe and microspectroscopic investigations. Accurate distinction for these diseases is essential for optimal medical management. Treatment options, especially surgical interventions, are dramatically different between these diseases, and the difference in disease response indicates the need for improved evaluation and discrimination of IBD types. To this end, GEE models were implemented for peak ratios that were strongly correlated with disease diagnosis in this colectomy specimen dataset. The regression models depicted in Figure 5.4 reveal that disease specific trends support discrimination of IBD type based on differences in the Raman spectroscopic signals from excised tissues. The ratio of lipid to collagen content (Figure 5.4A) shows no difference between CD and control specimens but a significant increase ($p < 0.05$) for UC specimens. This is likely a combination of the decreased collagen content associated with superficial UC disease. Similarly, for the ratio of lipids to carotenoids (Figure 5.4B), no significant differences were found between

control and CD specimens, however there was a significant decrease for UC specimens ($p < 0.05$). This may be attributed to the increased oxidative stress seen in the UC specimens that would reduce the prevalence of reactive oxygen species scavenging carotenoids in the tissue.[23,24] One confounding factor in this analysis is the impact of disease severity on Raman spectra and the distribution of severity in each colon segment as a function of disease type. This analysis is not adequately powered to consider the impact of activity in combination with IBD type and thus other latent factors may be impacting the separation (as seen for other comparisons in Table 5.3). Despite this limitation, the differences in peak ratios here further support the potential for disease discrimination based on Raman spectroscopy.

The impact of IBD on the colon wall differs between disease types. CD is generally a deep disease with inflammation extending into the submucosa and muscularis layers of the bowel wall, often resulting in thickening of the colon with fibrotic changes, fissuring ulcers, and transmural inflammation. Conversely, UC is generally a superficial disease that is characterized by erosion and sloughing of the epithelium and mucosal ulceration with severe disease.[22] Bowel layer thicknesses were expected to significantly differ between disease severity and IBD type based on the differential presentation of these diseases (superficial versus deep effects). However, none of the model relationships pertaining to bowel wall thickness were robust or significantly correlated with spectral features for this histological score (Table 5.3). A

challenge for the scoring of this metric during histopathological review is the effect of tissue orientation in the cassette, which can create artefactual differences in the relative thickness of these layers on a per sample basis. In many tissue sections, layers were absent from a section or the thickness of a particular layer was highly variable across the extent of the section. Furthermore, due to handling of the specimens, it is not possible to say that every sample represented a full-thickness section of the colon tissue. However, it is possible that with more control and an objective metric, this ratio could provide information about the Raman spectral differences observed.

5.5.3 Chronic disease

Analysis of markers of chronic disease and colon segment revealed a general increase in the ratio of phenylalanine to collagen as severity of chronic disease increased (Table 5.3). Amino acid content (peak ratio numerator) is considered to be a marker of cellularity in the colon wall.[25] In the healthy colon, the mucosal crypts are generally 400 μm – 700 μm deep and rich with mucous secreting goblet cells. During severe disease activity, there is an influx of inflammatory cells (PMN leukocytes) that can form abscesses at the crypt bases in the mucosa. The crypt architecture can be completely obliterated by wound healing and epithelial recovery mechanisms.[24,26] This remodeling of the mucosal layer of the colon wall has implications on nutrient and water absorption and is likely accompanied by changes in the molecular profile that

Raman spectroscopy detects. The influx of inflammatory cells and the higher density of cellular components in the absence of healthy crypt architecture accounts for the increased cellularity measured by Raman spectra with increasing chronic severity. Interestingly, there were no strong correlations between lymphoid hyperplasia and other global markers of chronic inflammation in these tissue sections. Lymphoid hyperplasia refers to a proliferation of lymphocytes in the lamina propria or submucosa, sometimes forming organized germinal centers as seen in a lymph node. In the context of IBD, lymphoid hyperplasia can be considered a marker of chronic disease. However, in the proximal colon there is normally a natural abundance of lymphoid hyperplasia that is highly organized in contrast to the rather disordered proliferation in IBD.[27] It is likely that as volume integrating fiber optic Raman probes are more sensitive to concentrations of biomolecules than the organization of these molecules in tissue, that no differences in lymphoid presence were detected based on natural variations in content.

5.5.4 Acute inflammation markers

To decouple the complex interplay of the effects of inflammation and colon segment, GEEs were implemented for Raman features that were highly correlated with disease activity as a function intra-specimen variations. Figures 5.5 and 5.6 depict curves for two peak ratios modeled by both disease activity and colon segment measured. An initial comparison of these curves indicates

that disease severity causes different responses between segments when comparing Raman spectra. For example, Figure 5.5 indicates a consistent decrease in protein to lipid content for increasing inflammation severity across all segments of the colon. The protein to carotenoid ratio (Table 5.3) increases for all segments and could be a combined effect of increasing collagen as inflammation damages the tissue as well as decreased carotenoids present in the tissue based on the cellular protection mechanism of scavenging reactive oxygen species.[23] The discrepancy between these GEE modeled peak ratios indicate that not all features of a Raman spectrum are sensitive to the same sources of variability. The greatest differences between segment responses to worsening disease are seen in Figure 5.6 where the prevalence of collagen has opposite trends between the proximal and distal colon segments. This is likely a function of the different disease presentations of CD and UC. Nearly 70% of CD involves a combination of the colon and small bowel. Many cases of severe disease will have pancolitis (inflammation in colon spreading proximally to the splenic flexure) with rectal sparing; however 30% of CD patients will have segmental disease, with the majority of the inflammation confined to a single segment of the tissue. Conversely, 97% of UC involves inflammation in the rectum and 80% of mild UC is confined to the rectum and sigmoid colon segments.[22] Since severe CD exhibits fibro-collagenous changes in colon tissues, it is likely that the increase in the collagen signatures in the proximal colon (Figure 5.6) is likely due to the higher percentage of the measurements of

severe disease in those segments coming from patients with CD while in the distal colon, most of the severe disease was measured from UC specimens. This differences in severe CD and UC disease presentation and disease processes further emphasize the importance of decoupling disease severity and colon segment effects on the obtained Raman spectra.

5.5.5 Submucosal fat deposition

Each biomolecule has an associated Raman cross-section that is related to the likelihood of causing a Raman scattering event. Raman scattering cross sections for lipids are larger than many other biomolecules encountered in soft tissues.[20] Therefore, sensitivity to signals related to adipose content in the sample is a strength of this non-invasive Raman technique. Submucosal fat deposition is a clinical feature that has been reported in potential association with IBD in the past. While this aspect of disease presentation does not indicate discrimination of IBD, submucosal fat deposition has been observed in radiological studies. Called the “halo effect,” this deposition of fat in the bowel wall that may represent a response to diffuse injury in the context of IBD and commonly manifests as a ring of fatty attenuation in cross sectional computed tomography evaluations of the abdomen.[28,29] The large Raman scattering cross-section of fat and the use of NIR excitation wavelengths enable the interrogation of submucosal changes between 400 microns and 1 mm deep in tissue. The histological scoring of submucosal fat deposition and markers of active and

chronic disease were significant ($r > 0.5$). The GEE regression coefficients (Table 5.3) indicate that, when accounting for the severity of disease, the ratio of protein to lipid content decreases as submucosal fat deposition increases. Furthermore, there is a more pronounced effect of submucosal fat deposition on Raman spectra when active disease is more severe, which is consistent with reports of the halo effect in IBD.

This analysis is based upon a large number of spectra collected across the extent of excised colon specimens. It should be noted that the GEEs used in the analysis of these relationships do not fully account for complex correlation structures that may be present in the data obtained in this study with spatial relationships. It is likely that measurements made closer to one another in space are more correlated, both histopathologically and spectrally, than measurements collected with greater distance. Future investigations could incorporate spatiotemporal models[30,31] that more fully define the correlation structure relationship of these interacting variables, which could more precisely evaluate these complex interactions. However, fully defining the correlation structure of these variables could be extremely difficult. Thus, GEEs were selected such that the importance of the specific correlation structure is minimized and comparisons are made by grouping measurements from a single subject. The results reported here support the individual and combined influence imposed by both patient and disease-based sources of variation. Analysis and discrimination techniques may be able to achieve higher sensitivity and specificity rates by

accounting for these influential variables, as has been demonstrated in other investigations using Raman spectroscopy for disease evaluation.

5.6 Conclusions

Inflammatory bowel disease is a complex entity with diverse. This complexity continues to present challenges for medical management and indicates the need for better understanding of the association between tissue changes and disease pathways. While Raman spectroscopy has demonstrated potential for *ex vivo* and *in vivo* discrimination and characterization of IBD type and severity, numerous sources of variability have been implicated as confounding factors. This work has utilized tissue specimens from excisional procedures of the colon to investigate the complex interactions of several variables with respect to disease presentation: active and chronic disease markers, gross tissue changes, and patient specific factors such as age, BMI and diagnosis. Variables whose interaction had previously been considered confounding have now been decoupled using regression modeling of spectral feature combinations against histological scoring. Significant differences were identified between colon segments in the presence of active and chronic disease that strongly correlate with spectral features related to the disease process and anatomy of the colon. Age and BMI demonstrated weaker effects, while disease specific variables including IBD type and submucosal fat deposition were

significantly predictive of Raman spectral signatures. These complex interactions between disease and anatomy support the need for thorough investigation of the latent factors that can impact measured Raman spectra from tissues, either *ex vivo* or *in vivo*, and to account for these variables when developing algorithms for discrimination. Despite these disease interactions, the results presented further support the sensitivity of Raman spectra to disease and physiological variations in colon tissues and the potential for disease discrimination for complex conditions like inflammatory bowel disease.

5.7 Acknowledgements

The authors would like to acknowledge technical assistance from Erik Brooks and Adah Hall, as well as all of the staff of the Surgical Pathology suite at VUMC for assistance and patience during tissue specimen acquisition. This work was supported in part by the following funding sources: NIH R01 HD081121, NIH F31 CA168238, ASLMS student research grant, the Vanderbilt CTSA grant UL1 TR000445 from NCATS/NIH, NCI/NIH Cancer Center Support Grant 2P30 CA068485-14 and the Vanderbilt Mouse Metabolic Phenotyping Center Grant 5U24DK059637-13. Whole slide imaging was performed in the Digital Histology Shared Resource at Vanderbilt University Medical Center (www.mc.vanderbilt.edu/dhsr).

5.8 References

1. Ananthakrishnan AN. Epidemiology and risk factors for IBD. *Nature reviews Gastroenterology & hepatology.* 2015;12(4):205-217.

2. Bi X, Walsh A, Mahadevan-Jansen A, Herline A. Development of spectral markers for the discrimination of ulcerative colitis and Crohn's disease using Raman spectroscopy. *Diseases of the colon and rectum.* 2011;54(1):48-53.

3. Bielecki C, Bocklitz TW, Schmitt M, et al. Classification of inflammatory bowel diseases by means of Raman spectroscopic imaging of epithelium cells. *J Biomed Opt.* 2012;17(7):076030.

4. Pence IJ, Beaulieu DM, Horst SN, et al. Clinical characterization of in vivo inflammatory bowel disease with Raman spectroscopy. *Biomedical optics express.* 2016;In Review.

5. Pence IJ, Nguyen QT, Bi X, et al. Endoscopy-coupled Raman spectroscopy for in vivo discrimination of inflammatory bowel disease. 2014.

6. Pence I, Mahadevan-Jansen A. Clinical instrumentation and applications of Raman spectroscopy. *Chem Soc Rev.* 2016;45(7):1958-1979.

7. Haka AS, Shafer-Peltier KE, Fitzmaurice M, Crowe J, Dasari RR, Feld MS. Diagnosing breast cancer by using Raman spectroscopy. *Proc Natl Acad Sci U S A.* 2005;102(35):12371-12376.

8. Bergholt MS, Zheng W, Lin K, et al. Characterizing variability in in vivo Raman spectra of different anatomical locations in the upper gastrointestinal tract toward cancer detection. *J Biomed Opt.* 2011;16(3).

9. Vargis E, Byrd T, Logan Q, Khabele D, Mahadevan-Jansen A. Sensitivity of Raman spectroscopy to normal patient variability. *J Biomed Opt.* 2011;16(11):117004.

10. Pence IJ, Vargis E, Mahadevan-Jansen A. Assessing Variability of In Vivo Tissue Raman Spectra. *Appl Spectrosc.* 2013;67(7):789-800.

11. Bergholt MS, Zheng W, Lin K, et al. Characterizing Variability of In Vivo Raman Spectroscopic Properties of Different Anatomical Sites of

Normal Colorectal Tissue towards Cancer Diagnosis at Colonoscopy. *Anal Chem.* 2015;87(2):960-966.

12. Ross MH, Pawlina W. *Histology.* Lippincott Williams & Wilkins; 2006.

13. Young B. *Wheater's functional histology: a text and colour atlas.* Edinburgh: Churchill Livingstone/Elsevier; 2006.

14. Lui H, Zhao J, McLean D, Zeng H. Real-time Raman Spectroscopy for In Vivo Skin Cancer Diagnosis. *Cancer Res.* 2012;72(10):2491-2500.

15. Lieber CA, Majumder SK, Ellis DL, Billheimer DD, Mahadevan-Jansen A. In vivo nonmelanoma skin cancer diagnosis using Raman microspectroscopy. *Lasers in Surgery and Medicine.* 2008;40(7):461-467.

16. Mahadevan-Jansen A, Mitchell MF, Ramanujam N, et al. Near-infrared Raman spectroscopy for in vitro detection of cervical precancers. *Photochem Photobiol.* 1998;68(1):123-132.

17. Hanley JA, Negassa A, Edwardes MD, Forrester JE. Statistical analysis of correlated data using generalized estimating equations: an orientation. *Am J Epidemiol.* 2003;157(4):364-375.

18. Zeger SL, Liang KY. Longitudinal data analysis for discrete and continuous outcomes. *Biometrics.* 1986;42(1):121-130.

19. Zhu G, Zhu X, Fan Q, Wan X. Raman spectra of amino acids and their aqueous solutions. *Spectrochimica acta.* 2011;78(3):1187-1195.

20. Czamara K, Majzner K, Pacia MZ, Kochan K, Kaczor A, Baranska M. Raman spectroscopy of lipids: a review. *J Raman Spectrosc.* 2015;46(1):4-20.

21. de Oliveira VE, Castro HV, Edwards HGM, de Oliveira LFC. Carotenes and carotenoids in natural biological samples: a Raman spectroscopic analysis. *J Raman Spectrosc.* 2010;41(6):642-650.

22. Shaffer EA, Thomson ABR. *First Principles of Gastroenterology: The Basis of Disease and an Approach to Management.* Canadian Association of Gastroenterology; 1997.

23. D'Odorico SBRCRDIDMAFGCSA. Reduced Plasma Antioxidant Concentrations and Increased Oxidative DNA Damage in

Inflammatory Bowel Disease. *Scandinavian journal of gastroenterology.* 2001;36(12):1289-1294.

24. Rieder F, Brenmoehl J, Leeb S, Scholmerich J, Rogler G. Wound healing and fibrosis in intestinal disease. *Gut.* 2007;56(1):130-139.

25. Cheng JX, Xie XS. *Coherent Raman Scattering Microscopy.* CRC Press; 2016.

26. Stumpf M, Krones CJ, Klinge U, Rosch R, Junge K, Schumpelick V. Collagen in colon disease. *Hernia: the journal of hernias and abdominal wall surgery.* 2006;10(6):498-501.

27. Geboes K. Histopathology of Crohn's disease and ulcerative colitis.

28. Ahualli J. The fat halo sign. *Radiology.* 2007;242(3):945-946.

29. Mesa H, Drawz S, Dykoski R, Manivel JC. Morphometric measurement of submucosal thickness in areas of fat deposition in the terminal ileum and colonic sections, with correlation with body mass index, weight and age: a male autopsy study. *Histopathology.* 2015;67(4):457-463.

30. Diggle PJ. *Statistical Analysis of Spatial and Spatio-Temporal Point Patterns, Third Edition.* Taylor & Francis; 2013.

31. Shaddick G, Zidek JV. *Spatio-Temporal Methods in Environmental Epidemiology.* CRC Press; 2015.

CHAPTER 6

CHARACTERIZING THE IMPACT OF ACTIVE INFLAMMATION ON RAMAN SPECTRA IN EXPERIMENTAL COLITIS

6.1 Abstract

Inflammatory bowel disease (IBD), comprising Crohn's disease and ulcerative colitis (UC), causes appreciable morbidity for patients and poses a challenge to medical management. Raman spectroscopy, a biochemically specific optical technique, has demonstrated potential as an adjunct tool to improve *in vivo* discrimination and objective characterization of disease severity. Prior *in vivo* and *ex vivo* investigations of colon tissues for IBD and cancer have implicated patient and disease variations as significant influences on measured Raman spectra. One potential factor that has been uncontrolled in studies thus far is the influence of acute disease severity. Using a dextran sulfate sodium (DSS) as a murine colonic injury model with similarities to human UC, we assessed the impact of mucosal injury on the Raman microspectroscopic biochemical profile of tissues relative to clinical parameters and histological scores of disease severity. Tissue maps were acquired with a 785 nm Raman microscope from the rectum and areas of most severe disease presentation from 17 mouse colon specimens and spectral features that significantly correlate with

mucosal injury metrics were identified for further analysis. Spectral profiles for carotenoids and amino acids related to oxidative stress significantly decreased with increasing disease severity, while lipid signatures that may be linked to prostaglandin regulation increased. Furthermore, several features demonstrated linear changes in Raman spectral features as a function of disease while others demonstrated a binary response, indicating that some Raman features are sensitive to the biochemical processes associated with mucosal injury prior to the manifestation of microscopic histological changes of disease. These spectral changes in a controlled model for colon inflammation and mucosal injury support the need to account for disease severity in differential analysis of inflammatory bowel disease with Raman spectroscopy techniques.

6.2 Introduction

Inflammatory bowel disease (IBD) is a complex condition that is characterized by cycles of disease flare and quiescence. Depending upon the type of IBD a patient has, disease may affect the entire gastrointestinal tract. IBD is commonly first diagnosed in 15-30 year old patients, and generally requires life-long treatment.[1,2] Millions of Americans and Europeans suffer from the serious detriments to quality of life associated with IBD and incidence is increasing worldwide, including emergence in Asian, eastern European, Indian populations.[3,4] As a continuing challenge to the medical community, the

exact etiology of IBD is unknown, but the disease is characterized by dysregulated immune responses to commensal flora in genetically susceptible individuals.

Crohn's disease (CD) and ulcerative colitis (UC) represent two distinct forms of IBD, and have different causes and discrete mechanisms of tissue damage.[2,5] Different immune responses to microbial antigens of commensal microorganisms have been proposed for UC and CD. In CD, the T-cell response is T-helper (Th)1 dominant, while in UC, the response is either Th2 [interleukin (IL) -4, IL-13] or is mediated by specialized cells such as natural killer (NK) T cells.[6,7] The activation of central immune-cell populations is eventually accompanied by the production of a wide variety of nonspecific mediators of inflammation, such as cytokines, chemokines, and growth factors.[8-10] These mediators enhance the inflammatory process itself and tissue destruction, which eventuate in the clinical manifestations of disease.[11] The alterations in the micro-environment and macro-morphology of the inflammatory tissue are evident, and ultimately result in clinical manifestation of IBD. Key features of UC include diffuse mucosal inflammation that is restricted to the colon. In conjunction with severe inflammation and the coincident production of a complex mixture of inflammatory mediators, extensive superficial mucosal ulceration develops. Histopathological features include the presence of a significant number of neutrophils within the lamina propria and the crypts,

where they form micro-abscesses.[12] CD is characterized by aggregation of macrophages that frequently form noncaseating granulomas.[12]

A tool that has seen recent investigation for translational medicine is Raman spectroscopy. This non-destructive optical technique can be applied *in vivo* for disease detection and physiological monitoring.[13] The strength of Raman spectroscopic techniques is its inherent sensitivity to vibrational bonds that comprise a tissue or sample of interest. The interaction of the excitation light with the vibrational bonds result in biochemical specific peaks and valleys that can be used to distinguish changes within a sample.[13]

A majority of previous Raman spectroscopy studies in colon research have focused on cancer and pre-cancer detection. Early work on colon cancer using near infrared Raman spectroscopy found differences between normal tissue and adenocarcinoma corresponding to nucleic acid changes.[14] More recently Wilson *et al*. reported the study of this technique in the colon for classifying colon polyps and obtained an accuracy of 93-95% in distinguishing between adenomatous and hyperplastic polyps both *in vitro* and *in vivo*.[15] A higher diagnostic accuracy (> 99%) was reported in following *ex vivo* studies.[16,17] Stone *et al*. has developed a database cataloging the intrinsic Raman signatures of various gastrointestinal cancers including those of the colon and showed that colon tissues can be classified with near 90% efficiency.[18] Finally, Bergholt *et al.* have reported clinical evaluation of colorectal cancers *in vivo* using Raman spectroscopy in combination with colonoscopy procedures with

high diagnostic accuracy compared with histology.[19] These reported successes demonstrated the capability and efficacy of Raman spectroscopy in detecting subtle changes in diseased tissue.

Several research groups, including ours, have investigated IBD in humans with Raman spectroscopy. Raman scattering is sensitive to subtle changes in diseased tissues and to the physiological environment in the body. Hormone status, disease, and treatment history have an impact on the optical properties of tissues, and thus result in subtle changes in Raman spectra.[20] Bi *et al.* was the first to demonstrate that Raman spectra are sensitive to the subtle changes between CD and UC in a small set of *ex vivo* patient biopsy samples.[21] Bielecki *et al.* has previously investigated the potential for IBD classification based on high resolution Raman microspectroscopic imaging of *ex vivo* colon specimens.[22] Subsequent work by our group has demonstrated for the first time sensitivity of Raman spectra obtained *in vivo* during colonoscopy to changes in tissue that correlate with IBD type, severity, and anatomical location of disease.[23,24] The success of these studies demonstrate the need for further refinement of Raman spectroscopic techniques prior to clinical utility.

Prior work has indicated that there are variations in detected Raman spectra that are dependent upon severity of disease presentation.[23,24] As specific disease presentation cannot be controlled *in vivo* in a patient population, many studies of IBD rely on *ex vivo* human tissues and animal models with similarities to human IBD. Such studies also enable the evaluation of new

strategies for adjunct therapeutic options for this complex disease.[25-27] The preliminary *in vivo* work for IBD demonstrates the need to understand the effect of active inflammation on the spectral characteristics of IBD. To objectively quantify inflammation in the colon, this study will use an animal model. Mouse models are an imperfect replicate of human IBD; however, it will enable a systematic study of the course of disease development for colitis (colon inflammation) in a shortened time frame (7-10 days depending on protocol), and thoroughly analyze the colon tissue of an epithelial injury model with immune dysregulation. The goal of this work is to compare normal mouse colon tissue with induced inflammatory injury tissues at points of disease progression to investigate which underlying biochemical and structural properties correlate with Raman spectral features.

Dextran sulfate sodium (DSS) is a heparin-like polysaccharide that has been successfully utilized to induce colonic mucosal injury in mice.[25,26,28] This model was selected for the current research due to the similarities that the DSS-induced colitis model exhibits with respect to the characteristics of UC disease in humans. Manifestations of injury include weight loss, diarrhea, rectal bleeding, and loss of epithelium followed by ulceration and leukocyte infiltration.[27,29]

Here, we report the use of the DSS-induced colitis model to assess the effects of active inflammation on Raman spectra obtained from colon tissues during acute colitis. Results from Raman microspectroscopic mapping are

correlated with clinical parameters of mucosal injury and effects are decoupled from the bowel wall layer measured. Specific Raman features are identified that are sensitive to tissue changes consistent with acute inflammatory responses and provide a basis for comparisons between different levels of disease severity. The results of this pilot study demonstrate that Raman spectral changes from the mouse colon are sensitive to biomolecular processes of colitis as a function of injury severity.

6.3 Materials and methods

6.3.1 Animals

Seven week-old female house-bred WT C57BL/6 mice were used for this study. All procedures using mice were reviewed and approved by the Institutional Animal Care and Use Committee of the Vanderbilt University Medical Center and the Research and Development Committee of the Veterans Affairs Tennessee Valley Healthcare System.

6.3.2 Induction of DSS colitis

DSS (mol wt 36,000 –50,000; TdB Consultance, AB, Uppsala, Sweden) was added to the drinking water as a 4% (wt/vol) solution for the time periods indicated. The animals were allowed free access to the DSS-containing water during the experiment. On the day the animals were euthanized, the colons were removed and colon length was measured; then the colon was cut longitudinally,

cleaned, and Swiss-rolled for histology, with two proximal and two distal 2-mm pieces preserved for RNA and protein analysis.

6.3.3 Body weight measurement

For assessment of the effects of DSS treatment on changes in mouse body weight, the animals were monitored daily over the course of colitis development.

6.3.4 Assessment of histological injury scores

Swiss-rolled colons were snap frozen (Super Friendly Freeze'It media, Fisher Scientific) and embedded in OCT mounting media (Fisher Healthcare Tissue-Plus O.C.T Compound, Fisher Scientific). Serial sections of 20 μm and 8 μm were cut; 8 μm sections were placed on standard microscope slides and stained with hematoxylin and eosin (H&E), while 20 μm sections were placed on 75 mm x 20 mm × 1 mm Raman-grade CaF_2 microscope slides (Crystran, Poole, UK), fixed in 100% ethanol and allowed to air dry in a sterile hood under laminar flow for 24 hours. H&E slides were examined in a blinded manner by a gastrointestinal pathologist; the summation of inflammation severity (0 –3) and inflammation extent (0 –3) was multiplied by the percent involvement (1 = 0–25%, 2 = 25–50%, 3 = 50–75%, and 4 = 75–100%) to yield the inflammation score (0 –24). The parameter of crypt damage (0–4) was multiplied by the percent involvement to yield an epithelial injury score (0 –16). These scores were then added together to yield the histological injury score (0–40), as

described previously.[25,30,31] H&E stained slides were then imaged at 40X magnification by the Digital Pathology Shared Resource (VUMC) for further section comparison and analysis. Reviewing the images for each colon, an area of the swiss-rolled colon that is consistent with the mouse rectum as well as an area consistent with worst disease severity were identified for subsequent Raman imaging.

6.3.5 Raman imaging analysis

Raman spectra were acquired using a confocal Raman microscope (inVia Raman Microscope, Renishaw PLC, Gloucestershire, UK) with a 785 nm laser diode (Renishaw PLC, Gloucestershire, UK). Illumination and epi-detection of Raman scattered light were accomplished through a 50X (N PLAN EPI, NA=0.75, Leica, Weltzlar, Germany) objective, with a ~1 μm laser spot focused onto the tissue surface. Collected light passed through a 35 μm slit and was dispersed by a holographic grating (1200 lines/mm) onto a thermoelectrically cooled (-70 ˚C) deep-depleted, CCD providing 1 cm^{-1} spectral resolution. The theoretical spatial resolution of the confocal Raman microscope system is ~0.6 μm. Laser power was measured daily at the sample before and after measurements to ensure consistent exposure to 35-mW laser power. System Raman shift calibration was accomplished using a neon lamp and a silicon standard with Renishaw software to account for grating motion. The calibration measurements before and after data collection ensured

consistency of wavenumber calibration and collection arm throughput. Samples were held on a motorized XYZ stage and spectral collection was controlled by WiRE 4.2 software (Renishaw PLC). Raman maps were collected from identified tissue regions at an acquisition time of 20 s per pixel at 5-μm spatial resolution. A total of 127 661 spectra from 18 tissue maps were analyzed. All spectra were background subtracted with EMSC and linear baseline subtraction.[32]

6.3.6 Multivariate analysis

White light reflectance images of unstained sections were compared with the digital bright field images of serial H&E sections to identify sample regions that correspond to lamina propria, muscularis mucosa, submucosa, and muscularis externae. Regions of interest for each bowel layer were selected and average spectra were utilized to identify Raman peaks that differ between layers and severity of inflammation. Peak ratios were correlated (Pearson's $|r| > 0.8$) with indicators of disease severity: colon length; inflammation severity score; inflammation severity, depth and extent; architectural distortion and extent. Identified peak ratios were then compared across disease groups with one-way ANOVA with multiple comparisons tests performed based on Tukey's honestly significant difference criterion. Peak ratios were used to recreate image projections from the detected spectral data for visualization of maps.

6.4 Results

Clinical indicators of DSS-induced colitis are presented in Figure 6.1. Body weights of the 17 mice (control, n=6; DSS 3 days, n=5; DSS 6 days, n=6) were measured daily and presented as a percentage of their initial body weight. No significant differences in mouse body weight were seen during the acute phase of DSS injury (Figure 6.1A). At sacrifice, colons were removed, measured, cleaned, and swiss-rolled for further analysis. Colon length is presented in Figure 6.1B and displays significant difference between the DSS day 6 treatment group and both control and day 3 treatment groups. The decrease in colon length is consistent with DSS injury and correlates with DSS injury score (Figure 6.1C). The injury scores for 3 days of DSS administration, similar to the results from colon length do not display significant differences in disease presentation; however, there is marked increase in histologic score at peak inflammation for 6 days of DSS administration in agreement with prior work.[25,26] The histologic scoring, as previously reported and utilized, along with the other clinical features of disease serve as the basis of comparison for spectral analysis.

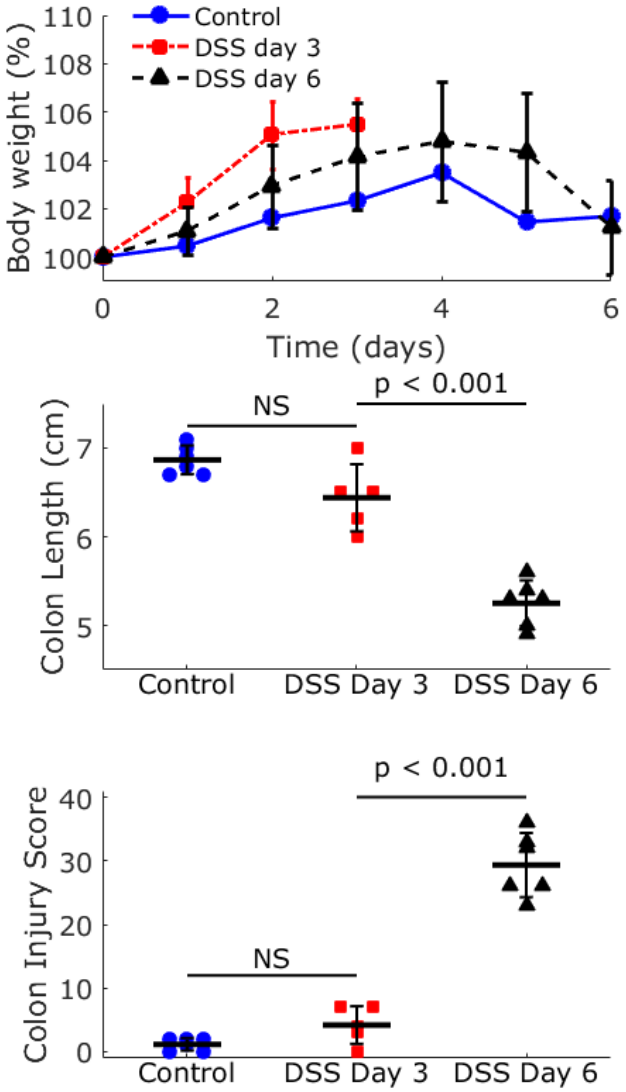

Figure 6.1. Clinical parameters and histologic scoring of DSS-induced colitis.

Raman imaging was performed on 17 swiss-rolled colon specimens, 10 of which are used in this analysis (control, n=2; DSS 3 day, n=4; DSS 6 day, n=4). For each sample, comparison of digitally imaged H&E slides and bright field microscopy images of the unstained serial sections enabled the co-

localization of Raman mapping with regions of interest indicated by a collaborating histopathologist with extensive expertise in DSS-induced colitis. Once the region of interest was matched in an unstained slide, a grid-based Raman map was initialized to acquire spectra from the tissue surface at high spatial (5 μm) and spectral (1 cm^{-1}) resolution. A representative Raman spectrum from a control mouse is depicted in Figure 6.2 including tentative labels for peaks based on literature. The tissue mapping enables acquisition of high SNR spectra (>15) from identified spatial locations of the swiss-rolled colon.[33] These spectra provide a fingerprint of the biomolecules comprising the tissue. Strong bands from amino acids, lipids, proteins, and DNA/RNA bases are consistent across colons.

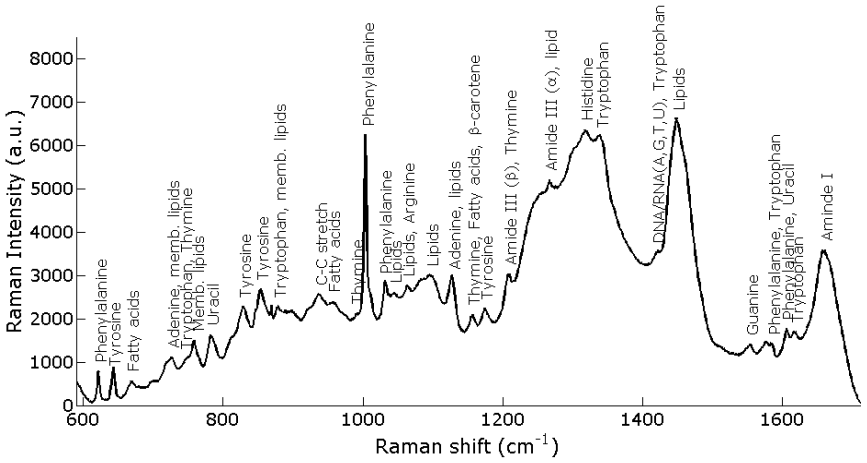

Figure 6.2. Representative spectrum from rectum of control mouse with tentative peak assignments listed. Assignments are based on reported reference libraries.[34-36]

To investigate the impact of inflammation severity on the Raman spectra from the colon, several steps were taken to minimize the influence of

potential confounding factors. Previous Raman studies of human colon tissues have indicated that inter-anatomical variability from colon segment and bowel wall layer can significantly influence acquired data.[22,23,37,38] To verify that Raman microspectroscopic imaging of mouse colons were also sensitive to these inter-anatomical variations, regions of interest from the mucosa (lamina propria), submucosa, and muscularis externae were identified in each digital image of H&E section with corresponding Raman maps. Figure 6.3 contains the average spectra obtained from the regions of each bowel wall layer of a control mouse colon. The spectral line shapes differ as a function of bowel layer measured, especially in wavenumber regions indicated by vertical gray bands. This comparison was performed in control mice to avoid confounding influence of disease severity and indicated the need to consider spectral changes in bowel layers individually.

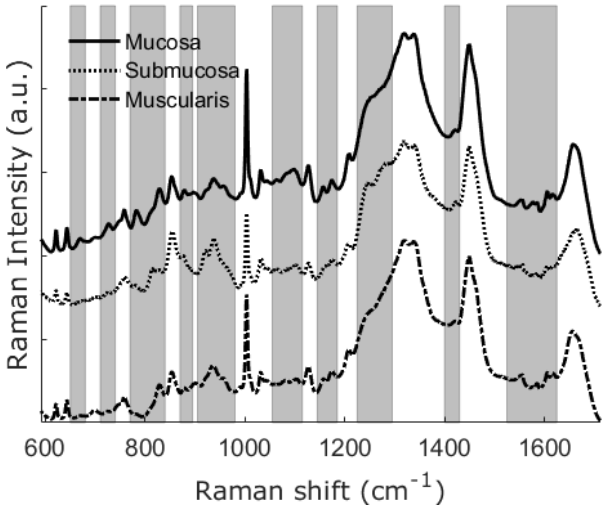

Figure 6.3. Mean spectra obtained from Raman maps corresponding to different layers of bowel wall in control mice. Gray bands indicate peaks and regions that qualitatively differ between layers and justify stratification of analysis.

After selection of regions of interest in the Raman maps that correspond with mucosal and submucosal bowel layers, correlation analysis was performed between Raman peak ratios and clinical and histological indicators of DSS-induced colitis injury. All separate clinical and histopathological parameters highly correlated with duration of DSS administration ($|r| > 0.7$). Peak ratios were individually correlated with each disease metric (DSS duration, colon length, histological injury score, and individual parameters (described in *Assessment of* histological injury scores*)*. Peak ratios that correlated with disease metrics ($|r| > 0.8$) were selected for subsequent analysis. The individual peaks from the identified ratios are listed in Table 6.1 along with tentative peak assignments based on reported library values for Raman active biomolecules. Separate comparisons between Raman maps were evaluated: (1) comparison of map data acquired from the rectum area of each swiss-roll, and (2) comparison of map data acquired from the area of greatest injury in each DSS swiss-roll.

Table 6.1. Raman spectral features that significantly correlated with DSS-induced colitis.[34-36]

Raman feature (cm^{-1})	Tentative Peak Assignment
642	Tyrosine
670	Fatty acids, Glycoprotein ν(C-S)
697	Cholesterol
747	Thymine, Tryptophan
757	Membrane lipids, Tryptophan
828	Tyrosine
854	Serine, Tyrosine
879	Membrane lipids, Tryptophan
901	Fatty acids, Proline
935	Arginine, Collagen ν(C-C)
958	Fatty acids
991	Thymine
1004	Phenylalanine
1043	Fatty acids
1063	Arginine, Cholesterol, Fatty acids, Triglycerols
1099	Cholesterol, Fatty acids, Triglycerols
1156	β-carotene, Fatty acids, Thymine
1207	Amide III (β-sheet), Thymine
1265	Amide III (α-helix) Cholesterol, Fatty acids, Triglycerols
1301	Amide III δ(N-H), ν(N-C) Cholesterol, Fatty acids, Membrane lipids, Triglycerols
1317	Histidine
1339	δ(C-H), Threonine, Tryptophan
1421	Adenine, Guanine, Thymine, Tryptophan, Uracil, Fatty acids
1616	Tryptophan

Based on the identified peak ratios that correlate with DSS-induced colitis, analysis was performed to investigate what Raman signatures are significantly changing with mucosal injury. Significant peak ratios from the mucosal and submucosal layers measured in the rectum of each swiss-rolled colon are depicted in Figure 6.4 and Table 6.2. In general, ratios with lipid signals that are associated primarily with cholesterol, fatty acids, or triglycerols (denominators of 747/1043 cm^{-1}, 991/1063 cm^{-1}, 642/1156 cm^{-1}) indicate that the concentrations of these lipids decrease in rectal tissues with increasing severity of DSS-injury. Membrane lipid signatures (757/828 cm^{-1}, 757/854 cm^{-}

^{1}) increase while independent of other lipid signatures, although when all lipid signatures are present in a ratio, the influences conflict (879/958 cm^{-1} versus 757/1043 cm^{-1}). Amino acid peaks are ubiquitous across the ratios that significantly vary and indicate complicated fluctuations in the proteomic profile of the tissues during the mucosal injury and epithelial recovery process. Of note is the decreasing ratio of 757/854 cm^{-1} which may correlate with decreases in serine content in the mucosa, and the increase of 642/1156 cm^{-1} which may indicate that β-carotene content is decreasing relative to amino acids in the submucosa. The trends for some Raman peak ratios indicate linear trends with increasing severity of disease (Figure 6.4, 879/958 cm^{-1}) while others appear more as a binary function between mild or no disease and severe injury.

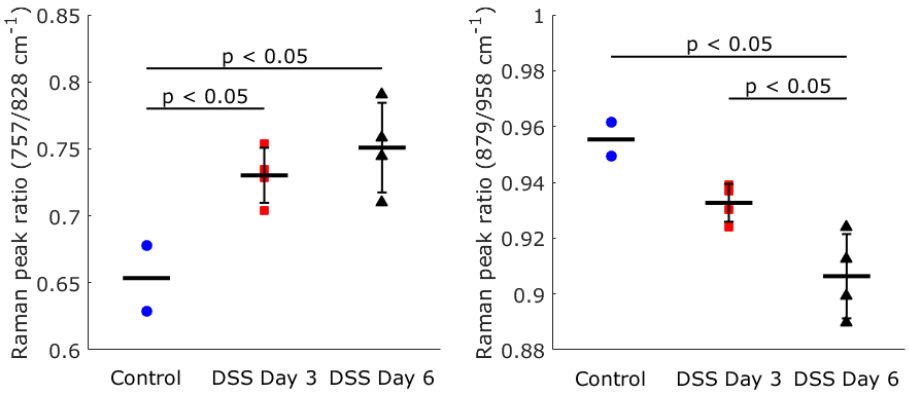

Figure 6.4. Peak ratios from spectral regions of interest in the mucosal layer of maps acquired from the rectum area of the swiss-rolled colon tissue. Significant differences were calculated based on the Tukey's criterion for multiple correction of one-way ANOVA.

Table 6.2. Mean Raman peak ratios significantly correlated with parameters of DSS injury.

Mapped regions in the rectum				
Mucosa				
Peak Ratio (cm^{-1})	Control	DSS day 3	DSS day 6	P-value
747/1043	0.43	0.48	0.51	0.047
757/828	0.65	0.73	0.75	0.017
757/854	0.56	0.62	0.65	0.035
757/1043	0.58	0.60	0.66	0.017
757/1099	0.51	0.52	0.58	0.008
879/901	1.06	1.05	1.02	0.011
879/958	0.96	0.93	0.91	0.040
879/991	1.06	1.05	0.98	0.009
991/1063	0.80	0.81	0.89	0.002
Submucosa				
642/1156	0.29	0.32	0.34	0.008
697/747	0.50	0.44	0.40	0.023
757/854	0.43	0.48	0.52	0.003
Mapped regions of worst mucosal injury				
Mucosa				
Peak Ratio (cm^{-1})		DSS day 3	DSS day 6	P-value
670/854		0.20	0.23	0.007
670/879		0.25	0.28	0.018
670/935		0.21	0.24	0.006
828/1004		0.43	0.38	0.014
901/1004		0.40	0.35	0.005
935/1004		0.49	0.44	0.003
1265/1616		2.67	2.62	0.033
1339/1421		1.70	1.76	<0.001
Submucosa				
1004/1043		2.13	2.84	0.009
1156/1207		0.66	0.62	0.024
1301/1317		0.90	0.88	0.007
1317/1421		1.64	1.69	0.010
1339/1421		1.65	1.72	0.009

Blue = Upregulated, Red = Downregulated

Investigating the changes is DSS-induced colitis tissues that have the greatest insult are likely to most completely capture the influence of active inflammation on Raman spectra. Figure 6.5 displays scores for colon tissue maps for some of the peak ratio comparisons listed in Table 6.2. Significant changes in peak ratios again indicate that disease severity impacts the biomolecular profile that Raman scattering detects. Consistent features that correlate with disease severity in the most damaged areas of tissue are related to amino acids, carotenoids, DNA/RNA bases, glycoprotiens, and lipids (Table 6.2). Significant increases are observed in ratios associated with fatty acids, glycoproteins (collagen), and certain amino acids like threonine and phenylalanine; decreases occur for ratios associated with collagen, carotenoid, and histidine signatures. The total change in ratio value between groups is minimal, but despite a small sample set, the differences are singificant. The changes in amino acid, DNA base, and lipid proiles between different regions of the colon tissue further suggest that visualizing peak ratios of interest in a two-dimensional format that allows co-localization of histologic features with spectral markers of disease severity could be informative. Figure 6.6 depicts the comparison of bright field images from H&E and unstained slides with the corresponding Raman spectral maps. As a demonstration of this technique, the 1004/1339 cm^{-1} ratio is presented, showing the treadeoff of phenylalanine to threonine and tryptophan. The increasing disorder of the crypt architecture that coincides with increasing mucosal injury is well captured by this map.

Furtehrmore, the submucosa can be more readily visualized at severe disease relative to control and minimal injury indicating layer specific interactions with inflammaiton.

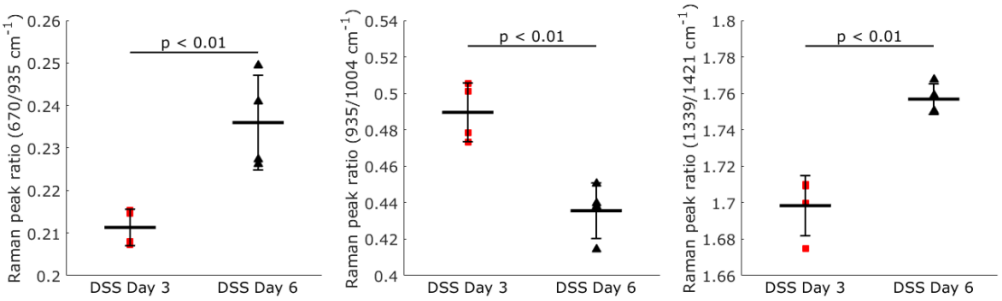

Figure 6.5. Peak ratios from spectral regions of interest in the mucosal layer of maps acquired from the swiss-rolled colon tissue area of most severe injury. Significant differences were calculated based on a one-way ANOVA.

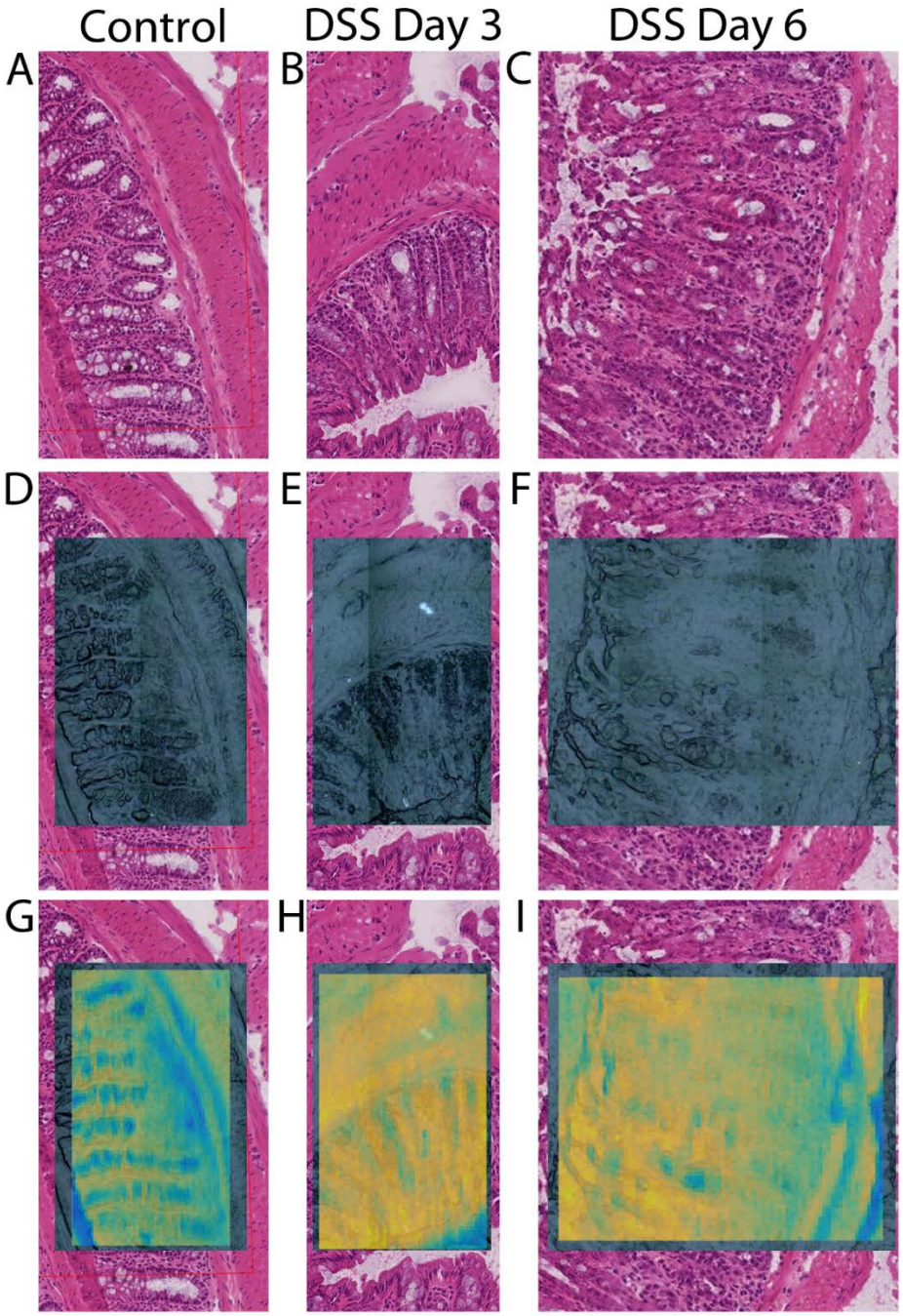

Figure 6.6. Example bright field and Raman images of tissue sections from DSS-induced colitis. *Top row*: Bright field images of H & E stained sections. *Middle:* Bright field images of unstained serial sections on CaF_2 slides of identified regions. *Bottom:* Raman image projection of 1004/1339cm^{-1} peak ratio after mapping protocol. Control mouse in A, D and G; DSS Day 3 mouse in B, E, and H; DSS Day 6 mouse in C, F, and I. Colors are consistent across all panels.

6.5 Discussion

Raman spectroscopy is a biochemically specific technique that has potential to aid in the medical management of complex conditions like inflammatory bowel disease. Previous work has demonstrated the sensitivity of Raman spectra to IBD class for differentiation, and our group has begun to investigate potential latent factors that decrease classification performance.[23] In prior work based on *in vivo* and *ex vivo* measurements from patients, numerous factors have been outside the control of researchers: the anatomical location of disease, the level of disease severity, the duration/chronicity of disease, the prior therapeutic or surgical interventions, and the lifestyle or dietary habits of study subjects. In this work, we have employed a model of experimental colitis that exhibits similarities to the mucosal injury process of ulcerative colitis in order to target the impact of inflammation severity on Raman spectra, independent of these other latent factors.

The DSS-induced colitis model for mucosal injury has been demonstrated and established by several research groups to investigate mucosal injury and potential adjunct therapies for bowel inflammation.[25,26,28] The DSS concentration utilized in this study is expected to reach peak inflammation damage at day 7 of administration. As seen in Figure 6.1, the clinical markers of disease and histological scores indicate that DSS administration causes dramatic alterations in colon tissues in a time course that can readily be initiated and controlled for thorough comparison of injury effects. Measurements of

control mice, and mice at days 3 and 6 of DSS injury were selected to represent different stages of inflammatory disease, including a baseline for comparison with mild and severe acute response and the initial stages of wound healing and epithelial recovery.[39,40] By inducing different levels of colon epithelial injury, we are now able to investigate the impact of disease severity in a controlled manner.

The results presented in Figure 6.2 and Figure 6.3 support previous reports of the sensitivity of Raman spectra to subtle changes in tissues. As demonstrated by these results, the Raman spectra obtained from the mouse colons were highly sensitive to amino acid, lipid, and protein features.[34-36] However, despite the level of control afforded to research by moving from human populations to animal models, there is concern that experimental colitis models do not completely recapitulate the human IBD process. By comparing the results reported by Bielecki *et al.* who performed similar Raman spectral mapping of human IBD tissues towards disease discrimination, the spectral shapes from mouse colons presented in Figure 6.2 and Figure 6.3 are nearly identical to those obtained from human colon sections.[22] Furthermore, in the previous analysis, the authors indicated the influence bowel layer specific signals and used multivariate statistical algorithms to isolate only one layer for comparison. While the approach utilized herein is simpler, the results in Figure 6.3 indicate the importance of making comparisons between consistent layers of tissue when using Raman microspectroscopy.

When comparing Raman spectra from mucosa and submucosa tissues across the levels of DSS administration, several peak ratios were found to strongly correlate with colitis. Presented in Table 6.2, only features that were strongly correlated with inflammatory severity ($|r| > 0.8$) were considered for further analysis. This threshold was selected due to the high-dimensionality of the Raman data from the mapping procedure (each spectrum has over 1000 variables) and the high correspondence between parameters of experimental colitis ($|r| > 0.7$). A few peak ratios that significantly differ between regions of the mucosa and submucosa in the rectum are presented in Figure 6.4 and Figure 6.5. Numerous biomolecules contribute to the differences between disease severities (Table 6.2). The contribution of lipid signatures present interesting trends. In these samples, there are increases in cholesterol, fatty acid, and triglycerol signals with increasing disease severity. The increase in lipid constituents may be the result of prostaglandin production. Prostaglandins are fatty acid based molecules that are upregulated at the onset of an inflammatory response prior to leukocyte recruitment.[41] Other biomolecules, such as arginine have demonstrated decreases in concentration with immune response. Arginine is a semi-essential amino acid that in important for protein synthesis. Oxidative stress can deplete arginine in the body and supplementation of this amino acid in the diet of DSS colitis mice improves responses to injury and inflammation.[25,31,42] In agreement with these reports, arginine signals decrease as inflammation worsens in the spectra obtained from colon sections. A similar

trend is apparent for β-carotene, which acts as an antioxidant scavenger of free radicals associated with oxidative stress pathways, such as those activated during inflammation.[43,44]

Similar to the results depicted in the rectum, for spectra acquired from tissues with the most severe presentation of inflammation and mucosal injury, numerous biomolecular components demonstrate significant differences with disease. Again, consistent increases are demonstrated for fatty acid content that likely correlates with prostaglandin upregulation. Also, β-carotene and histidine are significantly decreased in colon tissues with higher levels of inflammation. Histidine is an efficient scavenger of both hydroxyl radicals and singlet oxygen species and has been shown to inhibit oxidative stress and secretion of cytokines including interleukin-8 (IL-8) and tumor necrosis factor-alpha (TNF-α).[45] Both IL-8 and TNF-α are dysregulated in the immune response of intestinal epithelium associated with IBD. The depletion of histidine in the colon tissue is likely the result of increased reactive oxygen species in the colon tissue during inflammatory response.

A few of the features implicated in these significant peak ratios demonstrate conflicting signatures. Serine/threonine are strongly correlated with the Raf family of kinases that are essential for the activation of tissue protective nuclear factor (NF)-κB pathway in colon epithelium.[46] In the ratios identified, serine content in the rectum appears to decrease with severity as expected while in the areas of worst disease, threonine content increases.

Conversely, in human UC and DSS colitis alike, mucus secreting Goblet cells that usually reside in the mucosa become depleted. The resulting decrease in mucin production with disease would likely cause decreases in serine and threonine which comprise nearly half of a large central region of the mature mucin glycoprotein structure.[47] The conflicting signatures for these amino acids are also demonstrated for collagen signatures. Amide III complexes and collagen peak ratios identified in this analysis generally decrease with disease severity. This is counterintuitive with respect to the formation of granulation tissue in epithelial would healing. As part of the mucosal healing process, a dense population of macrophages, fibroblasts, and neovasculature is embedded in a loose collagen, fibronectin, and hyaluronic acid matrix known as granulation tissue. As this tissue is predominated by types I and III collagen, these features are expected to increase with disease severity based on the acquired Raman spectra.[39,40,42] However, as this is an acute model of disease, granulation tissue formation may still be in an early stage. Potential investigation of these granulation tissue changes may be more evident in a cyclic DSS-injury and recovery model as previously reported.[25,26,28]

Similar to other microscopic techniques that enable the projection of hyperspectral information onto an image (like overlaying multiple images from immunohistochemical staining), Raman peaks and ratios from mapping can be converted into images. Figure 6.6 demonstrates the relationship of images acquired in this study for bright field imaging of the H&E and unstained tissues

with Raman map data. The ratiometric presentation of Raman data here represents only two data points per image pixel; over 1000 such wavenumbers exist for each image pixel and indicate the need for more complex analysis techniques. Potential avenues for combining this high-dimensional data include principal component analysis, vertex component analysis, or k-means clustering.[32] While such steps are currently beyond the scope of this preliminary study, further investigations of the complex interactions of subtle Raman features may be possible. Despite the algorithmically simple analysis performed here, the Raman map images displayed in Figure 6.6 reveal that phenylalanine to DNA and lipid features recapitulate the crypt architecture from H & E staining. Furthermore, the relative intensity of this ratio is maintained in the mucosa of these samples as disease severity increases, again likely correlated with consistent metabolism of both phenylalanine, tryptophan, and threonine with increase disease. However, the expansion and appearance of submucosal layers becomes more appreciable as colitis injury occurs. This Raman imaging analysis and the significant biochemical changes that occur in the submucosa as a function of inflammatory disease may help to elucidate the underlying changes that occur in the bowel wall's potential space that is not significant prior to disease onset.

Some limitations exist for this study that require further attention in moving forward. Some features identified in the correlation analysis appear to have binary responses to disease, while others are more linear relative to

severity. A potential explanation is that for features that do not exhibit a gradient with disease, the tissue changes are too subtle to be detected by Raman scattering at the mild inflammation present with 3 days of DSS administration while other features are significantly different between day 3 and control specimens. Further including Raman mapping data from the remaining 7 mouse colons, will increase the statistical power for these analysis and aid inferences between group differences. A final challenge in this analysis is that several of the features of interest demonstrate correlations with numerous biomolecules of interest, potentially adding to the conflicting signatures indicated for amino acids and collagen. Building a descriptive model of inflammation based on Raman spectral measurements of pure components would be both cumbersome and likely ineffective based on these feature correlations. It is likely that to isolate the exact influence of competing biomolecules, alternate strategies including imaging mass spectrometry or proteomic analysis are necessary complementary techniques to fully evaluate the complex processes occurring within these tissues.

6.6 Conclusion

The results presented in this study show that Raman spectroscopy is sensitive to subtle biochemical changes that coincide with the severity of acute inflammation in the colon. In detail, 18 Raman maps of mouse colon tissues

from 10 control and DSS-induced colitis animals were generated and evaluated relative to clinical and histopathological parameters of disease severity. Raman peak ratios that significantly differ between treatment groups were isolated for mucosal and submucosal layers of the tissues and linked with biologically relevant contributors in colon tissue and mucosal injury of inflammatory disease, including lipid, carotenoid, amino acid, and collagen related features. Furthermore, Raman peak ratios were found that depicted significant differences between control and DSS administration for 3 days, time points that did not demonstrate significant differences based on traditional DSS disease metrics. Contrary to the arguments that this experimental colitis model does not recapitulate human IBD, the spectra presented here from mouse colon tissues were consistent with previously reported human tissue biopsies for IBD patients. This work demonstrates the influence of active inflammation on Raman spectra acquired from the colon and the potential for objective staging of inflammatory disease severity based on Raman spectroscopy.

6.7 Acknowledgements

This work was supported in part by the following funding sources: NIH R01 HD081121, NIH F31 CA168238, NIH grant R01AT004821 (K.T.W.), a Department of Veterans Affairs Merit Review grant I01BX001453 (K.T.W.), the Vanderbilt Digestive Disease Research Center funded by NIH grant

P30DK058404 (K.T.W.), the Thomas F. Frist Sr. Endowment (K.T.W.), and the Vanderbilt Center for Mucosal Inflammation and Cancer (K.T.W.), the Vanderbilt CTSA grant UL1 TR000445 from NCATS/NIH, NCI/NIH Cancer Center Support Grant 2P30 CA068485-14 and the Vanderbilt Mouse Metabolic Phenotyping Center Grant 5U24DK059637-13. Whole slide imaging was performed in the Digital Histology Shared Resource at Vanderbilt University Medical Center (www.mc.vanderbilt.edu/dhsr).

6.8 References

1. Ananthakrishnan AN. Epidemiology and risk factors for IBD. *Nature reviews Gastroenterology & hepatology.* 2015;12(4):205-217.
2. Shaffer EA, Thomson ABR. *First Principles of Gastroenterology: The Basis of Disease and an Approach to Management.* Canadian Association of Gastroenterology; 1997.
3. Baldassano RN, Piccoli DA. Inflammatory bowel disease in pediatric and adolescent patients. *Gastroenterology clinics of North America.* 1999;28(2):445-458.
4. Sandler RS, Everhart JE, Donowitz M, et al. The burden of selected digestive diseases in the United States. *Gastroenterology.* 2002;122(5):1500-1511.
5. Kugathasan S, Fiocchi C. Progress in basic inflammatory bowel disease research. *Semin Pediatr Surg.* 2007;16(3):146-153.
6. Cobrin GM, Abreu MT. Defects in mucosal immunity leading to Crohn's disease. *Immunol Rev.* 2005;206:277-295.
7. Targan SR, Karp LC. Defects in mucosal immunity leading to ulcerative colitis. *Immunol Rev.* 2005;206:296-305.

8. Berrebi D, Besnard M, Fromont-Hankard G, et al. Interleukin-12 expression is focally enhanced in the gastric mucosa of pediatric patients with Crohn's disease. *Am J Pathol.* 1998;152(3):667-672.

9. Heller F, Florian P, Bojarski C, et al. Interleukin-13 is the key effector Th2 cytokine in ulcerative colitis that affects epithelial tight junctions, apoptosis, and cell restitution. *Gastroenterology.* 2005;129(2):550-564.

10. Parronchi P, Romagnani P, Annunziato F, et al. Type 1 T-helper cell predominance and interleukin-12 expression in the gut of patients with Crohn's disease. *Am J Pathol.* 1997;150(3):823-832.

11. Podolsky DK. Inflammatory bowel disease. *N Engl J Med.* 2002;347(6):417-429.

12. Xavier RJ, Podolsky DK. Unravelling the pathogenesis of inflammatory bowel disease. *Nature.* 2007;448(7152):427-434.

13. Pence I, Mahadevan-Jansen A. Clinical instrumentation and applications of Raman spectroscopy. *Chem Soc Rev.* 2016;45(7):1958-1979.

14. Feld MS, Manoharan R, Salenius J, et al. Detection and Characterization of Human Tissue Lesions with Near Infrared Raman Spectroscopy. Paper presented at: Proceedings of SPIE 23881995; Bellingham, WA.

15. Molckovsky A, Song LMWK, Shim MG, Marcon NE, Wilson BC. Diagnostic potential of near-infrared Raman spectroscopy in the colon: differentiating adenomatous from hyperplastic polyps. *Gastrointestinal endoscopy.* 2003;57(3):396-402.

16. Chowdary MV, Kumar KK, Thakur K, et al. Discrimination of normal and malignant mucosal tissues of the colon by Raman spectroscopy. *Photomedicine and laser surgery.* 2007;25(4):269-274.

17. Widjaja E, Zheng W, Huang ZW. Classification of colonic tissues using near-infrared Raman spectroscopy and support vector machines. *International journal of oncology.* 2008;32(3):653-662.

18. Stone N, Kendall C, Shepherd N, Crow P, Barr H. Near-infrared Raman spectroscopy for the classification of epithelial pre-cancers and cancers. *J Raman Spectrosc.* 2002;33(7):564-573.

19. Bergholt MS, Lin K, Wang J, et al. Simultaneous fingerprint and high-wavenumber fiber-optic Raman spectroscopy enhances real-time in vivo diagnosis of adenomatous polyps during colonoscopy. *Journal of biophotonics.* 2016;9(4):333-342.

20. Kanter EM, Majumder S, Kanter GJ, Woeste EM, Mahadevan-Jansen A. Effect of hormonal variation on Raman spectra for cervical disease detection. *Am J Obstet Gynecol.* 2009;200(5):512 e511-515.

21. Bi X, Walsh A, Mahadevan-Jansen A, Herline A. Development of spectral markers for the discrimination of ulcerative colitis and Crohn's disease using Raman spectroscopy. *Diseases of the colon and rectum.* 2011;54(1):48-53.

22. Bielecki C, Bocklitz TW, Schmitt M, et al. Classification of inflammatory bowel diseases by means of Raman spectroscopic imaging of epithelium cells. *J Biomed Opt.* 2012;17(7):076030.

23. Pence IJ, Beaulieu DM, Horst SN, et al. Clinical characterization of in vivo inflammatory bowel disease with Raman spectroscopy. *Biomedical optics express.* 2016;In Review.

24. Pence IJ, Nguyen QT, Bi X, et al. Endoscopy-coupled Raman spectroscopy for in vivo discrimination of inflammatory bowel disease. 2014.

25. Coburn LA, Gong X, Singh K, et al. L-arginine supplementation improves responses to injury and inflammation in dextran sulfate sodium colitis. *PLoS One.* 2012;7(3):e33546.

26. Singh K, Chaturvedi R, Barry DP, et al. The apolipoprotein E-mimetic peptide COG112 inhibits NF-kappaB signaling, proinflammatory cytokine expression, and disease activity in murine models of colitis. *J Biol Chem.* 2011;286(5):3839-3850.

27. Yan F, Cao H, Cover TL, et al. Colon-specific delivery of a probiotic-derived soluble protein ameliorates intestinal inflammation in mice through an EGFR-dependent mechanism. *J Clin Invest.* 2011;121(6):2242-2253.

28. Okayasu I, Hatakeyama S, Yamada M, Ohkusa T, Inagaki Y, Nakaya R. A novel method in the induction of reliable experimental acute and chronic ulcerative colitis in mice. *Gastroenterology.* 1990;98(3):694-702.

29. Olivares-Villagomez D, Algood HM, Singh K, et al. Intestinal epithelial cells modulate CD4 T cell responses via the thymus leukemia antigen. *J Immunol.* 2011;187(8):4051-4060.

30. Bove PF, Wesley UV, Greul AK, Hristova M, Dostmann WR, van der Vliet A. Nitric oxide promotes airway epithelial wound repair through enhanced activation of MMP-9. *Am J Respir Cell Mol Biol.* 2007;36(2):138-146.

31. Wu G, Morris SM, Jr. Arginine metabolism: nitric oxide and beyond. *Biochem J.* 1998;336 (Pt 1):1-17.

32. Hedegaard MAB, Bergholt MS, Stevens MM. Quantitative multi-image analysis for biomedical Raman spectroscopic imaging. *Journal of biophotonics.* 2016;9(5):542-550.

33. McCreery RL. *Raman spectroscopy for chemical analysis.* New York: New York : John Wiley & Sons; 2000.

34. Czamara K, Majzner K, Pacia MZ, Kochan K, Kaczor A, Baranska M. Raman spectroscopy of lipids: a review. *J Raman Spectrosc.* 2015;46(1):4-20.

35. De Gelder J, De Gussem K, Vandenabeele P, Moens L. Reference database of Raman spectra of biological molecules. *J Raman Spectrosc.* 2007;38(9):1133-1147.

36. Zhu G, Zhu X, Fan Q, Wan X. Raman spectra of amino acids and their aqueous solutions. *Spectrochimica acta.* 2011;78(3):1187-1195.

37. Bergholt MS, Zheng W, Lin K, et al. Characterizing variability in in vivo Raman spectra of different anatomical locations in the upper gastrointestinal tract toward cancer detection. *J Biomed Opt.* 2011;16(3).

38. Bergholt MS, Zheng W, Lin K, et al. Characterizing Variability of In Vivo Raman Spectroscopic Properties of Different Anatomical Sites of Normal Colorectal Tissue towards Cancer Diagnosis at Colonoscopy. *Anal Chem.* 2015;87(2):960-966.

39. Rieder F, Brenmoehl J, Leeb S, Scholmerich J, Rogler G. Wound healing and fibrosis in intestinal disease. *Gut.* 2007;56(1):130-139.

40. Stumpf M, Krones CJ, Klinge U, Rosch R, Junge K, Schumpelick V. Collagen in colon disease. *Hernia : the journal of hernias and abdominal wall surgery.* 2006;10(6):498-501.

41. Ricciotti E, FitzGerald GA. Prostaglandins and inflammation. *Arterioscler Thromb Vasc Biol.* 2011;31(5):986-1000.

42. Mutsaers SE, Bishop JE, McGrouther G, Laurent GJ. Mechanisms of tissue repair: from wound healing to fibrosis. *Int J Biochem Cell Biol.* 1997;29(1):5-17.

43. D'Odorico SBRCRDIDMAFGCSA. Reduced Plasma Antioxidant Concentrations and Increased Oxidative DNA Damage in Inflammatory Bowel Disease. *Scandinavian journal of gastroenterology.* 2001;36(12):1289-1294.

44. de Oliveira VE, Castro HV, Edwards HGM, de Oliveira LFC. Carotenes and carotenoids in natural biological samples: a Raman spectroscopic analysis. *J Raman Spectrosc.* 2010;41(6):642-650.

45. Son DO, Satsu H, Shimizu M. Histidine inhibits oxidative stress- and TNF-alpha-induced interleukin-8 secretion in intestinal epithelial cells. *FEBS Lett.* 2005;579(21):4671-4677.

46. Edelblum KL, Washington MK, Koyama T, Robine S, Baccarini M, Polk DB. Raf protects against colitis by promoting mouse colon epithelial cell survival through NF-kappa B. *Gastroenterology.* 2008;135(2):539-551.

47. Shirazi T, Longman RJ, Corfield AP, Probert CSJ. Mucins and inflammatory bowel disease. *Postgraduate medical journal.* 2000;76(898):473-478.

CHAPTER 7

CONCLUSIONS

7.1 Summary and integration

This dissertation represents the ongoing development of Raman spectroscopy for detecting changes in the colon associated with inflammatory bowel disease. Despite the continued advances by the medical community for managing IBD, a universally definitive gold standard for differential diagnosis is elusive.[1] This project has demonstrated the potential for a new diagnostic method to accurately differentiate Crohn's disease and ulcerative colitis, regardless of patient differences. With continued development, the resulting tool may provide doctors with another indicator of a patient's disease in a matter of seconds during standard colonoscopy procedures. Furthermore, this tool has demonstrated feasibility for objective scoring of disease severity, with the potential to aid in evaluating relative therapeutic response. These advancements could significantly improve the management of inflammatory bowel disease with respect to both time and cost.

The first part of this work established a platform for evaluating fiber optic Raman spectroscopy probe designs in regards to specific applications for translational medicine. These probes are the primary tool used to interface with

patients and tissue samples, yet have largely been designed based on theoretical performance in non-scattering situations that do not represent most biomedical applications. The modeling and experimental validation results indicate the improved superficial performance of probe designs with maximized overlap for excitation and collection cones at the sample surface. Conversely, the probe design to interrogate deep signal sources becomes less important depending upon the optical properties of the sample of interest. These findings suggest that probe designs should be selected in the context of the specific optical properties of the target application rather than informed only by the theoretical depth interrogated.

The second segment of work reported here utilized an optimized fiber optic Raman spectroscopy probe for the first *in vivo* study applied to IBD during colonoscopy. Preliminary discrimination performance was poor, but upon subsequent investigations accounting for the impact of the disease process and other patient variables, classification based on measured Raman spectra was improved to rates as high as 90% sensitivity and 75% specificity. This demonstration of the success of Raman techniques for detection of IBD in a diverse, relevant clinical population establishes the potential for Raman spectroscopy as a clinical adjunct in objective disease discrimination and staging of disease severity.

The final pair of investigations comprised in this dissertation work investigated the influence of patient and disease variables from excised human

tissues and the influence of disease severity in a controlled animal model of experimental colitis. These studies underscored the influence of disease severity, patient variables, and colon segments on the measured Raman spectra and provided support for implementing stratified classification schemes incorporating these factors.

Current protocols for clinical discrimination of IBD cannot provide definitive information for every patient and underline the need for further development of adjunct technologies.[1,2] Previous work in the field of biophotonics has demonstrated the potential of Raman spectroscopy techniques for differentiating IBD types.[3,4] This work, applied to *ex vivo* tissue biopsy samples, merited extension to a clinical population with measurements performed during colonoscopy procedures.

The preliminary studies, referenced in Chapter 2 laid the foundation for work presented in this dissertation. Work spanning the past two decades demonstrate the technological and application developments for Raman spectroscopy for clinical and translational medicine.[5] The studies we conducted in this dissertation evaluated the fiber optic probe technology used for data collection from colon mucosal tissues during colonoscopy, measured a patient population with IBD for discrimination, and investigated *ex vivo* and experimental colitis tissues to understand the contributions of disease and patient variables on measured spectral data. The previous reports applying Raman spectroscopy for IBD achieved promising classification performance

based on small sample sizes of *ex vivo* tissues and multivariate classification algorithms.[3,4] However, studies utilizing Raman spectroscopy for the colon and other tissue *in vivo* demonstrated potential confounding factors that were not investigated in the initial IBD studies.[6-9] A major challenge for translationing applications of biophotonics to clinical medicine is extending of findings from a controlled and often simplified *ex vivo* model of pathology to the native presentation of disease in the body. With this transition to *in vivo* studies, care mus be taken to consider alterantive sources of signals that were previously controlled. This PhD dissertation has sought to not only implement Raman spectroscopy *in vivo* for IBD detection but also to characterize the sources of confounding signals and develop a tool that is broadly applicable to clinical colonoscopy prodecures. This challenge required that this tool work not only in a controlled laboratory setting but in a clinical setting without ideal conditions. To enable this translation, care was required to thoroughly characterize equipment, diease, and physiological variations to identify the features relevant to disase presentation.

The first step of this PhD dissertation, as presented in Chapter 3, addresses Aim 1 and the evaluation of fiber optic probe designs utilized for *in vivo* Raman spectroscopy studies. As the target application for this dissertation required integration of Raman instrumentation with standard colonoscopy systems and the disease processes for these inflammatory disease differed from many prior clinical applications, a thorough evaluation of the tools utilized for

data collection was necessary. To this end, a probabilistic model was developed and experimentally validated with biological tissue phantoms. The model reported here is novel as it explicitly incorporates multiple distinct and independent optical phenomena all of which are simultaneously detected during Raman spectroscopic measurements. By evaluating the performance of Raman probes for detecting Raman signals with respect to the competing light-tissue interactions for biologically relevant optical properties, more realistic estimation of *in vivo* performance may be obtained. This work highlights the importance of proper selection of fiber optic probe designs for interfacing with tissue targets based on the intended biomedical application. The developed model also has the potential to improve the way fiber optic probes are tailored for biomedical applications by providing a platform for assessment that is relevant to most fiber optic probe based detection modalities. Considering the superficial disease target and reported tissue properties, this work supported the selection of a micro lens probe design for undertaking *in vivo* investigation of clinical IBD.

In Chapter 4, a clinical Raman spectroscopy system with a superficially focused probe design was implemented to address Aim 2. By recruiting a sample population of IBD and control patients undergoing surveillance colonoscopy procedures at the Vanderbilt University Medical Center (VUMC), we were able to demonstrate *in vivo* Raman spectroscopy the potential for disease discrimination. Initially, the heterogeneity of disease presentation

proved challenging for differentiation of spectral signatures based multivariate statistical analysis, achieving 62-83% sensitivity and 22-55% specificity for separating Crohn's disease and ulcerative colitis. This performance, while providing an early benchmark for *in vivo* detection, is not as promising as the previous *ex vivo* studies of IBD samples. However, by integrating patient and disease variables into the classification algorithm, improved performance was attained, reaching values as high as 90% sensitivity and 75% specificity. This improvement in disease discrimination indicated promise for *in vivo* Raman techniques for IBD applications. Unlike in the previous reports where small, *ex vivo* samples were utilized and controlled for measurement locations and tissue condition, this *in vivo* assessment provides a more realistic indication of the performance of Raman spectroscopy as a clinical tool. These results also confirmed prior reports of the potential influence of patient and disease variables on classification performance. Due to the lack of control over patient tissues and limited access to patients during colonoscopy procedures, it was not feasible to assess most patient variables from the data obtained during endoscopy. The questions of which factors were most influential on Raman spectra of colitis required *ex vivo* human and animal tissues for more thorough investigation and control.

To evaluate variables that impact IBD differentiation based on *in vivo* Raman spectroscopy tissue measurements, the research reported in Chapter 5 and Chapter 6 was conducted. For this part of the research, different methods

of evaluating colon tissues relating to IBD were investigate to characterize the influence of patient and disease variables. The first of these studies utilized tissue specimens from patients recruited at VUMC scheduled to undergo partial or total resection of the colon in relation to inflammatory diseases. Exploring the interplay of the anatomical position in the colon from which a measurement was made and the histological markers of inflammatory disease, Chapter 5 demonstrated that several patient and disease variables significantly impact Raman spectra. To decouple these effects, generalized linear models were implemented to model Raman peak ratios as a function of patient and histological disease scores. Generalized estimating equations were utilized to group measurements from a single specimen to account for complex correlations within the dataset. Patient BMI and IBD type significantly impacted Raman spectra acquired while patient age was a non-significant parameter. Colon segment, chronic disease, and acute inflammation were all significant factors predictive of Raman peak ratios confirming the importance of these variables reported in Chapter 4. Other factors of chronic and acute IBD that had not been previously explored with Raman techniques were identified based on histopathological evaluation and may provide further avenues for investigation.

While the work reported in Chapter 5 took steps to control for several patient (age, BMI, colon segment) and disease variables (active & chronic inflammation, lymphoid hyperplasia, submucosal fat deposition) while

investigating IBD presentation, measurements from a patient population are often rife with latent variables. To avoid unintended influence of patient variables such as the gender, diet, smoking status, duration of disease, and prior surgical and therapeutic interventions, Chapter 6 reports work that utilized a well characterized mouse model of experimental colitis. In this model, chemical induction of mucosal injury enables a graded response of disease severity that can be controlled on a relatively short time scale and has established metrics for scoring independent parameters of inflammation and damage.[10-12] Utilizing high-resolution Raman microspectroscopy of mouse colon tissue after mucosal injury, spectral maps of tissue were acquired that provide spatial context to the biochemical changes that occur as a function of disease severity. The results of this pilot evaluation of DSS-induced experimental colitis reveal several Raman features that are highly correlated with clinical and histological scores of disease severity. Furthermore, specific Raman peak ratios could be tied to biological processes associated with inflammation, oxidative stress, epithelial recovery, and wound healing.[13-15] A concern for utilizing animal models to study human disease stems from the uncertainty regarding the extent to which mouse models are representative of the human disease process for IBD. The Raman spectra obtained from this model of mucosal injury in mice were nearly perfect replicates of spectra collected from *ex vivo* human biopsy tissues from IBD patients previously reported in literature.[4] From this finding, we can assert that the DSS-induced colitis model in mice is relevant for human UC in multiple

aspects including clinical presentation of symptoms, histological features of disease presentation, and biomolecular composition of control and diseased tissues. The results of this study further indicate the sensitivity of Raman scattering to subtle biochemical changes associated with acute inflammatory processes and the need to account for disease severity in discrimination of IBD type.

In Appendix I, results from an *in vivo* assessment of numerous sources of variability that influence Raman spectra are reported. While the demonstration for some of these variables is conducted in skin due to the ease of access, the impacts of users, instruments, and the inherent physiological changes present across an organ are all support our findings relevant to the *in vivo* application of Raman spectroscopy during colonoscopy for IBD. The Raman data reported herein relates that physiologically induced variability is highly influential relative to other sources when instruments are properly designed and calibrated and the users of those instruments are adequately trained. These results have clear and significant implications for the future application of Raman spectroscopic tools with respect to clinical and translational medicine, extending far beyond the specific applications presented as part of this dissertation.

A number of significant challenges were overcome during the course of this PhD. While our group had conducted a number of other *in vivo* studies utilizing Raman spectroscopy, none had previously been integrated with

endoscopic procedures prior to this work. Based on demonstrations of endoscope compatible probe designs from other research groups and the physical constraints of the instruments used by our clinical collaborators, new endoscope compatible instrument designs and data collection and processing software were created and implemented for real-time feedback for *in vivo* evaluation of IBD during brief colonoscopy procedures. However while the fiber optic probes utilized for Raman studies are made with materials and methods that allow for clinical implementation, they are not rugged and durable devices. Over the course of the patients recruited during this dissertation, five separate Raman probes of identical design were utilized for data collection, four of which were broken during clinical measurement or disinfection. As alluded to in Chapter 2, strict calibration procedures are not standardized across the global Raman spectroscopy community at large and inter-device calibration is an ongoing challenge. To that end, nearly 70% of the patients recruited for this work have not been included in the analysis, yet stand as a potential independent validation set pending further developments in the field for instrument comparison. Another obstacle in this work is the challenge of controlling disease presentation for a human population. A broad range of patient backgrounds, BMIs, ages, disease durations, and prior therapeutic interventions are represented in the data reported, most of which could not be controlled in the analyses. Despite this latent and potentially confounding factors for *in vivo* investigation, the performance of disease classification was improved by

accounting for disease and patient variables. By more thorough investigation of influential factors that impact *in vivo* Raman spectra from colon tissues, such as both those listed above and those considered in Chapter 5 and Chapter 6, we can develop a comprehensive understanding of the variables that must be integrated into the prediction algorithms to further improve IBD discrimination.

7.2 Recommendations

Based on the conclusions from the work presented here, there are a number of recommendations for immediate research avenues as well as long-term studies. With the multimodal Monte Carlo model for evaluating fluorescence and Raman scattering for differing fiber optic probe designs, the immediate need is to implement the code in a parallelized and efficient language, such as C++. The results from this improvement would enable the use of significantly higher numbers of photons in models for more powerful conclusions. This combined model has the potential to facilitate further investigation of optimized probe designs for specific applications relevant to translational medicine for any instrument based on fiber optic detection, including spectroscopic techniques for Raman scattering, fluorescence, elastic scattering, and diffuse reflectance. A direct next step would be to systematically evaluate the impact of reduced scattering coefficient on detected signals for Raman fiber optic probe designs. The results from investigation would have

direct implications for the entire field of Raman spectroscopy for clinical applications. As a majority of the probe designs utilized for detection have not been optimized in reference to specific tissue optical properties, this model based evaluation could improve the designs of instruments utilized for applications in almost every human tissue or disease target.

The *in vivo* investigation of Raman spectroscopy for discrimination of IBD type should be expanded to include a larger patient population and perform independent validation of the results reported here. To this end, a primary need is to establish methods for instrument standardization that is capable of accounting for fiber optic probe specific signals as a result of fabrication. By improving the procedures and algorithms for inter-instrument standardization, it would be possible to conduct multi-center trials and combine data collected by multiple independent groups for maximized statistical power. The obstacle of correcting for fiber optic probe dependent responses is the direct limitation to utilizing the total combined dataset for analysis and evaluation the performance of Raman spectroscopy for IBD discrimination. A directed investigation utilizing multiple probes fabricated from the same batch of materials and utilized to collect spectra from identical standard and biological tissue samples is a necessary step to establish the between instrument standardization needed. This obstacle remains a challenge facing the entire field of Raman spectroscopy for clinical biomedical applications, and merits concerted effort.

As this work represents the first *in vivo* study utilizing Raman spectroscopy for IBD applications, there is a direct need to independently substantiate the results presented here. Further studies, ideally conducted in clinical IBD populations of different regions or demographics, are needed to demonstrate that the performance reported for discrimination extends to a larger patient population. Furthermore, as the classification performance for IBD discrimination improved based on the stratification of measurements by disease and measurement location, a larger more robust dataset is essential to establish realistic estimates of the prediction performance after incorporating the appropriate factors. A powered study with a complete block design for age matched patients with consistent prior therapies would provide a controlled comparison of the performance while minimizing the influence of some previously uncontrolled factors.

A limit to the practical adoption of Raman spectroscopy for IBD differentiation is the requirement for endoscopic evaluation. Based on the differences between the common disease presentations of ulcerative colitis and Crohn's disease, an interesting approach would be to utilize only measurements obtained from the rectum to investigate minimally-invasive disease discrimination. While sigmoidoscopy procedures are less commonly performed for clinical IBD evaluation, successful demonstration of this evaluation may reduce the need for colonoscopy procedures with anesthesia and the associated preparation protocols, benefitting both patients and medical providers.

Another interesting, if long term, investigation is the extension of Raman spectroscopy for disease discrimination in the patient population of greatest need: indeterminate colitis or IBD unspecified. A longitudinal study of IC patients to evaluate disease classification based on Raman spectra relative to eventual differential diagnosis would demonstrate the potential value of this clinically relevant optical technique as an adjunct for IBD evaluation during colonoscopy. A primary difficulty in such a study is the unknown timeline associated with the determination of a differential diagnosis; as such, this study may require a set time frame for recruitment and evaluation prior to analysis and subsequent follow-up. By investigating the biochemical signatures of this challenging disease entity, the potential for disease discrimination and assessment by Raman spectroscopy may prove to be of greater utility to clinicians. A similarly informative investigation, utilizing this technique to objectively score active inflammation prior to and at a set time point after initiating a new therapeutic intervention, such as anti-TNF-α medication, would provide another indicator of the value of Raman techniques for IBD evaluation. Based on the *in vivo* study that showed sensitivity to the severity of active inflammation, and the confirming data from the *ex vivo* studies of sources of influential variation, Raman scattering may provide a valuable tool for unbiased characterization of disease severity. By investigating the sensitivity of Raman scattering relative to outcome based interventions for therapeutic response, this tool could aid in the clinical care of IBD patients.

Finally, with respect to the studies characterizing the impact of patient and disease variables on Raman spectra of inflammatory disease, there are a number other studies that should be pursued. One investigation should target true control colon specimens for anatomical heterogeneity and spatial variability. As healthy colon tissue is not generally removed from the body, these investigations may be best performed with cadaver tissues that are truly independent of inflammatory disease effects. A promising continuation of the studies of experimental colitis would be to correlate the acquired Raman signatures obtained from mouse colon tissues with proteomic analysis of the frozen colon collected as part of the protocol for tissue removal. This study could further establish the sensitivity of confocal Raman mapping to biochemical changes associated with inflammatory disease presentation. Exploring the Raman profiles of colon tissues from mice after the administration of supplements that inhibit inflammation, such as L-arginine, may provide interesting insights into the biomolecular changes that are employed for tissue protection and broaden our understanding of anti-inflammatory pathways. The final suggestion for integrating the disease characterization studies would be to compare human and experimental colitis specimens under the same conditions for clinical, histological, and spectral similarities. Such a study, combining the information content obtained from patient samples and the controlled model of mucosal injury would confirm the appropriateness of this experimental colitis model for studying the human

disease process and enable stronger conclusions to be made from experimental investigations about the potential application to patients.

7.3 Contributions to the field and societal impact

The work detailed in this dissertation comprises contributions to the field of biophotonics and gastroenterology, but more broadly to the clinical translation of optical technologies for unmet medical needs. To that end, combined data collection and real-time processing software was written for clinical implementation. The *in vivo* study performed here is the first report of colonoscopy coupled Raman spectroscopy in patients for IBD. Furthermore, while Raman scattering techniques have often been applied to cancer applications, this work is, to our knowledge, the first set of Raman spectroscopy studies focused on differentiating the biochemical changes that occur between two inflammatory processes *in vivo*. This demonstration of the potential of vibrational spectroscopy represents a new area of research for biophotonics with numerous research targets for clinical medicine such as Eosinophilic esophagitis or gastroesophageal reflux disorder.

The probabilistic Monte Carlo model reported in this dissertation represents a novel combination of models for the competing optical phenomena that are detected during probe based Raman spectroscopy measurements. Based on the model predictions and experimental validation that enable direct

comparison of multiple probe designs, these results demonstrate the fundamental need for instrument designs based on tissue applications with respect to the optical properties of the targets. Subsequent investigations may reveal optimized instrument designs and clarify the tissues and optical properties for which certain probe designs are of greatest benefit.

The development of data collection and processing algorithms for clinical implementation and the design of the instrumentation to meet the constraints for integration in a clinical workflow mark essential developments that are paramount for the translation of Raman spectroscopy, and other fiber optic probe based optical techniques, to clinical use. By combining the optimized instrumentation and algorithms developed, real-time data collection, processing, and multivariate analysis can be performed such that immediate feedback is available without disrupting clinical workflow. This work has also extensively characterized the biochemical changes that occur in *in vivo*, *ex vivo*, and animal model tissues as a function of inflammatory disease. These combined evaluations of variability sources associated with IBD represent the most extensive investigations of colon heterogeneity for clinical deployment of Raman spectroscopic techniques.

7.4 References

1. American Society for Gastrointestinal Endoscopy Standards of Practice C, Shergill AK, Lightdale JR, et al. The role of endoscopy in

inflammatory bowel disease. Gastrointestinal endoscopy. 2015;81(5):1101-1121 e1101-1113.

2. Melmed GY, Targan SR. Future biologic targets for IBD: potentials and pitfalls. Nature reviews Gastroenterology & hepatology. 2010;7(2):110-117.

3. Bi X, Walsh A, Mahadevan-Jansen A, Herline A. Development of spectral markers for the discrimination of ulcerative colitis and Crohn's disease using Raman spectroscopy. Diseases of the colon and rectum. 2011;54(1):48-53.

4. Bielecki C, Bocklitz TW, Schmitt M, et al. Classification of inflammatory bowel diseases by means of Raman spectroscopic imaging of epithelium cells. J Biomed Opt. 2012;17(7):076030.

5. Pence I, Mahadevan-Jansen A. Clinical instrumentation and applications of Raman spectroscopy. Chem Soc Rev. 2016;45(7):1958-1979.

6. Bergholt MS, Zheng W, Lin K, et al. Characterizing variability in in vivo Raman spectra of different anatomical locations in the upper gastrointestinal tract toward cancer detection. J Biomed Opt. 2011;16(3).

7. Bergholt MS, Zheng W, Lin K, et al. Characterizing Variability of In Vivo Raman Spectroscopic Properties of Different Anatomical Sites of Normal Colorectal Tissue towards Cancer Diagnosis at Colonoscopy. Anal Chem. 2015;87(2):960-966.

8. Pence IJ, Vargis E, Mahadevan-Jansen A. Assessing Variability of In Vivo Tissue Raman Spectra. Appl Spectrosc. 2013;67(7):789-800.

9. Vargis E, Byrd T, Logan Q, Khabele D, Mahadevan-Jansen A. Sensitivity of Raman spectroscopy to normal patient variability. J Biomed Opt. 2011;16(11):117004.

10. Coburn LA, Gong X, Singh K, et al. L-arginine supplementation improves responses to injury and inflammation in dextran sulfate sodium colitis. PLoS One. 2012;7(3):e33546.

11. Okayasu I, Hatakeyama S, Yamada M, Ohkusa T, Inagaki Y, Nakaya R. A novel method in the induction of reliable experimental acute and chronic ulcerative colitis in mice. Gastroenterology. 1990;98(3):694-702.

12. Singh K, Chaturvedi R, Barry DP, et al. The apolipoprotein E-mimetic peptide COG112 inhibits NF-kappaB signaling, proinflammatory cytokine expression, and disease activity in murine models of colitis. J Biol Chem. 2011;286(5):3839-3850.

13. D'Odorico SBRCRDIDMAFGCSA. Reduced Plasma Antioxidant Concentrations and Increased Oxidative DNA Damage in Inflammatory Bowel Disease. Scandinavian journal of gastroenterology. 2001;36(12):1289-1294.

14. Ricciotti E, FitzGerald GA. Prostaglandins and inflammation. Arterioscler Thromb Vasc Biol. 2011;31(5):986-1000.

15. Rieder F, Brenmoehl J, Leeb S, Scholmerich J, Rogler G. Wound healing and fibrosis in intestinal disease. Gut. 2007;56(1):130-139.

APPENDIX 1

ASSESSING VARIABILITY OF *IN VIVO* TISSUE RAMAN SPECTRA

A1.1 Abstract

Raman spectroscopy (RS) has received increasing attention as a potential tool for clinical diagnostics. However, the unknown comparability of multiple tissue RS systems remains a major issue for technique standardization and future multi-system trials. In this study, we evaluated potential factors affecting data collection and interpretation utilizing the skin as an example tissue. The effects of contact pressure and probe angle were characterized as potential user-induced variability sources. Similarly, instrumentation-induced variability sources of system stability and system-dependent response were also analyzed on skin and a non-volatile biological tissue analog. Physiologically-induced variations were studied on multiple tissue locations and patients. The effect of variability sources on spectral line shape and dispersion was analyzed using analysis of variance methods and a new metric for comparing spectral dispersion was defined. In this study, *in vivo* measurements were made on multiple sites of skin from five healthy volunteers with four stand-alone fiber optic probe-based tissue RS systems. System stability and controlled user-induced variables had no effects on obtained spectra. By contrast,

instrumentation and anatomical-location of measurement were significant sources of variability. These findings establish the comparability of tissue Raman spectra obtained by unique systems. Furthermore, we suggest steps for further procedural and instrumentation standardization prior to broad clinical applications of the technique.

A1.2 Introduction

Numerous research groups have capitalized on the sensitivity of Raman spectroscopy (RS) to subtle changes in biochemistry to study tissues *in vivo* without exogenous dyes, contrast agents, or extensive sample preparation. Raman scattering has been utilized for decades to identify substances, detect changes in chemical bonding, and monitor the quality of chemicals by probing inherent vibrational modes. Publications using RS to study disease markers associated with several organs are available, including the cervix,[1-4] bladder and prostate,[5] lung,[6] skin,[7-12] bone,[13, 14] breast,[15, 16] and GI tract.[17-20] Providing information regarding healthy tissues, disease progression, and the effects of treatment, RS has been noted as a potential tool for medical screening, diagnosis, and guidance. Due to the underlying weak optical phenomenon, the technology for *in vivo* measurement has only become available in the last 2 decades with NIR sources and detectors to minimize competing autofluorescence signals and avoid tissue scattering and absorption peaks. A typical tissue RS system consists of an NIR excitation source, fiber optic probe

to interrogate the tissue and collect the scattered photons, a high-throughput spectrograph, and a NIR-optimized, back-illuminated, deep-depletion charge coupled device (CCD) detector.[21] Several excitation wavelengths have been investigated, including 785 and 830nm, but reports suggest tissue-dependent responses and indicate advantages for using 785nm for epithelial applications.[22] In general for *in vivo* implementation, the parameters for generating Raman signal are optimized to provide the best SNR in a short measurement time with minimal laser power. Since the initial reports of human tissue spectra in 1992,[23] technological development and technique refinement have enabled *in vivo* Raman measurements. Spectra can now be collected, corrected for undesirable signal components, and processed to rapidly provide feedback for users.[12, 24, 25] Previous work has identified criteria required for adopting a novel biomedical diagnostic technique, which is a primary goal for many tissue spectroscopists.[26] In medical applications, many of these requirements are satisfied by RS for *in vivo* use: sensitivity to changes in tissue, application to *in vivo* studies, and novelty of information obtained non-invasively.[27] However, standard Raman spectral databases are not available for tissue, limiting RS's role in influencing clinical decisions and patient prognoses. Both research lab and private industry studies using RS to diagnose disease or understand tissue are becoming more common, but the RS community lacks standardization and a thorough understanding of the comparability of measurements made across multiple systems, tissue locations, and collection times.

Epithelial tissues such as the cervix, skin, oral mucosa, esophagus, and GI tract have been common targets of study with RS. Because of several characteristics, including ease of access, the skin is a convenient organ for conducting the necessary standardization studies. Skin is a complex and turbid tissue, with a layered structure, multiple functions, and inhomogeneous composition that can vary widely between patients and among various locations on a single patient. Thus, as a challenging organ, standardization findings should translate to other tissues. Beyond studying the tissue itself, the skin also acts as a good model for other epithelial tissues that are common targets for optical detection. Most importantly, all sources of potential variability identified for the skin are generalizable to other tissues as well.

Several research groups have reported using RS for a variety of applications including the detection of subtle changes in the skin related to wound healing,[28] disease progression[10, 29], natural moisturizing factor levels[30], protective antioxidants such as carotenoids β-carotene and lycopene,[8, 31] and cosmetics.[32] The non-destructive nature of RS is ideal as an analytical or clinical tool for non-invasively monitoring the skin for changes associated with damage, disease, or treatment. Several groups have demonstrated the feasibility of using RS to differentiate between skin malignancies and healthy tissues in vitro.[11, 12, 33] These studies also showed that different spectra correlate with specific skin disease types. Tissue components and structural conformations for several biomolecules related to skin function, including proteins, lipids, and

carotenoids, have been determined based on Raman vibrations. These results have yielded new information about skin aging and structural properties that may differentiate disease types from normal tissues.[8, 9, 31] Furthermore, the healing of acute and chronic skin wounds has been monitored non-invasively with RS to provide new information on the biochemistry and progression of this complex process.[28, 34, 35] Benign conditions like psoriasis and atopic dermatitis, hydration differences, and the effect of topical treatments have also been studied using RS.[29, 30, 36-38]

Before RS can be effectively applied to a clinical problem, technique standardization is necessary to account for confounding sources of variability. Current reports suggest that RS can be translated into the clinical setting with portable systems and fiber optic probes. However, as a clinical tool, RS measurements must be repeatable and free of confounding factors introduced by the system operator. With the probe-tissue interface of these systems, both contact pressure and probe angle can change, so the effects of user-induced variability must be understood and controlled. Other research groups have reported the effects of probe contact pressure on measurements of diffuse optical spectroscopy and fluorescence spectroscopy in soft tissues.[39-42] Shim *et al.* reported no specific major spectral artifacts from contact pressure and probe angle on *in vivo* RS measurements during clinical gastrointestinal endoscopy.[20] To ensure that user perception of contact pressure and probe angle will not

confound spectral measurements of tissue, the effect of each user-induced variability source will be isolated in this study.

Recent studies have demonstrated the effectiveness of RS for *in vivo* detection.[10] To our knowledge, previous reports include measurements made with a single instrument, thereby eliminating factors of instrumentation-induced variability. When limited to one instrument, however, multi-system studies or simultaneous data collection from multiple patients are impractical. Unlike other established medical tools, RS lacks standardized methods for system calibration, measurement, processing, data analysis, and reporting. Many Raman systems used in research are assembled from several vendors' components, and while core components remain the same, system response may vary. Even for multi-system studies where investigators will likely have identical or nearly-identical instruments at each collection site, there are currently no reports indicating how measurements from the instruments would compare for tissue spectroscopy applications. Reports on inter-device comparison and cross-validation studies of multiple medical instruments are available for other optical techniques such as confocal spectral imaging, dual energy x-ray absorptiometry, functional magnetic resonance imaging, and fluorescence spectroscopy.[43-47] The only report using RS, by Rodriguez *et al.* addresses chemical analysis.[48] The consistency of pharmaceutical spectra measured across multiple devices suggests that reliable spectral libraries can be generated from Raman spectra of homogeneous samples. Measurements of

tissues, like the skin, pose more rigorous challenges for cross-validation, as the tissue characteristics may vary between location and time of measurement. If system variation is accounted for, RS offers diagnostic potential because it can discriminate between subtle changes in normal, benign, and malignant tissues. Using multiple RS systems during data collection will likely add instrument-dependent variables. If these variables are ignored, changes in the data may be incorrectly attributed to the samples measured and limit diagnostic accuracy. The resulting potential decrease in sensitivity and specificity indicate the need for standardizing RS systems, regardless of the application. This manuscript is concerned with parameters that most likely affect the signals obtained during data collection once the study and research instrument have been developed. To evaluate the influence of utilizing multiple systems on the comparability of Raman spectra, system stability and measurement repeatability will be validated and the effects of instrumentation-induced variability sources will be isolated.

For tissue, physiological variations may exist due to age, gender, race, measurement location, tissue type, thickness, and hydration. Any of these patient variables could be used to distinguish or characterize measurements. Previous *in vivo* Raman studies have demonstrated depth-dependent changes in tissue composition and anatomical location-dependent changes in obtained spectral shape and intensity.[32, 49, 50] Knudsen *et al.* investigated variations in skin Raman spectra between persons, spots on the same body region, repeated

measurements on a single spot, diurnal, day-to-day, and different levels of pigment.[51] In these reports, however, the authors utilized either Raman microspectroscopy, which has different instrumentation considerations than probe-based techniques, or Fourier-Transform Raman Spectroscopy, which has practical limitations for clinical efficacy. Along with the differences between techniques, the reports do not consider the influence of multiple instruments. In this study, the effects of physiologically-induced variability sources will be examined including multiple patients and anatomical locations.

The goal of this study is to examine potential sources of variability for *in vivo* tissue RS, specifically for the skin, and to suggest steps for limiting the influence of confounding factors to standardize Raman for clinical applications. The effects of contact pressure and probe angle were characterized as potential user-induced variability sources. Similarly, the instrumentation-induced variability sources of system stability and system dependent response were also analyzed on skin and a non-volatile biological tissue analog. Physiologically-induced variations were studied on multiple tissue locations and patients. The effect of variability sources on spectral line shape and dispersion was analyzed using statistical methods. In this study, *in vivo* measurements were made on healthy human skin with four stand-alone fiber optic probe-based RS systems. This manuscript reports the results from this study of influential variability sources when comparing Raman spectral measurements of tissue.

A1.3 Methods

A1.3.1 Instrumentation, data processing, & statistical analysis

Raman spectra were acquired using RS systems with similar optical components. Based on what is widely accepted as a standard tissue system, 4 unique instruments were used as described in Table A1.1.[21] Each instrument was controlled by a laptop computer. A custom fiber optic probe consisting of 7 collection fibers (300 μm), without beam-steering modifications, surrounding a central excitation fiber (400 μm) was used to deliver 80mW of power to the sample surface. The tissue was cleaned with an alcohol swab prior to the initial spectral measurement. Spectra were collected with a 3 second acquisition time with the room lights and computer monitor turned off.

Table A1.1. Instrumentation components for standard tissue Raman spectroscopy systems utilized for multiple system comparison.

System	Fiber Optic Probe	Excitation Source	Spectrograph	Detector
1	7x1 fiber optic probe (EmVision LLC, Loxahatchee, Florida)	785nm laser (Process Instruments, Inc., Salt Lake City, Utah, # PI-ECL-785-300)	Holospec f/1.8i imaging spectrograph (Kaiser Optical systems, Ann Arbor, Michigan)	Pixis 256BR CCD camera (Princeton Instruments, Princeton, New Jersey)
2	7x1 fiber optic probe (EmVision LLC)	785nm laser (Innovative Photonics Solutions (IPS), Monmouth Junction, New Jersey, # I0785MM0350MS)	Acton LS 785 imaging spectrograph (Princeton Instruments)	Pixis 400BR CCD camera (Princeton Instruments)
3	7x1 fiber optic probe (EmVision LLC)	785nm laser (IPS, # I0785MU0350MS)	Holospec f/1.8i imaging spectrograph (Kaiser)	Newton DU920-DR-BB CCD camera (Andor Technologies, Belfast, Northern Ireland)
4	7x1 fiber optic probe (EmVision LLC)	785nm laser (IPS, # I0785MM0350MS)	Holospec f/1.8i imaging spectrograph (Kaiser)	Pixis 256BR CCD camera (Princeton Instruments)

Spectral calibration was performed for each system independently using a neon-argon lamp with naphthalene and acetaminophen standards to correct for day to day variations. A National Institute of Standards and Technology-calibrated tungsten lamp was also used to account for the wavelength-dependent response of the instrument. The spectra were processed for fluorescence subtraction and noise smoothing using the modified polynomial fit and Savitzky–Golay methods, as described previously.[24]

Data analysis was performed on the spectral range 900-1800 cm^{-1}, a spectral region rich with information from proteins, lipids, and other tissue constituents. Following data processing, each spectrum was normalized to its mean spectral intensity across all Raman bands to account for intensity variability. This normalization method was chosen to ensure that all wavenumbers retained statistical independence, which is required for statistical analysis and is compromised when spectra are normalized to the intensity of a single peak. Statistical analysis was performed on the data at each relative wavenumber. An Analysis of Variance (ANOVA) model was used at each wavenumber to separate groups and calculate appropriate confidence intervals. To quantify the changes in spectral dispersion between groups of measurements, a metric was defined: total spectral variability ($TSV = \sum_{i=1}^{n} \sigma_i$), or the sum of calculated standard deviation (σ) at each relative wavenumber *i* across the entire spectrum. A common measure of relative dispersion, the coefficient of variation ($CV = \sigma_i/\mu_i$) was also used to compare spectral spread.

The minimum and maximum values of CV for major Raman bands were reported to provide a consistent indicator of variability. The TSV is an absolute measure, indicating the combined dispersion in the measured data, while the CV indicates the variability as a percentage of the spectral mean. Samples with low variability would have TSV values approaching zero and a low range of CV, indicating reproducible and consistent spectral measurements.

A1.3.2 Patients and samples

Since inter-patient differences have been previously addressed by Knudsen *et al.*, volunteers were of similar age and phototype with no history of skin disease; measurements were obtained from multiple, visibly-normal locations avoiding hair follicles, nevi, and other dark spots. Skin is a potentially variable standard that undergoes continuous changes in hydration; therefore, a non-volatile biological tissue analog was also measured in each study to standardize spectral measurement and comparison. In this manuscript, generic intact vitamin E gel capsules were chosen as a homogeneous sample to isolate the impact of each variable, independent of tissue changes. Vitamin E gel capsules were chosen because they have several Raman scattering bands of varying intensity within the fingerprint region. Its peaks are broader than other drug formulations and measurements exhibit broad fluorescence signal likely due to the capsule composition (gelatin and glycerol). The layered composition and spectral traits of the capsules mimic the structure of skin and detected

signals; accordingly, identical collection, processing, and analysis procedures were used to draw comparisons.

A1.3.3 User-induced variability

Contact pressure and probe angle were the user-induced sources investigated. To isolate the impact of probe pressure, force values were quantified while five instrument operators applied probe pressures at three different levels. Raw chicken breast, used as a tissue phantom, was placed on a calibrated scale, and the force applied by each operator was recorded as the operator held the probe in contact with the tissue for 3 seconds. The contact pressure tests were repeated at arbitrarily defined low, medium, and high levels, as perceived by the user. For these tests, operators were instructed that low pressure should minimally indent the skin surface while maintaining contact for the duration of the simulated measurement. Similarly, high pressure should simulate firm, stable contact with tissue that deforms. Subsequent RS measurements were made with calibrated weights attached to a fiber optic probe mounted in a uni-axial stage, as previously described.[42] Spectra were acquired while applying different pressures at levels encompassing the range of values observed during the probe operator tests. The effect of the angle between the tip of the probe and the tissue surface was examined by incorporating a rotational stage into the previous setup. Replicate measurements were acquired in 2° increments up to ±10° from normal and the order randomized to remove

bias. For consistency, all measurements of the skin were obtained from the volar surface (palm side) of the forearm.

A1.3.4 Instrumentation-induced variability

System stability was investigated for drift between collections and measurement repeatability after probe replacement. For measurement repeatability across time, measurements were made from vitamin E and a 1 cm^2 region of skin on the inner surface of the forearm. Measurements were made over the course of 1-1.5 hours at 10 minute intervals in 2 sets over the course of a single day. A uni-axial translation stage held the probe in gentle contact with the sample controlling for pressure and angle. Six time points were collected in the morning and 9 more in the afternoon. For probe replacement, the uni-axial translation stage was used to measure skin and vitamin E controlling for contact pressure and angle of incidence. Repeated collections were acquired with the probe in contact with the sample. Subsequent measurements were made after the probe was translated away from and back into contact with the sample to mimic a controlled replacement of the probe and limit any photobleaching effects.

The performance of the 4 different systems was assessed through measurements of both the skin and vitamin E. Measurements were made of the skin using the systems listed in Table A1.1. All measurements were obtained in a single room on a single afternoon to control for temporal or environmental

effects. Contact pressure, probe angle, and the presence of visible superficial blood vessels were controlled during probe placement.

A1.3.5 Physiologically-induced variability

The measurements obtained with each of the 4 systems were repeated on 5 volunteers (3M, 2F, age 24-28) at multiple anatomical locations. The 5 skin sites measured were: 1) crease in index finger, 2) base of palm, 3) inner surface of forearm, 4) outer surface of forearm, and 5) cheek. In addition, measurements were also made on the inner surface of the forearm above and adjacent to a visibly-appearing large superficial blood vessel to probe the effect of subsurface blood vessels on the acquired spectrum. All measurements were controlled for temporal and environmental variables, as well as for contact pressure, probe angle, and the presence of visible superficial blood vessels. The biological analog was measured with each RS system for reliability analysis. Data was processed as described above.

A1.4 Results

A1.4.1 User-induced variability

Figure A1.1 illustrates the influence of low, medium, and high pressure levels on RS of the skin. Significant differences were found between forces applied by probe operators and between pressure levels applied ($p<0.05$) using a 2-way ANOVA, as indicated by Figure A1.1A. However, significant

differences were not detected between low and moderate pressure levels. The applied pressures, which were subjectively determined by each probe operator, exhibit large standard deviations for each of the three levels. As a result of the bimodal distribution of high pressures applied by probe operators during simulation, an extreme level, which is beyond what is expected for clinical application is included. Raman spectra (n=120) were acquired from normal skin at 22 different force values spanning the 4 pressure levels listed in Table A1.2. The resulting spectra exhibit many visual similarities (Figure A1.1B) as peak positions remained constant across test parameters, but intensities varied. Statistical analysis determined that over 56% of wavenumbers significantly differed between extreme pressure versus high, medium, and low pressure levels at the 95% confidence level, indicated by asterisks in Figure A1.1. By comparison, fewer than 2% of wavenumbers were significantly different between high, medium and low pressures and fewer that 1% of wavenumbers differed between medium and low pressures at the same confidence level.

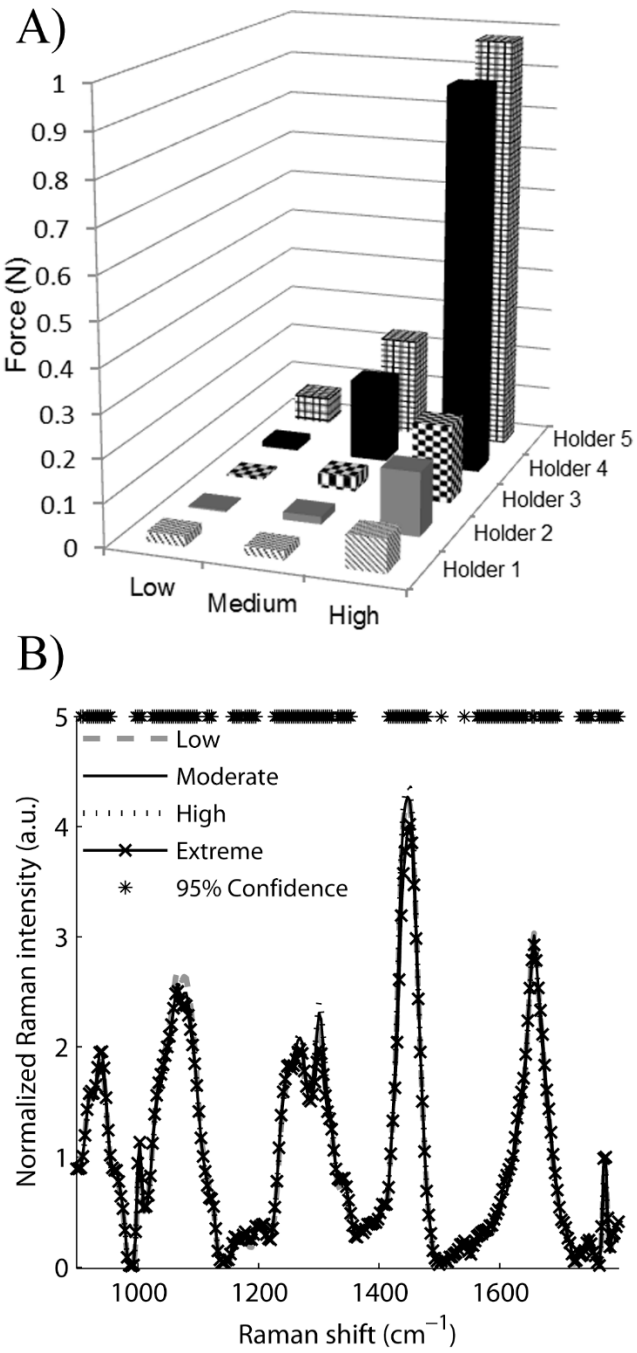

Figure A1.1. (A) Averaged forces applied by probe operators during RS collection simulation. Values were obtained from blinded tests performed on raw chicken breast. (B) Raman spectra acquired from healthy normal skin (volar forearm) during application of probe pressure. Asterisks indicate statistical difference between extreme pressure and other measures.

Raman measurements (n=150) were compared at 11 different angles on the inner surface of the forearm accounting for normal (n=50), counter-clockwise (n=50) and clockwise (n=50) changes in the probe angle. The differences in probe angle had minimal impact on the obtained Raman spectra and resulted in no systematic change in fluorescence or background signal. Mean spectra from each group displayed minor changes in peak intensity. Significant differences between groups occurred in fewer than 5% of wavenumbers (data not shown).

Table A1.2. Contact force ($\mu \pm \sigma$) applied by multiple probe operators during simulated RS collection experiment.

Low	4.4±2.9 mN
Medium	33.8±9.4 mN
High	122.5±39.7 mN
Extreme	645.9±382.3 mN

A1.4.2 Instrumentation-induced variability

In this study, Raman spectra (n=15 for each) of vitamin E and the five anatomical locations on five healthy volunteers were obtained on the four different RS systems. Mean results from the biological analog and one location (cheek) from a single patient are presented for each RS system in Figure A1.2A and B, respectively. The skin spectra obtained were visibly similar and reproducible with minor variations in peak intensities. Significant differences ($p<0.05$) were found among systems at over 50% of the wavenumbers after

system calibration and spectral processing, which was observed across all tissue locations measured.

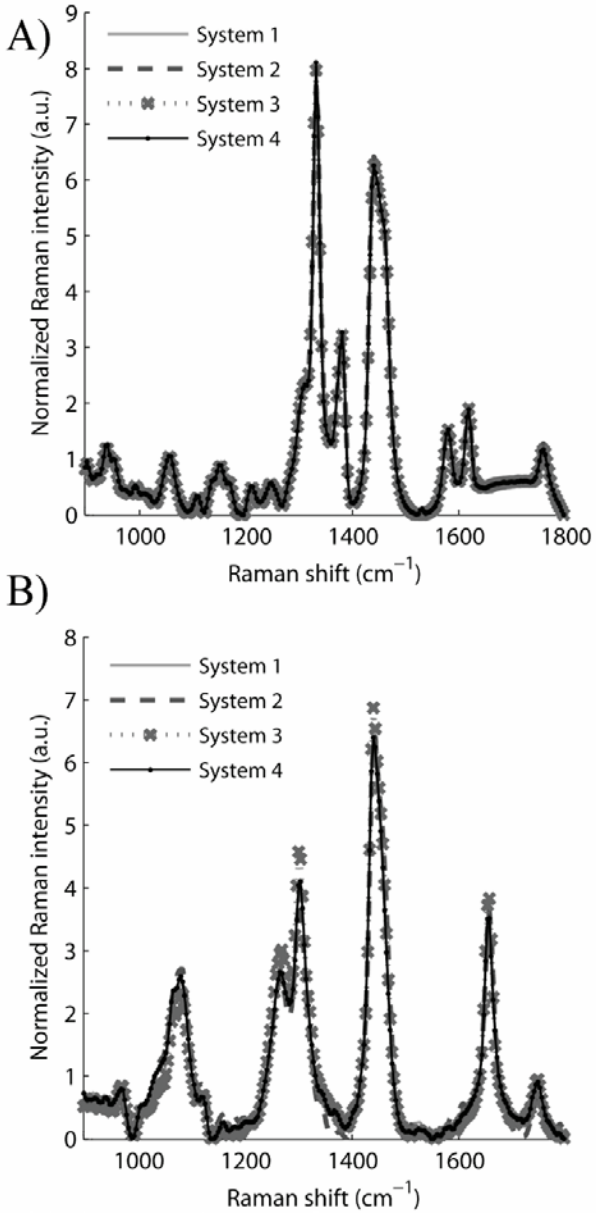

Figure A1.2. (A) Raman spectra of Vitamin E as a biological analog measured by 4 RS systems. Identical signals were obtained after uniform collection and processing algorithms were used. (B) Mean Raman spectra (n=15) of one skin site measured by 4 RS systems.

To test for system stability between measurements, Raman spectra (n=15 for each) were acquired from skin and vitamin E at 15 times over the course of a day. Spectral shape and intensities were reproducible and consistent with the results obtained from 4 different systems. However, changes in spectral intensity of the skin resulted in significant differences ($p<0.05$) for over 50% of wavenumbers after calibration and processing. Measurements for probe placement were compared with measurements after the probe was replaced at nearly the same location via the uni-axial translation stage, to more accurately replicate probe position than replacement by a human operator. After replacement, 5% of wavenumbers significantly differed between the groups for skin (data not shown).

To confirm that the observed variations between spectra were associated with the skin sample, vitamin E was measured during each study protocol. Vitamin E was included to represent a best case scenario as a completely repeatable biological sample, and serves as the benchmark for performance. For all variables considered, including contact pressure, angle, repeatability, probe replacement, and measurements made across systems, there were no systematic differences between vitamin E spectra. For example, as depicted in Figure A1.2A and quantified in Table A1.3, vitamin E spectra acquired across systems after data processing were completely reproducible. Measurements by a single system are expected to have a low total spectral variability (TSV) and CV range. When the data collected from multiple systems are pooled prior to calculation,

the TSV indicates the absolute dispersion induced by data collection with multiple systems, assuming no changes in the sample. A single system had a maximum TSV of 2.84 for vitamin E and 17.44 for a single skin location. Similar trends were demonstrated by the CV for vitamin E peaks, ranging from 0.2-2.73%, while for skin the CV ranged from 1.44-12.06%. The pooled data across all systems for vitamin E had a TSV of 10.92 and maximum CV of 5.47%, while the pooled measurements on a single skin location resulted in a TSV of 36.58 and maximum CV of 26.38%. For both individual system and pooled calculations, the values for a single skin location are higher than for vitamin E. The greater values for skin compared with vitamin E suggests that detected changes are primarily the result of the sample and not the system. Comparison of a single system and pooled data for vitamin E suggests a high level of overlap in the measurements obtained by different RS systems, while more complex interactions are associated with the skin.

Table A1.3. Quantified spectral variability for skin and biological analog for individual RS systems and pooled data. CV range represents the minimum and maximum percentage values obtained at peak maxima for meaningful Raman bands.

Sample	**System**	**TSV (AU)**	**CV Range**
Vitamin E	1	1.79	(0.20% - 1.31%)
	2	2.84	(0.38% - 1.89%)
	3	2.23	(0.26% - 1.79%)
	4	2.69	(0.39% - 2.73%)
Single Skin Site	1	15.34	(1.75% - 10.64%)
	2	17.44	(2.02% - 12.06%)
	3	13.58	(2.05% - 7.39%)
	4	13.04	(1.44% - 9.61%)
Vitamin E	All	10.92	(0.86% - 5.47%)
Skin Site	All	36.58	(5.81% - 26.38%)

A1.4.3 Physiological-induced variability

Raman spectra (n=15) were obtained from each of 5 anatomical locations on the upper extremity and face from 5 healthy volunteers. Based on the results, substantial intra-patient differences are present between unique anatomical locations (Figure A1.3A). Measurements were repeatable across days and patients for each location. The peaks with intensity variations have previously been correlated with tissue protein and lipid content (1440 cm^{-1} and 1750 cm^{-1}) and Amides I (1645-1680 cm^{-1}) and III (1230-1300 cm^{-1}).[52, 53] The spectra group together into spectral families, each having a unique line shape. For example, there are few variations between the spectra acquired from family 1, the finger and palm, but these variations are not consistent with the few variations between family 2, the face and both sides of the arm. As quantified in Table A1.4, when all the data from the 5 sites across a single system are pooled, the TSV is 59.06 and maximum CV is 38.39%. When separated into the two families described above, the values decrease. Combined spectra from the arm and cheek result in a TSV and maximum CV of 35.67 and 28.67%, respectively. The finger and palm spectra have a TSV of 34.36 and maximum CV of 23.26% when combined. When a single location was considered the values were lower still, with a maximum TSV and CV of 18.26 and 7.38%, respectively. The decrease in TSV indicates consistent spectral families when the data is grouped. The CV ranges suggest that the relative dispersion is highly variable for even the most uniform comparison and can increase for a peak as

groups are combined. The families differ in peak intensities at 1440 cm^{-1}, the presence of defined peaks at 1300cm^{-1} and 1750cm^{-1}, and the full width at half maximum (FWHM) intensity of the Amide I band centered at 1658cm^{-1}.

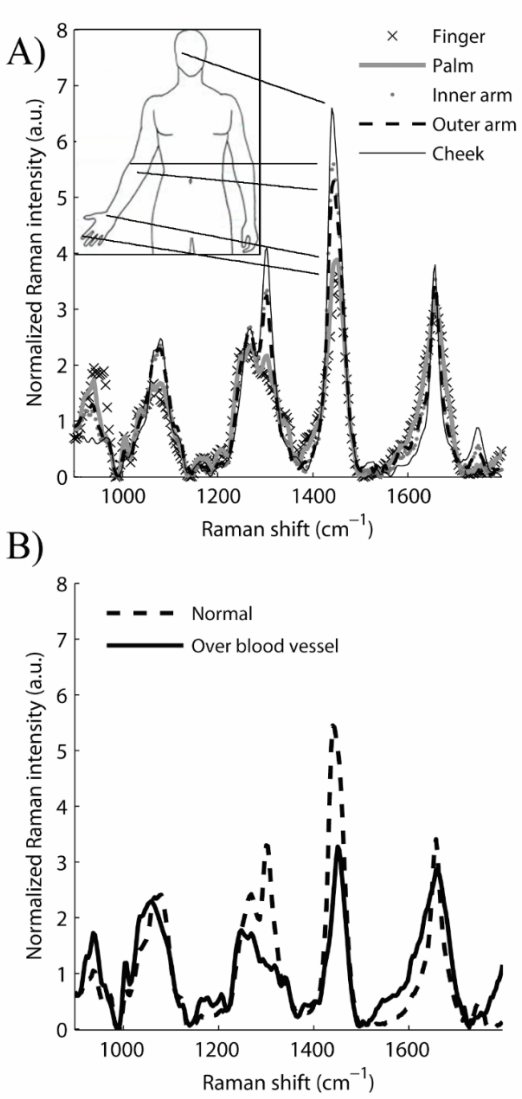

Figure A1.3. (A) Intra-patient location based differences in Raman spectra. (B) Raman spectra acquired from healthy skin above and adjacent to a large superficial blood vessel.

Table A1.4. Quantified RS single system variability for skin sites grouped into spectral families and pooled data. Intra-patient variability is representative and consistent with data obtained from all systems analyzed.

Grouping	TSV (AU)	CV Range
Single Skin Site	18.26	(2.57% - 7.38%)
Family 1	34.36	(5.66% - 23.26%)
Family 2	35.67	(4.76% - 28.67%)
All skin sites	59.06	(5.36% - 38.39%)

To evaluate the effect of superficial blood vessels beneath the sampling volume of a normal measurement, Raman measurements (n=15) were obtained from normal tissue directly above a visible vein and adjacent to the same vein. As Figure A1.3B shows, there are changes in spectral signatures including notable spectral disintegration from 1200-1300 cm^{-1}, decreased intensity at 1440 cm^{-1}, and a broader 1658 cm^{-1} peak, which are all reproducible for measurements above a vessel. When comparing the normal measurements obtained from skin over the vessel in Figure A1.3B to the spectra in Figure A1.3A, the measurements over a vessel on the forearm more strongly resemble the spectral family from the finger than the forearm itself. Grouping spectra from above the vein with those from the adjacent forearm resulted in a TSV of 62.5, compared to 50.6 when grouping above the vein and finger spectra.

Representative mean spectra from multiple systems for 2 locations on a single patient are presented in Figure A1.4. Each location retains the unique spectral signature measured and presented in Figure A1.3A for the finger (site 1) and the cheek (site 2), but measurements from individual systems contribute characteristic variations to the data. With differences in filtering and tissue

fluorescence, the spectral response calibration and signal processing for background removal was unequal between systems and anatomical locations. Despite the systematic effects on data collection by each instrument, the data still group consistently into spectral families with similar line shape.

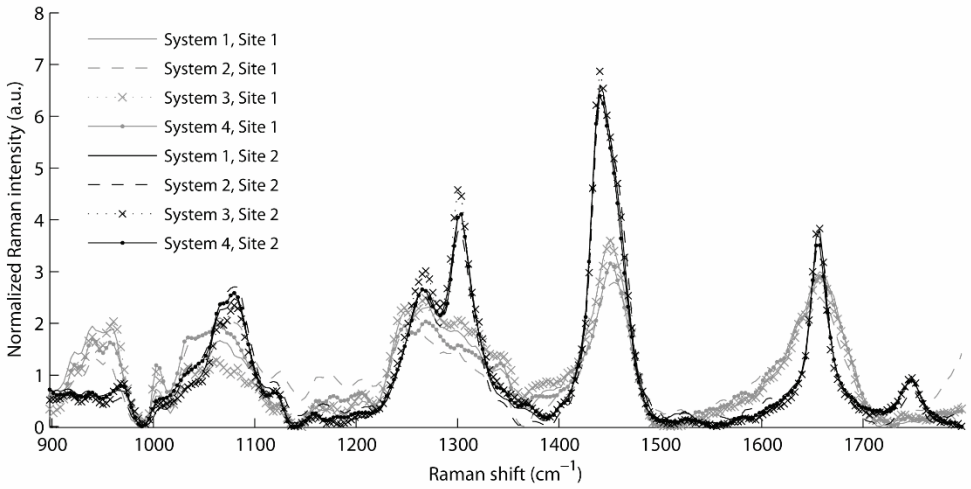

Figure A1.4. Raman spectra from 2 anatomical locations on a single patient measured on 4 RS systems.

Figure A1.5 extends the previous analysis to include multiple patients and depicts spectral changes associated with locations on multiple patients measured with different systems. The results mirror those of multiple locations on a single patient, where strong location-specific signals are present and repeatable between patients and system-based changes impact each measurement similarly. Measurements from a single location resulted in a consistent spectral line shape between patients and systems. However, the intensity of acquired spectra differed between patients and between systems. This is most clearly depicted in Figure A1.5 by grouping site 2 measurements.

Also, the intensities for spectra from patient 1 exhibit low dispersion compared to the spread of patient 2 spectra. This effect is most obvious at the peak intensities for 1440 cm^{-1} (CH_2 bending) and 1300 cm^{-1} (Amide III CH stretch).

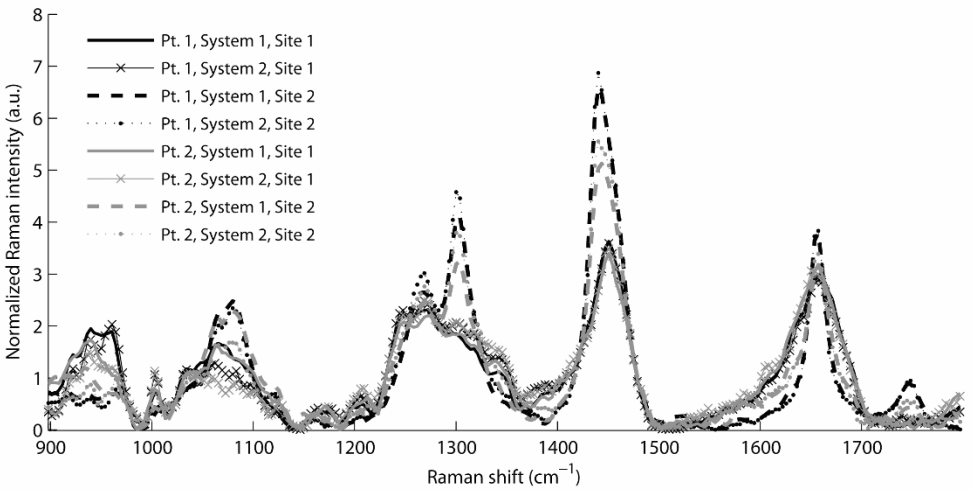

Figure A1.5. Representative Raman spectra of 2 anatomical locations reproduced for 2 patients measured on 2 RS systems.

Based on the ANOVA analysis presented in Figure A1.6 for the complete block design of measurements made from 5 locations on 5 people with 4 instruments, the intra-patient variation ("Location") is the most influential factor. The inter-patient differences in the spectra account for less than 7% of the variance from the entire dataset. This value was minimized by controlling for inter-patient variables prior to the study. The inter-patient differences were insignificant compared to 29.7% contribution from system and 48.9% from location. The interaction between inter-patient and intra-patient differences is consistent with the patient-specific changes presented in Figure A1.5. These results are in agreement with both the TSV and CV range values from Table

A1.3 and Table A1.4, such that, by controlling parameters, the intra-patient variation (location) is more influential than system-induced variation.

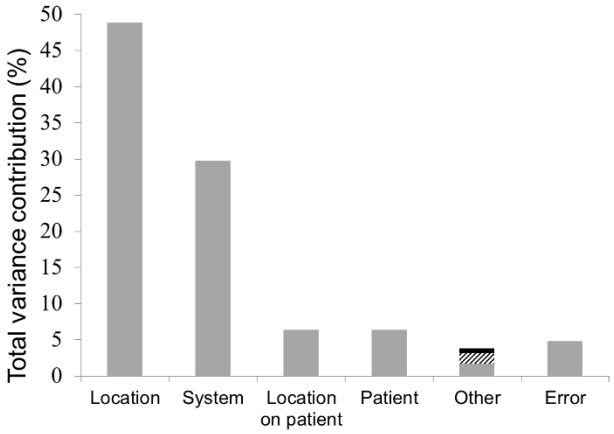

Figure A1.6. Percent contribution by source and interaction terms to the variance of RS data. The presence of the "Location on Patient" interaction term indicates that a location may take a unique intensity level for each patient measured. Non-significant interaction terms are combined in "Other" and represent less than 4% of total variance.

A1.5 Discussion

Previous studies have investigated the use of RS to detect changes in tissue for numerous applications, but few have addressed the latent sources for variability during measurement or the potential issues when comparing biological measurements between systems. The initial goal of this study was to understand how different sources of variability impact the measured Raman spectra of tissue. While this study has focused on skin as the tissue of interest, subsequent investigations should consider the influence of variability sources on other clinical applications and targets of RS. An obstacle to testing these variables in tissue is the inherent inconsistency and sample inhomogeneity. To

avoid this innate biological variation, a biological tissue analog, vitamin E, was introduced as an ideal tissue that is not subject to variation and presents the best-case for measurement reproducibility. In this paper, Raman spectra acquired from both normal tissue and vitamin E are evaluated for the effects of three broad categories: user-induced, instrumentation-induced, and physiologically-based sources of variability.

A1.5.1 User-induced variability

As a new and increasingly-used clinical tool, RS users need to understand the impact of contact pressure and fiber probe angle on obtaining consistent and accurate results regardless of the user. Analysis in this study found no significant differences or increased variability introduced when user-induced factors were properly controlled. Even with high variability in the subjectively determined pressure exerted by different probe operators, demonstrated in Figure A1.1A, spectra with low variability were obtained. The results of applying varying pressure during spectral measurement suggest that a range of applied pressures are acceptable for collecting reproducible and reliable Raman spectra (Figure A1.1B and Table A1.2). Spectral change was observed only in measurements made under extreme pressure, in this case over 55kPa. Previous studies have shown that increasing pressure can change the interactions between light and tissue, for example by decreasing fluorescence and increasing optical penetration depth.[21-23, 34] Increased probe pressure will compress the tissue and more densely pack Raman active molecules, potentially

leading to more frequent Raman scattering events. Likewise, increased pressure could lead to occlusion under the tip of the probe, altering perfusion and blood content within the sample. The acceptable range of applied pressures may depend on variable thickness, hydration, elasticity, or other patient, location, or age related changes. In general, however, the probe should minimally or reversibly displace the tissue surface and remain in contact during the measurement. The increased variability introduced by high contact pressure can be avoided if users are trained to operate under low pressures.

By changing the angle of contact between the probe and sample, the volume of tissue being measured will change as the light scatters. Despite this subtle change in interrogated tissue, few significant spectral differences were collected between signals over the range of measured angles. The sampling volumes of fiber-optic probes are relatively large compared with tissue structures, yielding a low probability that a slight variation in probe angle will cause dramatic changes in the spectrum. However, because probe collection geometries have many designs, slight variations in probe angle may collect signal from a different location than intended. Probe operators should understand the importance of using consistent angles between measurements.

A1.5.2 Instrumentation-induced variability

The common practice of using a single instrument during data collection has had both positive and negative consequences for RS. While it has simplified

data interpretation for researchers by removing a significant variable, it has also hindered both data comparison and spectral database development, which are prerequisites for generating reliable diagnostic algorithms. In this study, the contribution of instrumentation-induced variability to the acquired spectra was validated and quantified for several potential sources. Variability between repeated measurements for time points and probe placement was found to be insignificant, confirming previous reports.[51] During Raman measurements, instrumentation-induced variability was considered a system dependent response. This is demonstrated in Figure A1.2B, where minimal intensity differences between systems were detected within a single location of the skin. These small differences were obtained after spectral response calibration, processing, and normalization, which are important steps in reducing differences between instruments. However, these steps alone may not be sufficient to remove the effects of multiple instruments and probes. Spectral response calibration accounts for only the detection arm of an RS system and requires system isolation for calibration, which is impractical in a clinical setting. Other data processing options are currently under investigation. Because probe-based RS systems can have variable components, calibration methods need to account for the specific and collective responses of the system. Several research groups, including ours, have proposed the use of reflective standards or other similar calibration techniques that account for both excitation and collection branches of the system to address and potentially minimize these

responses. When comparing spectra from a single location measured by multiple systems, as presented in Figure A1.2, there are no significant differences. However, comparing spectra from a different tissue location or patient (Figure A1.4 and Figure A1.5), these signals are complicated by other factors.

Isolating system-dependent responses with vitamin E also generated negligible differences in spectra acquired by different instruments after processing. The narrow range of detected Raman signal for the biological analog, depicted in Figure A1.2A, confirm the instrument stability and reliability which is needed for cross-validation and spectral library generation. As the interrogated sample becomes more heterogeneous, the complex interactions of inherent scattering and system-dependent response increase spectral variability. This result is demonstrated in Table A1.3, where the sum of TSV for vitamin E of individual systems is approximately equal to the pooled value for all systems. In contrast, the TSV for skin of separate systems are individually half the value for the data pooled for all systems, demonstrating that the complexity of skin results in increased variability that differs between RS systems. For measurements made with separate RS systems, users must understand the implications for cross-system comparison and determine how spectral changes introduced by separate instruments will influence the diagnostic capability of an algorithm. Using a biological analog can aid in

evaluating multiple RS instruments for consistent measurement and comparison of tissue spectra.

A1.5.3 Physiologically-induced variability

Variability sources based on characteristic tissue differences between multiple locations on a single patient and between patients were identified as important factors for RS of the skin. The anatomical location analysis yielded spectra with visibly and statistically significant differences (Figure A1.3A). This result is consistent with knowledge of the heterogeneity of skin anatomy. Multiple studies have documented the anatomical location-based changes in many skin properties including thickness, presence of hair, tissue hydration, pigmentation, sun exposure/damage, subsurface structures, and compositional differences of lipids and proteins.[9, 54-56] Raman scattering signals from different anatomical locations are distinct, so tracking where such measurements are made is critical when comparing across locations. Separating the anatomical locations into distinct spectral families, based on intensity and line shape as in Table A1.4, may be a more thorough comparison of physiologically-induced changes that are not directly caused by variations in the measurement location.

Statistical analysis reveals that the spectral variance and primary source of variability depends on peak intensity. TSV is dominated by fluctuations in peak intensity of major Raman active bands, with 1440 cm^{-1} (CH_2 bending) accounting for nearly 30% of total variability in the data and 1300 cm^{-1} (Amide III CH stretch) for another 10%. Despite accounting for intensity, the maximum

CV reported for each group is mediated by fluctuations in peak intensity and can be amplified for low peaks and shoulders. Physiologically-induced variability, due to measurement location, dominates the dispersion sources when comparing multiple anatomical locations for a single system and appears at strong Raman peaks. Instrumentation-induced variability dominates regions of peak shoulders and background subtraction when comparing a single measurement location across different systems.

Significant spectral differences were also observed between patients (Figure A1.5). Studies from our lab and others have reported the sensitivity of RS to patient-based variables.[51, 57] Some of the potential variables that may contribute to the observed inter-patient changes in spectral signature for normal healthy skin include hormonal variations, BMI, gender, race/ethnicity, age, accumulated photodamage/UV exposure, and skin type. Knudsen *et al.* reported significant peak intensity ratio differences between patients, which agree with findings presented here. In that report, a single location across 13 patients yielded mean values ranging from 0.94-1.15 for the intensity ratio of Amide I (1660 cm^{-1})/CH_2 bending (1440 cm^{-1}). The mean values measured between patients here ranged from 0.70-0.76 for this ratio. The differences between the reported peak ratios are likely the result of variations in study equipment and processing procedures. However, the variation in values is consistent between reports, indicating inter-patient changes detected in the skin. Further analysis of our data suggests that these ratios are dependent upon location of the

measurement. The mean values obtained here range from 0.86 on the hand to 0.56 on the cheek of a single patient.

To simplify comparisons between patients, age and skin type were controlled. The inter-patient differences detected here demonstrate minor spectral changes when controlling for other variability sources. Physiological variability between locations within a single patient has been reported in the literature and suggests the need to account for anatomical site prior to comparison.[49] A potential method to overcome these variations would utilize paired spectral measures, or the collection of adjacent and contralateral normal measurements for each measurement of interest. Difference spectra between the variable and paired normal locations would normalize a measurement to its inherent location-based signal, which could remove influences of intra-patient variation. Selection of the location for a paired measurement is critical due to the location-based variability in signal. A further complication is introduced by the presence of superficial blood vessels beneath the measurement location. The obtained spectrum from atop the vessel neither replicates skin measurements nor the reported spectra of blood, suggesting that signal changes are not derived from the blood alone.[7, 32] While the source of the altered spectrum is currently unclear, some potential physiological explanations include the components of the vessel wall, muscles lining vessels, increased collagen content and microvasculature surrounding these vessels, as well as the blood cells and serum proteins in the measurement area. The results in Figure A1.3B suggest

that paired measurements should come from adjacent or contralateral locations of normal tissue, avoiding hair and visible superficial blood vessels. Adjacent measurements from the same small area of tissue were found to be reproducible, but the total size of this area is unknown. In general, the closer the paired measurement to the original measurement location, the more likely a measurement will account for normal variations.

Statistical comparison indicated that anatomical location most significantly impacts collected data, followed by instrumentation-induced variability and inter-patient changes (Figure A1.6). These findings mirror conclusions drawn from the TSV and CV range values and suggest that when patient variables are controlled, the detected inter-patient differences exert less influence on the data than alternate sources. The significant interaction term ("Location on patient") is likely the result of inter-patient variation that affects intra-patient changes. Each patient will have unique effects on the spectra that will cause individual anatomical location to vary in intensity. The presence of this interaction complicates the interpretation and impact of multiple patients. As all other interaction terms combined have little influence, it is logical to conclude that the primary concerns for spectral variability will be the effects from anatomical location, system, and patient based differences. These patient specific differences may become the dominant source as a more diverse population of normal tissues is analyzed. This result further emphasizes the need to control for the measurement location.

Because the influence of a particular source of variation is not uniform across the spectrum, understanding and minimizing variability sources is important. Through ANOVA of spectra at each wavenumber, the relative impact of each source of variability can be discerned. Spectral libraries and algorithms for diagnosis or tissue classification need to perform independently of these confounding variability sources. Algorithms may need to account for the variances introduced by multiple instruments or compare spectral regions that are dominated by a common variability source. For example, the intensity of CH_2 bending (1440 cm^{-1}) is dominated by physiologically-induced variability, while the FWHM of the 1070 cm^{-1} feature, which is linked in-part to silica fiber signal, is dominated by instrumentation-induced variability. A ratio of these features would give inconsistent and instrument-dependent results. The dispersions of strong Raman active bands are associated with differences in anatomical location and should be used for intra- and inter-patient comparison. Comparing regions of background subtraction will represent variations between multiple instruments.

The purpose of this paper is to examine different sources of variability that can impact *in vivo* RS measurements of tissue and to suggest steps for limiting the influence of these confounding factors. Table A1.5 briefly outlines the sources examined and the influences detected. These results indicate that, when properly used, contact pressure, probe angle, and probe replacement have no significant contribution to spectral variance. The use of multiple RS

instruments will undoubtedly introduce some variation into the collected data, but options to limit these influences are under investigation. Despite these findings, thorough analysis of the potential sources of measurement error should be conducted with any system to understand the obtained results, ideally prior to the beginning of the study. We suggest that several steps be taken during the design and execution of *in vivo* RS tissue measurements to address potential sources of variability. These steps are as a follows: 1) Standardized tissue cleaning protocols, such as cleaning with an alcohol swab, should be used to minimize error contribution (especially for measurements of the skin due to cosmetics and lotions); 2) Measurements with the probe should use low but consistent pressure during collection, keeping the probe approximately normal to the surface (user should be trained); 3) For normal measurements, a single collection per location is sufficient; 4) Paired measurements may provide normalization of a spectrum to the inherent signal based on anatomical location and person specific signals; 5) The selection of the location for a normal paired measurement should be carefully determined, avoiding hair follicles and major superficial blood vessels. Furthermore, adjacent and contralateral normal measurements at a single location should be investigated for consistency.

Table A1.5. Variability sources investigated and determined effects.

Variable	Effect
Contact pressure	For low or medium pressure, no detected effect High pressure, significant effect detected
Probe angle	No detected effect
Probe replacement	No detected effect
Instrument stability	No detected effect for biological analog Significant effect detected between tissue measurements
Multiple instruments	No detected effect for biological analog Significant effect detected for biological samples
Anatomical location	Significant effect detected
Presence of blood vessel	Significant effect detected
Inter-patient	Significant effect; Minimized by controlling patient variables

A1.6 Conclusions

In general, these findings apply to probe-based measurements for all optical modalities; other collection configurations, such as confocal microspectroscopy, will likely contain alternate variability sources to address. Practically, normal tissues are not often studied, as they are not the focus of a novel diagnosis or treatment. The default assumption is that all normal samples are similar; however, complex interrelationships and differences between separate normal tissues exist. By expanding our understanding of normal tissues and the influence of data collection and instrumentation, the potential exists for more accurate and effective analyses to differentiate unique variables of interest. The analytic methods for RS should consider the major sources of variance contribution prior to the development of classification algorithms. Thorough analysis of instrument response, stability, and calibration are important to standardize RS as a clinically viable tool. Measurements by

separate instruments will likely exhibit unique responses. If these variations are understood and accounted for, measurements can be compared across systems and spectral libraries can be compiled. Here, practical considerations and results are presented that suggest how RS can and should be used *in vivo* to minimize sources of variation prior to processing, comparison, and classification, leading to an application that can be used to accurately differentiate disease classes.

A1.7 Acknowledgements

The authors acknowledge the financial support of the National Institutes of Health Grant No. R01-CA-095405 and Dept. of Defense Grant No. BC085165. Special thanks to Christine O'Brien, Chetan Patil, and Quyen Nguyen for their help and to Amy Rudin for proofreading this paper.

A1.8 References

1. E. M. Kanter, S. Majumder, E. Vargis, A. Robichaux-Viehoever, G. J. Kanter, H. Shappell, H. W. Jones, 3rd, and A. Mahadevan-Jansen, Journal of Raman spectroscopy : JRS **40**, 2, 205 (2009).
2. E. M. Kanter, E. Vargis, S. Majumder, M. D. Keller, E. Woeste, G. G. Rao, and A. Mahadevan-Jansen, J Biophotonics **2**, 1-2, 81 (2009).
3. A. Mahadevan-Jansen, M. F. Mitchell, N. Ramanujam, A. Malpica, S. Thomsen, U. Utzinger, and R. Richards-Kortum, Photochem Photobiol **68**, 1, 123 (1998).
4. A. Mahadevan-Jansen, W. F. Mitchell, N. Ramanujam, U. Utzinger, and R. Richards-Kortum, Photochemistry and Photobiology **68**, 3, 427 (1998).

5. P. Crow, A. Molckovsky, N. Stone, J. Uff, B. Wilson, and L. M. WongKeeSong, Urology **65**, 6, 1126 (2005).

6. Z. Huang, A. McWilliams, H. Lui, D. I. McLean, S. Lam, and H. Zeng, Int J Cancer **107**, 6, 1047 (2003).

7. P. J. Caspers, G. W. Lucassen, and G. J. Puppels, Biophys J **85**, 1, 572 (2003).

8. M. E. Darvin, C. Sandhagen, W. Koecher, W. Sterry, J. Lademann, and M. C. Meinke, J Biophotonics (2012).

9. M. Gniadecka, O. Faurskov Nielsen, D. H. Christensen, and H. C. Wulf, J Invest Dermatol **110**, 4, 393 (1998).

10. H. Lui, J. Zhao, D. McLean, and H. Zeng, Cancer Res **72**, 10, 2491 (2012).

11. A. Nijssen, T. C. B. Schut, F. Heule, P. J. Caspers, D. P. Hayes, M. H. A. Neumann, and G. J. Puppels, Journal of Investigative Dermatology **119**, 1, 64 (2002).

12. J. Zhao, H. Lui, D. I. McLean, and H. Zeng, Skin Res Technol **14**, 4, 484 (2008).

13. M. V. Schulmerich, J. H. Cole, J. M. Kreider, F. Esmonde-White, K. A. Dooley, S. A. Goldstein, and M. D. Morris, Appl Spectrosc **63**, 3, 286 (2009).

14. M. V. Schulmerich, K. A. Dooley, M. D. Morris, T. M. Vanasse, and S. A. Goldstein, J Biomed Opt **11**, 6, 060502 (2006).

15. A. S. Haka, K. E. Shafer-Peltier, M. Fitzmaurice, J. Crowe, R. R. Dasari, and M. S. Feld, Cancer Res **62**, 18, 5375 (2002).

16. A. S. Haka, Z. Volynskaya, J. A. Gardecki, J. Nazemi, J. Lyons, D. Hicks, M. Fitzmaurice, R. R. Dasari, J. P. Crowe, and M. S. Feld, Cancer Res **66**, 6, 3317 (2006).

17. M. S. Bergholt, W. Zheng, K. Lin, K. Y. Ho, M. Teh, K. G. Yeoh, J. B. So, and Z. Huang, J Biomed Opt **16**, 3, 037003 (2011).

18. X. Bi, A. Walsh, A. Mahadevan-Jansen, and A. Herline, Dis Colon Rectum **54**, 1, 48 (2011).

19. A. Molckovsky, L. M. W. K. Song, M. G. Shim, N. E. Marcon, and B. C. Wilson, Gastrointestinal Endoscopy **57**, 3, 396 (2003).

20. M. G. Shim, L. M. Song, N. E. Marcon, and B. C. Wilson, Photochem Photobiol **72**, 1, 146 (2000).

21. M. D. Keller, E. M. Kanter, and A. Mahadevan-Jansen, Spectroscopy **21**, 11, 33 (2006).

22. C. J. Frank, D. C. Redd, T. S. Gansler, and R. L. McCreery, Anal Chem **66**, 3, 319 (1994).

23. A. C. Williams, H. G. M. Edwards, and B. W. Barry, International journal of pharmaceutics **81**, 2-3, R11 (1992).

24. C. A. Lieber and A. Mahadevan-Jansen, Applied Spectroscopy **57**, 11, 1363 (2003).

25. J. T. Motz, S. J. Gandhi, O. R. Scepanovic, A. S. Haka, J. R. Kramer, R. R. Dasari, and M. S. Feld, J Biomed Opt **10**, 3, 031113 (2005).

26. J. Serup, B. E. Jemec, and G. L. Grove, *Handbook of non-invasive methods and the skin* (CRC/Taylor & Francis, 2006).

27. E. B. Hanlon, R. Manoharan, T. W. Koo, K. E. Shafer, J. T. Motz, M. Fitzmaurice, J. R. Kramer, I. Itzkan, R. R. Dasari, and M. S. Feld, Physics in medicine and biology **45**, 2, R1 (2000).

28. A. Alimova, R. Chakraverty, R. Muthukattil, S. Elder, A. Katz, V. Sriramoju, S. Lipper, and R. R. Alfano, Journal of photochemistry and photobiology. B, Biology **96**, 3, 178 (2009).

29. J. Wohlrab, A. Vollmann, S. Wartewig, W. C. Marsch, and R. Neubert, Biopolymers **62**, 3, 141 (2001).

30. L. Chrit, P. Bastien, G. D. Sockalingum, D. Batisse, F. Leroy, M. Manfait, and C. Hadjur, Skin Pharmacol Physiol **19**, 4, 207 (2006).

31. T. R. Hata, T. A. Scholz, I. V. Ermakov, R. W. McClane, F. Khachik, W. Gellermann, and L. K. Pershing, J Invest Dermatol **115**, 3, 441 (2000).

32. P. J. Caspers, G. W. Lucassen, E. A. Carter, H. A. Bruining, and G. J. Puppels, J Invest Dermatol **116**, 3, 434 (2001).

33. M. Gniadecka, H. C. Wulf, O. F. Nielsen, D. H. Christensen, and J. Hercogova, Photochem Photobiol **66**, 4, 418 (1997).

34. K. L. A. Chan, G. J. Zhang, M. Tomic-Canic, O. Stojadinovic, B. Lee, C. R. Flach, and R. Mendelsohn, Journal of Cellular and Molecular Medicine **12**, 5B, 2145 (2008).

35. N. J. Crane and E. A. Elster, J Biomed Opt **17**, 1, 010902 (2012).

36. M. Egawa, T. Hirao, and M. Takahashi, Acta dermato-venereologica **87**, 1, 4 (2007).

37. E. E. Lawson, H. G. Edwards, B. W. Barry, and A. C. Williams, Journal of drug targeting **5**, 5, 343 (1998).

38. A. C. Williams, B. W. Barry, H. G. Edwards, and D. W. Farwell, Pharm Res **10**, 11, 1642 (1993).

39. A. Cerussi, S. Siavoshi, A. Durkin, C. Chen, W. Tanamai, D. Hsiang, and B. J. Tromberg, Appl Opt **48**, 21, 4270 (2009).

40. A. Nath, K. Rivoire, S. Chang, D. Cox, E. N. Atkinson, M. Follen, and R. Richards-Kortum, J Biomed Opt **9**, 3, 523 (2004).

41. R. Reif, M. S. Amorosino, K. W. Calabro, O. A'Amar, S. K. Singh, and I. J. Bigio, J Biomed Opt **13**, 1, 010502 (2008).

42. Y. Ti and W. C. Lin, Opt Express **16**, 6, 4250 (2008).

43. P. Colombo, A. Baldassarri, M. Del Corona, L. Mascaro, and S. Strocchi, Magnetic resonance imaging **22**, 1, 93 (2004).

44. L. Friedman, G. H. Glover, D. Krenz, and V. Magnotta, Neuroimage **32**, 4, 1656 (2006).

45. Y. Guo, P. W. Franks, T. Brookshire, and P. Antonio Tataranni, Obesity research **12**, 12, 1925 (2004).

46. B. M. Pikkula, O. Shuhatovich, R. L. Price, D. M. Serachitopol, M. Follen, N. McKinnon, C. MacAulay, R. Richards-Kortum, J. S. Lee, E. N. Atkinson, and D. D. Cox, J Biomed Opt **12**, 3, 034014 (2007).

47. R. M. Zucker and J. M. Lerner, Microsc Res Tech **68**, 5, 307 (2005).

48. J. D. Rodriguez, B. J. Westenberger, L. F. Buhse, and J. F. Kauffman, Analyst **136**, 20, 4232 (2011).

49. P. J. Caspers, G. W. Lucassen, R. Wolthuis, H. A. Bruining, and G. J. Puppels, Biospectroscopy **4**, 5 Suppl, S31 (1998).

50. M. S. Bergholt, W. Zheng, K. Lin, K. Y. Ho, M. Teh, K. G. Yeoh, J. B. Y. So, and Z. W. Huang, Journal of Biomedical Optics **16**, 3 (2011).

51. L. Knudsen, C. K. Johansson, P. A. Philipsen, M. Gniadecka, and H. C. Wulf, Journal of Raman Spectroscopy **33**, 7, 574 (2002).

52. B. W. Barry, H. G. M. Edwards, and A. C. Williams, Journal of Raman Spectroscopy **23**, 11, 641 (1992).

53. A. Mahadevan-Jansen and R. Richards-Kortum, Journal of Biomedical Optics **1**, 1, 31 (1996).

54. R. S. Greene, D. T. Downing, P. E. Pochi, and J. S. Strauss, J Invest Dermatol **54**, 3, 240 (1970).

55. K. Robertson and J. L. Rees, Acta dermato-venereologica **90**, 4, 368 (2010).

56. J. Sandby-Moller, T. Poulsen, and H. C. Wulf, Acta dermato-venereologica **83**, 6, 410 (2003).

57. E. Vargis, T. Byrd, Q. Logan, D. Khabele, and A. Mahadevan-Jansen, J Biomed Opt **16**, 11, 117004 (2011).